UNIVERSITY OF CALIFORNIA SAN DIEGO

Roles and regulation of nonbilayer lipids in biological membranes

A Dissertation submitted in partial satisfaction of the requirements

for the degree Doctor of Philosophy

in

Biochemistry and Molecular Biophysics with a Specialization in Multiscale Biology

by

Daniel Milshteyn

Committee in charge:

Professor Itay Budin, Chair
Professor Neal Devaraj
Professor Tatiana Mishanina
Professor Padmini Rangamani
Professor Johannes Schonenberg

2026

The Dissertation of Daniel Milshteyn is approved, and it is acceptable in quality and form for publication on microfilm and electronically.

University of California San Diego

2026

TABLE OF CONTENTS

LIST OF FIGURES

LIST OF TABLES

ACKNOWLEDGEMENTS

I would like to foremost acknowledge my parents, Viktoriya and David, and brother, Mark, as well as my grandmothers, Bella and Lida. Immigrating from Uzbekistan following the collapse of the Soviet Union, my parents have tirelessly worked to support my upbringing and education. My mom's unbounded selflessness and my dad's work ethic established core values that have guided me throughout my life, while my grandmas instilled a curiosity and love for nature which led me to pursue biology. I would like to thank my brother for being supportive and understanding throughout my education. I feel so proud to watch him grow and develop into a mature, considerate, and clever teenager. I cannot thank my family enough for their patience, support, and for believing in me.

Starting my PhD at the height of the COVID pandemic in 2020, I was kindly welcomed into the Budin Lab by Dr. Hyesoo Kim, Dr. Israel Juarez-Contreras, Dr. William Moore, and Dr. Yi-Ting (Meli) Tsai. This group provided a supportive community in which I felt comfortable to ask questions, make mistakes, and start developing my skills in cell biology and lipid biochemistry. I am very grateful for all our hangouts, travels, and shared meals. Joining the lab with Dr. Kailash Venkatraman, I made an unexpected and lifelong friend who I grew alongside through all the highs (dream team summer 2023) and lows (leaving cyclohexane in lipid SAXS samples). I would also like to thank the lab mates that came after me, Olivia Seidel, Kelly Isbell, Adrian Wong, Emma Dunbar, Elida Kocharian, and Riley Lehman for making a safe and healthy lab environment. Each of them shines a light that makes coming into lab a joy. Through the hardest of times, they have all supported me with calmness, humor, and empathy which I do not think I would have completed my PhD without.

Throughout the most challenging stretches of time during my graduate studies, my relationships outside of work served as a strong grounding force and escape. I am grateful to have maintained connections with two of my oldest friends, Boris Rybalov and Timur Katsnelson, who I have known since elementary school. Halfway through my PhD, Boris and I started to backpack in the Sierra Nevada mountains, completing parts of the John Muir Trail and summiting Half Dome in Yosemite. These trips are some of my favorite memories and both gave me something to look forward to and come back from with refreshed motivation. My Santa Cruz friends Webster Quoc Nguyen, Zachary Rowson, Hattie Fletcher, Maia Hoffman, and Norah Hayden provided some of the greatest support helping me get away from San Diego when I needed it the most. I am forever grateful for the travels, camping trips, and crazy conversations we share. Close to the end of my PhD, I was lucky to meet my partner Olivia and bond with her over our love for music. I have come to learn what a compassionate, selfless, and passionate person she is and I am grateful to have a partner that is so supportive.

Finally, I would like to acknowledge Professor Itay Budin and Dr. Jacob Winnikoff for being great mentors, pushing me, and believing in me. From the start, Professor Budin has pushed me to pursue my own ideas and not be afraid to go outside of my comfort zone. He supported my development as a scientist with hands on teaching, productive criticism, and giving me the space to struggle, be creative, and think through scientific challenges. Professor Budin has given me countless opportunities to pursue a wide breadth of scientific topics by supporting my training in super resolution microscopy; cross-country travel to facilities with high pressure instrumentation at Cornell University, Harvard University, and the Rensselaer Polytechnic Institute; and international travel to conferences and a research cruise in Uruguay. So much of what I have learned throughout my PhD has come from Jacob's selflessness, work ethic, and encyclopedic

knowledge. Through many sleepless nights preparing samples and doing experiments, Jacob taught me how to analyze data, think carefully about experimental design, and work through scientific problems with rigorous controls and creativity.

Chapter 1, in part, is currently being prepared for submission for publication of the material. “Make room for dynamics: roles of nonbilayer lipids in the daily lives of cells”. Milshteyn, Daniel; Budin, Itay. The dissertation author is the primary researcher and author of this material.

Chapter 2, in full, is a reprint of the material as it appears in “Homeocurvature adaptation of phospholipids to pressure in deep-sea invertebrates”. Winnikoff, Jacob R; Milshteyn, Daniel; Vargas-Urbano, Sasiri J; Pedraza-Joya, Miguel A; Armando, Aaron M; Quehenberger, Oswald; Sodt, Alexander; Gillilan, Richard E; Dennis, Edward A; Lyman, Edward; Haddock, Steven HD; Budin, Itay. *Science*. 2024. The dissertation author was a primary investigator and second author of this paper.

Chapter 3, in full, is a reprint of the material as it appears in “Homeostatic regulation of intrinsic lipid curvature in eukaryotic cells”. Milshteyn, Daniel; Winnikoff, Jacob R; Kocharian, Elida; Armando, Aaron M; Dennis, Edward A; Girguis, Peter R; Budin, Itay. *Cell Reports Physical Science*. 2026. The dissertation author was a primary investigator and first author of this paper.

Chapter 4, in part, is currently being prepared for submission for publication of the material. “Energetics of stalk intermediates elucidated from hydrostatic pressure effects on membrane fusion”. Milshteyn, Daniel; Winnikoff, Jacob R; Morgan, Joel E; Golani, Gonen; Budin, Itay. The dissertation author is the primary researcher and author of this material.

VITA

2018 Bachelor of Science in Biomolecular Engineering, University of California Santa Cruz

2022 Master of Science in Chemistry, University of California San Diego

2026 Doctor of Philosophy in Biochemistry and Molecular Biophysics with a Specialization in Multiscale Biology, University of California San Diego

PUBLICATIONS

1. Venkatraman K, **Milshteyn D,** Sarto C, Kocharian E, Sakurai CM, Armando AM, Wong AM, Dennis EA, Fang Xi, Lee CT, Budin I. Saturated cardiolipins are potent disruptors of inner mitochondrial membrane structure and function. *Journal of Biological Chemistry*. In revision.
2. **Milshteyn D**, Winnikoff JR, Kocharian E, Armando AM, Dennis EA, Girguis PR, Budin I. Homeostatic regulation of intrinsic lipid curvature in eukaryotic cells. *Cell Reports Physical Science*. 2026
3. Winnikoff JR, **Milshteyn D**, Vargas-Urbano SJ, Pedraza-Joya MA, Armando AM, Quehenberger O, Sodt A, Gillilan RE, Dennis EA, Lyman E, Haddock SHD, Budin I. Homeocurvature adaptation of phospholipids to pressure in deep-sea invertebrates. *Science*. 2024
4. Venkatraman K, Lee CT, Garcia GC, Mahapatra A, **Milshteyn D**, Perkins G, Kim KY, Pasolli HA, Phan S, Lippincott-Schwartz J, Ellisman MH, Rangamani P, Budin I. Cristae formation is a mechanical buckling event controlled by the inner mitochondrial membrane lipidome. *EMBO J*. 2023
5. Moore WM, **Milshteyn D**, Tsai YT, Budin I. Engineering the bilayer: Emerging genetic tool kits for mechanistic lipid biology. *Curr Opin Chem Biol*. 2021
6. **Milshteyn D**, Cooper G, Deamer D. Chemiosmotic energy for primitive cellular life: Proton gradients are generated across lipid membranes by redox reactions coupled to meteoritic quinones. *Sci Rep*. 2019
7. **Milshteyn D**, Damer B, Havig J, Deamer D. Amphiphilic Compounds Assemble into Membranous Vesicles in Hydrothermal Hot Spring Water but Not in Seawater. *Life (Basel)*. 2018

FIELD OF STUDY

Major Field: Lipid Biophysics
Studies in nonbilayer lipid biology
Professor Itay Budin

ABSTRACT OF THE DISSERTATION

Roles and regulation of nonbilayer lipids in biological membranes

by

Daniel Milshteyn

Doctor of Philosophy in Biochemistry and Molecular Biophysics with a Specialization in Multiscale Biology

University of California San Diego, 2026

Professor Itay Budin, Chair

Beyond compartmentalization and protection, cellular membranes are highly dynamic and specialized structures that perform molecular transport and serve as platforms for protein localization and modulation of function. The lipid composition of membranes defines their identity, material properties, interacting partners, and cellular functions. While bilayer lipids

establish the dominant fluid lamellar topology, nonbilayer lipids destabilize uniform lipid packing and introduce elastic curvature stress that enables morphological changes, membrane fission and fusion, and protein interaction. Cells expend considerable energy to establish specific lipid compositions for specialized membrane compartments, and a growing body of literature has provided evidence for tight homeostatic regulation of lipid composition and biophysical properties. Through combinations of headgroups, linkages, and acyl chain chemistry, eukaryotic cells produce more than 2000 species of lipids, many of whose functional roles remain unknown. Thus, the central goal of my thesis has been to identify nonbilayer lipids in cells, characterize their biophysical contributions to membrane function, and identify lipidomic signatures of pathways by which cells regulate intrinsic curvature.

In Chapter 1, I introduce fundamental concepts in lipid biophysics, focusing on lipid intrinsic curvature and nonbilayer lipids, and provide a review of modern methods for studying the biophysical properties of membranes and lipids. I highlight the diversity of nonbilayer lipids in organelle and cell types, the roles of nonbilayer lipids in membrane fission and fusion, how nonbilayer lipids modulate membrane protein localization and activity, and open questions in the field pertaining to active regulation of nonbilayer lipid composition in cell membranes.

In Chapter 2, I identify nonbilayer lipids as an evolutionary adaptation of deep-sea ctenophores to extreme hydrostatic pressure environments. SAXS analysis of polar lipid extracts from shallow and deep sea ctenophores indicated that lipid adaptations preserve access between lamellar and nonlamellar membrane topologies under compression. Using lipidomic profiling, I find that these organisms selectively enrich plasmalogens, a nonbilayer lipid class. Characterization of plasmalogens using small angle X-ray scattering (SAXS) showed that

plasmalogens have high negative spontaneous curvature, and the heterologous expression of plasmalogen biosynthesis in *Escherichia coli* improved their pressure tolerance.

In Chapter 3, I extend these observations to model eukaryotic organisms and show that cells acclimate their lipidomes to curvature stress imposed by hydrostatic pressure incubation by increasing production of negative curvature lipids. A human cancer cell line showed increases in ether-linked lipids under pressure, while budding yeast increased production of phosphatidylinositol, which I characterized to bear negative spontaneous curvature.

In Chapter 4, I utilize hydrostatic pressure as an experimental variable to interrogate calcium-induced fusion of large unilamellar vesicles across a range of nonbilayer-to-bilayer lipid ratios. Kinetic analysis reveals that lipid intrinsic curvature features an exponential relationship with the rate of hemifusion stalk formation, demonstrating the biophysical link between lipid composition and membrane fusion energetics.

In summary, this dissertation presents work demonstrating that the balance between bilayer and nonbilayer lipids in biological membranes is important to cellular fitness. I present biophysical and lipidomic evidence that lipid intrinsic curvature is actively regulated by eukaryotic cells in ways similar to how deep-sea marine life has adapted to survive under extreme hydrostatic pressure. Hydrostatic pressure is established as an experimental tool to induce lipid curvature stress in both cells and synthetic membranes. These findings will motivate subsequent work linking the biophysical properties of nonbilayer lipids to mechanisms governing specialized membrane behavior, its regulation, and pathologies arising from their disruption.

Chapter 1 Make room for dynamics: roles of nonbilayer lipids in the daily lives of cells

Abstract

Bilayer and nonbilayer lipids shape biological membranes to be compartments that are protected from their external milieu while maintaining functional and structural flexibility that can accommodate fission, fusion, and membrane-associated proteins. A growing body of literature highlights the importance of nonbilayer lipids, but fundamental questions remain to understand which lipid species cells use to establish optimal biophysical membrane properties. Studies have shown whole cell lipidomic and biophysical evidence that indicate active regulation of intrinsic lipid curvature in response to curvature stress, but the proteins and organelles involved in lipid curvature sensing and regulation processes remain to be identified. Advances to answer these questions have required a better understanding of the quantitative relationship between lateral pressure profiles and conformational energetics of specific membrane proteins, which have been made possible by computational simulations. While it has been technically challenging to experimentally vary one membrane property at a time with lipid composition perturbation, recent studies present hydrostatic pressure as a useful tool to specifically target lipid intrinsic curvature with minimal effects on membrane fluidity. In this review, we discuss advances in our understanding of roles of nonbilayer lipids in organismal physiology, membrane protein function, fission or fusion, and organelle dynamics. We highlight developments in interdisciplinary methods that can help to study these questions and nonbilayer lipid regulation by overcoming traditional experimental barriers with far-reaching potential to answer questions in human health, disease, and drug delivery.

Introduction

Although biological membranes exist predominantly as fluid bilayers, they are composed of lipids that either stabilize or destabilize uniformly packed lamellar sheets. Bilayer-forming lipids enable membranes to form robust barrier structures that compartmentalize specialized cellular units. In isolation, nonbilayer lipids with non-zero intrinsic curvature self-assemble into nonlamellar topologies, such as the cubic (Q_{II}) or inverted hexagonal (H_{II}) phases, which are rarely observed as stable structures in cells (1). Nevertheless, nonbilayer lipids can constitute half or more of the lipid composition in organellar membranes, introducing packing frustration in the form of elastic curvature stress that influences membrane protein function and enables membrane dynamics (2, 3). Membrane fission and fusion require the formation of regions with high curvature and transient nonlamellar intermediates to support essential physiological processes, including synaptic transmission, fertilization, and intracellular trafficking (4). By storing potential energy within the bilayer, elastic curvature stress modulates the localization, conformation, and activity of both peripheral and integral membrane proteins, with downstream consequences for cellular signaling and membrane homeostasis (5). In this review, we discuss the roles of nonbilayer lipids in cellular function, highlighting recent methodological advances that can clarify their contributions to membrane dynamics and protein activity. We propose that continued investigation is warranted to fully understand how these lipids regulate membrane properties and how such regulation translates to broader cellular physiology.

Form and function of nonbilayer lipids

Biological membranes are composed of thousands of lipid species that vary in headgroup identity, acyl chain length and saturation, and linkage chemistry. Lipid compositions differ between organelles, between the two leaflets of a single bilayer, and across cell types, each

optimized to support unique and diverse physiological needs (6). Across all domains of life, membranes comprise mixtures of lipids that promote either bilayer or nonbilayer topologies, a duality exemplified by the two most abundant eukaryotic phospholipids phosphatidylcholine (PC) and phosphatidylethanolamine (PE) (7). The packing of these lipids is dictated by their molecular shape, holistically described by the effective areas that chemical moieties occupy, and is quantified by intrinsic or spontaneous curvature (c_0) (Fig. 1A). PC has a bulky headgroup that occupies a cross-sectional area nearly equal to its acyl chains, with a cylindrical geometry that results in $c_0 \approx 0$ favoring assembly into flat, lamellar bilayers (8). In contrast, PE has a headgroup which occupies a significantly smaller area than the acyl chains, resulting in an inverted-cone shape with negative intrinsic curvature ($c_0<0$). Negative-curvature lipids like PE possess a mismatch between headgroup and large chain cross-sectional areas, favoring nonlamellar phases such as H_{II} or Q_{II} which feature monolayer topologies characterized by negative curvature. Conversely, lysophospholipids, which possess a single acyl chain, have positive intrinsic curvature ($c_0>0$) and assemble into hexagonal (H_I) or micellar structures (Fig. 1B-C). Lipids non-zero intrinsic curvature are known as nonbilayer lipids and destabilize bilayers to facilitate the formation of membrane regions with high curvature in transient nonlamellar intermediates required for membrane dynamics (Fig. 1D).

It is important to emphasize that the molecular shape of a lipid is not solely determined by the steric bulk of its chemical groups. Lipid curvature is an emergent property, shaped by hydration, counterions, intramolecular interactions, and the physical environment. The cross-sectional area at any depth through the monolayer represents the area occupied by thermally fluctuating headgroups or chains. For the headgroups, electrostatic repulsion between charged species, hydration shell size, and hydrogen bonding networks contribute to the effective area and

are sensitive to pH and divalent cation concentration (8, 9). Divalent cations are well known to magnify the negative curvature of charged lipids including phosphatidic acid (PA) and phosphatidylserine (PS) (10, 11). For the acyl chains, increasing length and unsaturation expand the accessible conformational space, introducing widening at the membrane core through double bond-induced kinks (12). Unlike headgroups, the compression and thermal fluctuation of acyl chains is sensitive to both temperature and pressure, whereby the hydrocarbon chain volume is more pressure sensitive than that of headgroups. Finally, the chemical linkage connecting the acyl chains to the glycerophosphate backbone also modulates intrinsic curvature. While ester linkages are the most common moiety in glycerophospholipids, substitution with alkyl or vinyl ether linkages, as found in plasmalogens, can also promote more negative curvature (13).

In isolation under aqueous conditions, bilayer lipids assemble into gel-phase (L_β) or fluid lamellar (L_α) sheets, while nonbilayer lipids organize into curved topologies including the H_I, H_{II}, and Q_{II} bicontinuous cubic phases (14). In contrast to eukaryotic membranes, where PC is typically the most abundant lipid class, most bacterial membranes are dominated by PE, with lesser proportions of the charged phospholipids phosphatidylglycerol (PG) and cardiolipin (15). Despite the prevalence of nonbilayer prone lipids in both prokaryotic and eukaryotic membranes, nonbilayer structures are rarely observed as stable phases in living cells. The vast majority of biological membranes maintain a lamellar bilayer organization. Within these bilayers, however, nonbilayer lipids introduce packing frustration in the form of elastic energy stored within monolayer leaflets opposing uniform organization (3). This stored curvature elastic stress shifts the membrane toward a state in which it is more susceptible to deformation, curvature, and transition to a nonbilayer topology. The classical approach to defining the mean spontaneous curvature of a lipid mixture is the weighted sum of its individual components. Summed over the

many lipids in a membrane, this represents a substantial reservoir of stored mechanical energy that can be coupled to biological functions.

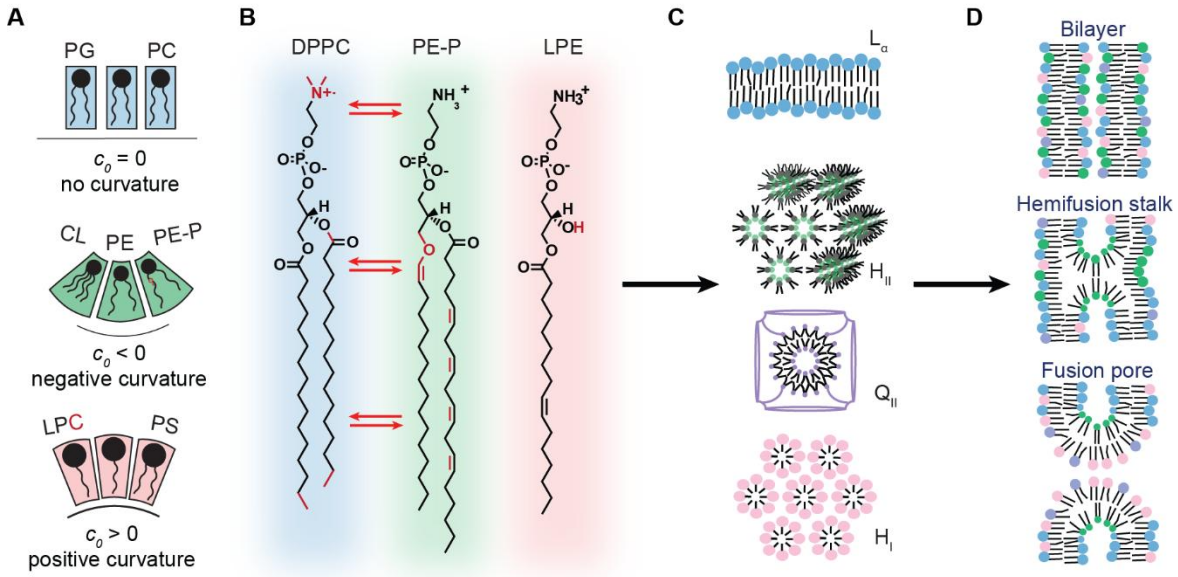

Figure 1.1 Lipid shape determines membrane topology.

(**A**) Phospholipids have molecular shapes that self-assemble into membranes with defined curvature. Lipids with equal headgroup and acyl chain areas have spontaneous curvature $c_0 \sim 0$, relatively smaller headgroups give lipids negative spontaneous curvature $c_0 < 0$, and larger headgroups produce positive curvature. (**B**) Changes in headgroup, linkage, and acyl chain chemistry determine lipid molecular shapes and intrinsic curvature. (**C**) Lipid intrinsic curvature produces a wide array of membrane topologies characterized by extreme curvature. Neutral curvature lipids produce flat lamellar sheets that can be fluid (L_α) or gel (L_β). Lipids with non-zero curvature that do not assemble into lamellar sheets are called nonbilayer lipids. Negative curvature lipids can form inverted hexagonal (H_{II}) or cubic (Q_{II}) phases, and positive curvature lipids form hexagonal (H_I) or micellar phases. (**D**) In cells, nonbilayer lipids in membrane regions of distinct curvature adopt arranges that structurally resemble nonbilayer phases, facilitating the formation of the hemifusion stalk and fusion pore.

Mismatch in lipid lateral pressure produces curvature elastic stress in membranes

The stored elastic energy in a bilayer represents competing forces and the distribution of internal pressures across depth through a bilayer, known as the lateral pressure profile, and varies with lipid chemistry. Repulsive and attractive forces along the bilayer normal can vary by hundred bars of pressure (16). In the headgroup region, steric, electrostatic, and hydration forces create a

repulsive positive pressure that pushes neighboring headgroups apart (17). At the hydrocarbon–water interface, the hydrophobic effect generates a large attractive negative pressure to minimize the nonpolar surface area exposed to water. In the acyl chain region, thermal fluctuations of hydrocarbon chains produce positive pressure. These attractive and repulsive pressures balance each other across monolayer depth producing no net lateral force at equilibrium. Substituting a nonbilayer lipid like PE for a bilayer-forming lipid like PC redistributes the lateral pressures, increasing repulsive pressure in the chain region relative to the headgroup region (18). Mixtures of lipids form complex force fields in the bilayer normal that emerge from competing attractive and repulsive pressures which can affect the energetics of membrane deformation and protein insertion.

Lipid packing defects and hydrophobic mismatch emerge from differences in lateral pressure profiles and mismatch in molecular geometry when nonbilayer lipids are forced into a flat bilayer among bilayer lipids. These differences disrupt shielding of the hydrophobic core, creating transient cavities at the bilayer–water surface where acyl chains are briefly exposed to the aqueous environment. Conical lipids and acyl chain unsaturation increase the frequency and depth of packing defects, which can be further exacerbated in membranes with positive curvature (19). Bending a membrane enriched in PE generates substantially more defects than bending a pure PC membrane to the same curvature (20). These defects serve as binding or insertion sites for amphipathic helices found in many membrane proteins, establishing a connection between nonbilayer lipid content and protein recruitment. Lipids with nonzero spontaneous curvature can relieve elastic strain associated with protein insertion by accommodating changes in the local monolayer curvature and protein conformation. This view of considering the local landscape of

interactions between lipids and proteins in an elastic curvature stress field prone to deformation has been presented as a new biomembrane model called the flexible surface model (FSM) (5).

The classical treatment of curvature stress assumes that the spontaneous curvature of a lipid mixture is a linear, additive function of its components. This assumption has recently been shown to deviate for physiologically important lipid combinations. It was recently demonstrated that sphingomyelin and cholesterol exhibit nonadditive curvature where cholesterol stiffens and orders the saturated chains of sphingomyelin, reducing their contribution to lateral pressure below the neutral plane of bending in a concentration dependent and nonlinear manner that cannot be predicted by averaging the c_0 values of the individual species (21). Two distinct softening mechanisms in multicomponent bilayers have recently been shown building on this. Lipids dynamically redistribute in response to local curvature fluctuations, and interconversion between different lipid dimer conformations with distinct curvature preferences provides additional mechanical softening (22). These findings suggest that the elastic properties of complex biological membranes are shaped not only by the stoichiometry of their constituent lipids, but also by specific intermolecular interactions, hydrogen bonds, chain ordering effects, and electrostatic bridging that emerge in the mixture. The complexity of the biophysical properties that emerge in membranes comes from the diversity of lipid chemistry, enabling the dynamic topological states and interactions with proteins that characterize biological membranes.

Diversity of nonbilayer lipids across organelles and cells

Organelles and cell types across eukaryotic biology can be distinguished by differences in membrane lipid profiles, suggesting that specific membrane compartments are tuned with unique biophysical properties, including curvature elastic stress, that support specialized functions. While PC is the most abundant phospholipid in nearly all eukaryotic organelles (40–50% of total

phospholipids), the relative proportions of other lipid classes vary along the secretory and endocytic pathways (6). The predominant nonbilayer lipids in organelles are PE and sterols like cholesterol. Cholesterol increases along the secretory pathway, serving pleiotropic roles in establishing membrane properties like thickness and rigidity while retaining access to curved topologies from its ability to rapidly flip-flop and fill packing defects. The endoplasmic reticulum (ER) membrane is loosely packed from enrichment in unsaturated PC and PE with relatively low cholesterol content. The Golgi apparatus has intermediate levels of cholesterol and sphingolipid concentrations, increasing from the cis to the trans Golgi cisternae, while also being increasingly enriched in the negative curvature lipid diacylglycerol (DAG) (23). The exoplasmic plasma membrane leaflet is enriched in cholesterol (up to 30–40 mol%), sphingomyelin, and saturated phospholipid species. This gradient has functional consequences by which proteins with short transmembrane domains are retained in the thin, loosely packed early compartments, while those with longer transmembrane domains are sorted forward to the plasma membrane, suggesting that hydrophobic mismatch acts as a physical sorting mechanism along the secretory pathway (24).

Membrane asymmetry between bilayer leaflets increases along the secretory pathway, ending at the exoplasmic leaflet of the plasma membrane, functioning as a barrier to a cell's external environment, while the cytoplasmic leaflet is optimized for signaling and transport (23). The exoplasmic leaflet is characterized by more saturated PC, sphingomyelin, and cholesterol producing a tightly packed, rigid barrier. On the other hand, the cytoplasmic leaflet is enriched in lipids that can promote packing disorder, curvature, and nonbilayer topologies: PE, PS, plasmenyl PE, PI, and a lesser amount of cholesterol, in addition to PC (25). Membrane asymmetry, and differences in lateral pressure profiles between opposing leaflets, has recently been proposed to increase differential stress that can affect membrane protein function (26, 27). Resolving

asymmetry in organelles has been technologically inaccessible largely until recently with the development of imaging techniques that provide insight on leaflet specific lipid compositions (28). Filling this gap in knowledge will aid our understanding of the differential stress profiles that are maintained in organelles that may play roles in dictating protein orientation during synthesis and trafficking.

The mitochondrial inner membrane is one of the most highly nonbilayer lipid enriched environments in the eukaryotic cell. PE constitutes 35–40% of inner membrane phospholipid and cardiolipin (CL), a dimeric phospholipid with four acyl chains found exclusively in mitochondria, accounts for approximately 15–20% of the total phospholipids (2). Both PE and CL are nonbilayer lipids with strongly negative spontaneous curvature, and their combined abundance places the mitochondrial inner membrane under high curvature elastic stress. This stress is essential for the formation and maintenance of cristae, the highly curved membrane invaginations that house the respiratory chain complexes and ATP synthase. CL is required for the assembly and stability of respiratory supercomplexes, and its four acyl chains, predominantly linoleoyl (18:2) in mammalian tissues, are actively remodeled by the transacylase tafazzin to achieve a specific molecular species composition optimized for mitochondrial function. Defects in CL remodeling, as in Barth syndrome, lead to the accumulation of monolysocardiolipin (MLCL) and depletion of mature tetralinoleoyl-CL, disrupting cristae architecture, supercomplex assembly, and mitochondrial dynamics (29). The roles of nonbilayer lipids in mitochondrial structure and function have been discussed in a recent review (30).

Specialized cell types further exemplify how lipid composition is optimized to functional demands. Neurons are highly enriched in plasmalogens, predominantly ethanolamine plasmalogens, that can constitute up to 50% of total PE in brain tissue and even higher fractions

in myelin (31, 32). The vinyl ether linkage at the sn-1 position of plasmalogens promotes stronger negative spontaneous curvature than the ester-linked species and increases the propensity for nonbilayer phase formation, properties thought to facilitate the rapid membrane fusion and fission events required for synaptic vesicle cycling (33, 34). Sperm cell membranes are also enriched in both plasmalogens and polyunsaturated PE species that lower the energetic barrier for the fusion reaction required for fertilization (35). Dysregulation of plasmalogens has been associated with many neurodegenerative and metabolic diseases including Alzheimer's and Parkinson's disease. Along with diversity of nonbilayer lipids comes complexity in the physical effects they introduce to membranes, often affecting more than one parameter and thus complicating experimental studies.

Methods to study the biophysical properties of nonbilayer lipids

Untangling the roles of nonbilayer lipids and their biophysical contributions to membrane material properties presents significant experimental challenges that emerge from combinatorial chemistry. Classically, genetic manipulation of lipid biosynthesis pathways has been used to perturb lipid composition and membrane properties. However, this approach is complicated by the interconnection of several membrane properties to individual lipid chemistry. Furthermore, elucidating lipid biology is challenged by cells' tendency to compensate for changes in lipid composition or membrane properties and feedback effects from downstream processes in cellular physiology that may rely on or interact with lipid composition. For example, deletion of the mitochondrial phosphatidylserine decarboxylase Psd1 in yeast, the major route for PE production, simultaneously impairs respiration, disrupts mitochondrial morphology, triggers ER stress, and upregulates over 50 genes spanning unrelated cellular processes (36–38). Similarly, cardiolipin deficiency in tafazzin mutants produces pleiotropic phenotypes affecting respiratory supercomplex

assembly, cristae morphology, iron-sulfur cluster biogenesis, and apoptotic signaling (2, 29). In mammalian systems, deleting Phosphatidylethanolamine N-methyltransferase (PEMT) simultaneously raises PE, lowers PC, and alters flux through the Kennedy and Lands' pathways, making it difficult to assign causation to any single physical parameter without additional controls (39). These pleiotropic complications suggest that genetic approaches alone cannot cleanly establish relationships between nonbilayer lipid content, curvature stress, and specific membrane functions.

Environmental levers to uncouple curvature and fluidity

A common challenge in the field is that many experimental manipulations that alter curvature stress simultaneously change membrane fluidity, making it difficult to attribute observations to one property or the other. Temperature has long been used to modulate membrane physical states, but it primarily affects acyl chain behavior and membrane viscosity (40, 41). Hydrostatic pressure has emerged as a complementary and more curvature-specific probe by targeting changes in molecular volume. This specificity arises because phospholipid shape is anisotropic due to the hydrocarbon chain volume being compressible, thus pressure-sensitive, while the polar headgroup region is largely incompressible (42). The temperature to pressure equivalency of a phase transition (dT/dP) is determined by the ratio of volumetric (ΔV) and enthalpic (ΔH) changes by the Clausius–Clapeyron relation. In model membranes, dT/dP of the curvature-mediated L_α to H_{II} transition is 0.05 K/bar, e.g. a pressure of 100 bar corresponds to a temperature drop of ~5°C at 1 bar (43, 44). In contrast, the dT/dP for the L_α to L_β transition is 3-fold smaller, so fluidity is dominated by temperature and weakly affected by pressure. Moreover, pressure is an attractive tool to target membrane properties due to lipids' high sensitivity to it compared with protein and nucleic acids which often require pressures over 1000 bar for structural

perturbation (42). High hydrostatic pressure compresses the acyl chain cross-sectional area relative to the headgroup, reducing the negative intrinsic curvature of negative curvature lipids and pushing them toward a more cylindrical geometry, without significantly changing headgroup hydration, electrostatics, or fluidity. This allows pressure to challenge a cell's ability to maintain curvature-dependent processes while minimally perturbing fluidity, providing an experimental tool to disentangle cellular responses to lipid curvature stress, with proper controls.

Characterizing biophysical parameters of synthetic and biological membranes

Understanding the biophysical properties of lipids in cell membranes often requires a reductionist approach in which simplified synthetic membranes are used to understand the contributions of individual lipid species from complex biological bilayers. Several key membrane properties, including spontaneous curvature, bilayer thickness, and the topology of lipid mesophases, can be determined by small-angle X-ray scattering (SAXS, Fig. 2A) (45). In a SAXS experiment, X-rays scattered by hydrated lipid assemblies produce intensity profiles with a series of peaks whose positions identify the mesophase geometry and reflect lattice dimensions (Fig. 2B). SAXS has been generally used for determining the spontaneous curvature of individual lipid species using a host-guest system, in which a well-characterized nonbilayer lipid that readily forms the H_{II} phase, most commonly DOPE, serves as a majority host matrix, and the lipid of interest is incorporated at defined mole fractions as a guest (Fig. 2C) (46). Because the spontaneous curvature of a lipid mixture is a weighted sum of its components, the c_0 of the guest lipid can be extracted from its effect on the total curvature relative to pure DOPE (47, 48). A comprehensive compilation of published c_0 values covering PE, PC, anionic phospholipids, lysophospholipids, and other species has been assembled by Dymond (2021), though the curvatures and phase behaviors of

many biologically relevant lipids, particularly those with polyunsaturated acyl chains or under physiological ionic conditions, remain to be characterized (Fig. 2D) (46).

High-pressure SAXS (HPSAXS) enables modulation of lipid curvature and characterization of lipid phase behavior and transition points by performing analysis in a pressure and temperature controlled sample cell (Fig. 2E) (49). Complementary phase identification by NMR, which can also be performed under pressure, distinguishes lamellar, hexagonal, and cubic phases (50). Polar lipid extracts from biological cell and organelle fractions can be subjected to SAXS and NMR to determine how close native compositions are to a lamellar-nonlamellar phase boundary, providing a measure of how much curvature elastic stress a given membrane stores. Membranes whose lipid compositions place them near the lamellar to H_{II} transition are optimized for the nonbilayer lipidic rearrangements that underlie processes such as vesicle budding, tubulation, and stalk-mediated fusion. Applying hydrostatic pressure to lipid extracts from different organelles could reveal, for example, whether the inner mitochondrial membrane, which is enriched in the nonbilayer lipids PE and cardiolipin, operates closer to a phase boundary than the endoplasmic reticulum or plasma membrane. Furthermore, comparing lipid extracts from cells grown under different metabolic or environmental conditions can test whether curvature homeostasis, as predicted by the intrinsic curvature hypothesis (Gruner, 1985), is maintained at the level of individual organelle membranes or only at the whole-cell level (3). HPSAXS is well suited for this purpose because pressure provides continuous, reversible access to the phase boundary without altering the lipid composition, temperature, or ionic environment of the sample. Combined with lipidomic profiling, this approach could ultimately map the relationship between lipidome composition, stored elastic energy, and the fusogenicity or fission competence of specific biological membranes.

Alongside biophysical characterization by SAXS and NMR, lipidomics has enabled computational estimation of spontaneous curvature in biological membranes. One model assigned individual lipid classes a numerical score based on how strongly their molecular geometry promotes or opposes membrane curvature (51). This approach allows for the estimation of the resting curvature elastic stress. The model was applied to over 500 mammalian cell lipidomes under varying growth conditions to estimate curvature elastic stress, finding evidence that changes in elastic stress may regulate membrane order. In a separate model, the phospholipid curvature index (PLCI) calculates mean lipidome curvature as a weighted average of lipid abundance and published c_0 values for each lipid species (52). This approach has been implemented in the computational tool "c0operate" which assigns curvature contributions based on headgroup identity, acyl chain length, and degree of unsaturation using multivariate regression fitted to available c_0 measurements. Because c_0 values do not exist for all acyl chain species of lipid classes, and are particularly sparse for polyunsaturated species, PLCI estimation involves approximations of chain structure effects. Applied to large-scale lipidomic datasets, these tools offer a path toward understanding how disease states, dietary perturbations, or pharmacological interventions alter the mechanical properties of specific cell and organelle membranes, potentially linking lipidome remodeling to changes in membrane protein function, trafficking efficiency, or susceptibility to fusion and fission.

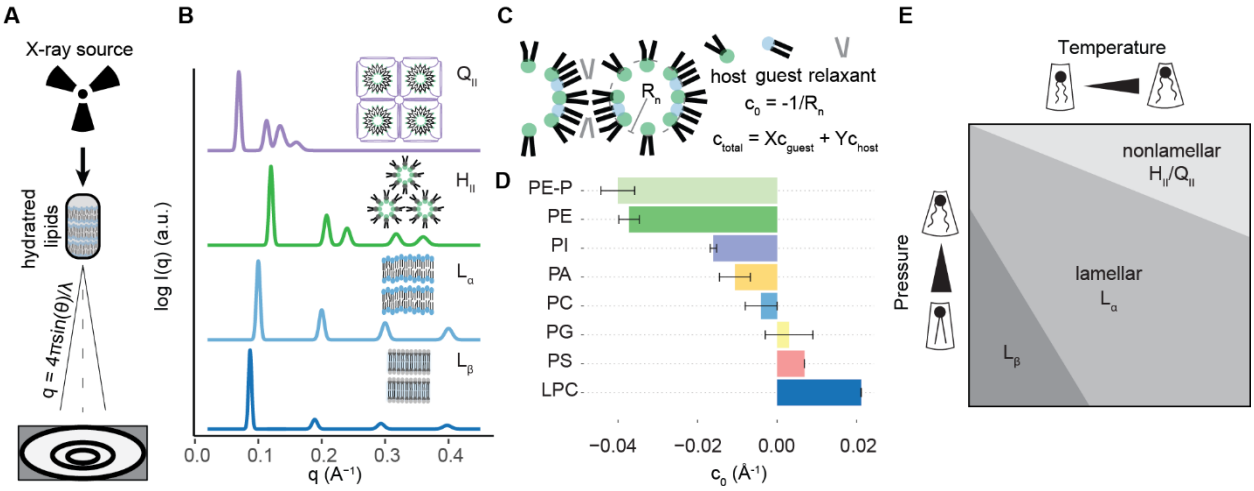

Figure 1.2 Biophysical methods and measurements of nonbilayer lipid properties

(**A**) Schematic of small angle X-ray scattering (SAXS). (**B**) Scattering profiles of lipid phases distinguished by unique spacing of peaks. (**C**) The spontaneous curvature of a lipid can be measured by determining its lipid contribution as a minority guest that is hosted with a H_{II} forming lipid, under a relaxed system including tricosene. The total curvature of this system is equal to a weighted sum of its constituents' intrinsic curvature and abundance. (**D**) A compilation of spontaneous curvatures of different phospholipid classes as measured by SAXS. (**E**) An example of a phase diagram showing how temperature and pressure can affect the curvature and fluidity of lipid membranes. Increasing pressure compresses lipid acyl chain area and reduces lipid curvature, with a less prominent effect on reducing fluidity. In comparison, decreasing temperature reduces the thermal motion of acyl chains which affects fluidity more than curvature with an ordering effect.

Biophysical parameters accessible from computational modeling

Molecular dynamics simulations provide access to physical quantities that are central to the curvature stress framework but remain experimentally inaccessible. All-atom simulations can directly compute the lateral pressure profile for membranes of defined composition (17, 53). The first moment of the computed pressure profile is equal to the negative product of the spontaneous curvature and bending modulus, providing access to the elastic parameters in a manner not possible with current experimental tools (54). Simulations can also quantify lipid packing defect distributions at the membrane surface, providing a direct link between curvature stress and the nanoscale features that mediate amphipathic helix binding (20). Recent studies have used coarse-

grained simulations of mitochondrial inner membrane models to demonstrate curvature-dependent partitioning of cardiolipin to negatively curved cristae regions, providing molecular-level insight into how lipid sorting might contribute to cristae architecture (55). The spatial extent (SPEX) method extracts the spontaneous curvature of individual lipids and lipid complexes from their redistribution on dynamically fluctuating simulated bilayers (22, 56). This method reveals the nonadditive aspects of curvature energetics that are invisible to experimental techniques that reflect averaged lipidome compositions. Increasingly, these computational approaches are being integrated with experimental lipidomics and reconstitution data to build predictive models of curvature elastic properties for specific organellar membranes in yeast and mammalian cells, as exemplified by the combined experimental-computational approach of Venkatraman et al. (2023), who developed a model for cristae tubule formation that integrates both lipid- and protein-mediated curvatures derived from coarse-grained simulations and lipidomic measurements (57).

Nonbilayer lipids in membrane fusion and fission

The concept that nonbilayer lipids directly participate in membrane fusion originated in the early 1980s with the stalk model proposed by Kozlov and Markin (1983), who argued that two opposing bilayers merge through a highly curved intermediate (58). In this model, contacting monolayers of two membranes mix into an hourglass shaped connection called a stalk, which then expands into a hemifusion diaphragm before a fusion pore opens to connect the enclosed compartments (Fig. 3A). Soon after, experimental support emerged showing that the shape of lipid molecules directly controls monolayer fusion rates (59). Lipids with negative spontaneous curvature such as PE, DAG, and cholesterol, which match the geometry of the stalk rim, promoted fusion when present in the proximal leaflets, whereas inverted-cone-shaped lysophosphatidylcholine (LPC) inhibited it (60, 61). Recent experimental measurements of lipid

mixing, content mixing and content leakage kinetics in osmotically driven fusion showed that liposomes containing more than 10 mol% PE or 20 mol% cholesterol have enhanced hemifusion formation rates, and more than 30 mol% PE permits a fusion mechanism that circumvents hemifusion diaphragm formation between stalk and pore formation (Fig. 3B) (62, 63). In reconstituted yeast vacuolar fusion, fusion requires the combined presence of three nonbilayer-prone lipids (PE, DAG, and ergosterol) for lipid mixing under physiological SNARE concentrations, while high SNARE levels bypass this requirement, potentially by mechanically bending the membrane to substitute for the absent curvature-promoting lipids (64).

A parallel body of work established that membrane fission proceeds through a topologically related nonbilayer intermediate called the hemifission state, in which the inner leaflets of a constricted tubule merge to form a stalk before the outer leaflets rupture to complete scission (65). As in fusion, nonbilayer lipids with negative spontaneous curvature lower the energy barrier for reaching a highly curved intermediate. In the plasma membrane, cholesterol is essential to lowering energy barriers in clathrin mediated endocytosis, with its absence resulting in stalled fission (66). Comprehensive coarse-grained molecular dynamics screens have quantitatively demonstrated that PE, DAG, and cholesterol each lower stalk formation free energies and revealed that the cytoplasmic leaflet of the mammalian plasma membrane is intrinsically far more fusogenic than the exoplasmic leaflet (67). Recent mechanical models calibrated by SAXS measurements have further shown that cardiolipin enrichment enables dynamin-family proteins to constrict mitochondrial necks into the hemifission range through a "snap-through" instability, providing a model for understanding how protein machineries exploit nonbilayer lipid curvature (68). Interactions between mitochondrial cardiolipin and dynamin related protein 1 (Drp1) show that

the lipid helps recruit Drp1 while reorganizing to promote local regions of high curvature and a nonbilayer phase transition (69).

Ether lipids represent a biologically distinctive class of nonbilayer-prone glycerophospholipids whose roles in fusion and fission are increasingly recognized in eukaryotic cell membranes. Ethanolamine plasmalogens (PPE) in particular are conical-shaped lipids with a strong tendency to form the inverted hexagonal phase at lower temperatures than their diacyl PE counterparts, and are enriched in tissues and organelles with high fusion activity, including plasma membranes, synaptic vesicles, and myelin (32). Early evidence linking ether lipid curvature to fusogenicity came from Glaser and Gross (1994), who used stopped-flow kinetics to show that vesicles containing PPE fused faster than compositionally matched vesicles containing diacyl PE (34). Defects in ether lipid biosynthesis have been reported to delay and reduce endocytosis rates (70). Furthermore, a recent study showed that when ceramide biosynthesis is inhibited, plasmalogen levels increase and promote cell fusion in coordination with the fusogenic protein Myomaker (71). Ceramide, a sphingolipid precursor generated from sphingomyelin hydrolysis by sphingomyelinases or through *de novo* synthesis, is another negative-curvature lipid (72). Enzymatic conversion of sphingomyelin to ceramide at the plasma membrane triggers vesicle aggregation and promotes fusion of PC-containing vesicles at concentrations as low as 5–10 mol% (73). Together, the diverse chemistries of these negative-curvature lipids illustrate how eukaryotic cells have converged on a common biophysical strategy of exploiting lipid shape to overcome the energetic barriers of membrane fusion and fission. Identifying additional nonbilayer lipid species that tune fusion and fission in specific cellular contexts remains an active frontier enabled by modern lipidomic and biophysical tools.

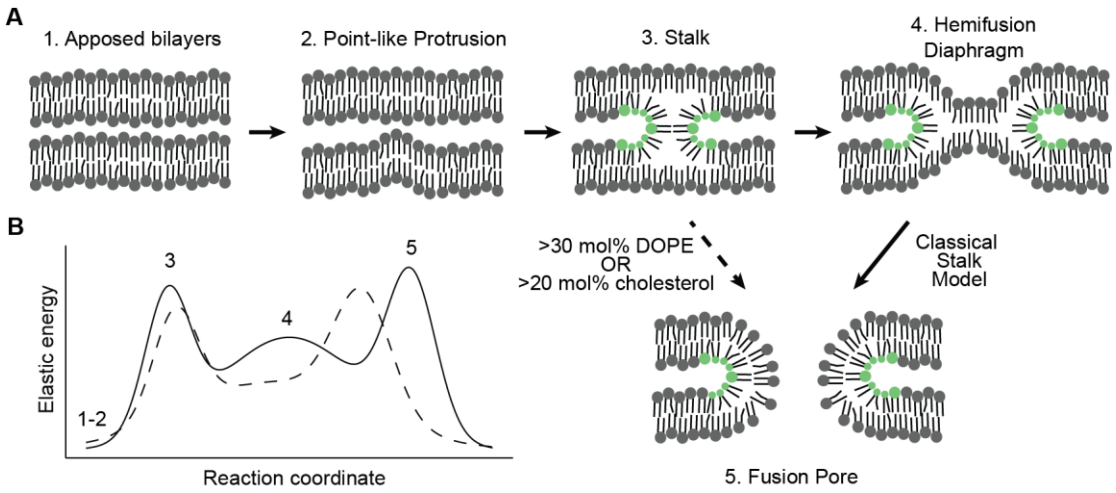

Figure 1.3 Nonbilayer lipids in membrane fusion.

(**A**) Schematic of fusion pathways including the classical stalk model which transitions from through the hemifusion diaphragm between stalk and pore formation. An alternate fusion pathway bypassing the hemifusion diaphragm has been proposed in membranes containing more than 30% PE, 20% cholesterol, or membrane binding peptides and protein. (**B**) Free energy landscapes of both fusion pathways.

Nonbilayer lipids modulate membrane protein localization and function

The proposal that nonbilayer lipids actively modulate membrane protein function emerged from observations that cellular membranes maintain abundant quantities of nonbilayer-prone lipids (14). Gruner's intrinsic curvature hypothesis proposed that cells optimize lipid composition to maintain a specific level of stored curvature elastic stress that in turn modulates the conformation and activity of embedded proteins (3). Cantor formalized this principle through the lateral pressure profile, in which the spontaneous curvature of lipid monolayers is expressed as an imbalance of lateral stresses distributed across the bilayer thickness (17). A transmembrane protein that undergoes a conformational change accompanied by a shift in its cross-sectional shape at different depths through the bilayer will couple to this pressure profile, with the free energy difference between conformations depending on the spontaneous curvature of the surrounding lipids (Fig. 4A-B).

The channel-forming peptide alamethicin provided the first quantitative demonstration of this principle. When alamethicin is inserted into planar bilayers of DOPC mixed with varying proportions of DOPE, the probability of higher conductance states increases with the nonlamellar character of the lipid composition, consistent with curvature elastic stress preferentially stabilizing the larger cross-sectional conformations of the multi-helix alamethicin barrel (74). Spontaneous curvature was shown to linearly affect the free energy of alamethicin partitioning from aqueous solution into the bilayer, establishing a quantitative template for identifying curvature-dependent behavior in other membrane proteins (75).

Since its discovery, several membrane proteins have been identified to exhibit sensitivity to nonbilayer lipid content similar to alamethicin. CTP:phosphocholine cytidylyltransferase (CCT), the rate-limiting enzyme of PC biosynthesis, is activated by membranes containing DOPE, DAG, or other negative-curvature lipids, with enzymatic activity scaling quantitatively with calculated curvature strain across chemically distinct lipid systems (76, 77). Because CCT's product is PC, a bilayer-forming lipid, this coupling creates a homeostatic feedback loop in which curvature elastic stress directly controls the rate of synthesis of a lipid that relieves that stress. The sarco/endoplasmic reticulum Ca^{2+}-ATPase (SERCA) is also activated by PE and inhibited by LPC in reconstituted membranes in a pattern consistent with modulation by the lateral pressure profile rather than specific headgroup recognition or membrane fluidity (78, 79). More recently, the mitochondrial proteins uncoupling protein 1 (UCP1) and adenine nucleotide translocase 1 (ANT1) were shown to sense stored curvature elastic stress, with their activity increasing when oxidative modification of PE reduces the membrane bending modulus and alters the lateral pressure profile, suggesting nonbilayer lipid properties may be linked to mitochondrial function under oxidative stress (80).

G-protein signaling is also sensitive to nonbilayer lipid content, as associations of some with the membrane are promoted by nonlamellar-prone lipids, suggesting that the lateral pressure profile modulates peripheral protein recruitment and downstream signal transduction (81). The G protein-coupled receptor rhodopsin shows an analogous dependence where the primary activation step in transduction shifts toward its active state as the spontaneous curvature of the surrounding lipids becomes more negative, with the free energy of the transition depending linearly on curvature elastic stress (82, 83). Collectively, these examples demonstrate curvature-dependent protein function as a general biophysical principle, making nonbilayer lipids essential regulators of membrane protein activity. More work is needed to identify protein whose localization and function are modulated by nonbilayer lipids and provide insight into diseases that may be connected to their disruption when lipid composition is dysregulated.

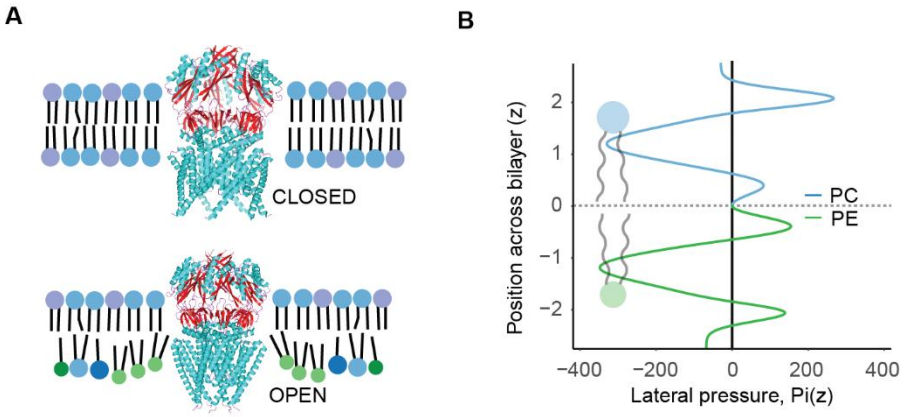

Figure 1.4 Protein localization, conformation and function determined by lateral stress profiles.

(**A**) Conformational states of membrane protein can be determined by lipid composition and leaflet asymmetry. (**B**) Membrane proteins are embedded in elastic stress fields determined by lipid composition, determining differential pressure profiles along bilayer depth. Lipid chemistry of headgroup, linkage, and acyl chain change lateral pressure profiles and can affect membrane embedded protein.

Regulation of nonlamellar lipids and lipid intrinsic curvature

Gruner first proposed that biological membranes maintain their lipid compositions near a lamellar to nonlamellar transition point, balancing the functional benefits of curvature elastic stress against the need for a permeability barrier (3). This intrinsic curvature hypothesis predicted that cells actively regulate the spontaneous curvature of their lipid mixtures to establish distinct biophysical properties. Studies have shown that wild-type *E. coli* maintain access to nonlamellar phases in response to temperature induced stress by remodeling acyl chain composition (84). Similarly in yeast, genetic depletion of PC caused cells to remodel their acyl chains toward shorter, more saturated species, changes that reduce the intrinsic curvature of PE and shift the H_{II} transition temperature upward (85). This combination of chain shortening and increased saturation is inconsistent with a homeoviscous response maintaining fluidity, which would predict opposite changes, and instead points to a distinct homeocurvature regulatory mechanism.

More recent work has provided experimental evidence that cells optimize membrane curvature as a physical property independent of fluidity (Fig. 5A-B). In lipidomes of deep-sea ctenophores, species evolutionarily adapted to high hydrostatic pressure were shown to be enriched in phospholipids with strong negative spontaneous curvature, particularly plasmalogens, which form nonbilayer phases at pressures under which the H_{II} phase is not normally stable (13). Expression of plasmalogen biosynthetic genes in *E. coli* was sufficient to enhance pressure tolerance, whereas incorporation of low-curvature lipids had the opposite effect. In complementary work using yeast and human cancer K562 cells as model eukaryotes, hydrostatic pressure was used to artificially reduce lipid curvature without changing temperature or composition, to which cells responded by remodeling their lipidomes toward compositions with greater propensity for nonlamellar phase formation, as confirmed by SAXS measurements on polar lipid extracts from

yeast (86). Diverse signatures of increasing lipidome curvature were observed suggesting that various homeostatic mechanisms may be employed by different organisms or cell types. Two divergently evolved yeast species employed distinct metabolic strategies to restore curvature under pressure, with *S. cerevisiae* increasing PI, which was identified as a negative-curvature lipid. In contrast, the yeast *Lachancea kluyveri* reduced positively curved PS and increased production of DAG. Both yeasts also made longer, unsaturated acyl chains in response to pressure indicating a curvature driven response instead of fluidity which favors shorter acyl chains. K562 cells acclimated with similar acyl chain remodeling but featured an increase in ether lipids, similar to evolutionary adaptation in deep-sea comb jellies. Data-driven modeling across approximately 500 diverse mammalian cell lipidomes has further shown that curvature elastic stress correlates strongly with membrane order, suggesting that curvature may be a property under homeostatic control that is balanced alongside fluidity (51, 87).

The molecular identity of the proteins that sense and transduce membrane physical properties into metabolic responses is an emerging area of investigation, with most characterized examples to date responding to lipid packing or fluidity rather than curvature elastic stress specifically. In yeast, the ER-resident paralogs Mga2/Spt23 sense the packing density of lipid acyl chains through conformational changes in their transmembrane helices, and when membranes become excessively saturated, ubiquitin-dependent proteolytic processing leads to an upregulation transcription of the *OLE1*, which encodes the desaturase Ole1, to restore fluidity (88, 89). In mammalian cells, AdipoR1/2 could perform an analogous function, detecting membrane rigidification caused by cold temperatures or dietary saturated fatty acids and promoting fatty acid desaturation (90, 91). While these sensors primarily regulate acyl chain unsaturation in response to fluidity perturbations, the eukaryotic enzyme PCYT1A (CCTα) represents a distinct class of

sensor that responds specifically to stored curvature elastic stress. At the inner nuclear membrane in yeast, fly, and mammalian cells, PCYT1A binds to membranes with high curvature frustration and is released when stress is relieved, regulating its roles in PC biosynthesis that contributes to balancing bilayer and nonbilayer lipids (92). The implication of negative curvature lipids including PI and plasmalogens in buffering lipidome curvature suggests that other mechanisms for sensing and regulating intrinsic lipid curvature remain to be identified. Identifying such proteins is an important goal for understanding how eukaryotic cells coordinate the regulation of lipidomes as observed in pressure acclimation, organelle biogenesis, and membrane trafficking.

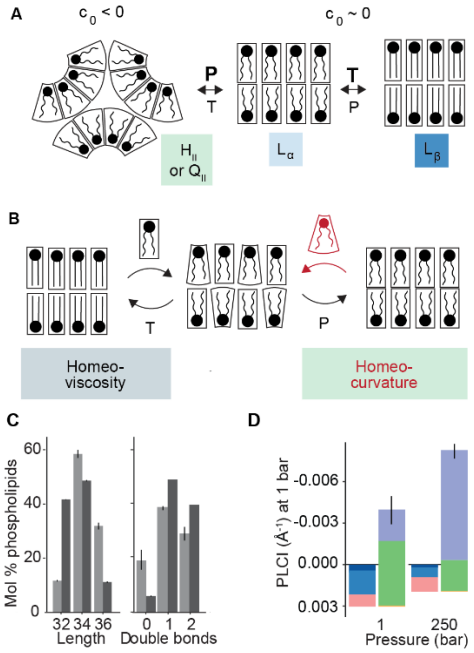

Figure 1.5 Metabolic regulation of membrane fluidity and lipid curvature in cells by homeoviscosity and homeocurvature feedback processes.

(**A**) Pressure has a strong inhibiting effect on nonbilayer phase and lipid curvature formation while temperature affects membrane fluidity more. (**B**) Homeoviscosity regulates membrane fluidity by increasing shorter, more unsaturated lipids in response to cold or rigidifying stress. (**C**) Example of homeoviscosity visualized by lipidomic analysis showing an increase in shorter, more unsaturated lipids in cells grown in the cold (dark grey) compared to native temperature (light grey). (**D**) Example of homeocurvature visualized by lipidomics and lipidome curvature estimation. In response to pressure incubation, lipidomes are enriched in more negative curvature lipids, compared to cells grown at ambient pressure.

Open questions and future directions

The material properties of biological membranes are tuned to support dynamic processes and interaction with specific proteins varying across organelle and cell type, developmental stages, and in response to stress conditions. Organismal physiology and health are tied to the maintenance of lipid composition and its dysregulation has been shown to be associated with a growing number of diseases. Identifying the lipids that help define membrane properties and how cells regulate them will be essential to developing therapies, something that is now possible with the convergence of high-throughput lipidomics, biophysical characterization, and computational modeling. Recent cryo-electron tomography measurements have confirmed that bilayer thickness varies across organelles, with thinner membranes in the ER and progressively thicker bilayers along the secretory pathway to the plasma membrane, consistent with the lipid compositional gradients that have long been inferred from fractionation and lipidomics (93). The curvature elastic stress stored in these membranes is expected to similarly vary, yet this quantity has never been determined for individual organelle membranes. Characterizing the roles of nonbilayer lipids in functionalizing local membrane regions, subcellular organelles, specific cell types, and emergent effects in physiology combines biology, chemistry and physics from molecule to organism.

The translational relevance of nonbilayer lipid dysregulation is becoming increasingly relevant across a range of human diseases. In the liver, the ratio of PC to PE has emerged as a key determinant of hepatocyte membrane integrity, with PEMT-deficient mice developing steatohepatitis and liver failure when the PC to PE ratio drops below approximately 1.0 (7, 39). Patients with nonalcoholic steatohepatitis (NASH) similarly exhibit a diminished hepatic PC to PE ratio compared to healthy controls, and the severity of liver disease correlates inversely with this ratio (94). In Barth syndrome, defective remodeling of the mitochondrial nonbilayer lipid

cardiolipin by Tafazzin leads to accumulation of MLCL, disrupted cristae architecture, and impaired respiratory supercomplex assembly (2, 95). Oxidative stress itself may challenge curvature homeostasis, as lipid oxidation products generated by reactive oxygen species reduce the stored curvature elastic energy of membranes, requiring cells to actively compensate through lipid remodeling to maintain membrane mechanical properties (96). This connection between oxidative damage and curvature stress may suggest that age-related declines in antioxidant capacity could progressively erode the curvature elastic stress that membranes require for normal protein function and trafficking, linking the biophysics of nonbilayer lipids to broader mechanisms of cellular aging.

Neurodegenerative diseases are another area where dysregulation of nonbilayer lipids may play a mechanistic role. Ethanolamine plasmalogens, among the most negatively curved lipids in mammalian membranes, are depleted in the brains of patients with Alzheimer's disease, and this depletion occurs early in disease progression, correlating with severity of cognitive decline (97–99). Because plasmalogens are enriched in synaptic vesicles and are required for rapid membrane fusion during neurotransmission, their loss could impair synaptic vesicle cycling and contribute to synaptic dysfunction (100). Consistent with a connection between plasmalogen levels and membrane remodeling, aged *Drosophila melanogaster* oenocytes exhibit a decline in mitochondrial plasmalogens that correlates with a failure to recruit Drp1 and execute stress-induced mitochondrial fission (101). The essential role of plasmalogen biosynthesis in development and aging is further underscored by the recent identification of PEDS1 variants that cause microcephaly and global developmental delay in humans, indicating genetic links between ether lipid metabolism and brain development (102, 103).

Similarly, in Fragile X syndrome, loss of FMRP is associated with reduced expression of diacylglycerol kinase (DGK) DGKκ and a consequent imbalance between DAG and PA that disrupts dendritic spine morphology and synaptic plasticity (104). Another DGK isoform, DGKϵ was shown to be recruited to membranes with negative Gaussian curvature which is dependent on lipid composition, and if disrupted may lead to cellular dysfunction (105). Whether these lipid imbalances represent primary drivers of disease pathology or secondary consequences of upstream dysfunction remains unclear, but the availability of lipidomic tools to quantify nonbilayer lipid composition, combined with biophysical characterization and modeling, now makes it feasible to ask whether restoring the curvature elastic stress of neuronal membranes through dietary, pharmacological, or genetic interventions can ameliorate disease phenotypes.

Identifying the molecular sensors that detect and regulate intrinsic lipid curvature remains an important open goal. While CCT has been established as a curvature-responsive enzyme that feeds back on PC synthesis, the diverse lipid remodeling profiles recently observed in response to curvature stress suggest that additional sensors exist that can control metabolic pathways to adjust intrinsic lipid curvature. Genetic and CRISPR-based screens in yeast and mammalian cells, combined with pressure or lipid feeding perturbations that selectively challenge curvature homeostasis, could identify genes whose loss abolishes compensatory lipidome remodeling responses. The distinction between fluidity sensors such as Mga2/Spt23, which respond to lipid packing density, and curvature sensors like PCYT1A, which respond to stored elastic energy, highlights the need for experimental approaches that can cleanly separate these two modes of membrane property sensing. Pressure, as a physical modulator of intrinsic curvature, represents an attractive experimental tool to identify these points of regulation.

The principles of nonbilayer lipid biophysics have direct applications to the rational design of lipid nanoparticles (LNPs) for drug delivery. The ionizable lipids used in mRNA-LNP formulations are designed to adopt a cone shape at endosomal pH, promoting the H_{II} phase transition and membrane destabilization required for cargo release into the cytoplasm (106, 107). SAXS-based fusogenicity metrics have recently been introduced to rank individual ionizable lipid species by their ability to promote nonbilayer transitions, providing a biophysical screening tool that can accelerate formulation development (108). Complementing this biophysical approach, genome-wide CRISPR screens have now been applied to identify host cell genetic determinants of LNP uptake and delivery efficiency (109). More broadly, the same reasoning that explains how nonbilayer lipids facilitate biological fusion and fission can be applied to understand and optimize how synthetic lipid mixtures interact with cellular membranes. Recently, monoolein-plasmalogen LNP were demonstrated to have neuroprotective properties, restoring ATP synthase activity, reducing intracellular reactive oxygen species, and attenuating neuroinflammation in neuronal stress models (110). As the field moves toward tissue-specific and organelle-targeted delivery, understanding how the nonbilayer lipid composition of target membranes influences LNP fusogenicity, and how disease states alter that composition, will be increasingly important for designing effective therapeutics.

Acknowledgments

The material in this chapter, in part, is currently being prepared for submission for publication. “Make room for dynamics: roles of nonbilayer lipids in the daily lives of cells”. Milshteyn, Daniel; Budin, Itay. The dissertation author is the primary researcher and author of this material.

References

1. de Kruijff, B. 1997. Lipid polymorphism and biomembrane function. *Curr. Opin. Chem. Biol.* 1:564–569.

2. Basu Ball, W., J.K. Neff, and V.M. Gohil. 2018. The role of nonbilayer phospholipids in mitochondrial structure and function. *FEBS Lett.* 592:1273–1290.

3. Gruner, S.M. 1985. Intrinsic curvature hypothesis for biomembrane lipid composition: a role for nonbilayer lipids. *Proc. Natl. Acad. Sci. U. S. A.* 82:3665–3669.

4. Siegel, D.P., and R.M. Epand. 1997. The mechanism of lamellar-to-inverted hexagonal phase transitions in phosphatidylethanolamine: implications for membrane fusion mechanisms. *Biophys. J.* 73:3089–3111.

5. Brown, M.F. 2012. Curvature forces in membrane lipid-protein interactions. *Biochemistry*. 51:9782–9795.

6. Harayama, T., and H. Riezman. 2018. Understanding the diversity of membrane lipid composition. *Nat. Rev. Mol. Cell Biol.* 19:281–296.

7. van der Veen, J.N., J.P. Kennelly, S. Wan, J.E. Vance, D.E. Vance, and R.L. Jacobs. 2017. The critical role of phosphatidylcholine and phosphatidylethanolamine metabolism in health and disease. *Biochim. Biophys. Acta Biomembr.* 1859:1558–1572.

8. Rand, R.P., and V.A. Parsegian. 1989. Hydration forces between phospholipid bilayers. *Biochim. Biophys. Acta*. 988:351–376.

9. Dymond, M.K., R.J. Gillams, D.J. Parker, J. Burrell, A. Labrador, T. Nylander, and G.S. Attard. 2016. Lipid Spontaneous Curvatures Estimated from Temperature-Dependent Changes in Inverse Hexagonal Phase Lattice Parameters: Effects of Metal Cations. .

10. Kooijman, E.E., V. Chupin, N.L. Fuller, M.M. Kozlov, B. de Kruijff, K.N.J. Burger, and P.R. Rand. 2005. Spontaneous curvature of phosphatidic acid and lysophosphatidic acid. *Biochemistry*. 44:2097–2102.

11. Fuller, N., C.R. Benatti, and R.P. Rand. 2003. Curvature and bending constants for phosphatidylserine-containing membranes. *Biophys. J.* 85:1667–1674.

12. Szule, J.A., N.L. Fuller, and R.P. Rand. 2002. The effects of acyl chain length and saturation of diacylglycerols and phosphatidylcholines on membrane monolayer curvature. *Biophys. J.* 83:977–984.

13. Winnikoff, J.R., D. Milshteyn, S.J. Vargas-Urbano, M.A. Pedraza-Joya, A.M. Armando, O. Quehenberger, A. Sodt, R.E. Gillilan, E.A. Dennis, E. Lyman, S.H.D. Haddock, and I. Budin. 2024. Homeocurvature adaptation of phospholipids to pressure in deep-sea invertebrates. *Science*. 384:1482–1488.

14. Cullis, P.R., and B. de Kruijff. 1979. Lipid polymorphism and the functional roles of lipids in biological membranes. *Biochim. Biophys. Acta*. 559:399–420.

15. Dowhan, W. 1997. MOLECULAR BASIS FOR MEMBRANE PHOSPHOLIPID DIVERSITY: Why Are There So Many Lipids? *Annu. Rev. Biochem.* 66:199–232.

16. Ding, W., M. Palaiokostas, G. Shahane, W. Wang, and M. Orsi. 2017. Effects of high pressure on phospholipid bilayers. *J. Phys. Chem. B*. 121:9597–9606.

17. Cantor, R.S. 1997. Lateral pressures in cell membranes: A mechanism for modulation of protein function. *J. Phys. Chem. B*. 101:1723–1725.

18. Cantor, R.S. 1999. Lipid composition and the lateral pressure profile in bilayers. *Biophys. J.* 76:2625–2639.

19. Vamparys, L., R. Gautier, S. Vanni, W.F.D. Bennett, D.P. Tieleman, B. Antonny, C. Etchebest, and P.F.J. Fuchs. 2013. Conical lipids in flat bilayers induce packing defects similar to that induced by positive curvature. *Biophys. J.* 104:585–593.

20. Vanni, S., H. Hirose, H. Barelli, B. Antonny, and R. Gautier. 2014. A sub-nanometre view of how membrane curvature and composition modulate lipid packing and protein recruitment. *Nat. Commun.* 5:4916.

21. Sodt, A.J., R.M. Venable, E. Lyman, and R.W. Pastor. 2016. Nonadditive compositional curvature energetics of lipid bilayers. *Phys. Rev. Lett.* 117:138104.

22. Lessen, H.J., K.C. Sapp, A.H. Beaven, R. Ashkar, and A.J. Sodt. 2022. Molecular mechanisms of spontaneous curvature and softening in complex lipid bilayer mixtures. *Biophys. J.* 121:3188–3199.

23. Holthuis, J.C.M., and A.K. Menon. 2014. Lipid landscapes and pipelines in membrane homeostasis. *Nature*. 510:48–57.

24. Sharpe, H.J., T.J. Stevens, and S. Munro. 2010. A comprehensive comparison of transmembrane domains reveals organelle-specific properties. *Cell*. 142:158–169.

25. Lorent, J.H., K.R. Levental, L. Ganesan, G. Rivera-Longsworth, E. Sezgin, M. Doktorova, E. Lyman, and I. Levental. 2020. Plasma membranes are asymmetric in lipid unsaturation, packing and protein shape. *Nat. Chem. Biol.* 16:644–652.

26. Hossein, A., and M. Deserno. 2020. Spontaneous curvature, differential stress, and bending modulus of asymmetric lipid membranes. *Biophys. J.* 118:624–642.

27. Doktorova, M., J.L. Symons, and I. Levental. 2020. Structural and functional consequences of reversible lipid asymmetry in living membranes. *Nat. Chem. Biol.* 16:1321–1330.

28. Moore, W.M., R.J. Brea, C.H. Knittel, E. Wrightsman, B. Hui, J. Lou, C.F. Ancajas, M.D. Best, C.J. Obara, N.K. Devaraj, and I. Budin. 2026. Leaflet-specific phospholipid imaging using genetically encoded proximity sensors. *Nat. Chem. Biol.* 22:128–139.

29. Hauff, K.D., and G.M. Hatch. 2006. Cardiolipin metabolism and Barth Syndrome. *Prog. Lipid Res.* 45:91–101.

30. Venkatraman, K., C.T. Lee, and I. Budin. 2024. Setting the curve: the biophysical properties of lipids in mitochondrial form and function. *J. Lipid Res.* 0:100643.

31. Braverman, N.E., and A.B. Moser. 2012. Functions of plasmalogen lipids in health and disease. *Biochim. Biophys. Acta*. 1822:1442–1452.

32. Koivuniemi, A. 2017. The biophysical properties of plasmalogens originating from their unique molecular architecture. *FEBS Lett.* 591:2700–2713.

33. Lohner, K. 1996. Is the high propensity of ethanolamine plasmalogens to form non-lamellar lipid structures manifested in the properties of biomembranes? *Chem. Phys. Lipids*. 81:167–184.

34. Glaser, P.E., and R.W. Gross. 1994. Plasmenylethanolamine facilitates rapid membrane fusion: a stopped-flow kinetic investigation correlating the propensity of a major plasma membrane constituent to adopt an HII phase with its ability to promote membrane fusion. *Biochemistry*. 33:5805–5812.

35. Fanani, M.L., and E.E. Ambroggio. 2023. Phospholipases and membrane curvature: What is happening at the surface? *Membranes (Basel)*. 13:190.

36. Chan, E.Y.L., and G.A. McQuibban. 2012. Phosphatidylserine decarboxylase 1 (Psd1) promotes mitochondrial fusion by regulating the biophysical properties of the mitochondrial membrane and alternative topogenesis of mitochondrial genome maintenance protein 1 (Mgm1). *J. Biol. Chem.* 287:40131–40139.

37. Calzada, E., E. Avery, P.N. Sam, A. Modak, C. Wang, J.M. McCaffery, X. Han, N.N. Alder, and S.M. Claypool. 2019. Phosphatidylethanolamine made in the inner mitochondrial membrane is essential for yeast cytochrome bc1 complex function. *Nat. Commun.* 10:1432.

38. Gsell, M., G. Mascher, I. Schuiki, B. Ploier, C. Hrastnik, and G. Daum. 2013. Transcriptional response to deletion of the phosphatidylserine decarboxylase Psd1p in the yeast Saccharomyces cerevisiae. *PLoS One*. 8:e77380.

39. Li, Z., L.B. Agellon, T.M. Allen, M. Umeda, L. Jewell, A. Mason, and D.E. Vance. 2006. The ratio of phosphatidylcholine to phosphatidylethanolamine influences membrane integrity and steatohepatitis. *Cell Metab.* 3:321–331.

40. Sinensky, M. 1974. Homeoviscous adaptation--a homeostatic process that regulates the viscosity of membrane lipids in Escherichia coli. *Proc. Natl. Acad. Sci. U. S. A.* 71:522–525.

41. Ernst, R., C.S. Ejsing, and B. Antonny. 2016. Homeoviscous adaptation and the regulation of membrane lipids. *J. Mol. Biol.* 428:4776–4791.

42. Winter, R., and W. Dzwolak. 2005. Exploring the temperature-pressure configurational landscape of biomolecules: from lipid membranes to proteins. *Philos. Trans. A Math. Phys. Eng. Sci.* 363:537–62; discussion 562–3.

43. So, P.T., S.M. Gruner, and S. Erramilli. 1993. Pressure-induced topological phase transitions in membranes. *Phys. Rev. Lett.* 70:3455–3458.

44. Shyamsunder, E., P. Botos, and S.M. Gruner. 1989. Comment on: X-ray diffraction study of the effects of pressure on bilayer to nonbilayer lipid membrane phase transitions. *J. Chem. Phys.* 90:1293–1295.

45. Rappolt, M., A. Hickel, F. Bringezu, and K. Lohner. 2003. Mechanism of the lamellar/inverse hexagonal phase transition examined by high resolution x-ray diffraction. *Biophys. J.* 84:3111–3122.

46. Dymond, M.K. 2021. Lipid monolayer spontaneous curvatures: A collection of published values. *Chem. Phys. Lipids*. 239:105117.

47. Rand, R.P., N.L. Fuller, S.M. Gruner, and V.A. Parsegian. 1990. Membrane curvature, lipid segregation, and structural transitions for phospholipids under dual-solvent stress. *Biochemistry*. 29:76–87.

48. Kollmitzer, B., P. Heftberger, M. Rappolt, and G. Pabst. 2013. Monolayer spontaneous curvature of raft-forming membrane lipids. *Soft Matter*. 9:10877–10884.

49. Brooks, N.J. 2014. Pressure effects on lipids and bio-membrane assemblies. *IUCrJ*. 1:470–477.

50. Cullis, P.R., and B. De Kruijff. 1978. Polymorphic phase behaviour of lipid mixtures as detected by 31P NMR. Evidence that cholesterol may destabilize bilayer structure in membrane systems containing phosphatidylethanolamine. *Biochim. Biophys. Acta*. 507:207–218.

51. Dymond, M.K. 2016. Mammalian phospholipid homeostasis: evidence that membrane curvature elastic stress drives homeoviscous adaptation in vivo. *J. R. Soc. Interface*. 13.

52. Winnikoff, J.R., and I. Budin. 2025. Homeocurvature: A new dimension of membrane adaptation to extreme environments. *Prog. Lipid Res.* 100:101355.

53. Ollila, O.H.S., H.J. Risselada, M. Louhivuori, E. Lindahl, I. Vattulainen, and S.J. Marrink. 2009. 3D pressure field in lipid membranes and membrane-protein complexes. *Phys. Rev. Lett.* 102:078101.

54. Marsh, D. 2007. Lateral pressure profile, spontaneous curvature frustration, and the incorporation and conformation of proteins in membranes. *Biophys. J.* 93:3884–3899.

55. Lee, C.T., K. Venkatraman, I. Budin, and P. Rangamani. 2025. Local enrichment of cardiolipin to transient membrane undulations. *Biophys. J.* 124:2476–2487.

56. Sapp, K.C., A.H. Beaven, and A.J. Sodt. 2021. Spatial extent of a single lipid's influence on bilayer mechanics. *Phys. Rev. E.* 103:042413.

57. Venkatraman, K., C.T. Lee, G.C. Garcia, A. Mahapatra, D. Milshteyn, G. Perkins, K.-Y. Kim, H.A. Pasolli, S. Phan, J. Lippincott-Schwartz, M.H. Ellisman, P. Rangamani, and I. Budin. 2023. Cristae formation is a mechanical buckling event controlled by the inner mitochondrial membrane lipidome. *EMBO J.* 42:e114054.

58. Kozlov, M.M., and V.S. Markin. 1983. Possible mechanism of membrane fusion. *Biofizika*. 28:242–247.

59. Chernomordik, L.V., M.M. Kozlov, G.B. Melikyan, I.G. Abidor, V.S. Markin, and Y.A. Chizmadzhev. 1985. The shape of lipid molecules and monolayer membrane fusion. *Biochim. Biophys. Acta Biomembr.* 812:643–655.

60. Chernomordik, L., M.M. Kozlov, and J. Zimmerberg. 1995. Lipids in biological membrane fusion. *J. Membr. Biol.* 146:1–14.

61. Chernomordik, L. 1996. Non-bilayer lipids and biological fusion intermediates. *Chem. Phys. Lipids*. 81:203–213.

62. Joardar, A., G.P. Pattnaik, and H. Chakraborty. 2021. Effect of phosphatidylethanolamine and oleic acid on membrane fusion: Phosphatidylethanolamine circumvents the classical stalk model. *J. Phys. Chem. B*. 125:13192–13202.

63. Mishra, S., and H. Chakraborty. 2023. Phosphatidylethanolamine and Cholesterol Promote Hemifusion Formation: A Tug of War between Membrane Interfacial Order and Intrinsic Negative Curvature of Lipids. *The Journal of Physical Chemistry B*.

64. Zick, M., C. Stroupe, A. Orr, D. Douville, and W.T. Wickner. 2014. Membranes linked by trans-SNARE complexes require lipids prone to non-bilayer structure for progression to fusion. *Elife*. 3:e01879.

65. Kozlovsky, Y., and M.M. Kozlov. 2003. Membrane fission: model for intermediate structures. *Biophys. J.* 85:85–96.

66. Anderson, R.H., K.A. Sochacki, H. Vuppula, B.L. Scott, E.M. Bailey, M.M. Schultz, J.G. Kerkvliet, J.W. Taraska, A.D. Hoppe, and K.R. Francis. 2021. Sterols lower energetic barriers of membrane bending and fission necessary for efficient clathrin-mediated endocytosis. *Cell Rep.* 37:110008.

67. Poojari, C.S., K.C. Scherer, and J.S. Hub. 2021. Free energies of membrane stalk formation from a lipidomics perspective. *Nat. Commun.* 12:6594.

68. Alimohamadi, H., E.W.-C. Luo, X. Liu, W. Iqbal, R. Yang, S. Gupta, K.A. Nolden, T. Mandal, R.B. Hill, L. Duan, and G.C.L. Wong. 2025. Dynamin-like proteins combine mechano-constriction and membrane remodeling to enable two-step mitochondrial fission via a "snap-through" instability. *J. Am. Chem. Soc.* 147:24258–24274.

69. Stepanyants, N., P.J. Macdonald, C.A. Francy, J.A. Mears, X. Qi, and R. Ramachandran. 2015. Cardiolipin's propensity for phase transition and its reorganization by dynamin-related protein 1 form a basis for mitochondrial membrane fission. *Mol. Biol. Cell*. 26:3104–3116.

70. Thai, T.P., C. Rodemer, A. Jauch, A. Hunziker, A. Moser, K. Gorgas, and W.W. Just. 2001. Impaired membrane traffic in defective ether lipid biosynthesis. *Hum. Mol. Genet.* 10:127–136.

71. Wherley, T.J., X. Zhao, S.M. Hindi, L.J.S. Lopes, E. Leikina, F.C. Rowan, K.D.R. Setchell, A.J. Sodt, L.V. Chernomordik, and D.P. Millay. 2026. Myomaker and ether lipids cooperate to promote fusion-competent membrane states. *Cell Rep.* 45:116900.

72. Kaltenegger, M., J. Kremser, M.P.K. Frewein, P. Ziherl, D.J. Bonthuis, and G. Pabst. 2021. Intrinsic lipid curvatures of mammalian plasma membrane outer leaflet lipids and ceramides. *Biochim. Biophys. Acta Biomembr.* 1863:183709.

73. Ruiz-Argüello, M.B., G. Basáñez, F.M. Goñi, and A. Alonso. 1996. Different effects of enzyme-generated ceramides and diacylglycerols in phospholipid membrane fusion and leakage. *J. Biol. Chem.* 271:26616–26621.

74. Keller, S.L., S.M. Bezrukov, S.M. Gruner, M.W. Tate, I. Vodyanoy, and V.A. Parsegian. 1993. Probability of alamethicin conductance states varies with nonlamellar tendency of bilayer phospholipids. *Biophys. J.* 65:23–27.

75. Lewis, J.R., and D.S. Cafiso. 1999. Correlation between the free energy of a channel-forming voltage-gated peptide and the spontaneous curvature of bilayer lipids. *Biochemistry*. 38:5932–5938.

76. Attard, G.S., R.H. Templer, W.S. Smith, A.N. Hunt, and S. Jackowski. 2000. Modulation of CTP:phosphocholine cytidylyltransferase by membrane curvature elastic stress. *Proc. Natl. Acad. Sci. U. S. A.* 97:9032–9036.

77. Davies, S.M., R.M. Epand, R. Kraayenhof, and R.B. Cornell. 2001. Regulation of CTP: phosphocholine cytidylyltransferase activity by the physical properties of lipid membranes: an important role for stored curvature strain energy. *Biochemistry*. 40:10522–10531.

78. East, J.M., O.T. Jones, A.C. Simmonds, and A.G. Lee. 1984. Membrane fluidity is not an important physiological regulator of the (Ca2+-Mg2+)-dependent ATPase of sarcoplasmic reticulum. *J. Biol. Chem.* 259:8070–8071.

79. Starling, A.P., K.A. Dalton, J.M. East, S. Oliver, and A.G. Lee. 1996. Effects of phosphatidylethanolamines on the activity of the Ca(2+)-ATPase of sarcoplasmic reticulum. *Biochem. J.* 320 (Pt 1):309–314.

80. Jovanović, O., K. Chekashkina, S. Škulj, K. Žuna, M. Vazdar, P.V. Bashkirov, and E.E. Pohl. 2022. Membrane lipid reshaping underlies oxidative stress sensing by the mitochondrial proteins UCP1 and ANT1. *Antioxidants (Basel)*. 11:2314.

81. Escribá, P.V., A. Ozaita, C. Ribas, A. Miralles, E. Fodor, T. Farkas, and J.A. García-Sevilla. 1997. Role of lipid polymorphism in G protein-membrane interactions: nonlamellar-prone phospholipids and peripheral protein binding to membranes. *Proc. Natl. Acad. Sci. U. S. A.* 94:11375–11380.

82. Botelho, A.V., N.J. Gibson, R.L. Thurmond, Y. Wang, and M.F. Brown. 2002. Conformational energetics of rhodopsin modulated by nonlamellar-forming lipids. *Biochemistry*. 41:6354–6368.

83. Soubias, O., and K. Gawrisch. 2012. The role of the lipid matrix for structure and function of the GPCR rhodopsin. *Biochim. Biophys. Acta*. 1818:234–240.

84. Morein, S., A. Andersson, L. Rilfors, and G. Lindblom. 1996. Wild-type Escherichia coli cells regulate the membrane lipid composition in a "window" between gel and non-lamellar structures. *J. Biol. Chem.* 271:6801–6809.

85. Boumann, H.A., J. Gubbens, M.C. Koorengevel, C.-S. Oh, C.E. Martin, A.J.R. Heck, J. Patton-Vogt, S.A. Henry, B. de Kruijff, and A.I.P.M. de Kroon. 2006. Depletion of phosphatidylcholine in yeast induces shortening and increased saturation of the lipid acyl chains: evidence for regulation of intrinsic membrane curvature in a eukaryote. *Mol. Biol. Cell*. 17:1006–1017.

86. Milshteyn, D., J.R. Winnikoff, E. Kocharian, A.M. Armando, E.A. Dennis, P.R. Girguis, and I. Budin. 2026. Active regulation of intrinsic curvature by eukaryotic phospholipid metabolism. *Cell Rep. Phys. Sci.* 0:103277.

87. Chapter Four - Estimating stored curvature elastic energy in biological membranes in vitro and in vivo. .

88. Covino, R., G. Hummer, and R. Ernst. 2018. Integrated Functions of Membrane Property Sensors and a Hidden Side of the Unfolded Protein Response. *Mol. Cell*. 71:458–467.

89. Ballweg, S., E. Sezgin, M. Doktorova, R. Covino, J. Reinhard, D. Wunnicke, I. Hänelt, I. Levental, G. Hummer, and R. Ernst. 2020. Regulation of lipid saturation without sensing membrane fluidity. *Nat. Commun.* 11:1–13.

90. Devkota, R., E. Svensk, M. Ruiz, M. Ståhlman, J. Borén, and M. Pilon. 2017. The adiponectin receptor AdipoR2 and its Caenorhabditis elegans homolog PAQR-2 prevent membrane rigidification by exogenous saturated fatty acids. *PLoS Genet.* 13:e1007004.

91. Bodhicharla, R., R. Devkota, M. Ruiz, and M. Pilon. 2018. Membrane fluidity is regulated cell nonautonomously by Caenorhabditis elegans PAQR-2 and its mammalian homolog AdipoR2. *Genetics*. 210:189–201.

92. Haider, A., Y.-C. Wei, K. Lim, A.D. Barbosa, C.-H. Liu, U. Weber, M. Mlodzik, K. Oras, S. Collier, M.M. Hussain, L. Dong, S. Patel, A. Alvarez-Guaita, V. Saudek, B.J. Jenkins, A.

Koulman, M.K. Dymond, R.C. Hardie, S. Siniossoglou, and D.B. Savage. 2018. PCYT1A regulates phosphatidylcholine homeostasis from the inner nuclear membrane in response to membrane stored curvature elastic stress. *Dev. Cell*. 45:481–495.e8.

93. Glushkova, D., S. Böhm, and M. Beck. 2026. Systematic membrane thickness variation across cellular organelles revealed by cryo-ET. *J. Cell Biol.* 225:e202504053.

94. Arendt, B.M., D.W.L. Ma, B. Simons, S.A. Noureldin, G. Therapondos, M. Guindi, M. Sherman, and J.P. Allard. 2013. Nonalcoholic fatty liver disease is associated with lower hepatic and erythrocyte ratios of phosphatidylcholine to phosphatidylethanolamine. *Appl. Physiol. Nutr. Metab.* 38:334–340.

95. Ikon, N., and R.O. Ryan. 2017. Barth syndrome: Connecting cardiolipin to cardiomyopathy. *Lipids*. 52:99–108.

96. Bahja, J., and M.K. Dymond. 2021. Does membrane curvature elastic energy play a role in mediating oxidative stress in lipid membranes? *Free Radic. Biol. Med.* 171:191–202.

97. Han, X., D.M. Holtzman, and D.W. McKeel Jr. 2001. Plasmalogen deficiency in early Alzheimer's disease subjects and in animal models: molecular characterization using electrospray ionization mass spectrometry: Plasmalogen Deficiency in Alzheimer's Disease. *J. Neurochem.* 77:1168–1180.

98. Goodenowe, D.B., L.L. Cook, J. Liu, Y. Lu, D.A. Jayasinghe, P.W.K. Ahiahonu, D. Heath, Y. Yamazaki, J. Flax, K.F. Krenitsky, D.L. Sparks, A. Lerner, R.P. Friedland, T. Kudo, K. Kamino, T. Morihara, M. Takeda, and P.L. Wood. 2007. Peripheral ethanolamine plasmalogen deficiency: a logical causative factor in Alzheimer's disease and dementia. *J. Lipid Res.* 48:2485–2498.

99. Ginsberg, L., S. Rafique, J.H. Xuereb, S.I. Rapoport, and N.L. Gershfeld. 1995. Disease and anatomic specificity of ethanolamine plasmalogen deficiency in Alzheimer's disease brain. *Brain Res.* 698:223–226.

100. West, A., V. Zoni, W.E. Teague Jr, A.N. Leonard, S. Vanni, K. Gawrisch, S. Tristram-Nagle, J.N. Sachs, and J.B. Klauda. 2020. How Do Ethanolamine Plasmalogens Contribute to Order and Structure of Neurological Membranes? *J. Phys. Chem. B*. 124:828–839.

101. Kumar, A., A. Das, T. Stewart, F.-F. Hsu, P. Kang, and H. Bai. 2026. Age-dependent decline in plasmalogen biosynthesis impairs stress-induced mitochondrial fission in Drosophila. *Exp. Cell Res.* 458:114974.

102. Amelan, A., S.C. Collins, N.S. Damseh, N. Hamada, A. Salim, E. Dvir, G. Monderer-Rothkoff, T. Harel, K.-I. Nagata, B. Yalcin, and S. Shifman. 2026. CRISPR knockout screens reveal genes and pathways essential for neuronal differentiation and implicate PEDS1 in neurodevelopment. *Nat. Neurosci.* 29:592–603.

103. Werner, E.R., M.A. Keller, S. Sailer, K. Lackner, J. Koch, M. Hermann, S. Coassin, G. Golderer, G. Werner-Felmayer, R.A. Zoeller, N. Hulo, J. Berger, and K. Watschinger. 2020. The

TMEM189 gene encodes plasmanylethanolamine desaturase which introduces the characteristic vinyl ether double bond into plasmalogens. *Proc. Natl. Acad. Sci. U. S. A.* 117:7792–7798.

104. Tabet, R., E. Moutin, J.A.J. Becker, D. Heintz, L. Fouillen, E. Flatter, W. Krężel, V. Alunni, P. Koebel, D. Dembélé, F. Tassone, B. Bardoni, J.-L. Mandel, N. Vitale, D. Muller, J. Le Merrer, and H. Moine. 2016. Fragile X Mental Retardation Protein (FMRP) controls diacylglycerol kinase activity in neurons. *Proc. Natl. Acad. Sci. U. S. A.* 113:E3619–28.

105. Bozelli, J.C., Jr, W. Jennings, S. Black, Y.H. Hou, D. Lameire, P. Chatha, T. Kimura, B. Berno, A. Khondker, M.C. Rheinstädter, and R.M. Epand. 2018. Membrane curvature allosterically regulates the phosphatidylinositol cycle, controlling its rate and acyl-chain composition of its lipid intermediates. *J. Biol. Chem.* 293:17780–17791.

106. Semple, S.C., A. Akinc, J. Chen, A.P. Sandhu, B.L. Mui, C.K. Cho, D.W.Y. Sah, D. Stebbing, E.J. Crosley, E. Yaworski, I.M. Hafez, J.R. Dorkin, J. Qin, K. Lam, K.G. Rajeev, K.F. Wong, L.B. Jeffs, L. Nechev, M.L. Eisenhardt, M. Jayaraman, M. Kazem, M.A. Maier, M. Srinivasulu, M.J. Weinstein, Q. Chen, R. Alvarez, S.A. Barros, S. De, S.K. Klimuk, T. Borland, V. Kosovrasti, W.L. Cantley, Y.K. Tam, M. Manoharan, M.A. Ciufolini, M.A. Tracy, A. de Fougerolles, I. MacLachlan, P.R. Cullis, T.D. Madden, and M.J. Hope. 2010. Rational design of cationic lipids for siRNA delivery. *Nat. Biotechnol.* 28:172–176.

107. Zheng, L., S.R. Bandara, Z. Tan, and C. Leal. 2023. Lipid nanoparticle topology regulates endosomal escape and delivery of RNA to the cytoplasm. *Proc. Natl. Acad. Sci. U. S. A.* 120:e2301067120.

108. Zheng, L., M. Baliga, S.F. Gallagher, A. Gao, J. Rueben, Y.K. Go, M. Deserno, and C. Leal. 2026. Introducing a fusogenicity metric for lipid nanoparticle formulation. *bioRxivorg*.

109. Wang, W., K. Chen, and Z. Wang. 2026. Genome-wide CRISPR screen reveals PIK3CA inhibition enhances lipid nanoparticle-mediated siRNA delivery. *Adv. Sci. (Weinh.)*. 13:e17617.

110. Luo, F., T. Akanchise, B. Angelov, and A. Angelova. 2026. In vitro models of oxidative stress, mitochondrial dysfunction, and inflammation for evaluation of neuroprotective biomaterials. *J. Mater. Chem. B Mater. Biol. Med.*

Chapter 2 Homeocurvature adaptation of phospholipids underlies pressure-specialization of deep-sea invertebrates

Abstract: Hydrostatic pressure increases with habitat depth in the ocean, but molecular bases of biological pressure-tolerance, and their distinctness from those of cold-tolerance, are largely unknown. Here we describe how deep-ocean comb jellies (ctenophores) maintain topological plasticity in their lipid membranes at extreme pressures via an adaptation that also constrains their depth range. Structural analysis of membrane lipids from depths up to 4 km showed that deep samples retain access to non-lamellar phases at pressures >250 bar. Lipidomics identified non-bilayer phospholipids with negative spontaneous curvature, including plasmalogens, as a hallmark distinguishing deep-sea membranes from those found in comparably cold but shallow waters. An additive model of curvature and a series of all-atom simulations both predicted that lipidomes from deeper habitats more readily form non-lamellar topologies that are inhibited by pressure. *Escherichia coli* engineered to synthesize higher-curvature lipids displayed enhanced pressure tolerance, whereas incorporation of low-curvature lipids had the opposite effect. Deep-sea lipidomes invert to form non-lamellar structures when brought to atmospheric pressure, and imaging indicates that this could drive the disintegration of deep-sea animals when brought to the surface.

Main Text

The deep sea encompasses more than 90% of Earth's habitable volume and is characterized by low temperature and high pressure, with the pressure increasing by about 1 bar per 10 m depth. In contrast to low-temperature adaptation, specific mechanisms of pressure tolerance in animals are unknown, with few exceptions (1). Pressure inhibits high-volume conformations of all

biomolecules, but has an especially strong effect on lipids due to the high compressibility of their hydrocarbon chains (2). When phospholipids in a fluid lamellar (L_α)-phase membrane are subjected to pressure, their packing increases, reducing fluidity and, eventually, causing a transition to a gel (L_β) phase like that induced by cold (3). For this reason, it has been largely assumed that the phospholipids of marine ectotherms adapt similarly to low temperature and high pressure, increasing acyl chain unsaturation and decreasing chain length to counteract the reduction of membrane fluidity by both conditions (2–4). However, phospholipid compressibility is also highly anisotropic, meaning that pressure has a strong effect on overall lipid shape. Lipids like phosphatidylethanolamine (PE) have a conical steric profile, which is rendered more cylindrical by high pressure. Conical lipids are important for membrane protein function (5) and favor the formation of non-lamellar topologies, like the inverse hexagonal (H_{II}) phase, that occur as intermediates in fusion and fission processes (6).

We investigated high-pressure adaptation using comb jellies (phylum Ctenophora): soft-bodied, poikilothermic invertebrates that inhabit diverse ocean environments. Based on extensive *in situ* observations (Fig. 1B), we have determined that multiple ctenophore lineages adapted independently to various depths (7), making ctenophores a powerful comparative system for studying deep-sea adaptation. In addition to their depth distributions, ctenophores show physiological responses consistent with pressure-specialization. When exposed to high pressures, shallow-adapted ctenophores exhibit constant, accelerated beating of their comb rows leading to eventual shearing (Fig. S1A, S1B). Loss of motor control in ctenophores and other animals (8) could implicate failure at synapses (9), which are enriched in cone-shaped lipids (10). In contrast, when deep-constrained species are brought isothermally to atmospheric pressure, their tissues disintegrate (Fig. 1A, Fig. S1C), a phenomenon also documented across several phyla (11, 12).

When imaged by spectral confocal microscopy, ectodermal tissue dissected from deep-constrained ctenophores showed a loss of membrane structure and an abrupt increase in the General Polarization (GP) of the fluorescent membrane label C-Laurdan – a lipid packing sensor – during disintegration (Fig. 1C). We did not observe this phenomenon in a shallow-constrained ctenophore species, whose habitat extends to the surface, that we collected on the same ROV dive. We asked whether pressure effects on cell membranes could underlie ctenophores' physiological tolerances and depth ranges.

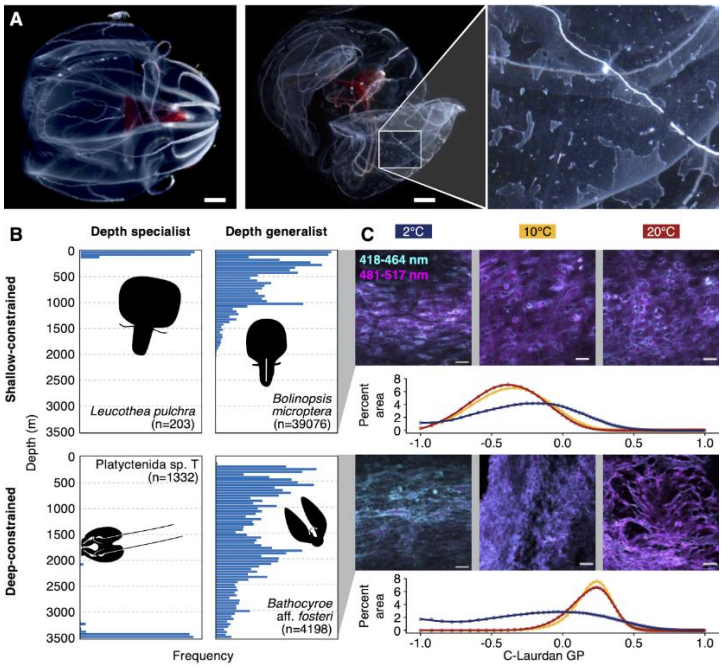

Figure 2.1 Ecological and physiological evidence for pressure specialization in ctenophores.

(**A**) Disintegration of the deep-constrained ctenophore *Bathocyroe* aff. *fosteri* at atmospheric pressure. The left image was taken in the specimen's native water at 2°C, immediately after recovery from the ROV. The right image is of the same animal and was taken 10 minutes later at 4°C. Scale bars, 5 mm. Inset shows disintegration of the ectodermal tissue. (**B**) Depth distributions of four ctenophore species with narrow, broad, shallow, and deep depth ranges. (**C**) Live *ex vivo* tissue mounts stained with solvatochromic C-Laurdan membrane label and imaged at increasing temperatures. Images are a composite of two emission ranges, which are used to calculate GP ratios. In *Bolinopsis microptera*, which occurs from 0-2000 m, GP value decreases with increasing temperature indicating a more fluid lamellar phase. In *Bathocyroe*, which occurs down to >3500 m but not shallower than 200 m, GP displays a sharp increase between 2 and 10°C, concurrent with a catastrophic collapse of membrane morphology. This increase in GP patterns is observed in synthetic lipid systems undergoing inversion (Figs. S3C, S8D). Scale bars, 10 µm.

Deep-sea membrane lipids access non-lamellar phases, even under high pressure

We first probed structural signatures of pressure adaptation in deep-sea membranes using High-Pressure Small Angle X-Ray Scattering (HPSAXS) (*13*) and High-Pressure Fluorescence Spectroscopy (HPFS). In HPSAXS, phospholipids produce X-ray scattering patterns (Fig. 2B) from which major phase changes, i.e. changes in the mobility and arrangement of lipids, can be identified. Using reconstituted polar lipid extracts, we were able to map the predominance of the lamellar fluid (L_α), lamellar gel (L_β), and non-lamellar inverted hexagonal (H_{II}) phases across pressure-temperature (P-T) space (Fig. 2C). Within lamellar regimes, membrane fluidity was assessed by HPFS measuring C-Laurdan GP (Figs. 2D, S1F). Using these approaches, we analyzed lipid extracts from 5 species (8 animals total) that provided sufficient biomass and were native to different domains of depth (0 - 4000 m, collected by SCUBA and ROV) and temperature (0 - 20°C, collected at different latitudes) (Fig. 2A). The comparison of *Beroe cucumis* from Arctic surface waters with Platyctenida sp. T. from the seafloor at ~4000 m was particularly informative, due to the similar temperatures but drastically different pressures of their environments. Although these analyses did not sample any single membrane in the organism nor account for membrane proteins or osmolytes, they allowed us to compare phase behavior trends intrinsic to the lipidome.

We observed that all ctenophore lipid extracts formed an L_α phase in the native P-T domain of the source animal. Within this phase, membrane fluidity was higher in both deep and shallow-cold samples than in temperate samples, consistent with homeoviscous adaptation (Fig. 2D). Pressure-dependent gel phase transitions ($L_\alpha \rightarrow L_\beta$) were observed at moderate pressures (~200 bar) in lipids from shallow temperate animals and at much higher pressures (>1000 bar) in deep species. However, shallow Arctic species, which are adapted to cold but not to high pressure, showed a gel phase transition indistinguishable from deep species. In contrast, there was a

consistent relationship between the animals' native P-T and the non-lamellar phase transition ($L_\alpha \rightarrow H_{II}$) of their lipids. In the deepest species, decreasing pressure ~200 bar from the native P-T – analogous to moving 2000 m shallower in an isothermal seawater column – caused lipids to invert to H_{II}, which coincided with non-monotonic trends in C-Laurdan GP. Similar habitat-specific patterns were observed in samples from a pair of closely related depth-specialist species that adapted independently to surface and deep waters (Fig. S1D, E, F). Thus, the deep-sea lipids we analyzed did not show reduced sensitivity to the $L_\alpha \rightarrow L_\beta$ transition (*14*) compared to shallow, cold-water animals, but did show enhanced access to the $L_\alpha \rightarrow H_{II}$ transition, which is modulated by lipid shape.

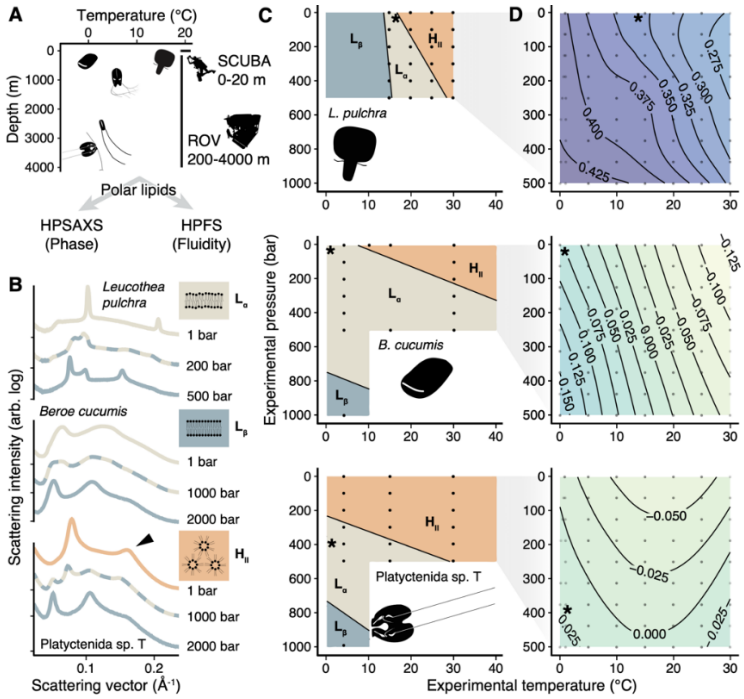

Figure 2.2 Biophysical signatures of depth-adaptation.

(**A**) Schematic of the pipeline carried out on a set of ctenophores collected in different P-T regimes. Polar lipids were isolated from collected animals and analyzed by HPSAXS for phase properties and HPFS for membrane fluidity. (**B**) Representative SAXS profiles used to determine the phase of total polar lipid dispersions from the shallow Arctic ctenophore *Beroe cucumis* (profiles shown at 4°C), the deep-constrained Platyctenida sp. T (4°C), and the shallow-constrained *Leucothea pulchra* (15°C). Profiles are colored by phase composition and baselines are offset for clarity. The broad peak indicated in Platyctenida sp. T results from the overlap of two close peaks characteristic of the H_{II} phase. The three main phases are shown in the inset cartoons. (**C**) Phase change diagrams for the same dispersions based on SAXS data. Points mark measured states and asterisks indicate the native P-T for each animal. (**D**) C-Laurdan GP values for liposomes from the same samples measured across a P-T grid. Within lamellar phase regions, GP reflects lipid ordering, with lower values corresponding to more fluid membranes. Near native conditions, GP pressure-sensitivity was greater in shallow than in deep samples. This sensitivity is reflected by the proximity of contour lines.

Ctenophore lipidomes show contrasting adaptations to pressure and cold

To identify the lipids responsible for pressure-specific physical properties, we analyzed ctenophores collected across a 4000-m depth range, as well as from surface waters at tropical, temperate, and polar latitudes (Fig. 3A, Table S1). This global sampling enabled us to distinguish

adaptations to high pressure from those to cold, as temperature also decreases in deeper ocean waters. Phospholipids were the dominant type of polar lipids in all 66 ctenophores sampled (across 17 species) but their headgroup composition displayed divergent relationships to high pressure and low temperature (Fig. 3B). Depth was associated with a 5-fold increase in the abundance of plasmenyl PE (PPE), which contains an *sn*-1 α-alkenyl ether linkage (*15*). Based on a phylogeny inferred from transcriptomes, depth-associated PPE accumulation evolved independently at least three times in ctenophores (Fig. 3C). PPE was not associated with cold-adaptation independent of depth; in fact, it was more abundant in warm-water shallow animals than cold-water ones. Shallow, cold-water animals instead displayed high levels of phosphatidylcholine (PC), a cylindrical lipid that increases membrane fluidity and has been previously observed in cold-adapted poikilotherms (*16*). Outside of phospholipids, ctenophore lipidomes contained modest levels of cholesterol (<5%), with the notable exception of warm-water animals, and low amounts of sphingomyelin (<0.5%) (Fig. S2C).

In addition to headgroups, divergent trends were seen in phospholipid acyl chains. Acyl chain unsaturation followed trends consistent with homeoviscous adaptation: the number of double bonds increased with both increasing depth and decreasing temperature. However, acyl chain length increased in deeper samples, in contrast to cold, shallow animals and the pattern predicted by homeoviscosity (Fig. 3D). P-T trends were most apparent when all acyl chains were averaged, however the *sn*-1 chains alone exhibited strong signals. The patterns among *sn*-2 chains were similar but non-significant (Fig. S2A). Acyl chain analysis of lysophosphatidylethanolamine (LPE) also indicated that variation in PPE levels between samples was not driven by oxidative degradation (Fig. S2B). Taken together, these results indicate that ctenophore lipidomes contain depth-specific adaptations that cannot be fully explained by a need to maintain membrane fluidity.

Although our analysis could not resolve ctenophore membrane composition at a subcellular level, the homogeneity of deep and cold-water lipidomes, containing predominantly polyunsaturated PC or PPE, suggest that they do not feature the extensive heterogeneity characteristic of mammalian cell membranes (*17*).

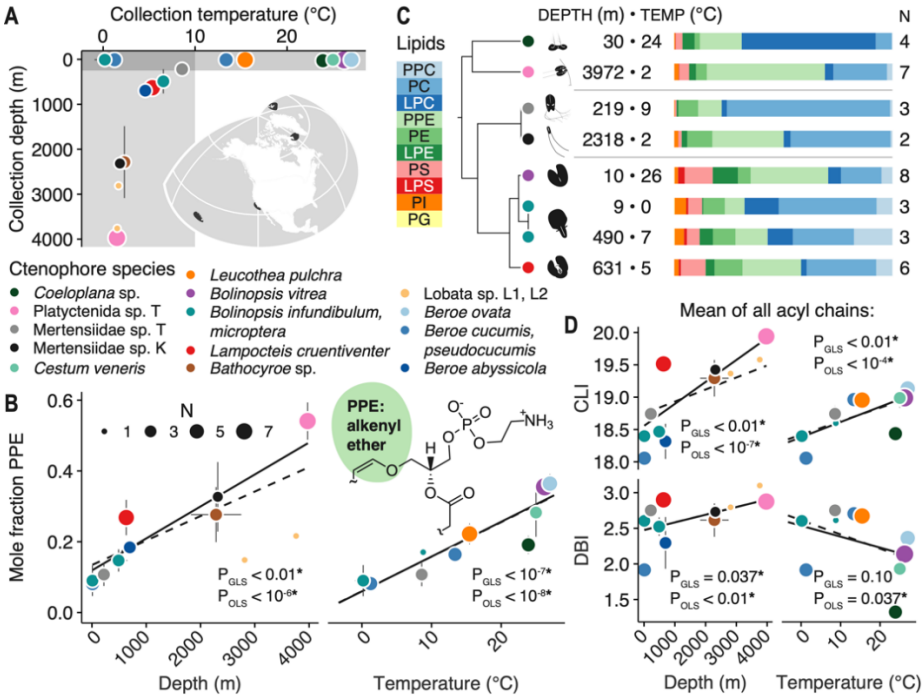

Figure 2.3 Lipidomic analysis of ctenophore phospholipids.

(**A**) Plot showing the depth and temperature regimes of the 66 ctenophores in the dataset. Each data point represents the mean for one of the 17 species collected; all error bars are +/- SEM. Subsets of the collections made ≤10°C and ≤250 m depth, shaded in gray, were used to assess depth and temperature trends, respectively. Collection locales are marked on the globe in black. (**B**) High relative abundance of PPE is correlated with both deep-cold and shallow-warm habitats. Structure of the PPE alkenyl ether linkage is inset. Ordinary least-squares regressions (OLS, solid lines) and phylogenetically generalized ones (GLS, dashed lines) are shown with their corresponding P-values; an asterisk indicates significance at the $\alpha \leq 0.05$ level. (**C**) Examples of independent lipidomic depth-adaptation in three ctenophore clades, delimited with gray lines. Phylogenetics have revealed that ctenophores have depth-specialized on multiple occasions. Within each clade, deeper cold species have higher fractions of PPE and PE, and lower fractions of PC and lysolipids. Temperature specialization of a shallow, tropical representative of genus *Bolinopsis* is also shown. (**D**) Phospholipid total chain length index (CLI) and unsaturation (double bond index; DBI) as a function of depth and temperature. Deeper cold lipidomes feature longer and more unsaturated acyl chains, while colder shallow lipidomes feature shorter and more unsaturated acyl chains. Regressions are shown as in **B**.

Biophysical measurements and simulations support a homeocurvature adaptation model

We analyzed the pressure-dependent properties of PPE, given that it was the only major depth-correlated lipid class (Fig. S2C) and constituted up to 73% of phospholipids in whole bodies – and slightly more in tentacle tissue – from the deepest samples (Fig. S2D). We observed that the midpoint pressure for the inverted phase transition ($L_\alpha \rightarrow H_{II}$) was higher for liposomes composed of PPE, with either monounsaturated or polyunsaturated *sn*-2 chains, than those made of the corresponding PE species. The pressure of the gel phase transition ($L_\alpha \rightarrow L_\beta$) also increased modestly, both shifting and narrowing the fluid lamellar region (Fig. 4A, Fig. S3A). Within the lamellar phase, PPE increased membrane fluidity at high pressures (Fig. S3B). High membrane fluidity and the ability of lipids to form non-lamellar topologies like H_{II} are thought to be required for membrane fusion (*17*). Accordingly, we found that Ca^{2+}-mediated fusion of liposomes *in vitro* was inhibited by moderate pressures (100 bar), but that this loss of activity could be rescued by substitution of PPE for PE (Fig. S4).

In light of the distinctive phase behavior of PPE, we asked whether there is a broader depth-adaptive trend in lipid shape. The conical or cylindrical nature of a lipid's steric profile is captured in the monolayer spontaneous curvature parameter c_0. This curvature, which has units of inverse length, is defined as the reciprocal of the radius circumscribed by an unstressed monolayer of a given lipid. A negative-curvature lipid forms monolayers curving toward the headgroup, as are observed in the H_{II} phase, while a zero-curvature lipid forms flat monolayers, thus favoring lamellar phases. It has remained unclear whether the propensity for PPE to promote the H_{II} phase corresponds to a more negative c_0 (also termed "higher curvature") for the lipid class (*18*, *19*). We measured the pressure-dependent c_0 of PPE relative to that of diacyl PE using HPSAXS and found that it was more negatively curved under all conditions, requiring 700 bar of pressure to match the

curvature of PE (Fig. 4B). PPE thus has the most negative curvature of any phospholipid class, although we cannot rule out other mechanisms by which it could promote the H_{II} phase. Based on these curvature values and previous measurements, we built a model that calculates the mean lipidome curvature at 1 bar, c_0, incorporating contributions from headgroup classes (Fig. 4C), lysolipids, and *sn*-1 acyl chain structure (Materials and Methods). Modeled c0 becomes more negative with habitat depth among cold-adapted ctenophores (Fig. S5C), as well as among all individuals (Fig. 4D). It does not correlate with temperature (Figs. 4D, S5D). The model also suggested that in shallow-warm animals, PPE negative curvature is offset by positively curved lysolipids and lower chain unsaturation (Fig. S5A).

The formula for c0 assumes ideal mixing of lipids, which is not the case in complex mixtures that typically compose cell membranes. To address this, we conducted molecular dynamics (MD) simulations of bilayers modeled after ctenophore lipidomes. Simulations were performed with all-atom resolution using the CHARMM36 force-field, which we were able to validate at high pressure (Supplementary Text) by predicting experimentally observed pressure-dependent changes to bilayer packing parameters and phase transitions (Fig. S6). We then constructed complex membranes containing representatives of the predominant (≥5%) lipid classes, including both phospholipids and cholesterol (Fig. S7A). When comparing cold-adapted Platyctenida sp. T (4000 m, 2°C) with *Bolinopsis infundibulum* (10 m, 0°C), whose lipidome is similar to that of *Beroe cucumis* used in HPSAXS (Fig. S2E), we observed similar pressure-dependencies for lipid packing (APL strain) and translational mobility (D_T). However, the first moment of the lateral stress profiles – a measure of membrane deformability that is equal to the negative product of the monolayer bending modulus (k_b) and spontaneous curvature (c_0) – displayed a large (~500 bar) pressure offset (Fig. 4E). Although simulations were constrained to a

bilayer state, the high $-k_b c_0$ values of Platyctenida sp. T lipids at low pressures was consistent with their tendency to form the non-lamellar H_{II} phase, as observed by HPSAXS.

We simulated two additional species from different P-T regimes: *Lampocteis cruentiventer* (630 m, 5°C) and *Bolinopsis vitrea* (10 m, 26°C) (Fig. S7). The *L. cruentiventer* simulations produced APL strain and D_T values indistinguishable from the other two cold species and a smaller $-k_b c_0$ than that of *B. infundibulum*. Because all simulations were carried out at 20°C and *L. cruentiventer* lives warmer than *B. infundibulum* and Platyctenida sp. T, this difference could reflect the interplay between temperature- and depth-adaptation. Of the four species, the *B. vitrea* simulations exhibited the lowest values for $-k_b c_0$ across simulated pressures (Fig. S7B), further indicating that lipidome components, including acyl chain composition, positively curved lipids, and cholesterol content, counterbalance the negative curvature of PPE in warm, shallow animals. At 1000 bar, *B. vitrea* bilayers exhibit regions of condensed, gel-like chains (Fig. S7D) that was not observed in the three cold-water species, consistent with the behavior of the warmest, shallow sample analyzed in HPSAXS (Fig. 2C).

Based on these analyses, we propose a *homeocurvature adaptation model* for depth specialization (Fig. 4F). In this model, lipidomes with more negative curvature (as measured at 1 bar) are required to maintain membrane plasticity at increasing pressures. For very deep animals, such compositions are incapable of forming stable bilayers when depressurized. Consistent with this tradeoff, we found that the increasing C-Laurdan GP of disintegrating *Bathocyroe* (c_0 = -0.013 +/- 1.9×10^{-3} $Å^{-1}$) cell membranes in Fig. 1 resembles that of synthetic (Fig. S3B) and animal-derived (Fig. 2D, Fig. S1F) liposomes inverting to form H_{II}. In contrast, the shallow-constrained species *Bolinopsis microptera* (c_0 = -0.0058 +/- 6.0×10^{-4} $Å^{-1}$), which does not disintegrate, showed

a decrease in GP under the same conditions, consistent with its membranes remaining lamellar and becoming more fluid as they were warmed (Fig. 1C, S8A).

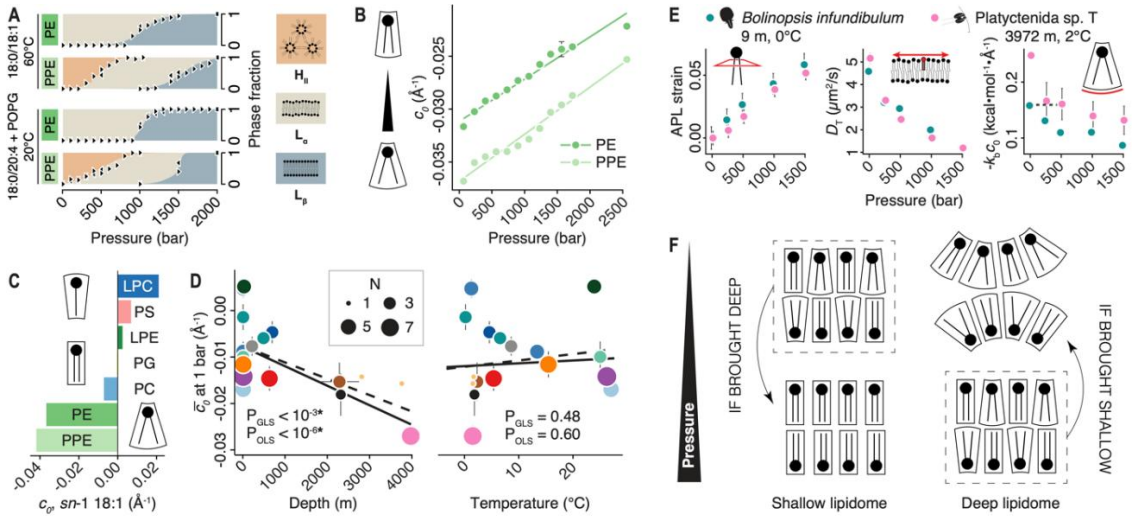

Figure 2.4 Exploring the role of lipid curvature in deep-sea lipidomes enriched in PPE.

(**A**) Lipid phase ratios estimated from HPSAXS data plotted as a function of pressure and of the PPE headgroup. At the temperatures tested, PPE was H_{II}-phase and PE was L_{α}-phase at 1 bar regardless of whether the *sn*-2 acyl chain was poly- or monounsaturated. The polyunsaturated phospholipids were chosen as the closest commercially available analogues to those in ctenopohres; 5 mole percent PG was added to bring the inverted phase transition within an instrumentally achievable P-T domain. Each black triangle denotes an individual X-ray exposure taken during a pressure sweep in the indicated direction. Black squares at upper right are exposures taken at maximum pressure. (**B**) Spontaneous curvature (c_0) values measured for PPE and PE species with a monounsaturated *sn*-2 chain. Cartoons by the vertical axis illustrate the relationship between c_0 and lipid shape. PPE shows a stronger negative curvature than PE and the effect of pressure on both is identical. Neutral-plane c_0 was inferred by fitting global models to HPSAXS profiles of the lipids (20%) hosted in a di-oleoyl PE (DOPE) H_{II} phase and relaxed with 10.7% w/w 9(Z)-tricosene. (**C**) Representative c_0 values for phospholipid classes. These were used along with linear corrections for *sn*-1 acyl chain structure (Materials and Methods) to estimate the mean phospholipid curvature at 1 bar (c_0) for all measured lipidomes. (**D**) The robust correlation of c0 with habitat depth among all animals sampled; deeper lipidomes feature a higher degree of lipidome curvature. Habitat temperature does not predict c0. Regressions are shown as in Fig. 3. (**E**) Comparison of simulated lipidomes modeled after a cold, shallow species (*B. infundibulum*) and a deep species (Platyctenida sp. T) Pressure-dependent properties include area per lipid (APL) strain relative to 1 bar, average lipid translational diffusion rate (D_T), and the first moment of the computed lateral stress profile, which is equal to $-k_b c_0$. All simulations were run at 20°C. For $-k_b c_0$, the pressure equivalency of shallow and deep systems is indicated with a dashed line. Simulation snapshots and additional details are shown in Fig. S7. (**F**) A homeocurvature adaptation model in which a more negative baseline (1 bar) lipidome curvature is required to offset the effects of high pressure on lipid shape. For both shallow and deep lipidomes, physiological membrane states (dashed boxes) contain a mixture of bilayer and non-bilayer lipids, but the chemistry of these species must differ to maintain this arrangement. When shallow membranes are compressed, lipidome curvature is lost, potentially disrupting membrane dynamics and plasticity. When deep membranes are decompressed, negative lipidome curvature increases, destabilizing membrane structure.

Modulating lipid curvature can enhance and reduce biological pressure tolerance

We sought to test the key prediction of the homeocurvature adaptation model – that lipidome curvature modulates biological pressure tolerance – using laboratory organisms whose membrane composition could be genetically manipulated. The inner membrane of *E. coli* K12 is composed primarily of PE, with acyl chains that maintain both fluidity (*20*) and curvature (*4*) in response to temperature changes. To test the effects of more negative lipidome curvature, we expressed a PPE synthesis cassette (plsAR) from *Clostridium perfringens (21)* in anaerobically grown BL21 (Fig. 5A), then exposed the cultures to high pressure for 48 hours. Upon induction of plsAR expression, 25% of total BL21 phospholipids were converted from PE to PPE (Fig. S9A), while the acyl chain profile remained similar (Fig. S9B). SAXS analysis of reconstituted *E. coli* lipid extracts showed that plsAR expression also promoted the H_{II} phase compared to control cells, consistent with an increase in negative lipidome curvature (Fig. 5B, S9C). When the BL21 strains were grown 500 bar, we found that both the doubling rate and survival of PPE-synthesizing cells were significantly less pressure-sensitive than those of the empty-vector control (Fig. 5C, D).

To test the effects of reduced negative lipidome curvature on high-pressure fitness, we used a P_{BAD}-PC synthase cassette (*22*) to replace PE with PC. PC has a higher fluidity than PE and better resists pressure-induced gelling (Fig. S3D), but its cylindrical profile inhibits non-lamellar topologies (*23*). It can thus be used to differentiate the effects of membrane fluidity and gel phase transitions from those related to curvature. SAXS analysis confirmed that lipids from PC-synthesizing cells had less ability to access the H_{II} phase and were also more resistant to the gel phase transition (Figs. 5F, S9C). Growth of PC-producing cells was diminished at 250 bar and survival ceased at 500 bar (Fig. 5G, H), suggesting that loss of lipidome curvature is deleterious to high-pressure fitness even when fluidity is increased. Both PC- and PPE-synthesizing strains

also showed lower levels of phosphatidylglycerol (PG), but loss of PG synthesis alone did not alter high-pressure fitness under our experimental conditions (Fig. S9D, E). Therefore, increase (by PPE synthesis) or decrease (by PC synthesis) of negative lipidome curvature can be sufficient to modulate high-pressure fitness in cells.

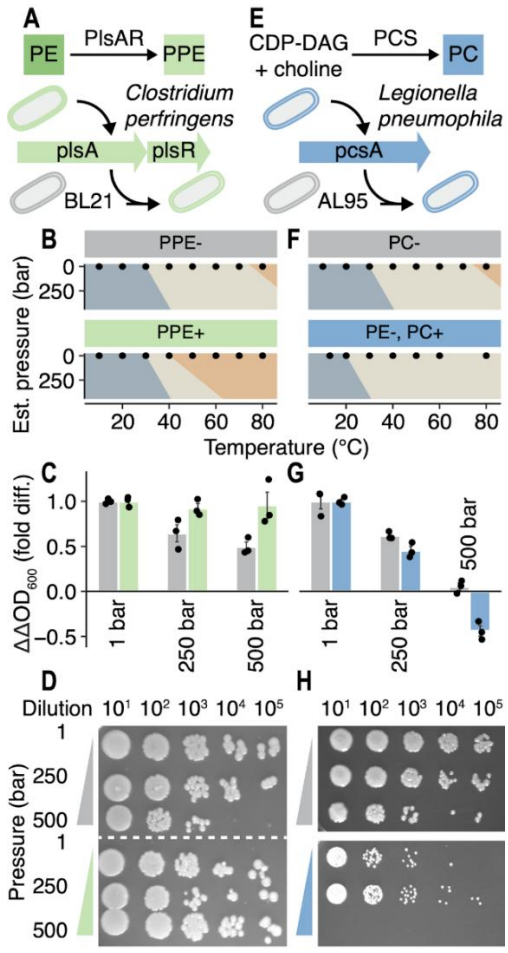

Figure 2.5 Testing the principles of pressure adaptation in engineered bacterial cells.

(**A**) Heterologous synthesis of PPE, using plasmid-based expression of the plsAR PE reductase from *Clostridium*, enhances *E. coli* lipidome curvature and its propensity to invert into H_{II}, as assayed by SAXS as a function of temperature. (**B**) Phase diagrams of *E. coli* polar lipids (inner and outer membrane) in PPE- (BL21 + pET28a, gray) and PPE+ (BL21 + pPlScp, green) strains. To facilitate comparison with the pressure treatments, these diagrams are extrapolated along a pressure axis using published temperature-pressure equivalencies (*24*). (**C**) Growth of PPE-lacking and PPE-containing *E. coli* in microaerobic culture under pressure. The difference in pressure-sensitivity of growth was significant (P = 0.009, multiple regression with F-test). (**D**) Post-decompression survival was similarly rendered pressure-insensitive by PPE (compare lower right colonies in both panels.) (**E**) Non-native synthesis of PC, using plasmid-based expression of the PC synthase (PCS) from *Legionella* in the PE-free background AL95, reduces lipidome curvature and propensity to invert into H_{II}. (**F**) Pressure-extrapolated phase diagrams of *E. coli* polar lipids in PC- (AAL9256 with an integrated P_{BAD}-pssA cassette, gray) and PE-, PC+ (AL95 + pPCSlp, blue) strains. (**G**) Growth and (**H**) survival were assessed as in **C** and **D**, except that outgrowth prior to pressurization was aerobic. The difference in pressure-sensitivity of growth was significant (p = 0.002), and the PC strain was inviable at 500 bar. Strain pairs were chosen to minimize differences in genetic background and promoters were identical within each pair.

Discussion

All biological membranes consist of cylindrical bilayer-forming lipids, which support membrane structure, and conical non-bilayer lipids, which support membrane plasticity (*25*). The high-pressure and low-temperature waters of the deep sea present a unique biophysical challenge to maintaining the latter. We found that reconstituted deep-sea lipids show a remarkable ability to access non-lamellar topologies like the H_{II} phase, even under these extreme conditions. Multiple molecular adaptations underlie this capability. The ether phospholipid PPE, a major component of deep-sea ctenophore membranes, maintains a conical shape under high-pressure deep-sea conditions due to its highly negative spontaneous curvature. We also observed elevated PPE in tropical surface animals, where it could fulfill previously proposed roles as an antioxidant (*26*) and as a driver of local heterogeneity in cholesterol-rich membranes (*27*). Exclusive to deep samples is the combination of abundant PPE, long and highly unsaturated acyl chains, and low amounts of lysolipids, all of which contribute to lipidomes with exceptionally negative spontaneous curvature at 1 bar. High pressure reduces this extreme curvature so that deep lipidomes form physiologically viable membranes under their native conditions.

Lipid adaptation in marine systems has mostly been explored in the context of temperature, with pressure- and cold-adaptation treated as functionally interchangeable. However, pressure is a stronger inhibitor of non-lamellar topologies because of their large molar volume. In contrast, temperature is dominant in controlling membrane fluidity and the formation of gel phases. Accordingly, we find that depth-adaptation in ctenophores is biochemically distinct from cold-adaptation. The hallmark of shallow, low-temperature lipidomes is a high fraction of low-melting-temperature PC lipids with shorter acyl chains, whose abundance decreases with depth. In contrast, deep-sea animals accumulate conical non-bilayer lipids, including PPE, which has both stronger

curvature and greater fluidity than diacyl PE. These differing responses to cold and pressure suggest that deeper environments might not substitute for contracting regions with cold surface waters, which has been proposed as a mechanism of ecological resilience in warming polar seas (*28*).

The homeocurvature adaptation model postulates that pressure-induced changes in lipid shape are relevant to the habitat ranges of both shallow and deep animals (Fig. 4F). The loss of motor function in shallow-constrained animals subjected to high pressure (Fig. S1A, B) is consistent with membrane-associated defects in the nervous system, for example in synaptic vesicle trafficking or ion channel function. Deep-specialized animals may mitigate such defects by accumulating high-curvature lipids, which are also enriched in the nervous systems of mesophiles (*29*). Because it is based on hydrocarbon compressibility, the effect of pressure on lipid shape is similar in all phospholipids, so counteracting it requires a more negative baseline (1 bar) curvature that may not sustain a lamellar phase at the surface. Through this mechanism, adaptation to extreme depths could have given rise to organisms that require pressure to maintain their membranes.

Acknowledgements

The material in this chapter, in full, is a reprint of the material as it appears in "Homeocurvature adaptation of phospholipids to pressure in deep-sea invertebrates". Winnikoff, Jacob R; Milshteyn, Daniel; Vargas-Urbano, Sasiri J; Pedraza-Joya, Miguel A; Armando, Aaron M; Quehenberger, Oswald; Sodt, Alexander; Gillilan, Richard E; Dennis, Edward A; Lyman, Edward; Haddock, Steven HD; Budin, Itay. *Science*. 2024. The dissertation author was a primary investigator and second author of this paper. Sol Gruner, George Somero, and Douglas Bartlett

contributed discussion that informed the direction of this work. Caitlyn Webster, Charlotte Havermans, Stefanie Meyer, Lynne Christianson, Shannon Johnson, and Darrin Schultz collected ctenophores for this study. Crews of the *R/V Western Flyer*, *R/V Rachel Carson*, *R/V Ka'imikai-O-Kanaloa*, *R/V Kilo Moana*, ROV Doc Ricketts, and ROV Ventana provided field support. Qingqiu Huang provided HPSAXS technical support.

References

1. P. H. Yancey, M. E. Gerringer, J. C. Drazen, A. A. Rowden, A. Jamieson, Marine fish may be biochemically constrained from inhabiting the deepest ocean depths. *Proc. Natl. Acad. Sci.* **111**, 4461–4465 (2014).

2. G. N. Somero, Adaptations to High Hydrostatic Pressure. *Annu. Rev. Physiol.* **54**, 557–577 (1992).

3. A. R. Cossins, A. G. Macdonald, The adaptation of biological membranes to temperature and pressure: Fish from the deep and cold. *J. Bioenerg. Biomembr.* **21**, 115–135 (1989).

4. S. Morein, A.-S. Andersson, L. Rilfors, G. Lindblom, Wild-type *Escherichia coli* Cells Regulate the Membrane Lipid Composition in a "Window" between Gel and Non-lamellar Structures. *J. Biol. Chem.* **271**, 6801–6809 (1996).

5. M. Wikström, A. A. Kelly, A. Georgiev, H. M. Eriksson, M. R. Klement, M. Bogdanov, W. Dowhan, Å. Wieslander, Lipid-engineered Escherichia coli Membranes Reveal Critical Lipid Headgroup Size for Protein Function. *J. Biol. Chem.* **284**, 954–965 (2009).

6. P. I. Kuzmin, J. Zimmerberg, Y. A. Chizmadzhev, F. S. Cohen, A quantitative model for membrane fusion based on low-energy intermediates. *Proc. Natl. Acad. Sci.* **98**, 7235–7240 (2001).

7. J. R. Winnikoff, S. H. D. Haddock, I. Budin, Depth- and temperature-specific fatty acid adaptations in ctenophores from extreme habitats. *J. Exp. Biol.* **224**, jeb242800 (2021).

8. G. L. Kooyman, *Diverse Divers* (Springer Berlin Heidelberg, Berlin, Heidelberg, 1989), vol. 23 of *Zoophysiology*.

9. P. Burkhardt, J. Colgren, A. Medhus, L. Digel, B. Naumann, J. J. Soto-Angel, E.-L. Nordmann, M. Y. Sachkova, M. Kittelmann, Syncytial nerve net in a ctenophore adds insights on the evolution of nervous systems. *Science*. **380**, 293–297 (2023).

10. S. Takamori, M. Holt, K. Stenius, E. A. Lemke, M. Grønborg, D. Riedel, H. Urlaub, S. Schenck, B. Brügger, P. Ringler, S. A. Müller, B. Rammner, F. Gräter, J. S. Hub, B. L. De

Groot, G. Mieskes, Y. Moriyama, J. Klingauf, H. Grubmüller, J. Heuser, F. Wieland, R. Jahn, Molecular Anatomy of a Trafficking Organelle. *Cell.* **127**, 831–846 (2006).

11. M. E. Gerringer, J. C. Drazen, T. D. Linley, A. P. Summers, A. J. Jamieson, P. H. Yancey, Distribution, composition and functions of gelatinous tissues in deep-sea fishes. *Royal Society Open Science*. **4**, 171063 (2017).

12. J. J. Childress, A. T. Barnes, L. B. Quetin, B. H. Robison, Thermally protecting cod ends for the recovery of living deep-sea animals. *Deep Sea Res. Part I*. **25**, 419–422 (1978).

13. D. K. Rai, R. E. Gillilan, Q. Huang, R. Miller, E. Ting, A. Lazarev, M. W. Tate, S. M. Gruner, High-pressure small-angle X-ray scattering cell for biological solutions and soft materials. *J. Appl. Crystallogr.* **54**, 111–122 (2021).

14. A. Maiti, S. Daschakraborty, Can Urea and Trimethylamine- *N* -oxide Prevent the Pressure-Induced Phase Transition of Lipid Membrane? *J. Phys. Chem. B*. **126**, 1426–1440 (2022).

15. J. M. Dean, I. J. Lodhi, Structural and functional roles of ether lipids. *Protein Cell*. **9**, 196–206 (2018).

16. R. Dawaliby, C. Trubbia, C. Delporte, C. Noyon, J.-M. Ruysschaert, P. Van Antwerpen, C. Govaerts, Phosphatidylethanolamine Is a Key Regulator of Membrane Fluidity in Eukaryotic Cells. *J. Biol. Chem.* **291**, 3658–3667 (2016).

17. J. H. Lorent, K. R. Levental, L. Ganesan, G. Rivera-Longsworth, E. Sezgin, M. Doktorova, E. Lyman, I. Levental, Plasma membranes are asymmetric in lipid unsaturation, packing and protein shape. *Nat. Chem. Biol.* **16**, 644–652 (2020).

18. K. Lohner, P. Balgavy, A. Hermetter, F. Paltauf, P. Laggner, Stabilization of non-bilayer structures by the etherlipid ethanolamine plasmalogen. *Biochimica et Biophysica Acta (BBA) – Biomembranes*. **1061**, 132–140 (1991).

19. K. Lohner, Is the high propensity of ethanolamine plasmalogens to form non-lamellar lipid structures manifested in the properties of biomembranes? *Chem. Phys. Lipids*. **81**, 167–184 (1996).

20. M. Sinensky, Homeoviscous Adaptation – A Homeostatic Process that Regulates the Viscosity of Membrane Lipids in *Escherichia coli*. *Proc. Natl. Acad. Sci.* **71**, 522–525 (1974).

21. D. R. Jackson, C. D. Cassilly, D. R. Plichta, H. Vlamakis, H. Liu, S. B. Melville, R. J. Xavier, J. Clardy, Plasmalogen Biosynthesis by Anaerobic Bacteria: Identification of a Two-Gene Operon Responsible for Plasmalogen Production in *Clostridium perfringens*. *ACS Chem. Biol.* **16**, 6–13 (2021).

22. M. Bogdanov, P. Heacock, Z. Guan, W. Dowhan, Plasticity of lipid-protein interactions in the function and topogenesis of the membrane protein lactose permease from *Escherichia coli*. *Proc. Natl. Acad. Sci.* **107**, 15057–15062 (2010).

23. R. Winter, A. Landwehr, T. Brauns, J. Erbes, C. Czeslik, O. Reis, "High-Pressure Effects on the Structure and Phase Behavior of Model Membrane Systems" in *High Pressure Effects in Molecular Biophysics and Enzymology*, J. L. Markley, D. B. Northrop, C. A. Royer, Eds. (Oxford University Press, 1996).

24. P. T. C. So, S. M. Gruner, S. Erramilli, Pressure-induced topological phase transitions in membranes. *Phys. Rev. Lett.* **70**, 3455–3458 (1993).

25. S. M. Gruner, Intrinsic curvature hypothesis for biomembrane lipid composition: a role for nonbilayer lipids. *Proc. Natl. Acad. Sci.* **82**, 3665–3669 (1985).

26. A. Broniec, R. Klosinski, A. Pawlak, M. Wrona-Krol, D. Thompson, T. Sarna, Interactions of plasmalogens and their diacyl analogs with singlet oxygen in selected model systems. *Free Radical Biology and Medicine*. **50**, 892–898 (2011).

27. L. J. Pike, X. Han, K.-N. Chung, R. W. Gross, Lipid Rafts Are Enriched in Arachidonic Acid and Plasmenylethanolamine and Their Composition Is Independent of Caveolin-1 Expression: A Quantitative Electrospray Ionization/Mass Spectrometric Analysis. *Biochemistry*. **41**, 2075–2088 (2002).

28. D. Cottin, A. Brown, A. Oliphant, N. C. Mestre, J. Ravaux, B. Shillito, S. Thatje, Sustained hydrostatic pressure tolerance of the shallow water shrimp *Palaemonetes varians* at different temperatures: Insights into the colonisation of the deep sea. *Comp. Biochem. Physiol. A Mol. Integr. Physiol.* **162**, 357–363 (2012).

29. X. Han, D. M. Holtzman, D. W. McKeel, Plasmalogen deficiency in early Alzheimer's disease subjects and in animal models: molecular characterization using electrospray ionization mass spectrometry: Plasmalogen Deficiency in Alzheimer's Disease. *J. Neurochem.* **77**, 1168–1180 (2001).

30. B. Schlining, N. Stout, *MBARI's Video Annotation and Reference System* (IEEE, 2006).

31. I. Budin, A. Debnath, J. W. Szostak, Concentration-Driven Growth of Model Protocell Membranes. *J. Am. Chem. Soc.* **134**, 20812–20819 (2012).

32. D. M. Owen, C. Rentero, A. Magenau, A. Abu-Siniyeh, K. Gaus, Quantitative imaging of membrane lipid order in cells and organisms. *Nat. Protoc.* **7**, 24–35 (2012).

33. E. G. Bligh, W. J. Dyer, A rapid method of total lipid extraction and purification. *Can. J. Biochem. Physiol.* **37**, 911–917 (1959).

34. G. Hamilton, K. Comai, Rapid separation of neutral lipids, free fatty acids and polar lipids using prepacked silica Sep-Pak columns. *Lipids*. **23**, 1146–1149 (1988).

35. H. Chung, M. Caffrey, The curvature elastic-energy function of the lipid–water cubic mesophase. *Nature*. **368**, 224–226 (1994).

36. Y.-F. Chen, K.-Y. Tsang, W.-F. Chang, Z.-A. Fan, Differential dependencies on [Ca^{2+}] and temperature of the monolayer spontaneous curvatures of DOPE, DOPA and cardiolipin: effects of modulating the strength of the inter-headgroup repulsion. *Soft Matter*. **11**, 4041–4053 (2015).

37. S. De Villiers, B. K. Nelson, Detection of Low-Temperature Hydrothermal Fluxes by Seawater Mg and Ca Anomalies. *Science*. **285**, 721–723 (1999).

38. B. Hopkins, R. E. Gillilan, S. Skou, *BioXTAS RAW*: improvements to a free open-source program for small-angle X-ray scattering data reduction and analysis. *J. Appl. Crystallogr.* **50**, 1545–1553 (2017).

39. O. Quehenberger, A. M. Armando, A. H. Brown, S. B. Milne, D. S. Myers, A. H. Merrill, S. Bandyopadhyay, K. N. Jones, S. Kelly, R. L. Shaner, C. M. Sullards, E. Wang, R. C. Murphy, R. M. Barkley, T. J. Leiker, C. R. H. Raetz, Z. Guan, G. M. Laird, D. A. Six, D. W. Russell, J. G. McDonald, S. Subramaniam, E. Fahy, E. A. Dennis, Lipidomics reveals a remarkable diversity of lipids in human plasma. *J. Lipid Res.* **51**, 3299–3305 (2010).

40. J. Hartler, A. M. Armando, M. Trötzmüller, E. A. Dennis, H. C. Köfeler, O. Quehenberger, Automated Annotation of Sphingolipids Including Accurate Identification of Hydroxylation Sites Using MS^n Data. *Anal. Chem.* **92**, 14054–14062 (2020).

41. N. Düzgünes, J. Wilschut, R. Fraley, D. Papahadjopoulos, Studies on the mechanism of membrane fusion. Role of head-group composition in calcium- and magnesium-induced fusion of mixed phospholipid vesicles. *Biochimica et Biophysica Acta (BBA) - Biomembranes*. **642**, 182–195 (1981).

42. T. Weber, B. V. Zemelman, J. A. McNew, B. Westermann, M. Gmachl, F. Parlati, T. H. Söllner, J. E. Rothman, SNAREpins: Minimal Machinery for Membrane Fusion. *Cell*. **92**, 759–772 (1998).

43. W. Tate, S. M. Gruner, Temperature dependence of the structural dimensions of the inverted hexagonal (HII) phase of phosphatidylethanolamine-containing membranes. *Biochemistry*. **28**, 4245–4253 (1989).

44. M. P. K. Frewein, M. Rumetshofer, G. Pabst, Global small-angle scattering data analysis of inverted hexagonal phases. *J. Appl. Crystallogr.* **52**, 403–414 (2019).

45. K. Dymond, Lipid monolayer spontaneous curvatures: A collection of published values. *Chem. Phys. Lipids*. **239**, 105117 (2021).

46. J. B. Klauda, R. M. Venable, J. A. Freites, J. W. O'Connor, D. J. Tobias, C. Mondragon-Ramirez, I. Vorobyov, A. D. MacKerell Jr, R. W. Pastor, Update of the CHARMM all-atom additive force field for lipids: validation on six lipid types. *J. Phys. Chem. B*. **114**, 7830–7843 (2010).

47. N. Leonard, R. W. Pastor, J. B. Klauda, Parameterization of the CHARMM All-Atom Force Field for Ether Lipids and Model Linear Ethers. *J. Phys. Chem. B*. **122**, 6744–6754 (2018).

48. W. L. Jorgensen, J. Chandrasekhar, J. D. Madura, R. W. Impey, M. L. Klein, Comparison of simple potential functions for simulating liquid water. *J. Chem. Phys.* **79**, 926–935 (1983).

49. J. Lee, X. Cheng, J. M. Swails, M. S. Yeom, P. K. Eastman, J. A. Lemkul, S. Wei, J. Buckner, J. C. Jeong, Y. Qi, S. Jo, V. S. Pande, D. A. Case, C. L. Brooks 3rd, A. D. MacKerell Jr, J. B. Klauda, W. Im, CHARMM-GUI Input Generator for NAMD, GROMACS, AMBER, OpenMM, and CHARMM/OpenMM Simulations Using the CHARMM36 Additive Force Field. *J. Chem. Theory Comput.* **12**, 405–413 (2016).

50. S. E. Feller, Y. Zhang, R. W. Pastor, B. R. Brooks, Constant pressure molecular dynamics simulation: The Langevin piston method. *J. Chem. Phys.* **103**, 4613–4621 (1995).

51. G. J. Martyna, D. J. Tobias, M. L. Klein, Constant pressure molecular dynamics algorithms. *J. Chem. Phys.* **101**, 4177–4189 (1994).

52. J.-P. Ryckaert, G. Ciccotti, H. J. C. Berendsen, Numerical integration of the cartesian equations of motion of a system with constraints: molecular dynamics of n-alkanes. *J. Comput. Phys.* **23**, 327–341 (1977).

53. T. Darden, D. York, L. Pedersen, Particle mesh Ewald: An N·log(N) method for Ewald sums in large systems. *J. Chem. Phys.* **98**, 10089–10092 (1993).

54. A. Harasima, "Molecular theory of surface tension" in *Advances in Chemical Physics* (John Wiley & Sons, Inc., Hoboken, NJ, USA, 2007), *Advances in chemical physics*, pp. 203–237.

55. J. Sonne, F. Y. Hansen, G. H. Peters, Methodological problems in pressure profile calculations for lipid bilayers. *J. Chem. Phys.* **122**, 124903 (2005).

56. C. E. ZoBell, C. H. Oppenheimer, Some effects of hydrostatic pressure on the multiplication and morphology of marine bacteria. *J. Bacteriol.* **60**, 771–781 (1950).

57. A. Kusters, W. Dowhan, B. de Kruijff, Negatively charged phospholipids restore prePhoE translocation across phosphatidylglycerol-depleted Escherichia coli inner membranes. *J. Biol. Chem.* **266**, 8659–8662 (1991).

58. Y. Asai, Y. Katayose, C. Hikita, A. Ohta, I. Shibuya, Suppression of the lethal effect of acidic-phospholipid deficiency by defective formation of the major outer membrane lipoprotein in Escherichia coli. *J. Bacteriol.* **171**, 6867–6869 (1989).

59. H. Hata, M. Nishiyama, A. Kitao, Molecular dynamics simulation of proteins under high pressure: Structure, function and thermodynamics. *Biochimica et Biophysica Acta (BBA) - General Subjects*. **1864**, 129395 (2020).

60. B. Wroblowski, J. F. Díaz, K. Heremans, Y. Engelborghs, Molecular mechanisms of pressure induced conformational changes in BPTI. *Proteins: Structure, Function, and Genetics*. **25**, 446–455 (1996).

61. D. B. Kitchen, L. H. Reed, R. M. Levy, Molecular dynamics simulation of solvated protein at high pressure. *Biochemistry*. **31**, 10083–10093 (1992).

62. G. Sgourakis, R. Day, S. A. McCallum, A. E. Garcia, Pressure Effects on the Ensemble Dynamics of Ubiquitin Inspected with Molecular Dynamics Simulations and Isotropic Reorientational Eigenmode Dynamics. *Biophys. J.* **95**, 3943–3955 (2008).

63. L. Meinhold, J. C. Smith, Pressure-dependent transition in protein dynamics at about 4 kbar revealed by molecular dynamics simulation. *Physical Review E*. **72**, 061908 (2005).

64. Wakai, K. Takemura, T. Morita, A. Kitao, Mechanism of Deep-Sea Fish α-Actin Pressure Tolerance Investigated by Molecular Dynamics Simulations. *PLoS One*. **9**, e85852 (2014).

65. M. Marchi, K. Akasaka, Simulation of Hydrated BPTI at High Pressure: Changes in Hydrogen Bonding and Its Relation with NMR Experiments. *J. Phys. Chem. B*. **105**, 711–714 (2001).

66. F. W. Starr, F. Sciortino, H. E. Stanley, Dynamics of simulated water under pressure. *Physical Review E*. **60**, 6757–6768 (1999).

67. K. Akasaka, H. Matsuki, Eds., *High Pressure Bioscience: Basic Concepts, Applications and Frontiers* (Springer Netherlands, Dordrecht, 2015), vol. 72 of *Subcellular Biochemistry*.

68. M. Kusube, H. Matsuki, S. Kaneshina, Thermotropic and barotropic phase transitions of N-methylated dipalmitoylphosphatidylethanolamine bilayers. *Biochimica et Biophysica Acta (BBA) - Biomembranes*. **1668**, 25–32 (2005).

69. H. Ichimori, T. Hata, H. Matsuki, S. Kaneshina, Barotropic phase transitions and pressure-induced interdigitation on bilayer membranes of phospholipids with varying acyl chain lengths. *Biochimica et Biophysica Acta (BBA) - Biomembranes*. **1414**, 165–174 (1998).

70. R. Sueyoshi, K. Tada, M. Goto, N. Tamai, H. Matsuki, S. Kaneshina, Barotropic phase transition between the lamellar liquid crystal phase and the inverted hexagonal phase of dioleoylphosphatidylethanolamine. *Colloids Surf. B Biointerfaces*. **50**, 85–88 (2006).

71. W. Helfrich, Elastic Properties of Lipid Bilayers: Theory and Possible Experiments. *Zeitschrift für Naturforschung C*. **28**, 693–703 (1973).

72. B. Canham, The minimum energy of bending as a possible explanation of the biconcave shape of the human red blood cell. *J. Theor. Biol.* **26**, 61–81 (1970).

73. A. Waugh, E. A. Evans, Thermoelasticity of red blood cell membrane. *Biophys. J.* **26**, 115–131 (1979).

74. M. Kaltenegger, J. Kremser, M. P. K. Frewein, P. Ziherl, D. J. Bonthuis, G. Pabst, Intrinsic lipid curvatures of mammalian plasma membrane outer leaflet lipids and ceramides. *Biochimica et Biophysica Acta (BBA) – Biomembranes*. **1863**, 183709 (2021).

75. P. Khakbaz, J. B. Klauda, Investigation of phase transitions of saturated phosphocholine lipid bilayers via molecular dynamics simulations. *Biochimica et Biophysica Acta (BBA) - Biomembranes*. **1860**, 1489–1501 (2018).

76. K. Uppulury, P. S. Coppock, J. T. Kindt, Molecular Simulation of the DPPE Lipid Bilayer Gel Phase: Coupling between Molecular Packing Order and Tail Tilt Angle. *J. Phys. Chem. B*. **119**, 8725–8733 (2015).

77. K. Tu, D. J. Tobias, J. K. Blasie, M. L. Klein, Molecular dynamics investigation of the structure of a fully hydrated gel-phase dipalmitoylphosphatidylcholine bilayer. *Biophys. J.* **70**, 595–608 (1996).

78. M. Venable, B. R. Brooks, R. W. Pastor, Molecular dynamics simulations of gel (LβI) phase lipid bilayers in constant pressure and constant surface area ensembles. *J. Chem. Phys.* **112**, 4822–4832 (2000).

79. E. Evans, W. Rawicz, Elasticity of "Fuzzy" Biomembranes. *Phys. Rev. Lett.* **79**, 2379–2382 (1997).

80. E. Fahy, S. Subramaniam, R. C. Murphy, M. Nishijima, C. R. H. Raetz, T. Shimizu, F. Spener, G. van Meer, M. J. O. Wakelam, E. A. Dennis, Update of the LIPID MAPS comprehensive classification system for lipids. *J. Lipid Res.* **50**, S9–S14 (2009).

Supplementary Text and Materials

Testing the use of CHARMM36 all-atom MD with varying hydrostatic pressure

Models and methods for MD simulations of lipid bilayers have been established under mesophilic conditions but have rarely been applied to understanding extreme life — particularly the effects of hydrostatic pressure on membranes. However, extensive modeling has been performed on soluble proteins at pressure (reviewed in (1), where there has been agreement with experimental observations on protein denaturation (2), compressibility (3), conformational states (4), and overall dynamics (5). In one biological example, MD using an earlier CHARMM force field was used to define the mechanism by which conserved mutations in α-Actin of deep sea fish contribute to stability and ATP binding at pressure (6). Thus, force fields developed for ambient conditions can be useful for analyzing systems under varying pressures. Because lipids are more compressible than proteins, the pressures needed to modulate their mesophases are lower than those often considered for proteins, alleviating some of the discrepancies between hydrogen bond lengths (7) and water structure (8) between very high-pressure simulations and experiments. Pressures that alter membrane structure and phase properties, 100 to 1000 bar, are an order of magnitude lower than those used to study protein denaturation. They also correspond to the range of ocean depths of interest for understanding pressure adaptation in marine life.

To establish the feasibility of using MD to understand pressure effects on membranes, we first ran simulations of several model lipid bilayers at pressures of 1 and 1000 bar (Table S3). Lipids were selected based on published experimental P/T phase diagrams (reviewed in Chapter 16 of (9) so that a range of pressure-dependent behaviors was expected. In general, high pressure favors more ordered chains because they occupy a lower molar volume. Beginning in the L_α phase ($T > T_m$), unsaturated DOPC remains fluid at 1000 bar but with a reduced area per lipid (APL),

while saturated DPPC at 50 ºC shows a much larger reduction in APL (Fig. S6A). This is because DPPC has been compressed into an ordered gel phase, which experimentally occurs starting at 500 bar at 50 ºC (10). Simulation snapshots reveal that DPPC at 1000 bar specifically forms an interdigitated gel phase (L_βI), where the ordered acyl chains span almost entirely across each leaflet (Fig. S6B). The observation of an L_βI phase is highly significant because it is a pressure-dependent phase that has been observed experimentally for DPPC at 1000 bar (11) but has not been observed under 1 bar pressure at any temperature.

We next asked if simulations quantitatively predict the increase in lipid packing of L_α phases as hydrostatic pressure increases (Fig. S6C). We simulated DOPE bilayers at 20 ºC and in the L_α phase at pressures from 500 to 1000 bar and computed the change in area per lipid (APL) as a measure of lipid packing strain:

$$APL\ strain\ (P)\ =\ \frac{APL(P) - APL(1000\ bar)}{APL(1000\ bar)}$$

We compared these values to HP-SAXS measurements of DOPE multi-lamellar vesicles, using the d-spacing of the L_α phase Bragg peaks to estimate lipid packing strain (Fig. S6D). In this case, we assumed a constant water layer, so changes to d-spacing reflected changes in bilayer thickness, which are then inversely proportional to APL strain:

$$APL\ strain\ (P)\ =\ \left(\frac{d(P) - d(1000\ bar)}{d(1000\ bar)}\right)^{-1}$$

These simulation and experimental methods obtained excellent agreement for pressures covering the L_α range of DOPE (Fig. S6C), with identical slopes that read out how much the area per molecule is reduced per bar of pressure (~4% reduction per 1000 bar).

Third, we considered the pressure-dependence of monolayer spontaneous curvature. For a lipid like PE — which prefers to bend with the headgroups on the inside of the curve, by

convention a negative spontaneous curvature — pressure reduces the volume of the chains relative to the headgroup, driving the monolayer from a curved to a flat state (Fig. S6E). Experimentally this can be assessed by the scattering profile obtained by SAXS, which is sensitive to phase transitions; curved monolayers form non-lamellar phases like H_{II}, which is the case for pure PE at low pressures (12). In our simulations, lipids are constrained by boundary conditions to bilayer phases, so these phase transitions cannot be observed. If unconstrained, their long equilibration times and the small size of bilayer patches in all-atom simulations would still be limiting. However, the tendency to form non-lamellar phases can be assessed through analysis of curvature stress, which is obtained from the lateral stress or pressure profile of the bilayer. Within the context of Canham-Evans-Helfrich theory (13–15). A more positive value of $F'(0)$ indicates more negative spontaneous curvature, corresponding to an H_{II} phase in experimental data (Fig. S6E). At 1 bar and 72 ºC, POPE – a lipid with a large negative spontaneous curvature of -0.03 $Å^{-1}$ (16) – is in an H_{II} phase, reflected by its comparatively large and positive first moment value (Fig. S6F). When pressure is increased to 1000 bar, POPE is driven toward L_α experimentally, and $F'(0)$ decreases ~25%. The trend is similar for DOPC, except that the values are 5x to 10x smaller, because DOPC has only a small, negative spontaneous curvature of -0.004 $Å^{-1}$ at 1 bar (17) and is thus in L_α phase at both pressures. The change in $-k_B c_0$ for both systems is similar, as it reflects the similar compressibility of their hydrocarbon chains. The change in $F'(0)$ corresponds to an increase in c_0 of 0.005 $Å^{-1}$ (assuming k_B remains constant at 9.5 kcal/mol for POPE (18). Experimentally, the change of c_0 per 1000 bar in a similar PE lipid (SOPE) is 0.0045 $Å^{-1}$ (Fig. 4B), so there is a reasonable agreement.

Taken together, these proof-of-concept simulations indicate that MD simulations using CHARMM36 all-atom force fields capture pressure dependent changes in membrane elastic and

structural properties. We do note two limitations to this approach we have observed. First, our simulations did not precisely predict phase transition pressures. For example, in DOPE at 20 °C, we have measured the gel phase transition (L_β) occurring at 1850 bar. In simulations, we see signatures of an L_β phase at 1500 bar. It is already well established that lipid phase transitions are very difficult to model quantitatively with MD simulations, due to limitations of sampling and finite size of the systems, as well as equilibration times. Prior work has considered the gel phase transition upon cooling of well studied lipid systems such as saturated PC (19), finding transition temperatures that differ by 2-10 °C from experiments, or saturated PE (20), 7-17 °C from experiments. Our error of 350 bar for DOPE $L_\alpha \rightarrow L_\beta$ corresponds to roughly equivalent to 7 °C, given a previously measured P/T equivalency of 480 bar/10 °C for DPPC (11), and is thus within the error range observed for temperature. Nonetheless, the structure and properties of the cold-induced phases match experiments quite well (21, 22), and our data above indicates that this is also true for pressure-induced transition.

The second limitation involves the extrapolation from lateral stress profile analysis, which yields values for $-k_B c_0$, as described above. Determining c_0 from this approach requires an independent measurement of the bending modulus k_B. Here, we do not attempt a rigorous measurement of the pressure-dependent bending modulus, since this would require many very large systems that are not compatible with all-atom simulations of complex membranes. Bending modulus should increase with pressure — as the chains are ordered and the area per molecule decreases, the hydrocarbon region becomes thicker. However, within the polymer brush of Evans (23), changes in k_B scale with the cube of hydrocarbon thickness. The thickness of fluid L_α membranes we have simulated increases only modestly with pressure, in line with the ~4% change

in APL from 1-1000 bar in DOPE as described above. Thus, changes in $-k_B c_0$ within systems as a function of pressure should predominantly reflect effective changes to c_0.

Materials and Methods

Ctenophore collection and culture

Ctenophores used for biochemical and biophysical analysis were collected between 2018 and 2023 using bluewater SCUBA techniques (0–25 m depth), a plankton net (0-48 m), and MBARI remotely operated vehicles (ROVs) Ventana and Doc Ricketts (200–4000 m depth). Arctic samples were collected during June and July 2018 and May 2021. One specimen of *Leucothea pulchra* (#158; see Table S1) was cultured at the Monterey Bay Aquarium in spring 2019. The arctic samples from 2018 were protected against oxidation with approximately 0.01% w/v butylated hydroxytoluene (MP Biomedicals) and frozen at −20°C. All other samples were flash-frozen whole in liquid nitrogen. All frozen material was brought back to the laboratory within 1 month and stored long-term at −80°C.

Depth and Temperature Measurements and Distributions

Collection coordinates for all specimens were recorded by GPS to a resolution of 1 km or finer. For specimens collected on SCUBA, depth and temperature were recorded using a dive computer. For specimens collected by ROV, the depth and temperature were recorded at time of collection using the vehicle's main conductivity-temperature-depth (CTD) sensor package (Sea-Bird Electronics). ROV CTD data were also incorporated into MBARI's Video Annotation and Reference System (VARS) database along with species-level identifications (24). VARS was used to generate the depth distributions in Fig. 1 by querying over ROV dive data between 1989 and

2020. Sightings of each species within a 50 m depth bin were normalized by total time spent diving within that bin.

Ctenophore high-pressure incubations

To observe the effects of elevated pressure on shallow-adapted ctenophores in real time, Cubette was adapted as follows. The internal quartz cuvette was replaced by a 1.2 mL glass autosampler vial. Short sections of silicone tubing were lodged in the bottom of the vial as a barrier to keep the subject animal within the field of view. The vial was filled with seawater and an individual *Hormiphora californensis* <5 mm in size was added, then a soft silicone internal plug was used to seal the opening. Each individual (n=3) was allowed 10 min to equilibrate in Cubette, which was held at a constant 12°C. Imaging was performed using a Sony A7SIII camera fitted with a Laowa 24mm macro probe lens via an E- to F-mount adapter. The lens was mounted at Cubette's excitation window and an LED fiber optic illuminator was mounted at the emission window to provide side lighting. Video was recorded at 4K resolution and 60 frames/s. Recording was initiated following the equilibration period for each individual ctenophore. The specimen was then held at 1 bar for 60 s, ramped linearly to 500 bar over the course of 50 s, held at 500 bar for 180 s, ramped back down at the same rate, then held again at 1 bar for 60 s.

Imaging of membrane inversion in ctenophore tissues and in synthetic liposomes

We have observed that certain depth-generalist species remain alive for several days in containers left on ice (~0°C, below native temperatures for mid-water species), allowing for their transport to the lab for imaging. We took advantage of this by collecting deep- and shallow-constrained generalists (*Bathocyroe fosteri* and *Bolinopsis microptera*, respectively) from similar

depths in Monterey Bay. After transport, we tested whether they showed tissue melting signatures when brought to or above their native temperatures on a Peltier-controlled microscope stage (TSA12i, Instec). This allowed melting at atmospheric pressure to be assayed without a pressure-controlled microscope stage, of which there exists no suitable design for imaging tissue mounts at high resolution. Auricle appendages were dissected from live ctenophores and were stained with C-Laurdan (5 μM in seawater) in microcentrifuge tubes on ice for 30 min. Laurdan dyes stain lipid membranes and other lipid structures and have no observable fluorescence in aqueous solutions. However, emission is sensitive to local lipid packing, so they are commonly used to image membrane fluidity. In the same way, they also detect changes in lipid phases (25), as we show for the H_{II} phase transition in Fig. S3C.

Cell monolayers isolated from the ctenophore auricles were mounted using 8-well cell trays coated with concanavalin A on ice. This lectin coating served to immobilize the auricle on the bottom glass of the tray. Imaging was then performed on an LSM 880 confocal microscope (Zeiss) using a 34-channel QUASAR detection unit to select emission wavelength. Images were acquired in two emission windows (418 – 464 nm and 481 – 517 nm) upon excitation with a 405 nm laser line and at 3 temperature steps (2°C, 10°C, 20°C). Following each temperature increase, samples were allowed to equilibrate for 10 min. At the elevated temperatures, tissue melting was confirmed by transmitted light. That observable melting corresponded with the loss of membrane structures imaged by C-Laurdan. The sudden shift in C-Laurdan GP indicated that this corresponded with a lipid phase transition.

A similar protocol was used for testing PPE-containing liposomes in Fig. S8D. Briefly, synthetic lipid mixtures were prepared in chloroform as described below to yield a 10 mM final concentration of liposomes. The chloroform was evaporated under N_2 and held under vacuum for

≥ 1 h to form a lipid film. The film was rehydrated by tumbling with ice-cold 20 mM HEPES, pH 7.4 for 1 h and stained with C-Laurdan (5 μM) for 30 min prior to imaging. All hydrated lipid films containing PPE were kept on ice or in a 4°C cold room until imaging to prevent phase transitions at room temperature. Analysis of C-Laurdan GP and generation of GP heat maps were performed as previously described (26).

Preparation of ctenophore lipids

Whole ctenophores were homogenized in a Dounce grinder on ice, then total lipids were extracted as previously described (27). Total lipids were concentrated by rotary evaporation at ≤30°C, then dried under a stream of nitrogen followed by high vacuum for ≥30 min. Dry lipids were weighed and resuspended to a concentration of 1 mg/mL in $CHCl_3$. 200 μL of this total lipid stock, or as much as was available, was used for lipidomic analysis. The headspace over all stocks was purged with N_2 prior to storage at -80°C. Lipid intactness and absence of major peroxidation products was routinely assayed by thin-layer chromatography on silica with a 65:25:4 v:v:v $CHCl_3$:MeOH:H_2O mobile phase. Lipid spots were visualized using phosphomolybdic acid.

Preparation of synthetic lipid mixtures

Pure phospholipids were purchased from Avanti Polar Lipids as chloroform solutions of known concentrations. All plasmalogens and polyunsaturated phospholipids were used within 1 day of unsealing the manufacturer's packaging. Plasmalogens were shipped in anaerobically sealed amber glass bottles inside heat-sealed mylar bags filled with inert gas. Constituents of lipid mixtures were measured using Wiretrol glass pipette tubes (Drummond) attached to micropipettes.

SAXS sample preparation

Polar lipids and neutral lipids were separated on 500 mg prepacked silica columns (Thermo Scientific) using a previously validated method (28). Polar lipids eluted in approximately 20 mL $CHCl_3$ were dried and weighed in the same way as total lipids. For SAXS analysis, 10 mg polar lipids were dissolved in 100 µL cyclohexane (C_6H_{12}, Fisher Chemical). 50 µL aliquots were transferred to 1.4 mm ID capillary melting point tubes (Kimble Chase), frozen at -80°C, and lyophilized for 1 h. Samples were rehydrated by the addition of 10 µL vacuum-degassed MilliQ water, then five rounds of freeze-thaw in an isopropanol-dry ice bath and homogenization with a 20 µL Wiretrol II microdispenser (Drummond Scientific) inside the melting point tube. The bottom of the tube was then scored, cut, and carefully wiped, and the suspension inside transferred to a 1.0 mm ID special glass X-ray capillary (Charles Supper). This thick suspension (50% w/v lipid) was settled to the bottom of the X-ray capillary by centrifugation (500 RCF, 5 min at 4°C) and topped with another 5 µL degassed water to ensure full hydration. A 22G x 100 mm needle (Air-Tite) was then used to add a pressure-transmitting cap of high vacuum grease (Dow Corning) to the top of the water. The X-ray capillary was cut near the top of the grease cap, attached to an acrylic sample cartridge using household epoxy, and stored in the dark at 4°C until use.

Pure water was used in these lipid dispersions because all salts introduce a risk of osmotically driven membrane tension, which alters phase properties (29), and because divalent cations only affect the curvature of anionic lipids (30), which were a minor component of these samples. The concentrations of major salts in seawater do not change dramatically with depth (31) and most marine invertebrates are osmoconformers, implying that the inorganic salt environment of their membranes is not strongly affected by depth; we thus deemed it reasonable to use water as a common background.

SAXS data acquisition and analysis

HP-SAXS data were collected on beamline 7A at the Cornell High Energy Synchrotron Source using a custom-built temperature-controlled pressure cell (32). Photon energy was 14 keV, spot size was 200 x 250 μm (W x H), and scattering data were collected for 0.005 $Å^{-1} \leq q \leq 0.7$ $Å^{-1}$ using an EIGER 4M detector (Dectris) within the beamline vacuum. 1 s exposures were taken at a flux of 1.8-3.6x10^{11} photons/s. Five initial exposures were used to test each sample for radiation sensitivity, then pressure up- and down-sweeps were made starting at the lowest temperature and proceeding to the highest. The sample was equilibrated for at least 60 s at each pressure stop and for 30 min following each change in temperature. Because photon scattering by the lipid dispersions was strong and background was low (as assessed by shooting a sealed capillary containing the same degassed water used to hydrate the lipids), no background subtraction was used. SAXS images were azimuthally integrated using BIOXTAS RAW software (33), and the resultant scattering profiles cropped to $q \geq 0.05$ $Å^{-1}$ to eliminate beamstop artifacts.

For the three ctenophore samples presented in Fig. 2B, SAXS data were acquired across P-T space in order to estimate phase diagrams. Interpolation was performed between the measured profiles as an aid to visual analysis. This was done by modeling *I(q)* as a function of pressure and temperature across all profiles, using a separate bivariate LOESS spline for each *q* value. Phase changes were identified by traversing along pressure and temperature gradients between the measured and interpolated scattering profiles. An interactive interface for these data is available at https://octopode.shinyapps.io/PTX_ctenos_overlay/.

Minimal systems composed of synthetic phospholipids displayed more distinct Bragg scattering peaks and could generally be observed as pure phases, so a more quantitative analysis

was used. For each sample at a fixed temperature, groups of SAXS profiles displaying only a single phase (with visible peaks indexing to [1, 2, 3, 4…] or [1, √3, 2, √7…]) were averaged to create representative profiles for the L_α, L_β, and H_{II} phases. Each SAXS profile obtained was modeled as a linear combination of the two most proximate pure phases, the coefficients for which correspond to data points in Fig. 3A. Univariate logistic regressions were fitted to these data in order to estimate phase transition midpoints.

Automated high-pressure fluorescence spectroscopy

To prepare each lipid sample for high-pressure fluorescence spectroscopy, 1 mg of material dissolved in $CHCl_3$ was dried to a film under N_2, then by vacuum for 30 min. The film was rehydrated by tumbling with 500 µL 20 mM HEPES, pH 7.4 for 2 h. This low-ionic strength buffer is standard for liposome experiments, in which high divalent cation concentrations can cause aggregation. Biological samples were rehydrated at the native temperature of the source animal. For synthetic samples, it was done at a temperature expected to facilitate a stable L_α phase. After tumbling, each sample was frozen at -80°C and thawed at 37°C 3 times in succession, then extruded using a handheld device (Avanti Polar Lipids) incorporating a 100 nm polycarbonate track-etch filter (Whatman). Extrusion was carried out at the same temperature as tumbling. Resultant Small Unilamellar Vesicles (SUVs) were dispensed into a cuvette for analysis.

Fluorescence of SUV samples was measured using a custom pressure cell dubbed Cubette, which was built in-house at MBARI (Fig. S9). Cubette was fabricated from 6Al4V titanium alloy, allowing a small 60 x 60 mm footprint for mounting versatility. The cell features 3 quartz windows (ISS) of 10 mm clear diameter and accommodates a standard 1 cm path length cuvette (Hellma) with a sample volume of 0.4-2 mL, sealed with a soft silicone plug (Smooth-On). The internal

cuvette and its contents can be brought to pressures of 1-650 bar and temperatures of 0-80°C. Cubette was mounted in an RF-5301PC spectrofluorometer (Shimadzu), connected to a 100DM supercritical fluid syringe pump (Teledyne ISCO) for pressure control, and to a RTE10 heater-chiller bath for temperature control (Thermo NESLAB). Pressure was measured using the syringe pump's internal transducer and temperature was read out using a Pt100 thermistor (Omega Engineering) in contact with Cubette's exterior. This external probe was calibrated to internal cuvette temperature using a NIST-traceable reference probe (QTI) at atmospheric pressure. To improve optical performance at low temperatures, small brass nozzles were incorporated into the baseplate supporting Cubette, and these were used to blow dry air on the windows when the cell was operating below ambient dew point.

Fluorescence data were collected across P-T grids using fully automated P-T control and data acquisition. This was accomplished using Python drivers and scripts, also developed in-house. Each experimental protocol was input as a delimited text file with each line specifying pressure, temperature, excitation and emission wavelengths, and equilibration time. Data streams were continuously written to another text file, which was then analyzed using R scripts. All above-mentioned software is available at https://github.com/octopode/spectackler.

Lipidomic analysis

Lipid extracts were brought to dryness and reconstituted in 18:1:1 v:v:v IPrOH:CH_2Cl_2:MeOH containing deuterated internal standard (Avanti) for each of the 15 lipid classes analyzed (Table S2), which include the major classes of phospholipids and sphingomyelin. These allow for semi-quantification of species within these classes. Other potential lipid species,

including ceramide derivatives, glycosylated lipids, and non-sterol terpenes, were not quantified using this method.

All polar lipids were measured according to the method described previously with slight modifications (34). The Vanquish UHPLC (Thermo Fisher Scientific) was interfaced with a Q-Exactive mass spectrometer (Thermo Fisher Scientific). A Waters T3 1.6 µM 2.1 mm x 150 mm column was used for chromatographic separation using a step gradient from 25% buffer A (10 mM ammonium formate and 0.1% formic acid in water) to 100% buffer B (70/30 isopropanol/acetonitrile with 10 mM ammonium formate and 0.1% formic acid) over 35 min. Flow rate was set at 0.3 mL/min. This LC gradient minimizes ion suppression.

Lipid analytes were analyzed using a data-dependent acquisition (DDA) with an NCE of 30 in negative mode and an NCE of 25 in positive mode. Ion source parameters were: Sheath Gas 48 AU; Aux Gas 11 AU; Sweet Gas 1 AU; Spray Voltage 3.5 kV for positive mode and 2.5 kV for negative mode; Capillary Temp. 250°C; S-lens RF level 60 AU; Aux Gas Heater Temp. 413°C. All ions in the mass range of 200-1200 m/z were monitored. MS1 resolution was set at 70,000 (FWHM at m/z 200) with an automatic gain control (AGC) target of 1e6 and Maximum IT of 200 ms. MS2 resolution was set to 17,500 with an AGC target of 5e4, fixed first mass of 80 m/z, and Maximum IT of 50 ms. The isolation width was set at 1.2; Dynamic Exclusion was set at 3 s. Lipid Identification and Quantification was done with Lipidomic Data Analyzer Software (35). Precision of this analysis was tested by running 4 replicate injections of a *Leucothea pulchra* sample: the average standard error across all 1716 phospholipid species detected was <0.01 mole %, while the maximum SEM among all phospholipids in this sample was 0.47 mole %. Raw data for the technical replicates can be found in Data S1.

For analysis of sterols, an aliquot of the polar lipid samples were dried down and resuspended in pyridine with ergosterol (Sigma-Aldrich, 10 μg/mL) added as an internal standard. 100 μL of N,O-bis(Trimethylsilyl)trifluoroacetamide with Trimethylchlorosilane (BSTFA + TMCS) was added (70°C, 1 hr) to derivatize sterols into trimethylsilyl esters. Samples were run on an Agilent 8890 GC coupled to a 5977B mass spectrometer. The GC was programmed to ramp from 40 to 300°C over 20 min, then held for 6 min. Identified sterols included cholesterol and trace amounts of desmosterol; these were quantified with external standards containing both sterols (Sigma-Alrich) derivatized in parallel with the samples.

Phylogenetically generalized regressions of headgroup and acyl chain composition to depth and temperature were fitted using a previously described method and phylogeny (36).

Identification of Phosphatidylethanolamine Plasmalogens (PPE)

Lipidomic Data Analyzer Software identified PPE molecular species in negative mode. The PE headgroup is identified by two fragments of $[C_2H_7O_4NP]^-$ at m/z 196.036 and $[C_5H_{11}O_5NP]^-$ at m/z 140.011 The fragments used for the sn-2 chain identification are the carboxy, neutral loss of the ketene, and neutral loss of the carboxy. The fragment used to identify the sn-1 is the alkenyl. For example, PPE-18:0/22:6 would give a fragmentation pattern of: Precursor $[C_{45}H_{77}O_7NP]^-$ at m/z 774.543, Neutral Loss of Ketene at $[C_{23}H_{47}O_6NP]^-$ 464.318, Neutral Loss of Carboxy $[C_{23}H_{45}O_5NP]^-$ at m/z 446.309, Carboxy 22:6 $[C_{22}H_{31}O_2]^-$ at m/z 327.236, Alkenyl P-18:0 $[C1_8H_{35}O]^-$ at m/z 267.269, and PE head fragments of $[C_5H_{11}O_5NP]^-$ at m/z 196.036 and $[C_2H_7O_4NP]^-$ at m/z 140.011. Noise filtering and fragmentation intensity rules were established in order to prevent false positive identification.

Assay of Ca^{2+}-induced membrane fusion under pressure

We tested the effects of pressure and PPE on membrane fusion by using the interaction between phosphoserine and Ca^{2+} to fuse liposomes *in vitro*. In this assay, two populations of liposomes are mixed; one of which contains both the FRET donor and FRET acceptor and the other contains no fluorophores; fusion causes dilution of the FRET pair, reducing quenching. Liposomes contained 1 mol di-oleoyl phosphoserine (DOPS): 3 mol either PE or PPE with 18:0/20:4 acyl chains. NBD-PE and rhodamine-DHPE (Invitrogen) were added to one vesicle population during film preparation at 2 mole percent each. The lipid mixtures were used to prepare SUVs using thin-film rehydration at 1 mg lipid/mL buffer, followed by two rounds of freeze-thaw and extrusion to 100 nm. Rehydration and subsequent assays were performed in 2 mM HEPES, pH 7.4 at 20°C, with 2 mM histidine, 0.1 mM EDTA, and 50 mM NaCl. Both populations of liposomes were added to Cubette at a concentration of 0.04 mg/mL each in a 396 µL total volume. Fluorescent emission intensity was measured at ex/em 460/538 nm with 3/5 nm ex/em slits. A baseline was collected for 60 s, then 4 µL 100 mM $CaCl_2$ was added for a final concentration of 1 mM. Cubette was sealed and the pressure generator activated immediately. Fusion rates were calculated for the 10-minute period starting 5 min after $CaCl_2$ addition. Normalized intensity values were calculated after sample solubilization by Triton X-100 using the approach described in (30, 31). n=2 assays were performed on PE and PPE-containing liposomes at 1 and 100 bar.

Measurement of PPE monolayer spontaneous curvature

For c_0 analysis, pure lipids were prepared as "hosted" mixtures in DOPE at a molar ratio of 1:4 guest:host for HPSAXS, as described above. 10.7% w/v 9-(Z)-tricosene was added in order to relax the H_{II} phase by filling the hydrophobic spaces between phospholipid tubules (37).

Intrinsic curvature values were estimated by global fitting of H_{II} scattering profiles using the GloboHex program (16). Independent fits were used to determine the pressure-dependent c_0 of the DOPE host lipid, and the resultant values were fixed in subsequent joint fits of the hosted mixtures. Separate joint fits were run for the pressure up- and down-sweeps of each hosted mixture (prepared as described above), and the results were averaged within each pair of pressure sweeps. Convergence of each Bayesian fit was verified using 10000 samples (including 2000 burn-in) on each of 15 independent chains.

Estimation of mean phospholipid curvature

Phospholipid c_0 values for 18:1/18:1 PE, 18:0/18:1 PE, and 18:0/18:1 PPE were measured as described above. Intrinsic curvature values for PE, LPE, PC, LPC, PS, and PG were compiled from literature (38). Published values were selected based on the following considerations: that the measurement was taken in pure water for consistency, that the H_{II} phase was "relaxed" with a filler compound (tricosene or tetradecane), that c_0 was measured at the neutral plane, that c_0 was measured at 20°C or that the dependency of c_0 on temperature was reported. For each headgroup class, prior measurements that fulfilled the greatest number of these criteria were used. Where possible, the reported dc_0/dT value was used to adjust c_0 to 20°C. This yielded multiple c_0 values for PE and PC species with *sn*-1 chains 16:0, 18:0, 18:1; single c_0 values for 12:0, 18:0, 18:1 LPC; and c_0 lower bounds for 12:0, 18:0, 18:1 LPE. Due to the sparsity of lysolipid data, the mean of the three available c_0 values for LPEs and LPCs was assigned to all species in each of those classes. All 4 selected values available for PG were likewise averaged. Only one value was used for PS. For PE and PC, a multiple regression was fitted using the formula:

$$c_0 = ((hl + iu) \mid l) + jg + k,$$

where *l* is *sn*-1 chain length, *u* is *sn*-1 unsaturation (either 0 or 1), and *g* is headgroup class (either PC or PE, coded as 0 or 1). *h*, *i*, *j*, and *k* are fitted coefficients. The fitted regression was used to predict c_0 for each PE and PC species based on its headgroup and *sn*-1 chain. For PPE, a constant offset of -0.00516 $Å^{-1}$, based on our own measurements, was applied to the regression predictions for PE. This was necessary because PPE was only available with an 18:0 *sn*-1 chain. Once c_0 values had been assigned to each lipid species in the 6 major headgroup classes, $\underline{c_0}$ was calculated as a weighted mean. Phylogenetically generalized regressions of $\underline{c_0}$ to depth and temperature were fitted using a previously described method and phylogeny (36).

Molecular dynamics simulations

Lipids were modeled with the CHARMM36 force-field and water (39, 40) with the tip3p model (41). For membranes containing a single lipid, initial configurations containing 128 lipids per leaflet were generated using the CHARMMGUI web server (42). Four additional systems were assembled that contained a mixture of lipid types representative of four ctenophore species: *Bolinopsis infundibulum*, *B. vitrea*, *Lampocteis cruentiventer*, and Platyctenida sp. T. These systems contained approximately 200 lipids (including cholesterol) per leaflet. Several types of headgroup/acyl chain combinations were added to the CHARMMGUI by the Im group to facilitate system building.

All simulations were performed using NAMD v2.14. Each system in Table S2 was prepared individually for production simulation through a series of 6 minimization and heating steps: (i) steepest descent to minimize the initial configuration; (ii) 125,000 steps of Langevin dynamics with a 1 fsec timestep and velocities reassigned every 500 steps; (iii) 125,000 steps of Langevin dynamics with a 1 fsec timestep, pressure controlled by the Langevin piston method (43,

44), and velocities reassigned every 500 steps; then a total of 750,000 steps of Langevin dynamics with a 2 fsec timestep and hydrogen positions constrained by SHAKE (45), pressure controlled by the Langevin piston method, and velocities reassigned every 500 steps. During equilibration, double bonds were restrained in the *cis* configuration to prevent isomerization; these restraints are gradually reduced during the final three stages of the equilibration protocol. Production simulations were performed in the NPT ensemble using the Langevin piston to control pressure (period of 50 fsec; damping timescale 25 fsec; coupled anisotropically to allow independent fluctuation of the in-plane and normal directions) and integrating the Langevin equation of motion to control temperature (damping coefficient = 1.0 $psec^{-1}$). Hydrogens were constrained with SHAKE (tolerance 10^{-5}), a 2 fsec timestep was used, and long-range electrostatics were computed every timestep using particle mesh Ewald (46) with a maximum grid spacing of 1 Å and interpolation order 6. Long-range dispersion was smoothly truncated over 10-12 nm using a force-switch cutoff scheme. Each system was run for at least 250 nsec of production simulation; actual simulation times are listed in Table S2. At least the initial 50 nsec of all simulation trajectories were discarded before any analysis.

Under increasing isotropic pressure the area per molecule decreases and the membrane increases in thickness. Each system was therefore checked to determine at what point the area had equilibrated by monitoring the area per lipid as a function of simulation time. In most cases, the system area relaxed during the equilibration phase, even at elevated pressures. There were three exceptions, however, indicated by an * in Table S3. Each case corresponds to a system that transitions to a gel phase at high pressures. In these cases, only the last 50 nsec of the production simulation were analyzed.

Simulation analyses

Errors on simple averages (area per lipid and average phosphate-phosphate distance) were obtained by computing the standard error among nonoverlapping blocks of simulation data for each trajectory. Block lengths corresponding to independent samples were determined from the autocorrelation of each observable, yielding at least 600 independent samples for the area per lipid (APL) and the P-P distances. The area compressibility modulus K_A was obtained from the fluctuations in system area via the fluctuation-response theorem:

$$K_A = \frac{k_B T < A >}{< \Delta A^2 >}$$

where ΔA is the deviation from the average area, indicates a thermodynamic average, and the errors were computed from 15 non-overlapping blocks. ^{2}H NMR order parameters (S_{CD}) were computed for each position of each hydrocarbon chain:

$$S_{CD} = \frac{1}{2}(3cos^2\theta_i - 1)$$

where i labels the carbon position and θ_i is the angle between the membrane normal and the C-H bond vector.

Lateral stress profiles $\pi(z)$ were computed using the Harasima contour (47), including electrostatic interactions computed via PME (48). The system was discretized into 250 slabs along the membrane normal, and $\pi(z)$ computed in each slab by postprocessing the simulation trajectory in NAMD. Starting from evenly spaced configurations (sampled once every 200 psec) during the production simulations (Table S2), 1 psec simulations were launched, during which the normal and transverse components of the pressure were obtained for each slab, and their difference averaged over the sampled configurations to obtain $\pi(z)$. A version of NAMD with bug fixes related to pressure profile calculations was used in this work and is available at:

https://github.com/alexsodt/namd_profile_patch.git. The discretized profile is splined into a smooth function using cubic splines (examples are shown in Fig. S7C), which is then integrated numerically to obtain the first moment. Diffusion constants were obtained by first "unwrapping" the lipid displacements to obtain continuous trajectories, removing overall center of mass motion, then calculating the in-plane mean squared displacements (MSDs) of the phosphates, averaged over both lag time and the ensemble of lipids. The obtained MSD was then fit to MSD = $4D_T$.

E. coli model systems for biological pressure tolerance

To model the increased negative curvature of deep-sea membranes achieved by PPE, we used previously described strains of BL21(DE3) *E. coli* (49) containing the pPlScp (PPE-producing) and pET28 (empty control) plasmids. Starter cultures were grown in LB + 50 mg/L kanamycin (Kn) while shaking at 250 RPM, overnight at 37°C. Each starter was diluted 1:100 v/v into LB + 100 mM HEPES pH 7.4 + Kn and incubated micro-aerobically while shaking at 250 RPM, 24 h at 37°C. Culture tubes were connected to a water airlock and the headspaces flushed with N_2 prior to culturing. At OD_{600} = 0.2, IPTG was added to 0.1 mM final concentration, headspaces were flushed again, and microaerobic culture was continued for another 24 h. Following this period, all cultures were normalized to OD_{600} = 0.2 using the same medium and 3 mL aliquots were loaded into 5 mL polypropylene syringes. Each strain (pPlScp and pET28) was loaded into 9 syringes. Each syringe also contained three 3-mm glass beads for agitation. Gas was manually purged from the syringes and each was sealed with a Luer-lock cap.

Three syringes containing each strain were loaded into each of three blind stainless pressure vessels (50) filled with distilled water and pre-warmed to 37°C. A manual rotary pump (High Pressure Equipment Co.) was used to bring one vessel to 500 bar and another to 250 bar; the third

was left at ambient pressure as a 1 bar control. All three pressure vessels were clamped horizontally to an orbital shaker and shaken at 250 RPM for 48 h at 37°C. Following high-pressure incubation, vessels were decompressed over the course of ~30 s. OD_{600} was measured for all three replicate cultures of each strain at each pressure and a qualitative survival screen was performed as follows. Each culture was serially diluted tenfold, yielding aliquots that were 10^1- to 10^5-fold dilutions of the decompressed culture. Six sets of these were transferred to an LB agar plate with Kn using a 48-pin tool (V&P Scientific) and each plate was incubated at 25°C for approximately 24 hours, then photographed. Resultant photographs were used in Fig. 4. The remainder of each decompressed culture was pelleted at 500 RCF, 5 min at 25°C and frozen at -80°C. Total lipids were later extracted from the frozen pellets by the Bligh-Dyer method and samples incubated at 1 and 500 bar were analyzed as described above.

To model a decrease in negative lipid curvature, we used previously described strains of PE-knockout (*pssA*-) AL95 *E. coli* containing arabinose-inducible cassettes for either PE rescue (strain pDD72) or for PC production from phosphoserine (AL95 + pAC-PCSlp) (*17*, *29*). Induction of these cassettes was reported to achieve a wild-type lipidome in pDD72 and a PC mole fraction of approximately 0.7 in AL95 + pAC-PCSlp. This represents roughly 1:1 replacement of wild-type PE with PC. A supplemented medium was used for this experiment, consisting of LB + 50 mM $MgCl_2$ + 0.2% w/v arabinose (for induction) + 2 mM choline (for PC synthesis). Strain pDD72 was grown with 25 mg/L Kn and AL95 + pAC-PCSlp with 12.5 mg/L streptomycin (St). Starter cultures were grown while shaking at 250 RPM overnight at 37°C. Each starter was diluted 1:100 v/v into the same medium and grown under the same conditions to an OD_{600} of 0.2-0.6. These cultures were normalized to OD_{600} = 0.2 for loading into pressure vessels, and high-pressure incubation, OD_{600} measurements, and survival screening were carried out as described above.

Since PG decreases in both PPE and PC producing *E. coli*, we directly tested whether changes in PG levels have an effect on pressure tolerance using a previously described strain HDL11 (23) in which negatively charged phospholipids PG and CL are produced at low levels (2%) in the absence of IPTG. HDL11 contains a *pgsA* gene, encoding phosphatidylglycerol phosphate synthetase, under control of a *lac* promoter and a deletion of the *lpp2* gene allowing for viability in both the presence and absence of IPTG (51). In the presence of IPTG, PG is present at normal levels (15-20%). The HDL11 strain was maintained by streaking on LB plates with 1 mM IPTG. Single colonies were used to inoculate LB with or without 200 μM IPTG and grown to OD_{600} of 1-1.5 overnight at 250 RPM and 37°C. Cultures were then diluted to an OD_{600} of 0.2 in LB with 100 mM HEPES with or without 200 μM IPTG. These cultures were loaded into pressure vessels, and high-pressure incubation, OD_{600} measurements, and survival screening were carried out as described above.

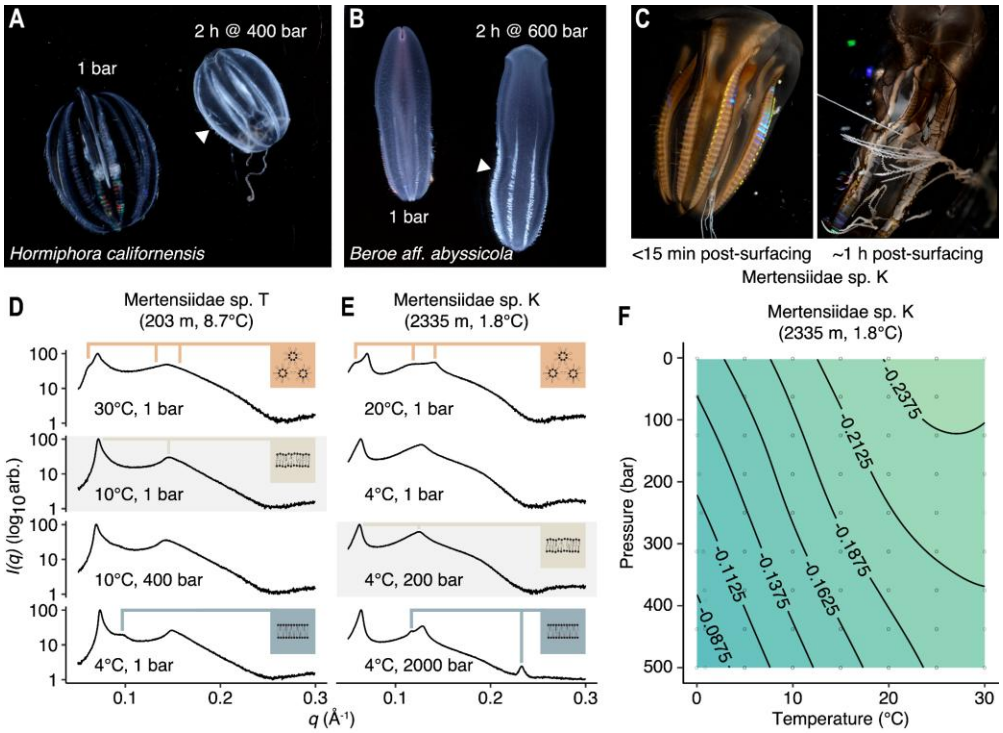

Supplemental Figure 2.1 Additional examples of habitat-dependent physiological responses and lipid phase properties

(**A**) *Hormiphora californensis*, a shallow-adapted ctenophore species, exposed to high pressure. Both individuals were collected on SCUBA at <30 m depth. One individual was incubated at 1 bar (control) while the other was held at an elevated pressure 400 bar for 2 h; both were at 4°C. The pressure-treated specimens were decompressed over ~30 s and photographed next to the control. Arrow indicates comb plates that have frayed due to sustained hyperactivity at high pressure (as in Movie S1, which shows a shorter, and thus reversible, incubation). (**B**) A pair of *Beroe aff. abyssicola*, a species very distantly related to *H. californensis*, following the same procedure as in panel **A**, but pressurized to 600 bar. (**C**) Disintegration of *Mertensiidae* sp. K. at surface pressure. (**D**) SAXS profiles for polar lipids from *Mertensiidae* sp. T, a shallow-living ctenophore. The profile taken nearest this individual's native pressure-temperature conditions is shown with a shaded background. Color-coded callouts identify scattering peaks associated with the pictured phase. Pressurization of this shallow sample to 400 bar initiated the formation of a gel phase, as did cooling the sample about 5°C below its native temperature. Warming the sample to 30°C caused an inverted phase to form. (**E**) Analogous SAXS profiles from the closely related (Fig. 3B), but deep-living *Mertensiidae* sp. K. At 4°C, gelling occurs only at physiologically implausible pressures of >1000 bar, but signatures of inversion begin to appear when the sample is brought to 1 bar pressure. Heating to 20° causes pronounced inversion, enabling the identification of q values associated with the H_{II} phase. (**F**) P-T grid of C-Laurdan GP values for polar lipids from the same Mertensiidae sp. K. specimen represented in **E**. Non-monotonic GP behavior in the low-pressure, high-temperature area of the plot resembles that of inverting PPE liposomes (Fig. S3B) and of Platyctenida sp. T liposomes (Fig. 2D).

Supplemental Figure 2.2 Ctenophore lipid composition across habitats.

(**A**) Analysis of acyl chain lengths and unsaturation (number of double bonds) trends at the *sn*-1 and *sn*-2 position of all phospholipids. 'Subset' panels refer to temperature (≤250 m, 41 samples, 10 species) or depth (T ≤10°C, 36 samples, 11 species) comparisons, as indicated in Fig. 3A. Ordinary least-squares regressions (OLS, solid lines) and phylogenetic generalized ones (GLS, dashed lines) are shown in each plot and those with trends significant by the more conservative GLS analysis ($P_{GLS} \leq 0.05$) are shaded gray. (**B**) Acyl chain composition of LPE is consistent with metabolic production, not oxidative degradation of PPE. The latter would be expected to produce LPE containing a polyunsaturated fatty acid (PUFA), since those comprise the vast majority of PPE *sn*-2 chains. However, the amount of PUFA-containing LPE is low (top plot) and is a minor fraction of the total LPE pool (bottom plot). Neither the total nor relative abundance of PUFA-containing LPE correlates with the total amount of PPE in samples, suggesting limited oxidation of the latter. (**C**) Analysis of lipid class trends across temperature or depth subsets (left) and all samples (right). Sample subsets and visualization of the regressions are the same as in panel A. Phospholipid mole fractions are normalized to all phospholipids; sphingomyelin (SM) and cholesterol fractions were not measured for all samples and are thus normalized to phospholipids + SM or + cholesterol. Outside of PPE, the only significant trends for depth or temperature are for LPS vs. temperature for all samples and PG vs. depth for shallow samples. However, both of these classes are minor components of the lipidomes. (**D**) The extreme PPE abundances — up to 73 mol% of all phospholipids — in a deep-sea species (*Platyctenida* sp. T) are maintained in isolated tentacles, which consist primarily of muscle and colloblast cells. Shown are all polar lipid species colored by headgroup measured in 4 individual animals collected at 3972.5 m, whose tentacles (Tent.) were dissected from whole bodies (Body) and their lipidomes profiled. (**E**) The overall lipid composition of two polar, shallow species used for HPSAXS analysis (*Beroe cucumis*) and MD simulations (*Bolinopsis infundibulum*) are both enriched in PC lipids and depleted in PPE and PE.

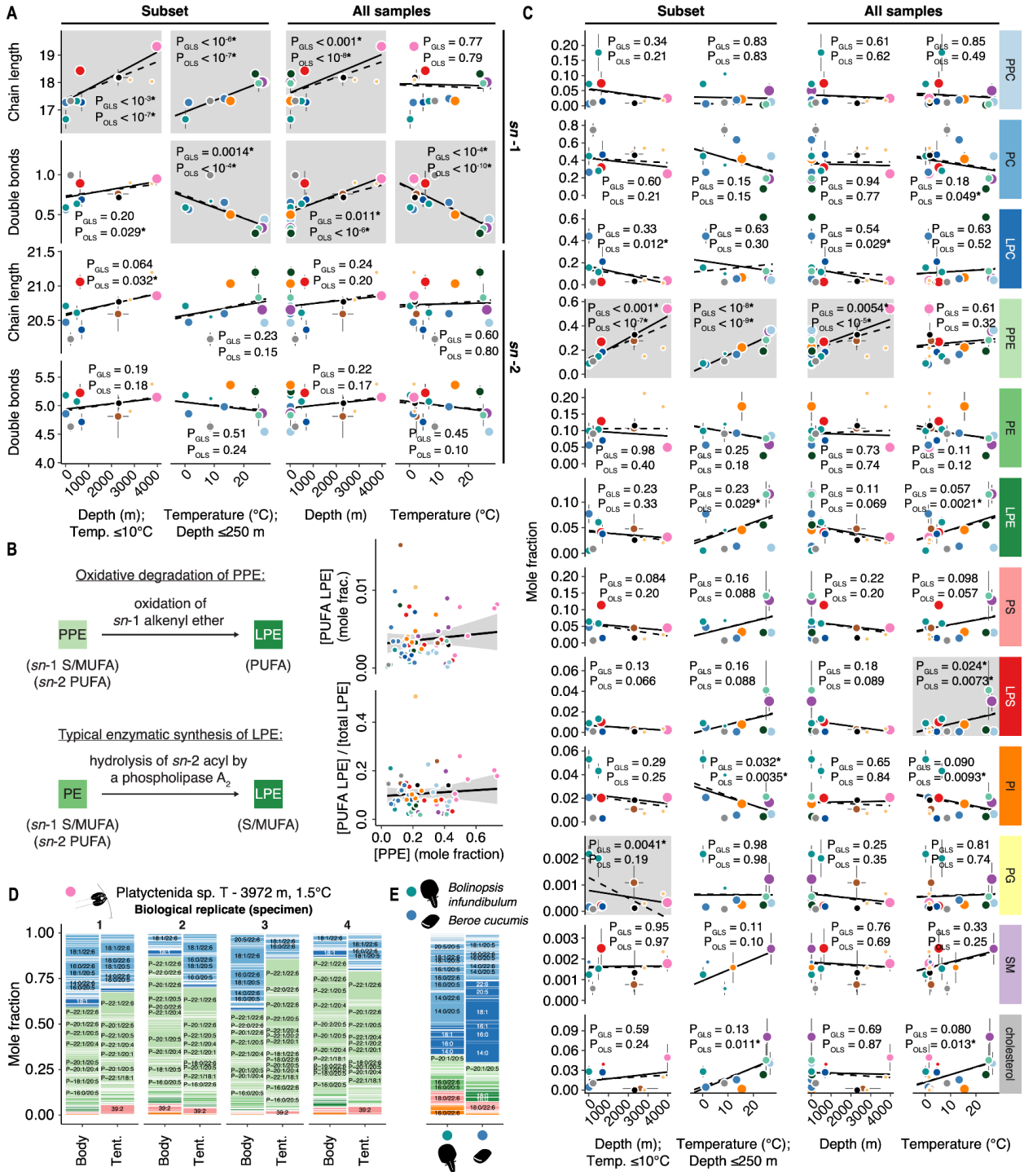
A
Subset
All samples
Chain length
Double bonds
sn-1
sn-2
Depth (m); Temp. ≤10°C
Temperature (°C); Depth ≤250 m
Depth (m)
Temperature (°C)
B
Oxidative degradation of PPE:
oxidation of sn-1 alkenyl ether
PPE
LPE
(sn-1 S/MUFA) (sn-2 PUFA)
(PUFA)
Typical enzymatic synthesis of LPE:
hydrolysis of sn-2 acyl by a phospholipase A2
PE
LPE
(sn-1 S/MUFA) (sn-2 PUFA)
(S/MUFA)
[PUFA LPE] (mole frac.)
[PUFA LPE] / [total LPE]
[PPE] (mole fraction)
C
Subset
All samples
PPC
PC
LPC
PPE
PE
LPE
PS
LPS
PI
PG
SM
cholesterol
Mole fraction
Depth (m); Temp. ≤10°C
Temperature (°C); Depth ≤250 m
Depth (m)
Temperature (°C)
D
Platyctenida sp. T - 3972 m, 1.5°C
Biological replicate (specimen)
Mole fraction
Body
Tent.
E
Bolinopsis infundibulum
Beroe cucumis

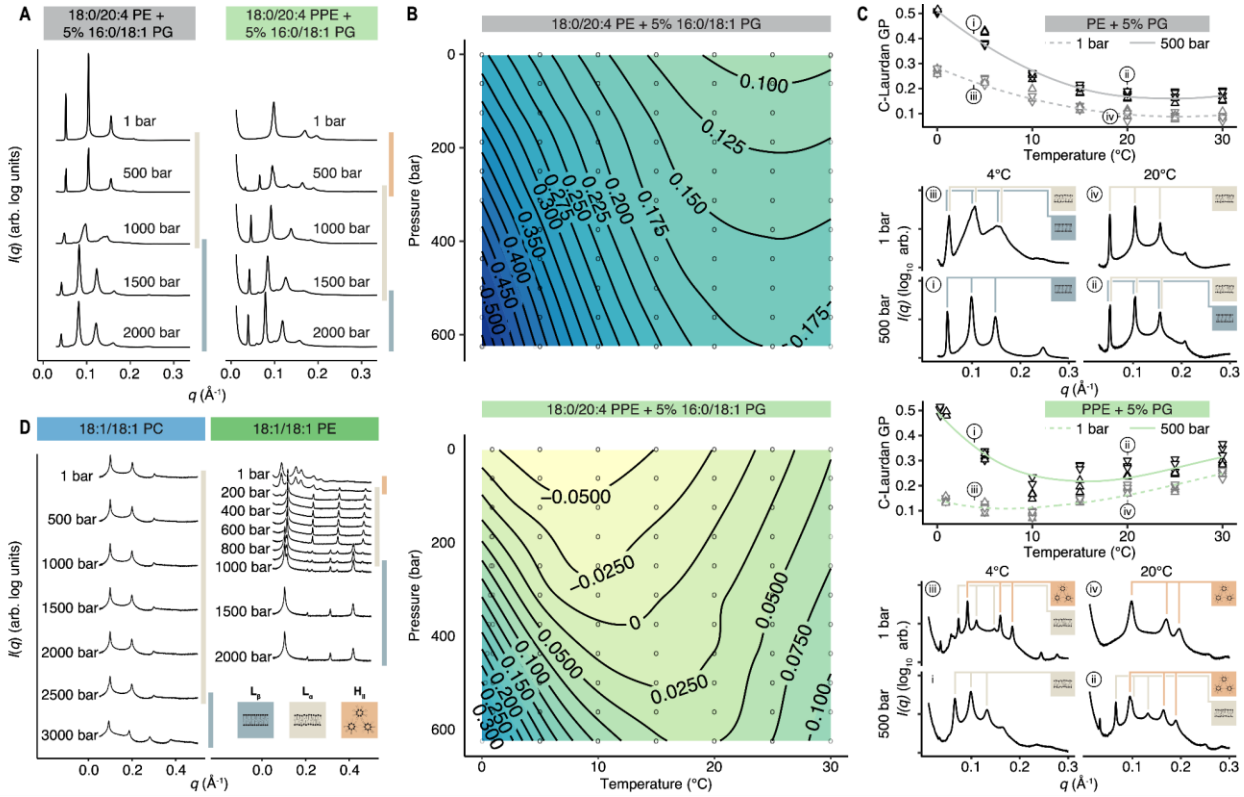

Supplemental Figure 2.3 Analysis of pressure effects on inversion and fluidity in model membranes.

(**A**) Scattering profiles as a function of pressure for PUFA-containing PE and PPE supplemented with 5% POPG at 4°C. The inversion-prone nature of the PPE sample is apparent from its characteristic H_{II} peak spacing at 0 bar, which transitions to L_α at 500-1000 bar. PE samples remain in L_α or L_β within this P-T regime. Phase is indicated by colored vertical lines to the right of the profiles. For this analysis, as well as Fig. 4A, 18:0/20:4 PE/PPE was used as the only commercially-available combination with a PUFA *sn*-2 chain, the dominant type in the lipidomes. (**B**) C-Laurdan GP landscapes for PUFA-containing PE and PPE, supplemented with 5% POPG. In cold conditions (< 10°C), pressure drives increasing GP in both systems but the PPE bilayers remain more fluid (lower GP). Under high-temperature conditions, the GP of both samples increases with temperature, indicating a change in phase. The increase in GP is mitigated by pressure and is more pronounced in PPE, suggesting it could reflect the $L_\alpha \rightarrow H_{II}$ transition. (**C**) An increase in Laurdan GP occurs alongside the $L_\alpha \rightarrow H_{II}$ transition in PPE bilayers. Shown are constant-pressure temperature sections of GP for the same PE and PPE preparations as in A. Roman numeral callouts reference GP data points to SAXS profiles obtained under the same P-T conditions, showing that the high-temperature rise in GP is associated with inverted phase formation. This increase in GP is also observed in ctenophore-derived liposomes (Fig. 2D, Fig. S1F) and tissue (Fig. 1C). (**D**) PC resists pressure-induced gelling. Scattering profiles for DOPC and DOPE are shown side-by-side at 4°C and a range of pressures; phase is indicated by colored vertical lines to the right of the profiles. DOPE forms a gel phase around 900 bar, but DOPC remains largely fluid to 2500 bar.

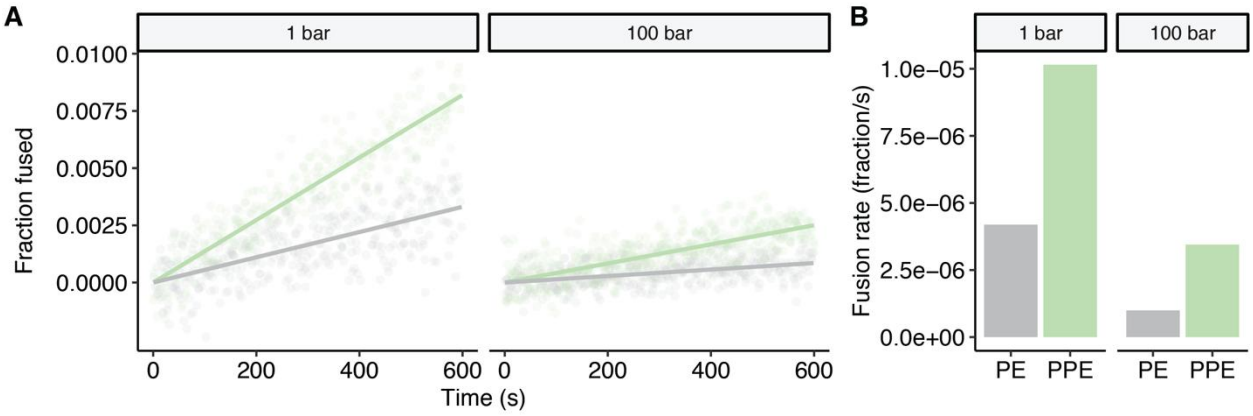

Supplemental Figure 2.4 PPE enhances vesicle fusion at high pressure.

(**A**) Kinetics of Ca^{2+}-induced liposome fusion measured using a FRET-based readout. Liposomes contained 3:1 mol:mol 18:0/20:4 PE or PPE : 18:1/18:1 PS. Representative traces shown span the period from 300-900 s post-addition of 1 mM $CaCl_2$ and are normalized to the difference between the Ca^{2+}-free fluorescence baseline and maximum fluorescence measured after the addition of detergent. (**B**) Fusion rates derived by linear regression of n=2 assays per treatment. At 100 bar, PPE-containing liposomes fuse about as fast as their PE-containing counterparts do at 1 bar.

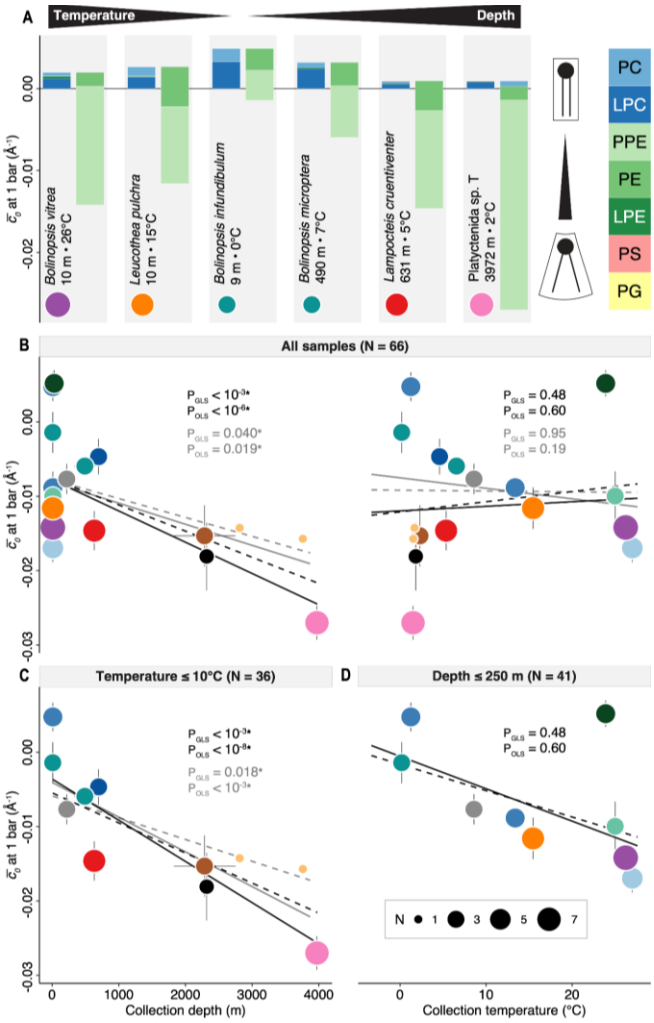

Supplemental Figure 2.5 Additional lipidome curvature analysis.

(**A**) Contributions of each phospholipid headgroup to $\bar{c}_0$ in 6 species that span temperature and depth ranges, calculated as described in the Materials and Methods. The contributions of lipids with positive c_0 are represented in the left-hand bar for each species, while those with negative c_0 are in the right-hand bar. The lower end of the right-hand bar represents the complete $\bar{c}_0$. Colder temperatures are not associated with lower $\bar{c}_0$ values, as the two warmer water species exhibit a more negative $\bar{c}_0$ than the cold, shallow species. In contrast, increasing depth correlated with a monotonic trend of more negative $\bar{c}_0$. This analysis does not account for non-ideal mixing nor the contributions of non-phospholipids (e.g. cholesterol). (**B**) Relationships between $\bar{c}_0$ and depth (left) or temperature (right) in all 66 samples in the dataset. (**C**) The same analysis in the depth data subset (T ≤10°C, 36 samples) subsets, as indicated in Fig. 3A. (**D**) The same analysis in the temperature data subset (≤250 m, 41 samples). In panels (B-D), ordinary least-squares regressions (OLS, solid lines) and phylogenetic generalized ones (GLS, dashed lines) are shown in each plot. Regressions with the deepest species (*Platyctenida* sp. T) removed from the depth analyses in panels (B) and (C) are shown in gray; significance of the relationship between $\bar{c}_0$ and depth is maintained in each case.

Supplemental Figure 2.6 Assaying the validity of all-atom MD simulations to model pressure effects on lipid bilayers.

(**A**) Area per lipid (APL) of di-oleoyl phosphatidylcholine (DOPC) and di-palmitoyl phosphatidylcholine (DPPC) bilayers simulated at 1 bar and 1000 bar. The saturated DPPC shows a larger change in APL. (**B**) Simulation snapshots of the system in (A). The DOPC bilayer stays fluid at 1000 bar, while the DPPC forms an interdigitated gel phase (L_{β}I), explaining the large drop in APL for that system in panel (A). (**C**) Autocorrelation traces for DOPC simulations at 1 bar (left) and 1000 bar (right). The time axis contains a break at 50 nsec to give a detailed view of the initial convergence phase. Convergence is slower at 1000 bar than at 1 bar, but both simulations reach zero autocorrelation before 10% of the total time has elapsed. (**D**) Comparison of extrapolated APL strain (change in APL vs. 1000 bar) for DOPE bilayers that are simulated (MD) and tested experimentally (SAXS). (**E**) Braggs peaks for DOPE bilayers used to extrapolate APL strain in panel (C). Red lines indicate the position of the 1st, 2nd, 3rd, and 4th order L_{α} peaks at 1000 bar to highlight the shifts used to calculate changes to bilayer thickness. (**F**) Schematic on how pressure-induced changes to lipid curvature, which manifest as phase changes in SAXS experiments, are measured by changes to the lateral stress profile of bilayer-constrained simulations. (**G**) The first moment of the lateral stress profile ($F'(0)$), which is equal to the negative product of the bending modulus (k_B) and the monolayer spontaneous curvature (c_0), for 1-palmitoyl-2-oleoyl PE (POPE) and DOPC bilayers at 1 and 1000 bar. The PE system features are a larger first moment value because it is made of lipids with large, negative c_0. In contrast, DOPC features a small, negative c_0. Pressure acts similarly on both systems, increasing c_0 and thus decreasing $-k_B c_0$.

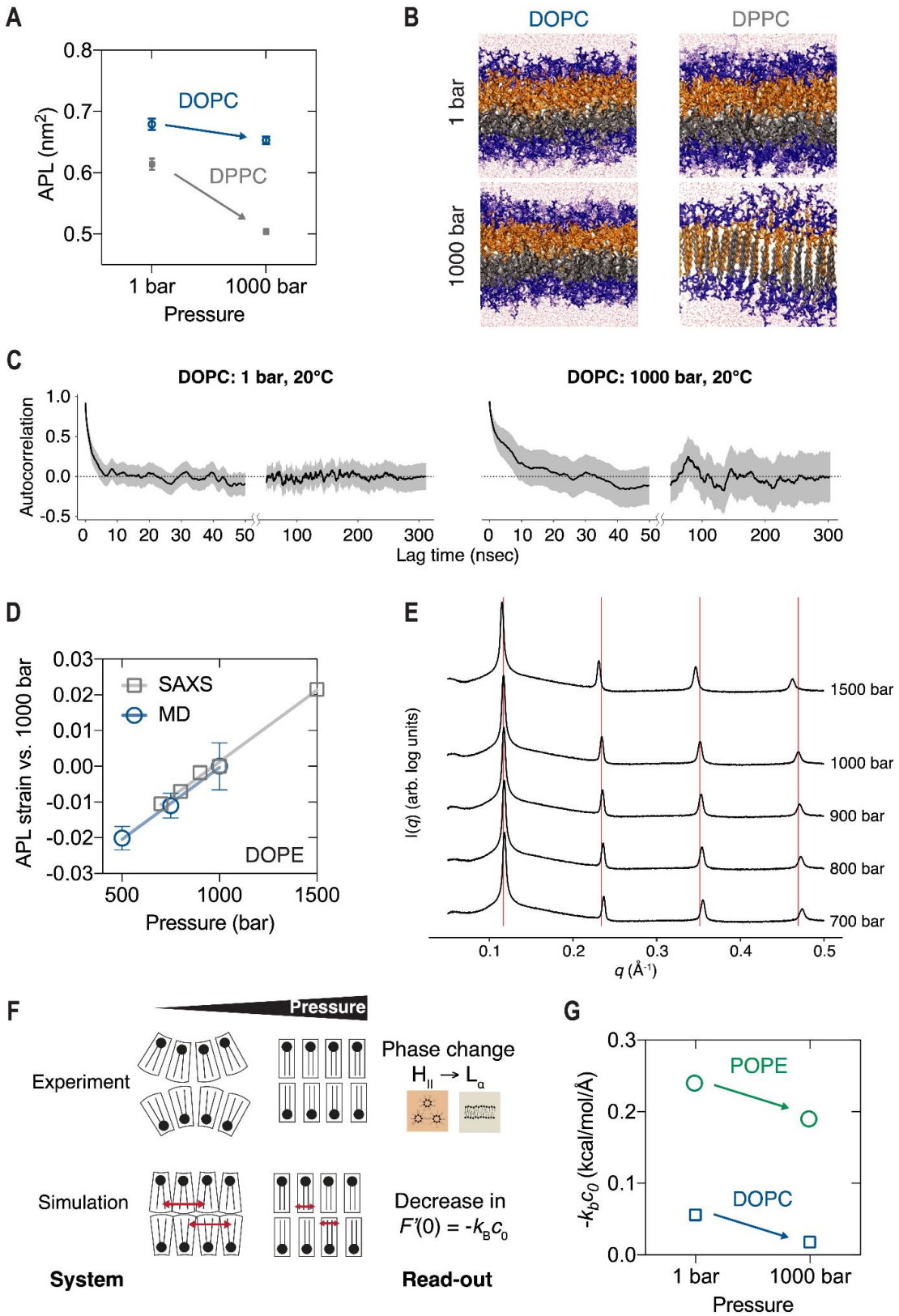
A
APL (nm²)
0.8
0.7
0.6
0.5
DOPC
DPPC
1 bar
1000 bar
Pressure
B
DOPC
DPPC
1 bar
1000 bar
C
DOPC: 1 bar, 20°C
DOPC: 1000 bar, 20°C
Autocorrelation
1.0
0.5
0.0
-0.5
0 10 20 30 40 50 100 200 300
Lag time (nsec)
D
APL strain vs. 1000 bar
0.03
0.02
0.01
0.00
-0.01
-0.02
-0.03
SAXS
MD
DOPE
500 1000 1500
Pressure (bar)
E
I(q) (arb. log units)
1500 bar
1000 bar
900 bar
800 bar
700 bar
0.1 0.2 0.3 0.4 0.5
q (Å⁻¹)
F
Pressure
Experiment
Simulation
Phase change
H_II → L_α
Decrease in
F'(0) = -k_B c_0
System
Read-out
G
-k_b c_0 (kcal/mol/Å)
0.3
0.2
0.1
0.0
POPE
DOPC
1 bar
1000 bar
Pressure

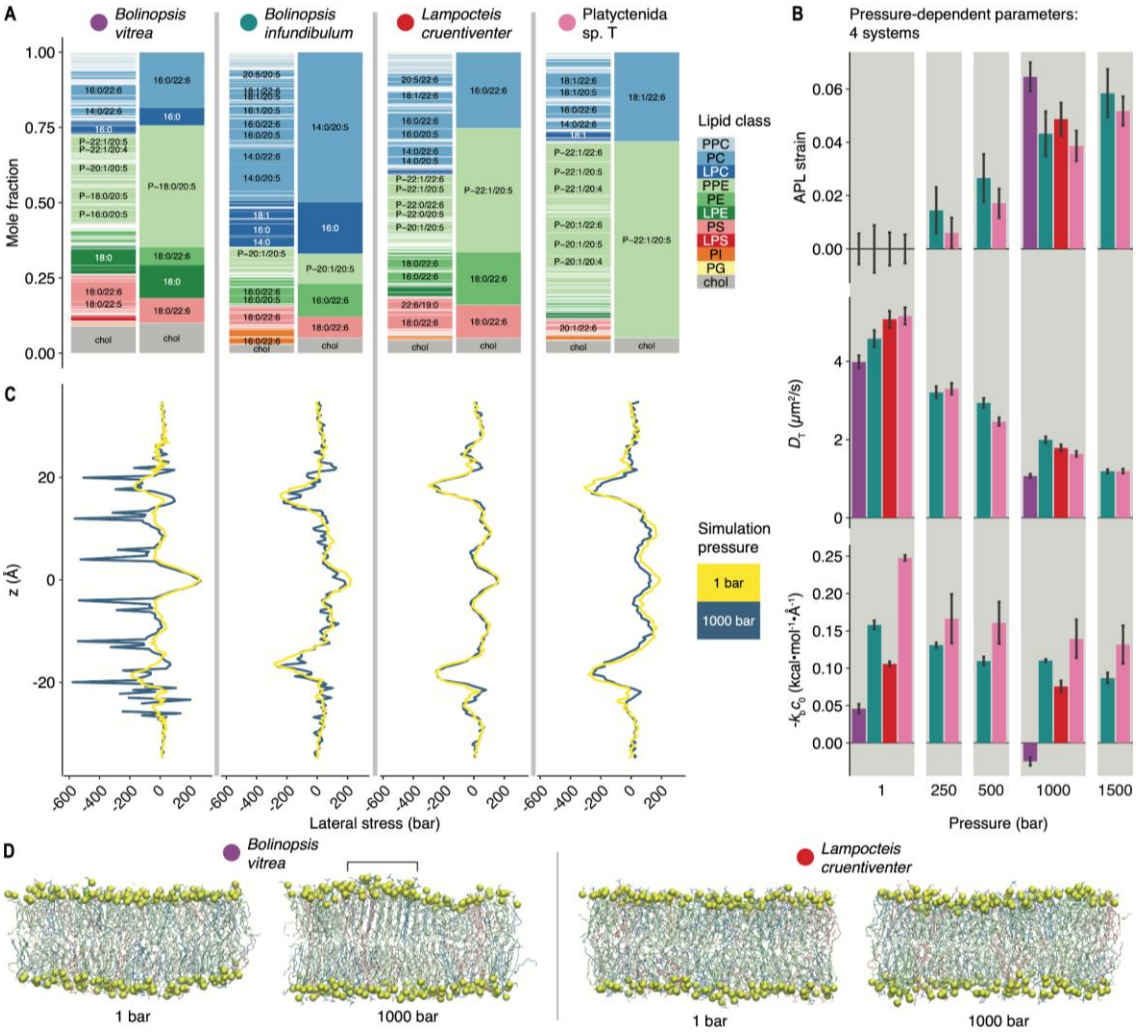

Supplemental Figure 2.7 MD simulations of bilayers composed of representative ctenophore lipids.

(**A**) Composition of the lipidomes (left bar) and their MD models (right bar) for four ctenophore species analyzed. MD compositions were generated as described in the Methods, by filtering the lipidomes to include only headgroup classes ≥5%, then scaling the result to 95% (90% for *Bolinopsis vitrea*) and filling the remaining 5 or 10% with cholesterol. The acyl chains selected for each lipid were the most common combination for that headgroup class in each species. Lipid classes with abundances <5% were excluded to avoid sampling issues associated with low number of molecules in a specific simulation. (**B**) Structural and dynamic parameters for the four systems as a function of pressure. For Platyctenida sp. T- and *B. infundibulum*-based systems, bilayers were simulated at five pressures, while *B. vitrea* and *L. cruentiventer* were simulated at two pressures. (**C**) Lateral stress profiles for the four systems at 1 and 1000 bar. Stress along the bilayer normal is shown as a function of distance (*z*) above and below the bilayer center. The irregular profile of *B. vitrea* at 1000 bar is due to a partial transition into a gel-like phase. (**D**) Simulation snapshots at 1 and 1000 bar for *B. vitrea* and *L. cruentiventer*. The horizontal bracket dictates a region of gel-like chain ordering in the former at the high pressure.

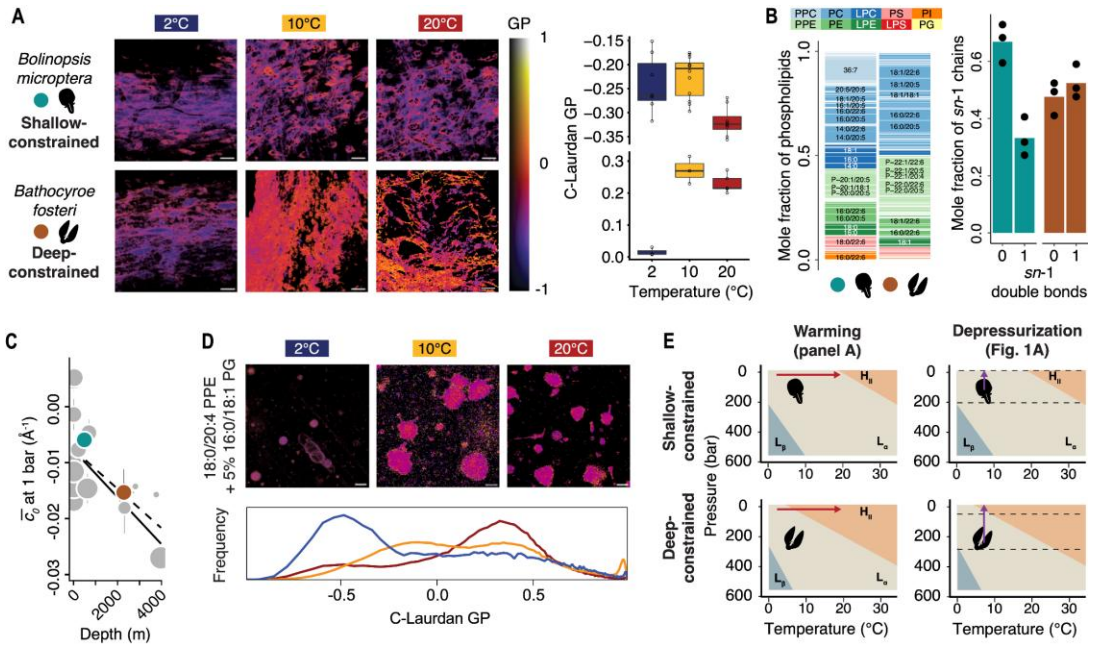

Supplemental Figure 2.8 Spectroscopic signatures of inversion in disintegrating tissues and liposomes.

(**A**) C-Laurdan GP false-colored micrographs corresponding to those in Fig. 1C; GP is calculated from pixel intensities from the two emission windows (418–464 nm and 481–517 nm). GP increases with temperature in dissolving ectodermal monolayers isolated from the deep-constrained species *Bathocyroe* aff. *fosteri*, which is not found shallower than 200 m depth. An increase in GP is consistent with a $L_\alpha \rightarrow H_{II}$ transition of lipids, which C-Laurdan exclusively stains (Fig. S3C). In contrast, the shallow-constrained *Bolinopsis microptera*, which often lives at surface pressure, retains its cellular structures during an identical experiment and does not show an increase in GP. Right: the distribution of mean GP from replicate micrographs for those shown in panel A, reflecting an increase in GP for *Bathocyroe fosteri* between 2 and 10°C that is not observed for *Bolinopsis microptera*. Further experimental details are in the Materials and Methods text. Scale bars are 10 µm. (**B**) Like other deep-constrained ctenophores, *Bathocyroe* has a highly negative $\bar{c}_0$. Mean $\bar{c}_0$ values for *Bathocyroe* and *Bolinopsis microptera* are highlighted in the context of all other species in this study (corresponding to Fig. 4D). Error bars indicate SEM for n=3 individuals. (**C**) (**D**) When shifted from 2 and 10°C, multilamellar vesicles composed of PUFA-containing PPE (18:0/20:4) supplemented with 5% POPG collapse into aggregates with high C-Laurdan GP. This temperature change corresponds to the measured $L_\alpha \rightarrow H_{II}$ transition temperature (Fig. S3B-C). Scale bars, 25 µm. (**D**) Proposed model for the cellular disintegration in panel A and surface melting. Left: Increasing temperature surrounding above the native range of *Bathocyroe* aff. *fosteri* (4-5 °C) at atmospheric pressure causes inversion of predominantly L_α membranes into H_{II} phase, which drives the melting of the animal as shown in Fig. 1A. The lower PPE content of the *Bolinopsis microptera* collected at the same depth and temperature allows its membranes to stay mostly lamellar across the same temperature range. Right: analogous process when animals are isothermally brought to surface, where the lower pressure causes the deep-constrained membranes to similarly invert. The mean native P-T for each species is shown via icons on the schematic phase diagrams and the native depth ranges are indicated by dashed lines in the right-hand panels.

Supplemental Figure 2.9 Controllable lipid curvature in *E. coli* strains.

(**A**) Average phospholipid compositions of strains/induction conditions used. Each bar represents a specific lipid species, with headgroup class indicated by color and acyl chains >1.5% specified in the text label. Mole fractions are averaged over n=3 biological replicates. BL21 + pPlScp and BL21 + pET28a are the PPE-producing strain and its corresponding control, respectively; AL95 + pPCSlp and AAL9256 are the PC-producing strain and its corresponding control, respectively; HDL11 is a strain with where PG synthesis is controlled by induction with Isopropyl β-D-1-thiogalactopyranoside (IPTG). (**B**) Number of acyl chain carbons, accounting for both length and cyclopropanation, and acyl chain unsaturation (number of double bonds) plus number of cyclopropane moieties, totaled across all headgroups, show similar profiles among the strains. (**C**) SAXS analysis of polar lipids from the PPE- and PC-producing strains and their corresponding controls. These data were used to generate the extrapolated phase diagrams in Figs. 5B and 5F. Here, temperature is used in lieu of pressure to probe the propensity of extracted lipids to form L_α, H_{II}, and L_β phases. (**D**) Analysis of pressure effects on growth of HDL11 in the presence (yellow, high PG) or absence (white, low PG) of IPTG. Cells were grown for 24 hours at the given pressure and OD_{600} was measured after depressurization, as in Fig. 5. The difference in growth between the two conditions is not significant (P = 0.44, multiple regression with F-test). (**E**) Analysis of pressure effects on survival of HDL11 in the presence (yellow, high PG) or absence (white, low PG) of IPTG. Cells were grown as for (D) and survival was assayed by colony forming units upon serial dilution. The low-PG condition (white) does not show enhanced survival, so this aspect of the lipidome is unlikely to contribute to the fitness effects observed for PPE- and PC-producing strains, both of which have reduced PG levels.

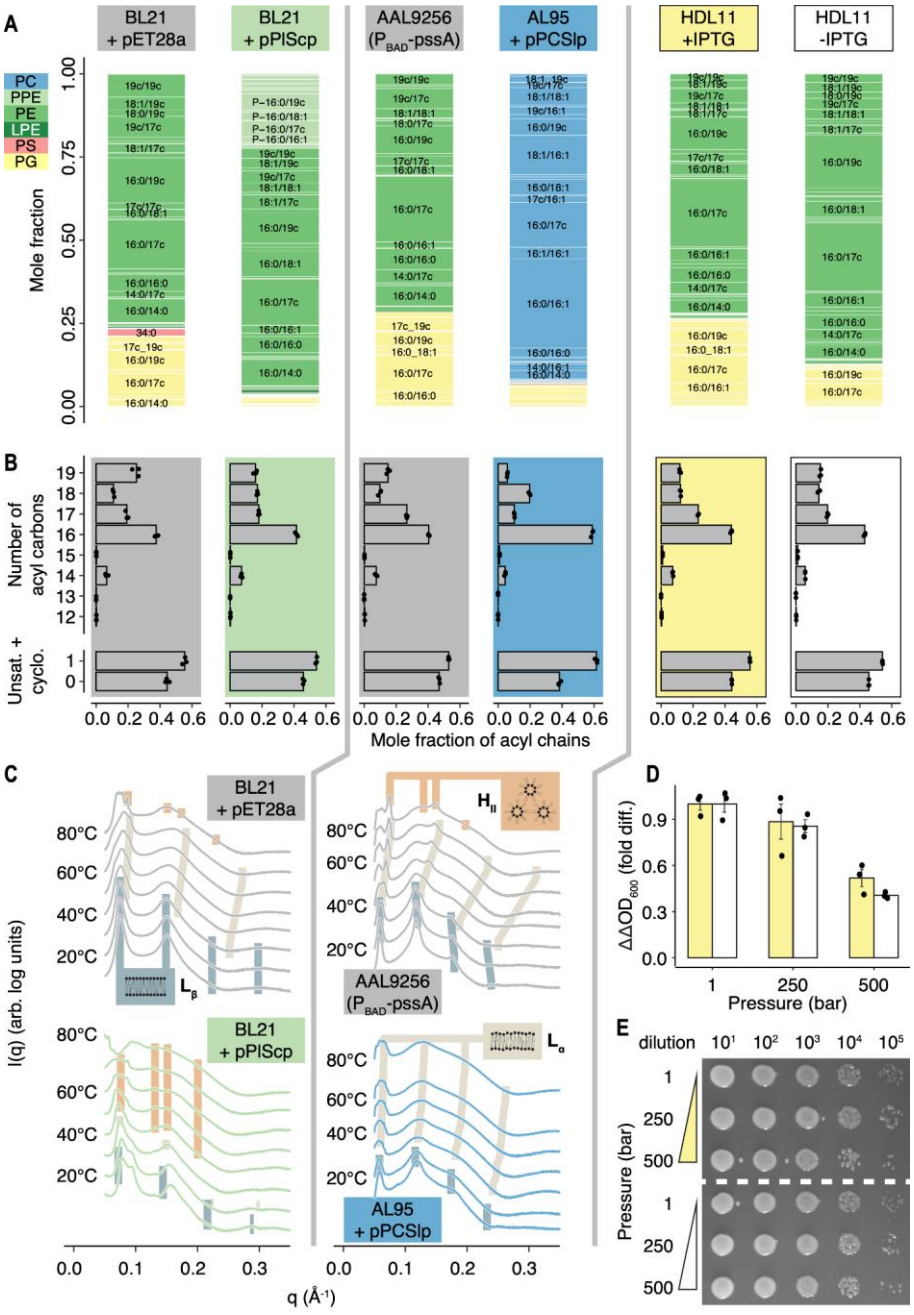
A
BL21 + pET28a
BL21 + pPlScp
AAL9256 (P_BAD-pssA)
AL95 + pPCSlp
HDL11 +IPTG
HDL11 -IPTG
PC
PPE
PE
LPE
PS
PG
Mole fraction
B
Number of acyl carbons
Unsat. + cyclo.
Mole fraction of acyl chains
C
BL21 + pET28a
AAL9256 (P_BAD-pssA)
BL21 + pPlScp
AL95 + pPCSlp
I(q) (arb. log units)
q (Å⁻¹)
D
ΔΔOD600 (fold diff.)
Pressure (bar)
E
dilution
Pressure (bar)

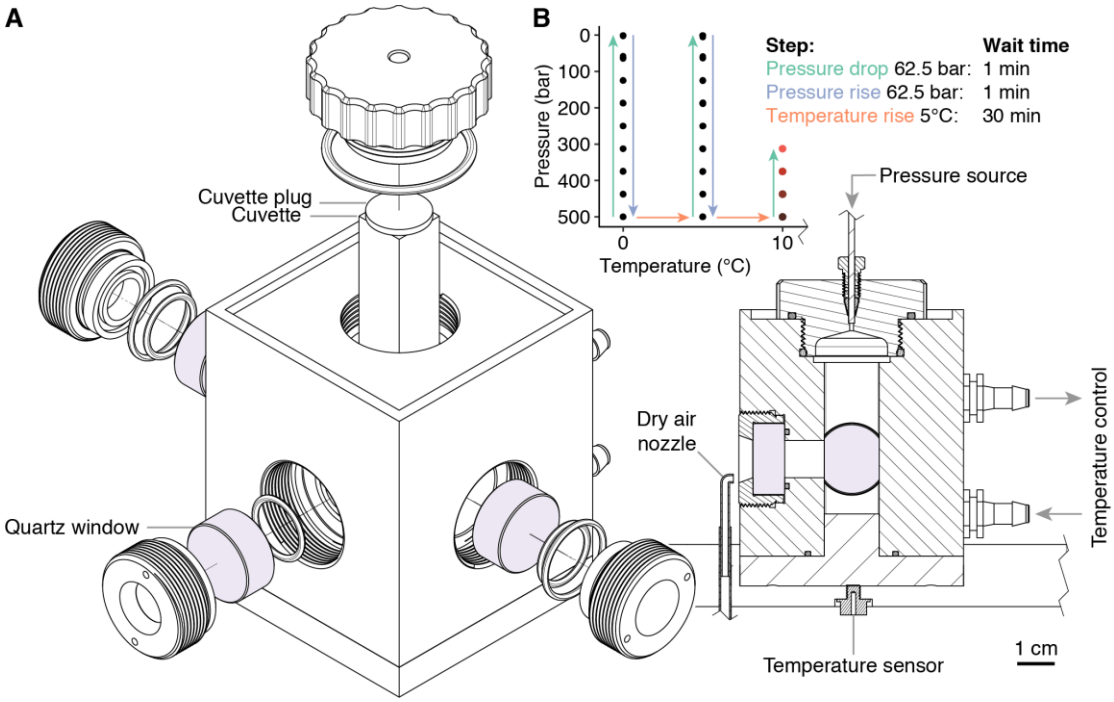

Supplemental Figure 2.10 Schematic of Cubette high pressure optical cell and C-Laurdan profile generation.

(**A**) Isometric and cutaway technical drawings of the home-built high pressure fluorescence cuvette chamber. Fused quartz optical windows are shown in light blue; all machined parts are 6Al4V titanium alloy, and fasteners are 316 stainless steel. O-rings are Buna-N durometer 90A and the pressure-transmitting cuvette plug is durometer 40 silicone (Smooth-On). External brass nozzles are used to direct dry air at the windows when Cubette is operating below the dewpoint in the sample chamber of the spectrofluorometer. This construction allows experimentation up to 650 bar and 80°C. (**B**) Pressure-temperature sweep scheme for a typical C-Laurdan experiment in Cubette. Pressure and temperature control are automated using a water pump and circulating water bath controlled by a Python script.

Supplemental Table 2.1 Taxonomic and environmental metadata for all ctenophores used in lipidomic and biophysical analyses.

For samples collected at ≤20 m depth whose encounter depth was not recorded *in situ*, a depth of 10 m was used in analyses, as this represents the mean depth of our bluewater diving effort. Samples are grouped by species and sorted warm → cold, shallow → deep. Figures in which these samples appear are indicated.

Project sample ID #	Species	Depth (m)	Temperature (°C)	Latitude (°)	Longitude (°)	Appears in figs:
336	*Beroe ovata*	10	27.6	19.423	-156.405	3, 4, S2, S5
337		10	27.6	19.638	-156.162	3, 4, S2, S5
338		10	27.6	19.638	-156.162	3, 4, S2, S5
334		10	26.1	19.662	-156.130	3, 4, S2, S5
335		10	26.1	19.275	-156.100	3, 4, S2, S5
42	*Bolinopsis vitrea*	10	27.6	19.775	-156.114	3, 4, S2, S5, S7
43		10	27.6	19.775	-156.114	3, 4, S2, S5, S7
44		10	27.6	19.775	-156.114	3, 4, S2, S5, S7
189		10	26.0	19.600	-156.262	3, 4, S2, S5, S7
190		10	26.0	19.600	-156.262	3, 4, S2, S5, S7
320		10	25.0	19.614	-156.057	3, 4, S2, S5, S7
321		10	25.0	19.650	-156.104	3, 4, S2, S5, S7
322		10	25.0	19.650	-156.104	3, 4, S2, S5, S7
323	*Cestum veneris*	10	25.0	19.622	-156.086	3, 4, S2, S5
324		10	25.0	19.650	-156.104	3, 4, S2, S5
325		10	25.0	19.650	-156.104	3, 4, S2, S5
326	*Coeloplana sp.*	30	23.9	19.670	-156.030	3, 4, S2, S5
327		30	23.9	19.670	-156.030	3, 4, S2, S5
328		30	23.9	19.670	-156.030	3, 4, S2, S5
329		30	23.9	19.670	-156.030	3, 4, S2, S5
158	*Leucothea pulchra*	1	18.0	(captive-reared)		2
363		10	17.2	35.500	-124.003	3, 4, S2, S5
364		10	17.2	35.500	-124.003	3, 4, S2, S5
365		10	17.2	35.500	-124.003	3, 4, S2, S5

Supplemental Table 2.2 Taxonomic and environmental metadata for all ctenophores used in lipidomic and biophysical analyses.

For samples collected at ≤20 m depth whose encounter depth was not recorded *in situ*, a depth of 10 m was used in analyses, as this represents the mean depth of our bluewater diving effort. Samples are grouped by species and sorted warm → cold, shallow → deep. Figures in which these samples appear are indicated.

Project sample ID #	Species	Depth	Temperature	Latitude	Longitude	Appears in figs:
366	*Leucothea pulchra*	10	17.2	35.500	-124.003	3, 4, S2, S5
166		10	12.0	33.847	-119.440	3, 4, S2, S5
167		10	12.0	35.500	-124.003	3, 4, S2, S5
339		10	13.4	36.392	-122.666	3, 4, S2, S5
340		10	13.4	36.392	-122.666	3, 4, S2, S5
341	*Beroe pseudocucumis* Mertensiidae sp. T	10	13.4	36.392	-122.666	3, 4, S2, S5
342		10	13.4	36.392	-122.666	3, 4, S2, S5
157		203	8.7	36.703	-122.043	3, 4, S1, S2, S5
159		206	8.6	36.703	-122.043	3, 4, S2, S5
346	Mertensiidae sp. T *Beroe cucumis*	249	8.5	36.689	-122.070	3, 4, S2, S5
191		10	2.0	64.658	-13.787	3, 4, S2, S5
161		10	1.5	64.653	-14.193	2
317	*Beroe cucumis* *Bolinopsis infundibulum*	10	1.0	78.608	5.068	3, 4, S2, S5
318		10	1.0	78.608	5.068	3, 4, S2, S5
319		10	1.0	78.608	5.068	3, 4, S2, S5
39		9	3.3	64.658	-13.787	3, 4, S2, S5, S7
28		9	0.6	79.150	11.750	3, 4, S2, S5, S7
34	*Bolinopsis infundibulum* *Bolinopsis microptera*	9	-3.3	70.481	-20.057	3, 4, S2, S5, S7
58		97	8.8	36.704	-122.040	3, 4, S2, S5
21		375	7.0	36.784	-122.023	3, 4, S2, S5
25	*Bolinopsis microptera* *Lampocteis cruentiventer*	999	3.9	36.697	-122.046	3, 4, S2, S5
244		506	5.8	36.709	-122.051	3, 4, S2, S5, S7
245		507	5.8	36.709	-122.051	3, 4, S2, S5, S7
243	*Lampocteis cruentiventer* *Beroe abyssicola*	508	5.8	36.709	-122.051	3, 4, S2, S5, S7
62		708	5.0	36.705	-122.054	3, 4, S2, S5, S7

Supplemental Table 2.3 Taxonomic and environmental metadata for all ctenophores used in lipidomic and biophysical analyses.

For samples collected at ≤20 m depth whose encounter depth was not recorded *in situ*, a depth of 10 m was used in analyses, as this represents the mean depth of our bluewater diving effort. Samples are grouped by species and sorted warm → cold, shallow → deep. Figures in which these samples appear are indicated.

Project sample ID #	Species	Depth	Temperature	Latitude	Longitude	Appears in figs:
148	*Lampocteis cruentiventer* *Beroe abyssicola*	736	4.9	36.415	-122.284	3, 4, S2, S5, S7
131		824	4.7	36.415	-122.284	3, 4, S2, S5, S7
344		580	5.0	35.499	-123.983	3, 4, S2, S5
345		626	4.7	35.950	-123.949	3, 4, S2, S5
343	*Beroe abyssicola* *Bathocyroe* aff. *fosteri*	885	4.1	36.688	-122.070	3, 4, S2, S5
173		1342	3.0	36.558	-122.252	3, 4, S2, S5
171		1645	2.4	35.950	-123.949	3, 4, S2, S5
172	*Bathocyroe* aff. *fosteri* Mertensiidae sp. K	3871	1.5	35.500	-124.003	3, 4, S2, S5
175		2300	1.9	35.950	-123.949	3, 4, S2, S5
174		2335	1.8	35.737	-122.749	3, 4, S1, S2, S5
170	Lobata sp. L2 Lobata sp. L1	2813	1.7	35.496	-123.988	3, 4, S2, S5
168		3761	1.5	34.574	-122.563	3, 4, S2, S5
177	Platyctenida sp. T	3963	1.5	35.496	-123.988	3, 4, S2, S5, S7
70	Lobata sp. L1	3964	1.5	35.497	-123.998	3, 4, S2, S5, S7
164	Platyctenida sp. T	3964	1.5	35.497	-123.998	2
176		3973	1.5	35.496	-123.988	3, 4, S2, S5, S7
178		3976	1.5	35.496	-123.988	3, 4, S2, S5, S7
188		3976	1.5	35.496	-123.988	3, 4, S2, S5, S7
99		3978	1.5	35.500	-124.000	3, 4, S2, S5, S7
100		3978	1.5	35.500	-124.000	3, 4, S2, S5, S7

Supplemental Table 2.4 Deuterated phospholipids used as internal standards for polar lipid analysis.

Analyte	Molecular Weight	Molecular Formula
15:0-18:1(d7) PC	753.11	$C_{41}H_{73}D_7NO_8P$
18:1(d7) Lyso PC	528.72	$C_{26}H_{45}D_7NO_7P$
15:0-18:1(d7) PE	711.03	$C_{38}H_{67}D_7NO_8P$
18:1(d7) Lyso PE	486.64	$C_{23}H_{39}D_7NO_7P$
15:0-18:1(d7) PG	764.02	$C_{39}H_{67}D_7NaO_{10}P$
15:0-18:1(d7) PI	847.13	$C_{42}H_{75}D_7NO_{13}P$
15:0-18:1(d7) PS	777.02	$C_{39}H_{66}D_7NNaO_{10}P$
15:0-18:1(d7)-15:0 TAG	812.37	$C_{51}H_{89}D_7O_6$
15:0-18:1(d7) DAG	587.98	$C_{36}H_{61}D_7O_5$
18:1(d7) Chol Ester	658.16	$C_{45}H_{71}D_7O_2$
d18:1-18:1(d9) SM	738.12	$C_{41}H_{72}D_9N_2O_6P$
C15 Ceramide-d7	530.92	$C_{33}H_{58}D_7NO_3$
C18(plasm)-18:1(d9) PC	781.19	$C_{44}H_{77}D_9NO_7P$
C18(plasm)-18:1(d9) PE	739.11	$C_{41}H_{71}D_9NO_7P$
18:0-CN-d3	430.1	$C_{25}H_{47}D_3NO_4$

Supplemental Table 2.5 Summary of all simulated lipid bilayer systems.

* denotes a system with gel-like properties that may not have converged on a steady state. In these cases, area per lipid, K_A, and D_T represent upper bounds. N/A = Not Analyzed.

System	Temp. (°C)	Press. (bar)	Duration (ns)	Area per Lipid (Å^2)	APL strain	K_A (dyn/cm)	D_T (μm^2/s)	P-P dist. (Å)	F'(0) = -k_{BC_0} (kcal/mol/Å)
Platyctenida sp. K model lipidome	20	1	444	64.06(0.17)	0	266.9(53.8)	5.16(0.21)	41.67(0.36)	0.248(0.004)
		250	432	63.67(0.20)	0.006	319.1(32.2)	3.30(0.14)	41.53(0.40)	0.166(0.032)
		500	435	62.96(0.17)	0.017)	212.5(34.0)	2.46(0.10)	41.5(0.38)	0.161(0.030)
		1000	435	61.58(0.19)	0.039	307.2(94.3)	1.64(0.07)	41.63(0.38)	0.139(0.026)
		1500	434	60.75(0.15)	0.052	269.3(33.9)	1.19(0.06)	41.59(0.37)	0.132(0.025)
***Bolinopsis infundibulum* model lipidome**	20	1	429	58.81(0.26)	0)	174.0(15.7)	4.58(0.21)	37.99(0.41)	0.158(0.006)
		250	459	57.96(0.22)	0.014)	252.1(26.8)	3.21(0.15)	37.89(0.37)	0.131(0.003)
		500	460	57.25(0.25)	0.027	258.9(56.1)	2.94(0.12)	37.97(0.43)	0.110(0.005)
		1000	464	56.27(0.15)	0.043)	294.2(81.8)	1.99(0.08)	37.96(0.37)	0.110(0.002)
		1500	461	55.38(0.22)	0.058	160.5(124.0)	1.19(0.05)	38.01(0.52)	0.087(0.007)
***Bolinopsis vitrea* model lipidome**	20	1	446	53.55(0.15)	0	382.7(23.9)	3.98(0.16)	42.23(0.42)	0.046(0.006)
		*1000	438	50.09(0.08)	0.064	194.1(116.9)	1.07(0.05)	43.1(0.48)	-0.025(0.005)
***Lampocteis cruentiventer* model lipidome**	20	1	452	62.90(0.19)	0	289.7(33.6)	5.07(0.22)	41.81(0.37)	0.106(0.003)
		1000	448	59.84(0.16)	0.049	259.2(23.5)	1.79(0.09)	42.00(0.39)	0.076(0.008)
18:1/18:1 PE (DOPE)	20	1	308	60.73(0.17)	0	286(19)	4.12(0.21)	41.30(0.46)	0.224(0.006)
		250	308	59.96(0.15)	0.013	262(19)	2.40(0.11)	41.81(0.44)	0.199(0.007)
		500	330	58.27(0.20)	0.041	285(10)	2.55(0.13)	41.81(0.44)	0.215(0.006)
		750	354	57.75(0.21)	0.049	284(81)	1.78(0.07)	41.74(0.52)	0.213(0.010)
		1000	364	57.12(0.4)	0.06	172(15)	1.21(0.06)	41.79(0.49)	0.178(0.009)
		*1500	316	49.11(0.91)	0.191	1902(3)	0.40(0.02)	44.96(1.0)	0.061(0.020)

Supplemental Table 2.6 Summary of all simulated lipid bilayer systems.

* denotes a system with gel-like properties that may not have converged on a steady state. In these cases, area per lipid, K_A, and D_T represent upper bounds. N/A = Not Analyzed.

System	Temp. (°C)	Press. (bar)	Duration (ns)	Area per Lipid (Å^2)	APL strain	K_A (dyn/cm)	D_T (μm^2/s)	P-P dist. (Å)	F'(0) = -k_{BC_0} (kcal/mol/Å)
18:1/18:1 PC (DOPC)	20	1	312	67.65(0.14)	0	267(8)	4.79(0.24)	38.57(0.40)	0.047(0.005)
		250	331	66.83(0.14)	0.012	254(5)	2.96(0.14)	38.48(0.45)	0.031(0.007)
		500	355	65.83(0.17)	0.027	264(5)	2.17(0.12)	38.52(0.42)	0.032(0.004)
		750	322	65.37(0.27)	0.034	260(10)	1.98(0.09)	38.42(0.36)	0.034(0.008)
		1000	303	64.61(0.18	0.045	340(11)	1.50(0.08)	38.46(0.36)	0.022(0.005)
		1500	312	63.07(0.18)	0.068	327(12)	N/A	38.69(0.36)	-0.001(0.006)
16:0/18:0 PE (POPE)	72	1	129	63.5(9)	0	349.7(32.9)	26.9(1.3)	3.96(5)	0.24
		1000	129	57.8(9)	0.09	375.7(45.1)	6.9(0.3)	4.07(5)	0.19
16:0/16:0 PC (DPPC)	50	1	74	61.4(9)	0	444.7(39.8)	12.6(0.6)	3.95(4)	N/A
		*1000	70	50.4(4)	0.18	N/A	0.9(0.1)	4.35(2)	N/A

Supplementary References

1. Hata, H., M. Nishiyama, and A. Kitao. 2020. Molecular dynamics simulation of proteins under high pressure: Structure, function and thermodynamics. *Biochimica et Biophysica Acta (BBA) - General Subjects*. 1864:129395.

2. Wroblowski, B., J.F. Díaz, K. Heremans, and Y. Engelborghs. 1996. Molecular mechanisms of pressure induced conformational changes in BPTI. *Proteins: Structure, Function, and Genetics*. 25:446–455.

3. Kitchen, D.B., L.H. Reed, and R.M. Levy. 1992. Molecular dynamics simulation of solvated protein at high pressure. *Biochemistry*. 31:10083–10093.

4. Sgourakis, N.G., R. Day, S.A. McCallum, and A.E. Garcia. 2008. Pressure Effects on the Ensemble Dynamics of Ubiquitin Inspected with Molecular Dynamics Simulations and Isotropic Reorientational Eigenmode Dynamics. *Biophys. J.* 95:3943–3955.

5. Meinhold, L., and J.C. Smith. 2005. Pressure-dependent transition in protein dynamics at about 4 kbar revealed by molecular dynamics simulation. *Physical Review E*. 72:061908.

6. Wakai, N., K. Takemura, T. Morita, and A. Kitao. 2014. Mechanism of Deep-Sea Fish α-Actin Pressure Tolerance Investigated by Molecular Dynamics Simulations. *PLoS One*. 9:e85852.

7. Marchi, M., and K. Akasaka. 2001. Simulation of Hydrated BPTI at High Pressure: Changes in Hydrogen Bonding and Its Relation with NMR Experiments. *J. Phys. Chem. B*. 105:711–714.

8. Starr, F.W., F. Sciortino, and H.E. Stanley. 1999. Dynamics of simulated water under pressure. *Physical Review E*. 60:6757–6768.

9. 2015. High Pressure Bioscience: Basic Concepts, Applications and Frontiers. Dordrecht: Springer Netherlands.

10. Kusube, M., H. Matsuki, and S. Kaneshina. 2005. Thermotropic and barotropic phase transitions of N-methylated dipalmitoylphosphatidylethanolamine bilayers. *Biochimica et Biophysica Acta (BBA) - Biomembranes*. 1668:25–32.

11. Ichimori, H., T. Hata, H. Matsuki, and S. Kaneshina. 1998. Barotropic phase transitions and pressure-induced interdigitation on bilayer membranes of phospholipids with varying acyl chain lengths. *Biochimica et Biophysica Acta (BBA) - Biomembranes*. 1414:165–174.

12. Sueyoshi, R., K. Tada, M. Goto, N. Tamai, H. Matsuki, and S. Kaneshina. 2006. Barotropic phase transition between the lamellar liquid crystal phase and the inverted hexagonal phase of dioleoylphosphatidylethanolamine. *Colloids Surf. B Biointerfaces*. 50:85–88.

13. Helfrich, W. 1973. Elastic Properties of Lipid Bilayers: Theory and Possible Experiments. *Zeitschrift für Naturforschung C*. 28:693–703.

14. Canham, P.B. 1970. The minimum energy of bending as a possible explanation of the biconcave shape of the human red blood cell. *J. Theor. Biol.* 26:61–81.

15. Waugh, R., and E.A. Evans. 1979. Thermoelasticity of red blood cell membrane. *Biophys. J.* 26:115–131.

16. Frewein, M.P.K., M. Rumetshofer, and G. Pabst. 2019. Global small-angle scattering data analysis of inverted hexagonal phases. *J. Appl. Crystallogr.* 52:403–414.

17. Kaltenegger, M., J. Kremser, M.P.K. Frewein, P. Ziherl, D.J. Bonthuis, and G. Pabst. 2021. Intrinsic lipid curvatures of mammalian plasma membrane outer leaflet lipids and ceramides. *Biochimica et Biophysica Acta (BBA) – Biomembranes*. 1863:183709.

18. Khakbaz, P., and J.B. Klauda. 2018. Investigation of phase transitions of saturated phosphocholine lipid bilayers via molecular dynamics simulations. *Biochimica et Biophysica Acta (BBA) - Biomembranes*. 1860:1489–1501.

19. Uppulury, K., P.S. Coppock, and J.T. Kindt. 2015. Molecular Simulation of the DPPE Lipid Bilayer Gel Phase: Coupling between Molecular Packing Order and Tail Tilt Angle. *J. Phys. Chem. B*. 119:8725–8733.

20. Tu, K., D.J. Tobias, J.K. Blasie, and M.L. Klein. 1996. Molecular dynamics investigation of the structure of a fully hydrated gel-phase dipalmitoylphosphatidylcholine bilayer. *Biophys. J.* 70:595–608.

21. Venable, R.M., B.R. Brooks, and R.W. Pastor. 2000. Molecular dynamics simulations of gel (LβI) phase lipid bilayers in constant pressure and constant surface area ensembles. *J. Chem. Phys.* 112:4822–4832.

22. Evans, E., and W. Rawicz. 1997. Elasticity of ``Fuzzy'' Biomembranes. *Phys. Rev. Lett.* 79:2379–2382.

23. Kusters, R., W. Dowhan, and B. de Kruijff. 1991. Negatively charged phospholipids restore prePhoE translocation across phosphatidylglycerol-depleted Escherichia coli inner membranes. *J. Biol. Chem.* 266:8659–8662.

24. Schlining, B., and N. Stout. 2006. MBARI's Video Annotation and Reference System. IEEE.

25. Budin, I., A. Debnath, and J.W. Szostak. 2012. Concentration-Driven Growth of Model Protocell Membranes. *J. Am. Chem. Soc.* 134:20812–20819.

26. Owen, D.M., C. Rentero, A. Magenau, A. Abu-Siniyeh, and K. Gaus. 2012. Quantitative imaging of membrane lipid order in cells and organisms. *Nat. Protoc.* 7:24–35.

27. Bligh, E.G., and W.J. Dyer. 1959. A rapid method of total lipid extraction and purification. *Can. J. Biochem. Physiol.* 37:911–917.

28. Hamilton, J.G., and K. Comai. 1988. Rapid separation of neutral lipids, free fatty acids and

polar lipids using prepacked silica Sep-Pak columns. *Lipids*. 23:1146–1149.

29. Chung, H., and M. Caffrey. 1994. The curvature elastic-energy function of the lipid–water cubic mesophase. *Nature*. 368:224–226.

30. Chen, Y.-F., K.-Y. Tsang, W.-F. Chang, and Z.-A. Fan. 2015. Differential dependencies on [Ca^{2+}] and temperature of the monolayer spontaneous curvatures of DOPE, DOPA and cardiolipin: effects of modulating the strength of the inter-headgroup repulsion. *Soft Matter*. 11:4041–4053.

31. De Villiers, S., and B.K. Nelson. 1999. Detection of Low-Temperature Hydrothermal Fluxes by Seawater Mg and Ca Anomalies. *Science*. 285:721–723.

32. Rai, D.K., R.E. Gillilan, Q. Huang, R. Miller, E. Ting, A. Lazarev, M.W. Tate, and S.M. Gruner. 2021. High-pressure small-angle X-ray scattering cell for biological solutions and soft materials. *J. Appl. Crystallogr.* 54:111–122.

33. Hopkins, J.B., R.E. Gillilan, and S. Skou. 2017. *BioXTAS RAW* : improvements to a free open-source program for small-angle X-ray scattering data reduction and analysis. *J. Appl. Crystallogr.* 50:1545–1553.

34. Quehenberger, O., A.M. Armando, A.H. Brown, S.B. Milne, D.S. Myers, A.H. Merrill, S. Bandyopadhyay, K.N. Jones, S. Kelly, R.L. Shaner, C.M. Sullards, E. Wang, R.C. Murphy, R.M. Barkley, T.J. Leiker, C.R.H. Raetz, Z. Guan, G.M. Laird, D.A. Six, D.W. Russell, J.G. McDonald, S. Subramaniam, E. Fahy, and E.A. Dennis. 2010. Lipidomics reveals a remarkable diversity of lipids in human plasma. *J. Lipid Res.* 51:3299–3305.

35. Hartler, J., A.M. Armando, M. Trötzmüller, E.A. Dennis, H.C. Köfeler, and O. Quehenberger. 2020. Automated Annotation of Sphingolipids Including Accurate Identification of Hydroxylation Sites Using MS^{n} Data. *Anal. Chem.* 92:14054–14062.

36. Winnikoff, J.R., S.H.D. Haddock, and I. Budin. 2021. Depth- and temperature-specific fatty acid adaptations in ctenophores from extreme habitats. *J. Exp. Biol.* 224:jeb242800.

37. Tate, M.W., and S.M. Gruner. 1989. Temperature dependence of the structural dimensions of the inverted hexagonal (HII) phase of phosphatidylethanolamine-containing membranes. *Biochemistry*. 28:4245–4253.

38. Dymond, M.K. 2021. Lipid monolayer spontaneous curvatures: A collection of published values. *Chem. Phys. Lipids*. 239:105117.

39. Klauda, J.B., R.M. Venable, J.A. Freites, J.W. O'Connor, D.J. Tobias, C. Mondragon-Ramirez, I. Vorobyov, A.D. MacKerell Jr, and R.W. Pastor. 2010. Update of the CHARMM all-atom additive force field for lipids: validation on six lipid types. *J. Phys. Chem. B*. 114:7830–7843.

40. Leonard, A.N., R.W. Pastor, and J.B. Klauda. 2018. Parameterization of the CHARMM All-Atom Force Field for Ether Lipids and Model Linear Ethers. *J. Phys. Chem. B*. 122:6744–6754.

41. Jorgensen, W.L., J. Chandrasekhar, J.D. Madura, R.W. Impey, and M.L. Klein. 1983. Comparison of simple potential functions for simulating liquid water. *J. Chem. Phys.* 79:926–935.

42. Lee, J., X. Cheng, J.M. Swails, M.S. Yeom, P.K. Eastman, J.A. Lemkul, S. Wei, J. Buckner, J.C. Jeong, Y. Qi, S. Jo, V.S. Pande, D.A. Case, C.L. Brooks 3rd, A.D. MacKerell Jr, J.B. Klauda, and W. Im. 2016. CHARMM-GUI Input Generator for NAMD, GROMACS, AMBER, OpenMM, and CHARMM/OpenMM Simulations Using the CHARMM36 Additive Force Field. *J. Chem. Theory Comput.* 12:405–413.

43. Feller, S.E., Y. Zhang, R.W. Pastor, and B.R. Brooks. 1995. Constant pressure molecular dynamics simulation: The Langevin piston method. *J. Chem. Phys.* 103:4613–4621.

44. Martyna, G.J., D.J. Tobias, and M.L. Klein. 1994. Constant pressure molecular dynamics algorithms. *J. Chem. Phys.* 101:4177–4189.

45. Ryckaert, J.-P., G. Ciccotti, and H.J.C. Berendsen. 1977. Numerical integration of the cartesian equations of motion of a system with constraints: molecular dynamics of n-alkanes. *J. Comput. Phys.* 23:327–341.

46. Darden, T., D. York, and L. Pedersen. 1993. Particle mesh Ewald: An N·log(N) method for Ewald sums in large systems. *J. Chem. Phys.* 98:10089–10092.

47. Harasima, A. 2007. Molecular theory of surface tension. In: Advances in Chemical Physics. Hoboken, NJ, USA: John Wiley & Sons, Inc. pp. 203–237.

48. Sonne, J., F.Y. Hansen, and G.H. Peters. 2005. Methodological problems in pressure profile calculations for lipid bilayers. *J. Chem. Phys.* 122:124903.

49. Jackson, D.R., C.D. Cassilly, D.R. Plichta, H. Vlamakis, H. Liu, S.B. Melville, R.J. Xavier, and J. Clardy. 2021. Plasmalogen Biosynthesis by Anaerobic Bacteria: Identification of a Two-Gene Operon Responsible for Plasmalogen Production in *Clostridium perfringens*. *ACS Chem. Biol.* 16:6–13.

50. Zobell, C.E., and C.H. Oppenheimer. 1950. Some effects of hydrostatic pressure on the multiplication and morphology of marine bacteria. *J. Bacteriol.* 60:771–781.

51. Asai, Y., Y. Katayose, C. Hikita, A. Ohta, and I. Shibuya. 1989. Suppression of the lethal effect of acidic-phospholipid deficiency by defective formation of the major outer membrane lipoprotein in Escherichia coli. *J. Bacteriol.* 171:6867–6869.

52. Fahy, E., S. Subramaniam, R.C. Murphy, M. Nishijima, C.R.H. Raetz, T. Shimizu, F. Spener, G. van Meer, M.J.O. Wakelam, and E.A. Dennis. 2009. Update of the LIPID MAPS comprehensive classification system for lipids. *J. Lipid Res.* 50:S9–S14.

Chapter 3 Active regulation of intrinsic curvature by eukaryotic phospholipid metabolism

Abstract

Membranes contain thousands of different lipids, but it is poorly understood why their compositions vary across cell types and environments. We report that lipid metabolism balances the molecular curvature of phospholipids, a parameter that describes their shape and propensity to destabilize flat sheets. We utilized extreme hydrostatic pressures, similar to those found in the deep ocean, to change the shape (reduce the curvature) of phospholipids in growing cells. Yeast and human cells respond to this stress by increasing synthesis of distinct high-curvature lipid species. The results support a model in which eukaryotic cells actively regulate lipid composition to maintain their membranes in a frustrated state, a dynamic that could be important for maintaining core functions in membrane trafficking.

Introduction

The chemistry of cellular lipids determines their shape and propensity to pack into both bilayer and non-bilayer structures. Phospholipids that are cylindrical in shape, like phosphatidylcholine (PC), pack readily into lamellar phases (bilayers). Since they form leaflets that are mechanically unstressed with little tendency to curve, such lipids are considered to have intrinsic lipid curvature (c_0) near zero. Other abundant lipids, like phosphatidylethanolamine (PE), have a smaller cross-section at the headgroup than in the hydrocarbon region, giving them a conical shape. In isolation, such phospholipids form non-bilayer structures, like the inverse hexagonal (H_{II}) or bicontinuous cubic (Q_{II}) phases, in which lipid monolayers curve towards the head groups(1). This is defined by convention as negative curvature, so such lipids have $c_0 < 0$. They are referred to herein as high-curvature lipids, since we primarily consider species with $c_0 \leq 0$. When incorporated into flat membranes, high-curvature lipids impose packing frustration also known as curvature elastic stress(2). In some compartments, like the inner mitochondrial

membrane, non-bilayer phospholipids make up the majority of membrane building blocks(3). The observation that cells synthesize diverse phospholipids that destabilize bilayer structure seems antithetical to the classical model of cell membranes as robust barrier structures. High-curvature lipids appear to balance this barrier function with a requirement for membrane dynamics: they modulate membrane protein conformations through changes in the bilayer's internal stresses(4, 5), generate packing defects for interactions with soluble proteins(6), and facilitate structural intermediates in membrane fission and fusion processes(7, 8). The relative amount of lipids that stabilize versus frustrate membranes has been proposed as a metabolic lever for keeping these structures robust yet dynamic(9).

Metabolism has long been known to maintain key properties of membranes by altering lipid stoichiometry in response to environmental changes. Classically, this homeostasis has been understood through the capacity of a wide range of organisms to maintain the fluidity of their membranes in response to temperature. Membranes contain mixtures of low- and high-melting temperature (T_m) lipids, which control membrane fluidity and are required for mechanisms of lateral organization. Low temperatures or increases in high-T_m lipids can drive fluid lamellar-phase (L_α) bilayers to a solid or gel-like phase (L_β)(10, 11). Cells control the fluidity of their bilayers and avoid L_β by modulating the unsaturation of phospholipid acyl chains(12, 13), the hydrogen bonding capacity of their head groups through changes in the PE/PC ratio(14), or the relative amount of other lipid classes, like sterols(15). In some systems, sensors for fluidity-related properties have been identified, which respond to changes in bilayer packing or thickness and transcriptionally regulate unsaturated fatty acid metabolism(16, 17). While these responses – generally termed homeoviscous adaptation or acclimation – are activated during changes in growth

temperature, they are also required for general optimization of fluidity-mediated processes like respiration(18).

Several lines of evidence have suggested that cells utilize homeostatic mechanisms for maintaining curvature stress analogous to those that maintain fluidity(2, 9, 19–21). However, a consistent challenge is that the experimental levers observed to cause changes in non-bilayer lipids – which include temperature or mutations in phospholipid metabolism – have pleiotropic effects on lipid properties. For example, while low temperatures reduce curvature by restricting the volume of phospholipid chains(19), they more strongly reduce membrane fluidity and promote gel phases, as described below. Similarly, restriction of PC synthesis promotes negative curvature and drives changes in PE metabolism(22), but loss of PC also inhibits membrane fluidity due to its low $T_{m(14)}$. Thus, it is unclear whether previously observed lipid changes were truly serving to maintain lipid curvature or were instead secondary effects of responses to membrane fluidity and associated properties. While important progress has been made, the complexity of the mechanisms involved in metabolic balancing of membrane properties deserve further investigation.

Recent work highlights hydrostatic pressure as an environmental variable that acts disproportionately on lipid intrinsic curvature. Among ctenophores (comb jellies), animals specialized for high pressure exhibit phospholipid chemistry that defends negative lipid curvature and access to non-bilayer phases (homeocurvature adaptation)(23). Pressure drives biomolecules into lower-volume conformations and has an especially large effect on lipids due to the high compressibility of their hydrocarbon chains. Pressure has a stronger effect on membrane curvature than on fluidity because phospholipid compressibility is anisotropic: the hydrocarbon chain volume is more pressure-sensitive than that of head groups. The temperature to pressure

equivalency of a phase transition (dT/dP) is determined by the ratio of volumetric (ΔV) and enthalpic (ΔH) changes by the Clausius–Clapeyron relation:

$$dT/dP = T\Delta V/\Delta H$$

In model membranes, dT/dP of the curvature-mediated $L_\alpha \rightarrow H_{II}$ transition is 0.05 K/bar(24, 25), e.g. a pressure of 400 bar corresponds to a temperature drop of ~20 °C at 1 bar. In contrast, the dT/dP for the $L_\alpha \rightarrow L_\beta$ transition is 3-fold smaller, so fluidity is dominated by temperature and weakly affected by pressure. In deep-sea ctenophores, adaptation to high-pressure evolved with increased synthesis of the high-curvature plasmenyl PE (P-PE), as well as incorporation of longer chains across all phospholipids(23, 26). In vitro, pressure inhibits processes like membrane fusion (23) that are dependent on lipid intrinsic curvature(27).

We hypothesized that if cells sense and regulate intrinsic curvature directly, then they would alter their lipid chemistry in response to high-pressure treatment that directly reduces it. Since terrestrial organisms are unlikely to have evolved *bona fide* hydrostatic pressure sensors, such acclimation would be driven by changes in membrane packing. In this way, high pressure could be utilized to delineate mechanisms of homeocurvature acclimation from other modes of membrane homeostasis in non-pressure adapted cells. Here we use this approach to identify an endogenous capacity of phospholipid metabolism to actively modulate lipidome curvature in both yeast and a human cancer cell line.

Results

Lower PE content reduces stability of non-lamellar phases and hydrostatic pressure tolerance

High pressures decrease the curvature of non-bilayer lipids(24), challenging cells' ability to access non-lamellar membrane topologies. As PC and PE are the most abundant lamellar and

non-lamellar lipids, respectively, in eukaryotic lipidomes, we chose to screen the effects of varying PE/PC ratios on fitness of yeast grown at pressure. The *PSD1* and *PEM1/2* genes in *Saccharomyces cerevisiae* (W303) are predominantly responsible for PE and PC biosynthesis in the CDP-DAG pathway, respectively(28). Alternative pathways for PE and PC synthesis channel through the CDP-choline or -ethanolamine branches of the Kennedy pathway and require choline or ethanolamine supplementation, offering an opportunity for rescue controls in defined growth media. Phospholipid profiles of wild-type (WT), *pem2*Δ, *psd1*Δ, and supplementation of 2 mM choline to *psd1*Δ (*psd1Δ* + CHO) were characterized by liquid chromatography-tandem mass spectrometry (LC-MS^2) (Fig. 1A). Due to the lipidomics platform used, PE quantification was confounded as it was not possible to distinguish between PE, monomethylethanolamine-PE (MMPE), and dimethylethanolamine-PE (DMPE). Disruption of PE methylation in *pem2*Δ resulted in an almost complete loss of PC, with an apparent increase of odd-numbered acyl chain PE lipids likely representing MMPE, which has an increased propensity to form nonlamellar phases than PC (MMPE; Supp. Fig. 1A)(29, 30). In the *psd1*Δ mutant, PE was depleted by >75% and partially rescued when supplemented with choline. Along with reduced PE or PC in the respective knockout strains, an increase in PS was observed in strains with lower PE levels, as PS is the substrate for PE-generating Psd1. A notable increase in PI was also observed in *pem2*Δ and *psd1*Δ cells, likely a consequence of UAS_{INO} element deregulation involved in PE and PC synthesis (31).

We next asked how changes in PE and PC affect the biophysical properties of yeast lipids. To characterize access to non-lamellar lipid phases, we measured small angle X-ray scattering (HPSAXS) behavior across 1-3000 bar of rehydrated polar lipid extracts from cultures grown at 1 bar. Samples were equilibrated to 85°C(30), which we determined through temperature sweeps to

ensure the formation of non-lamellar phases (unpublished data), before isothermally increasing pressure (Supp. Fig 1B). At 1 bar, scattering profiles for all strains except *psd1*Δ displayed a sharp primary peak near 0.05 $Å^{-1}$ whose intensity decreased with pressure; we interpreted this as a non-lamellar Q_{II} phase with repeat spacing of $2\pi/0.05$ $Å^{-1}$ ≈ 125 Å (Supp. Fig. 1B). As pressure increased, peaks with uniform spacing emerged (q:2q:3q:4q…), representing the diffraction signature of fluid (L_α) or gel (L_β) lamellar membranes. The sensitivity of the Q_{II} peak to pressure differed between strains: in *pem2*Δ it was detectable up to 3000 bar, while in WT and *psd1*Δ + CHO at 1 bar, it dissipated by 500 bar. The midpoints of barotropic phase transitions were used to construct phase diagrams (Fig. 1B). In parallel with phase analysis, we measured lipid packing in the same samples across a P/T grid using high-pressure fluorescence spectroscopy (HPFS). Liposomes were stained with C-Laurdan, a solvatochromic dye whose fluorescence changes with lipid packing and water penetration(32). Using the fluorescence intensities of C-Laurdan at two wavelength windows, General Polarization (GP) values can be ratiometrically calculated to quantify an emission shift that corresponds to membrane order. While we observed some differences in C-Laurdan GP values between the strains (Fig. 1C), they were modest and did not correspond to changes in $L_\alpha \rightarrow L_\beta$ transition temperatures (Fig. 1C, Supp. Fig. 1C).

Our biophysical analyses suggested that changes in PE vs. PC headgroup metabolism primarily affected curvature-driven phase behavior, and not membrane fluidity, thus allowing us to ask whether lipid curvature dictates pressure tolerance as previously observed in bacterial cells(23). We assessed the pressure tolerance of each strain by measuring growth during and survival following hydrostatic pressure incubation. For the former, relative pressure effects were calculated via changes in cell density (ΔOD_{600}) compared to identical 1 bar incubations ($\Delta\Delta OD_{600}$) (Fig. 1D). Cells lacking Psd1, with strongly reduced PE levels, showed a growth defect through

this analysis. Survival, measured by spotting culture aliquots after pressure incubation, was also strongly reduced in *psd1*Δ, as well as in *psd1*Δ + CHO, which exhibited a moderate PE reduction. Thus, loss of PE synthesis, which reduces accessibility to non-lamellar phases, renders cells sensitive to high pressure that further reduces lipid curvature.

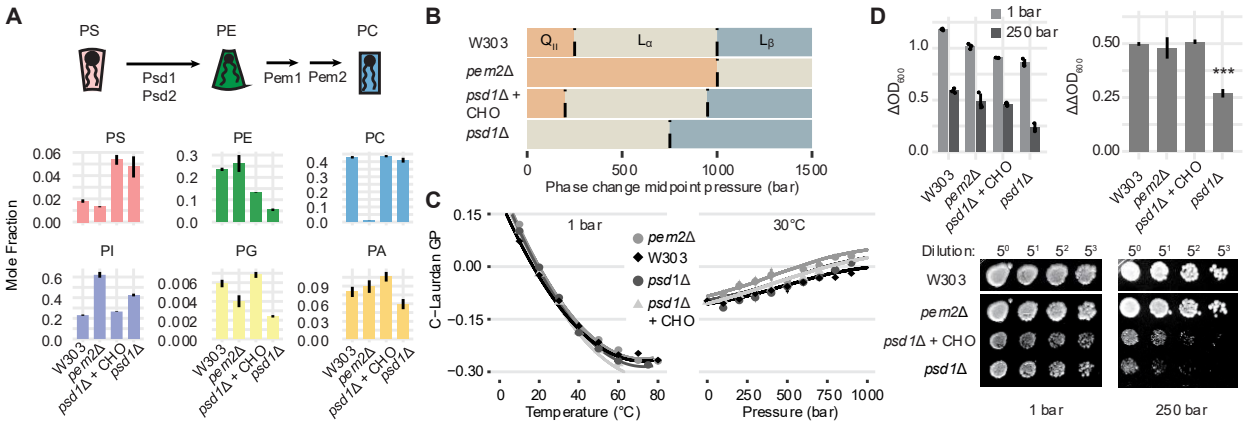

Figure 3.1 Restricted access to non-lamellar phases decreases high-pressure fitness.

(**A**) Phospholipid levels of W303 and mutants with knockouts in PC biosynthesis (*pem2*Δ), PE biosynthesis (*psd1Δ*), and *psd1Δ* with supplementation of 2 mM choline as a partial rescue (*psd1*Δ + CHO). Error bars indicate SEM from $N = 3$ cultures. (**B**) Pressure-dependent phases of extracted polar lipids as determined by HPSAXS. Cells were grown at 1 bar and 30°C; measurements were performed at 85°C. Scattering profiles shown in Supp. Fig. 1. Cells lacking Psd1 show reduced prevalence of the non-bilayer cubic phase (Q_{II}), while those lacking Pem2 show a stabler Q_{II}. (**C**) C-Laurdan GP values from polar lipid extracts of strains in HPFS experiments across a temperature (5-80 °C at 1 bar) and pressure (1-1000 bar at 30°C) range. Strains showed similar GP values. Full P/T profiles are shown in Supp. Fig. 1C. (**D**) Growth (top) and survival (bottom) of PE/PC variant strains after 1 or 250 bar pressure incubation. Strains, like *psd1*Δ, show growth defects at 1 bar, but these can be exacerbated at 250 bar. Cells with reduced PE show reduced comparative growth (*psd1*Δ) and survival (*psd1*Δ, *psd1*Δ + CHO) at 250 bar. For *psd1*Δ + CHO, 2mM choline supplementation was applied during the growth incubation, but not on the YPD plates that were used to assess survival. One row from the original survival plate images was omitted, indicated as a space, to omit a strain which was not used in this work. Error bars indicate SEM from $N = 3$ cultures. *** $P < 0.001$, 1-way ANOVA with Dunnet's test of *psd1*Δ compared against W303.

Cells under pressure compensate by increasing lipidome curvature, not membrane fluidity

While *psd1*Δ cells with reduced access to non-lamellar phases showed a growth defect at high pressure, we did not observe the corresponding growth enhancement for *pem2*Δ cells that

showed increased access to non-lamellar phases from PC depletion and MMPE enrichment. Importantly, our biophysical analyses were carried out in cells grown at 1 bar, so they did not account for any changes that pressure could cause to yeast lipid metabolism during extended incubations. We thus considered whether cells might acclimate their lipidomes to pressure, thereby preserving their fitness. Because HPSAXS analysis requires large amounts of biomass, we focused this analysis on WT cells grown in identical, large pressure vessels incubated either at 1 or 250 bar for 16 h, from which extracted polar lipids were used for both HPSAXS and HPFS to measure lipid phase properties membrane fluidity, respectively (Fig. 2A).

In HPSAXS experiments, reconstituted extracts formed non-lamellar phases at elevated temperatures 85°C (Fig. 2B): 1 bar-grown extracts showed a mixture of H_{II} and lamellar signatures, while the 250 bar-grown extracts showed a predominantly nonlamellar mixture of Q_{II} and H_{II} signatures. Taking advantage of the presence of a clear H_{II} phase in both samples, we were able to extract curvature values which correspond to differences in lipid composition in each extract (Fig. 2C). The 250 bar-grown H_{II} phase displayed larger peak spacing corresponding to a curvature c of -0.038 +/- 0.00025 $Å^{-1}$ compared to c = -0.030 +/- 0.00014 $Å^{-1}$ in the 1 bar-grown sample. Here, unrelaxed curvature c is expected to be modestly more negative than intrinsic curvature c_0, due to the absence of tricosene void filling relaxation and resulting chain stretching stress in the H_{II} lattice(33). In parallel, we tested whether pressure elicits a fluidity response in the same samples by measuring C-Laurdan GP across 10-80°C and 1-1000 bar (Fig. 2D). These experiments showed that the 250 bar extracts exhibited reduced fluidity compared to those from cells grown at 1 bar, which is clear at single-temperature or experimental pressure references (Fig. 2E). This difference was in contrast to what would be expected for a homeoviscous acclimation to pressure. Yeast cells

thus respond to pressure through a response that maintains lipidome curvature, not membrane fluidity.

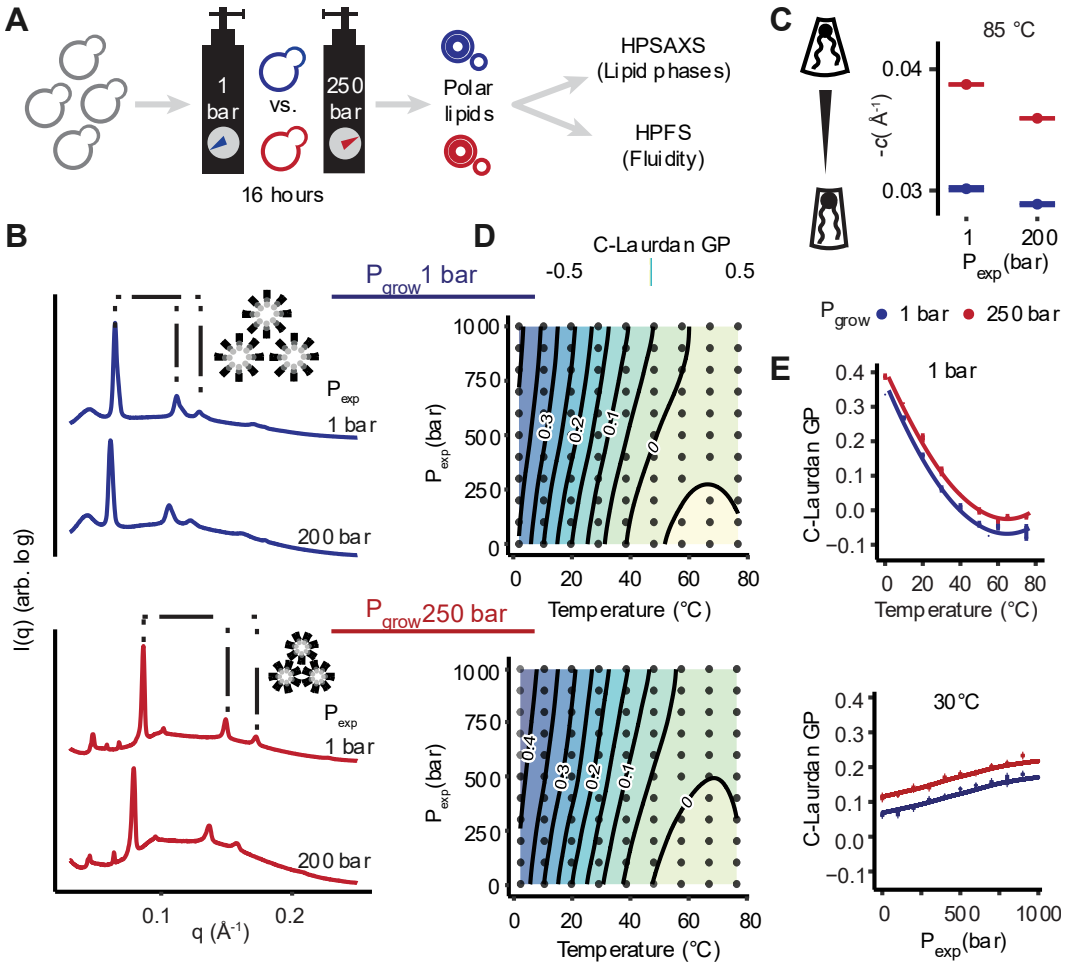

Figure 3.2 Signatures of homeocurvature acclimation in yeast grown under pressure.

(**A**) Schematic of workflow for high-pressure acclimation experiments. (**B**) Representative HPSAXS profiles from W303 grown at 1 and 250 bar. Profiles are shown for extracts at 1 and 200 bar SAXS cell pressure conditions at 85°C, with baselines offset for clarity. Characteristic H_{II} phase peak spacing (1, √3, 2) are labelled in each 1 bar profile along with schematics showing the corresponding difference in H_{II} size. (**C**) Differences in un-relaxed curvatures extracted from the H_{II} phase measured at 85°C. Lipidome adjustment more than offsets the effect of pressure on curvature. Error bars indicate SEM from a linear regression fit of curvatures determined at pressures from 1-400 bar. (**D**) C-Laurdan GP values of liposomes from the same samples measured across a P-T grid with HPFS. Lower GP corresponds to more fluid membranes. Non-linear behavior at higher temperatures is a result of the non-lamellar phase transition, which occurs at a higher pressure for the 250 bar extract. The color key at the top indicates GP values. (**E**) C-Laurdan GP across a single reference pressure (1 bar, left) and temperature (30°C, right). High-pressure extracts show a higher GP, reflecting reduced membrane fluidity.

Yeast promote negative curvature by increasing the abundance PI

We hypothesized that the propensity of high-pressure extracts to form nonlamellar topologies could be explained by upregulation of high-curvature lipids. We anticipated increased levels in PE and a reduction of PC as the canonical non-bilayer and bilayer-forming phospholipids, respectively. While the PE/PC ratio (0.31 +/- 0.05) did increase in cells grown at 250 bar (0.39 +/- 0.05), there was an overall decrease in both PC and PE (Fig. 3A). Instead, levels of PI increased more than 2-fold compared to cells grown at atmospheric pressure. Along with this, the abundance of lyso-PI (LPI) increased which is consistent with increased PI metabolism, similar decreases in LPC and LPE alongside their parent phospholipids. We also observed changes in the acyl chains across all phospholipids. High-pressure growth caused an increase in monounsaturated phospholipids at the expense of saturated and diunsaturated species (Fig. 3B). There was also an increase in long-chain phospholipids, a pattern previously observed in pressure-adapted ctenophore lipids(26). Lengthening of lipid chains without corresponding unsaturation promotes negative curvature while reducing membrane fluidity; it is thus clearly a curvature-specific response(34). Pressure-grown cells also showed a small decrease in ergosterol levels (Supp. Fig. 3G).

The dominance of PI in pressure-treated yeast cells motivated further investigation of its biophysical properties. Although PI is a ubiquitous eukaryotic phospholipid and is especially abundant in yeast, its phase and curvature properties have been less well characterized than those of its phosphorylated derivatives(35). However, one previous study observed that PI promoted cubic phases in mixtures with PC(36). We first tested the phase properties of Soy PI, which features a mixture of acyl chains but is available in bulk. Soy PI in water (50% w/v) displayed a complex mixture of cubic and lamellar signatures that were stable from 10°C and 80°C and from 1-1000

bar pressure (Supp. Fig. 2A). C-Laurdan measurements reflected an intermediate fluidity between PC and PE but were more challenging to interpret due to the phase coexistence (Supp. Fig. 2B). To measure PI's curvature directly, we extrapolated c_0 from hosted mixtures of 10 mol % PI in DOPE H_{II}-phase tubules (Fig. 3C). For these, the H_{II} phase was relaxed with the hydrocarbon (9Z)-tricosene. Both Soy PI and di-oleoyl PI (DOPI), with defined 18:1 chains in both positions, featured similar c_0 values of -0.015 $Å^{-1}$ at 1 bar and 35°C (Fig. 3D). This value was between DOPE's larger negative curvature and DOPC's near-zero curvature under these conditions. PI thus exhibits a negative intrinsic curvature that is intermediate to the other main yeast phospholipids PC and PE. These experiments were carried out in water with Na^+ counterions equimolar to PI; like other anionic lipids, properties of PI are likely to be additionally sensitive to changing salt concentrations, especially divalent cations.

Negative-curvature lipids facilitate membrane fusion by stabilizing non-bilayer intermediates. To test whether the negative curvature of PI could permit membrane fusion, we performed a FRET-based, Ca^{2+}-induced lipid mixing assay of liposomes containing phosphatidylserine (PS), PC, and either PE or PI (Fig. 3E). Unlike control liposomes with only PC and PS, those including either Soy PI or PE were fusogenic. Fusion rates with Soy PI were lower than those with PE, consistent with its more moderate negative curvature. It is known that many factors can affect fusion of PS containing liposomes induced by Ca^{2+}, including high surface charge and negative intrinsic curvature(37). As an additional control to account for changes in surface charge, we replaced Soy PI with POPG, an anionic lipid that has a curvature near zero(38). Unlike PI, POPG did not support membrane fusion. While the surface charge of PI may contribute to its fusion capacity, these results suggest that PI's negative spontaneous curvature is relevant for the dynamics of bilayer membranes.

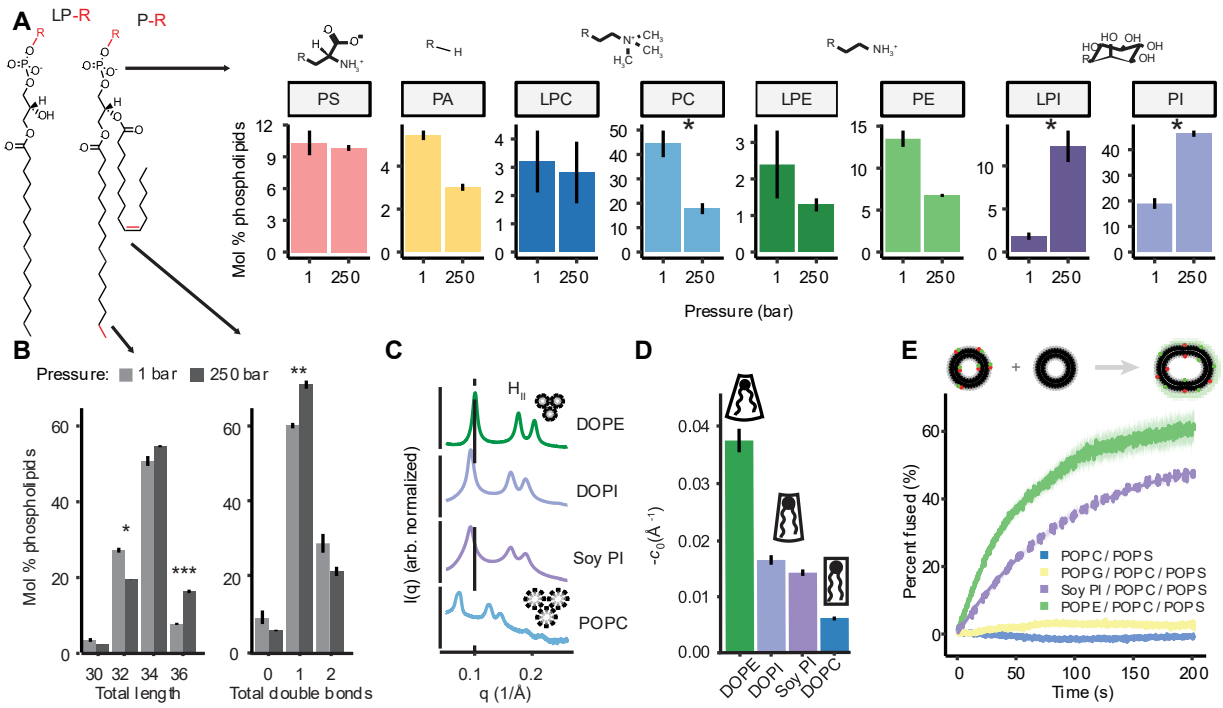

Figure 3.3 Identification of PI as a curvature-promoting phospholipid.

(**A**) Abundances of phospholipid classes in W303 grown at 1 or 250 bar, with structures of the representative headgroups above each. Error bars indicate SEM from N = 3 cultures. * $P < 0.05$ unpaired two-tailed t-test. (**B**) Corresponding total length (left, summed over both chains) and number of double bonds (right, summed over both chains) of all phospholipids. Error bars indicate SEM from N = 3 cultures. * $P < 0.05$, ** $P < 0.01$, *** $P < 0.001$ unpaired two-tailed t-test. (**C**) Representative SAXS profiles of the H_{II} phase of 100% DOPE and hosted (10%) DOPI, Soy PI, or POPC samples in DOPE (90%) relaxed with 12% (w/w) tricosene at 1 bar, 35 °C. The leftward shift in spacing of the first peak between each is denoted and represents a reduction in negative curvature. (**D**) Values of c_0 determined for DOPE, DOPI, Soy PI, and DOPC at 1 bar, 35 °C. Error bars indicate SEM from a linear regression fit determined from 1-1000 bar. (**E**) Lipid mixing assay comparing the fusion of liposomes with POPE/POPC/POPS (1:1:1), Soy PI/POPC/POPS (1:1:1), POPG/POPC/POPS (1:1:1), or POPC/POPS (2:1). FRET dequenching occurs when labeled liposomes (2 mol % Rh-PE, 2 mol % NBD-PE) fuse with unlabeled ones after addition of 10mM $CaCl_2$ at 37°C. Intensities are normalized to values for mixed liposomes.

Multiple mechanisms of homeocurvature acclimation across yeast and mammalian cells

Alongside an increase in PI levels, pressure induced multiple lipidome changes in yeast cells, affecting both the distribution of phospholipid head groups (Fig. 3B), chains (Supp. Fig. 3), and abundance of lysolipids, which contribute positive intrinsic curvature(39). To globally account for these changes, we applied a mathematical model (c0operate, (34)) for estimating a

phospholipid curvature index (PLCI) that assumes ideal mixing between phospholipid species and accounts for differences in their head groups and acyl chains. Analyzing the *S. cerevisiae* data (Fig. 4A), PLCI becomes more negative (higher curvature elastic stress) in 250 bar-grown cells and this change is primarily driven by substitution of PI for PC (Fig. 4B). We then performed a similar analysis on a different budding yeast, *Lachancea kluyveri* (FM628), that diverged from *S. cerevisae* at least 100 million years ago(40). Unlike *S. cerevisae* which can only produce monounsaturated acyl chains, *L. kluyveri* encodes desaturases that enable it to produce di- and tri-unsaturated acyl chains, offering an opportunity to assess the effect of PUFAs on pressure tolerance(41). *L. kluyveri* also responded to pressure by increasing PI levels, but featured a more prominent reduction in positively-curved PS(42), greater PE unsaturation, and an increase in very high-curvature diacylglycerol(43) (DAG) (Supp. Fig. 3H, I). In general, acyl chains of pressure-grown *L. kluyveri* increased in length and unsaturation, employing its ability to produce polyunsaturated fatty acids (PUFAs) (Supp. Fig. 3). Overall, both yeasts displayed a similar response of PLCI to 250 bar through overlapping but distinct modes (Fig. 4B).

Though PI is abundant in yeast, it is a smaller component in mammalian cells and is absent in most bacteria. We thus asked whether curvature maintenance is a general biophysical phenomenon in these systems. We subjected K562, a human leukemia suspension cell line, to incubations at 1 or 250 bar in the same chambers used in the yeast experiments, albeit for shorter 6 h incubations. While pressure-induced toxicity prevented longer treatments, staining membranes of cells incubated at these conditions with C-Laurdan showed no defects in cell morphology after 6 h (Supp. Fig. 4). We did observe enlargement of cells, which was also observed in yeast, and could be related to changes in membrane trafficking(44). Lipidomic analysis showed extensive changes due to pressure (Fig. 4C), including an increase in ether phospholipids, which include

monoalkyl PC (O-PC) and P-PE, and a corresponding reduction in PC (Fig. 4D). Ether linkages contribute directly to negative curvature and are an adaptive feature of ctenophores specialized for high-pressure(23, 34). K562 cells grown at 250 bar also showed an increase in phospholipid chain length, a signature of a curvature response(34), and unsaturation, which is shared by both curvature and fluidity responses (Fig. 4E). These changes were concentrated in the sn-2 chain position and were observed in almost all phospholipid classes (Supp. Fig. 5). Globally, when accounting for these changes, the PLCI became more negative in pressure-treated K562 cells (Fig. 4F) – a similar effect as in yeast but through different lipidic levers. The extent of curvature acclimation in K562 could be underestimated due to a paucity of reference c_0 values for phospholipids containing long-chain PUFAs.

As a model bacterium, *Escherichia coli* cannot produce the curvature-associated lipid classes PI or ether lipids but has been previously shown to maintain access to non-lamellar phases in response to temperature through acyl chain remodeling (19). However, when grown at 250 bar, we did not detect an increase to mean phospholipidome curvature in *E. coli* K12 (MG1655) cells (Supp. Fig. 6A-B). Pressure-grown MG1655 featured reduction in high-curvature PE and increases in low-curvature PG, along with no change in cardiolipin (CL), while the number of double bonds in acyl chains showed decreased unsaturation and length (Supp. Fig. 6C-D). These results suggest that curvature responses in *E. coli* are likely a side-effect of thermal acclimation. They are also consistent with work showing that fatty acid unsaturation is regulated by temperature sensitivities of enzymes in *E. coli*'s type II fatty acid synthesis(12), and so would not respond directly to loss of curvature frustration induced by high-pressure incubations.

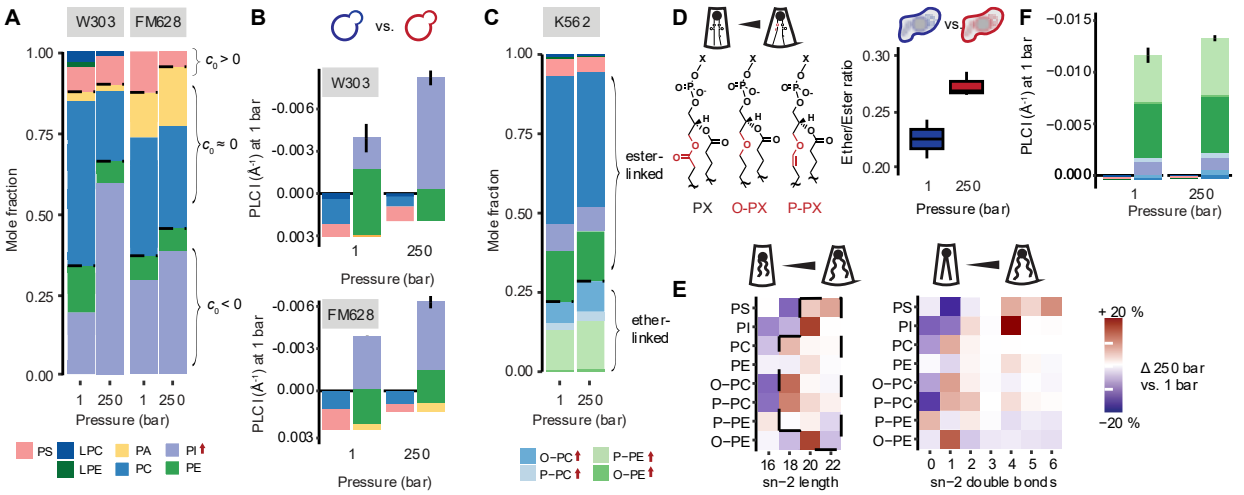

Figure 3.4 Homeocurvature acclimation across cell types.

(A) Phospholipid abundances of *S. cerevisiae* W303 and *L. kluyveri* FM628 from $N = 3$ cultures grown at 1 and 250 bar pressure. (**B**) PLCI of W303 and FM628 after growth at 1 or 250 bar. The y-axis is inverted to emphasize increases in negative c_0. Individual lipid contributions to positive c_0 are plotted to the left, and those contributing to negative curvature on the right. The latter are offset by the contribution of the former to show the change in net PLCI. Error bars indicate SEM, N = 3. P = 0.013 (W303, top), P = 0.027 (FM628, bottom); unpaired one-tailed t-test. (**C**) Phospholipid classes of K562 incubated at 1 or 250 bar. Ether-linked lipids (P-PE, O-PE, O-PC, and P-PC) increase in abundance. (**D**) Structures of ester (PX), alkyl ether (O-PX), and vinyl ether (P-PX) phospholipids, whose abundance compared to ester-linked lipids increases with pressure (right). Error bars indicate SEM from N = 3 cultures. P = 0.047, unpaired two-tailed t-test. (**E**) Heatmaps showing increases (red) in K562 phospholipids with longer (right) and more unsaturated (left) sn-2 chains in cells grown at 250 bar. These correspond to decreases in shorter and more saturated chains (blue). The dashed box highlights longer-chain species that specifically promote negative curvature. (**F**) PLCI analysis for K562 shows higher negative lipidome curvature at 250 bar. Error bars indicate SEM from N = 3 cultures. P = 0.054, unpaired one-tailed t-test.

Discussion

Non-bilayer phospholipids are regulated during the cell cycle(2, 22, 45) and in response to metabolic perturbations(20). However, it has not been shown whether their regulation is in response to curvature stress itself and if cells directly sense the shape of their phospholipids. To address this, we employed hydrostatic pressure as a tool to directly perturb phospholipid intrinsic curvature. We find that cells can respond by increasing curvature-promoting chemical features across the phospholipidome. Acclimation of phospholipids showed a tendency to overshoot with

respect to curvature: the estimated compensatory change of PLCI was between 1.5- (K562) to 3- (W303) fold higher than the change of c_0 we previously observed in model lipids like DOPE at 250 bar(23). Such an overcompensation was previously observed in native lipidome adaptation across deep-sea ctenophores(23) and transiently during cold acclimation in bacteria(12). Overshoot could result from a need for phospholipids to compensate for other membrane components – including transmembrane protein domains and sphingolipids – that inhibit non-lamellar topologies but are not amenable to metabolic acclimation. While we were not able to incorporate the curvature contribution of LPI into PLCI calculations, as its curvature has not yet been determined, the observed LPI increase in *S. cerevisiae* may act to buffer overshoot through PI metabolism. Importantly, our analyses did not account for subcellular compositions, asymmetric distributions across bilayer leaflets, or changes to membrane proteins. It is likely that maintenance of curvature stress at such specific sites within cells drives a global lipidome response. Our calculations also do not account for the effects of monovalent and divalent cations, the latter of which can have strong effects on anionic phospholipids. Nonetheless, whole cell lipidomes assessed under single solvent conditions yield general acclimatory trends that are likely to be relevant across different compartments.

Cells analyzed here show a range of responses that underlie curvature regulation. In yeast, high pressure increases levels of PI, a lipid that has been observed to promote the Q_{II} phase in mixtures with PC(36), but whose curvature had not been previously determined leading to disagreement over its classification as a non-bilayer lipid(3, 46). We found that PI features a negative curvature and promotes membrane fusion similar to non-bilayer lipids. It is important to note that our measurements of PI curvature were conducted only with Na^+ counterions, but additional monovalent and divalent cations can further enhance the negative curvature of anionic

lipids(47). The anionic nature of PI and its bulky headgroup would argue against a negative intrinsic curvature. However, NMR and neutron diffraction measurements show that PI's inositol takes on extended conformations from the bilayer plane that maximize intra- and inter-molecular hydrogen bonding and reduce bulk proximal to the bilayer(48–51). Hydrogen bonding between lipids contributes to negative curvature(52) and is a feature of sugar-containing lipids that form non-lamellar phases(53–55). Although PI has only a moderate negative curvature, it does not show the high ordering and melting temperature of PE(14, 56), suggesting a rationale for why its abundance is modulated more widely by *S. cerevisiae*. Consistent with this model, PI substitutes for PE in yeast engineered to have highly saturated acyl chains(57). In both *L. kluyveri* and mammalian cells, PUFA chains could help to mitigate the high T_m of PE, potentially allowing it to serve as a more dominant curvature modulator. Mammalian lipidomes additionally feature ether linkages as structural features that contribute to curvature(23), membrane fusion(8), and plasma membrane invaginations(58), roles that could be relevant to their dysregulation in metabolic disorders and neurodegenerative diseases(59, 60).

In addition to the eukaryotic lipidome changes reported here, acclimatory responses to maintain lipid curvatures were previously proposed from measurements of the H_{II} transition temperatures in bacterial lipids(19). Even though synthetic manipulation of lipidome curvature modulates *E. coli* high-pressure fitness(23), we find that its lipidome does not show a curvature response to high-pressure, suggesting that it is not regulated intrinsic curvature itself. Given that the pressure-regulated lipid classes we observed are features of eukaryotic lipidomes, it is possible that curvature-based regulation is found only in some bacteria(34, 61). Eukaryotic cells rely on membrane trafficking networks that depend on the ability of membranes to undergo fission and

fusion, processes strongly dependent on lipid curvature. Maintaining membrane properties to support these dynamics could have driven the evolution of eukaryotic phospholipid metabolism.

Since terrestrial organisms are unlikely to have evolved *bona fide* hydrostatic pressure sensors, acclimation reported here is likely to be driven by changes in the curvature frustration of cell membranes. An outstanding question includes the mechanisms by which these changes are sensed and regulate lipid metabolism. Choline cytidylyltransferase (CCT), which catalyzes the committed step in PC synthesis is inhibited by LPC but stimulated by PE or DAG, suggesting that it is regulated by curvature stress(62–64), and may explain the reduction in PC of pressure-treated cells. Low PC synthesis derepresses expression of *INO1(65)*, which encodes for inositol-3-phosphate synthase (Ino1) that catalyzes the first step of PI synthesis. Earlier studies showed a stimulation of *INO1* expression in pressure-treated yeast cells(66), consistent with this model for its regulation. Other mechanisms for the curvature regulation observed here are less clear. The Lands cycle generates tissue-specific acyl chain compositions in mammals(67), but few studies have investigated if its enzymes are regulated by the membrane's physical state. Similarly, regulation of ether lipid metabolism – a complex pathway occurring across both the peroxisome and the ER – has yet to be elucidated. Pressure, as a physical modulator of intrinsic curvature, represents an attractive experimental tool to identify these points of regulation.

Methods

Yeast strains and growth conditions

All *S. cerevisiae* strains used in this study are described in Supplementary Table 1. Cells were grown in complete supplement mixture (CSM) (0.5% Ammonium Sulfate, 0.17% yeast nitrogen base without amino acids and 2% glucose) lacking amino acids as appropriate for

selection. Amino acid concentrations in CSM-his (Sunrise Science Products) media consisted of 50 mg/L L-Arginine, 80 mg/L L-Aspartic Acid, 50 mg/L L-Isoleucine, 100 mg/L L-Leucine, 50 mg/L L-Lysine hydrochloride, 20 mg/L L-methionine, 50 mg/L L-Phenylalinine, 100 mg/L L-Threonine, 50 mg/L Tryptophan, 50 mg/L L-Tyrosine, and 140 mg/L L-Valine. 20 mg/L L-Histidine hydrochloride monohydrate was added when necessary to make complete CSM media. Yeast mutants were generated by PCR-based homologous recombination, ORFs *(PSD1, PEM2)* were replaced by *HIS3*. For standard incubations, cells were grown overnight at 30°C in a temperature-controlled shaker (200 RPM) in yeast extract-peptone-dextrose (YPD) medium using 14 mL culture tubes (18 mm diameter) with a snap/vent cap (Greiner). Cells were then back-diluted into 5 mL fresh CSM and grown until late-exponential phase (OD 1-1.5) prior to analysis. To partially rescue PE deficiency in the *psd1*Δ strain, 2 mM choline was supplemented in CSM media.

For high-pressure cell fitness and lipidomics analyses (Figures 1, 3, and 4A-B), cultures were pre-incubated in YPD in a shaker overnight at 30°C. Samples were then back-diluted to OD 0.1 in CSM containing 2% glucose and loaded into sterile polyethylene 4.5 mL transfer pipettes (Thermo Scientific), the bulbs of which were subsequently heat-sealed with a manual impulse sealer (YXQ)(68). The bulbs containing cultures were then loaded into each of two stainless steel pressure vessels (69) filled with distilled water and pre-warmed to 30°C. A manual rotary pump (High Pressure Equipment Co.) was used to bring one vessel to 250 bar, and a second was left at ambient pressure as a 1 bar control. All pressure vessels were clamped horizontally to an orbital shaker and shaken at 250 RPM overnight at 30°C. Following high-pressure incubation, vessels were decompressed over the course of ~30s. OD_{600} was measured for all replicate cultures of each strain at each pressure and a qualitative survival screen was performed as follows. Each culture was serially diluted fivefold, yielding aliquots that were 5^0- to 5^5-fold dilutions of the

decompressed culture. Six sets of these were transferred to a YPD agar plate using a 48-pin tool (V&P Scientific) and each plate was incubated at 30°C for approximately 24 h, then photographed. The remainder of each decompressed culture was pelleted at 3000 RCF, 5 min at 25°C and frozen at -80°C. Total lipids were later extracted from the frozen pellets by the Bligh-Dyer method(70) and samples incubated at 1 and 250 bar were analyzed as described below.

For high-pressure biophysical analyses (Fig. 2), single colony cultures were pre-incubated in YPD in a shaker overnight at 30°C. Samples were then back-diluted 1:100 into 2.5 L YPD in bleach-sterilized bags made from Mylar tube stock containing a magnetic stir bar. The bags were heat-sealed with a manual impulse sealer, leaving zero headspace. The cultures were loaded into custom-built 4 L titanium pressure vessels filled with distilled water and prewarmed to 30°C using water jackets. One of the pressure vessels was brought to 250 bar hydrostatic pressure using a manual hydraulic hand pump (Enerpac). Cultures were incubated overnight at 30°C with stirring at ~200 RPM. Following high-pressure incubation, the 250-bar vessel was decompressed and the bag contents of the culture bag were pelleted at 3000 RCF and 25°C. Pellets were flash frozen, total lipids were extracted by the Bligh-Dyer method and samples incubated at 1 and 250 bar were analyzed as described below.

Mammalian cell culture and pressure incubation

K562 cells (ATCC) were grown and maintained in Iscove's Modified Dulbecco's Medium (IMDM; Gibco) supplemented with 1% penicillin-streptomycin (Gibco) and 10% fetal bovine serum (Gibco). For pressure incubation, N=3 sterile transfer pipette bulbs were filled with 4 mL of K562 cells at ~7.5 x 10^6 cells/mL. After eliminating air bubbles, the bulbs were heat-sealed as described above and loaded into pressure vessels filled with water and pre-warmed to 37°C. A manual rotary pump (High Pressure Equipment Co.) was used to pressurize one vessel to 250 bar;

the other was left at ambient pressure as a 1 bar control. Both pressure vessels were incubated at 37°C for 6 h, after which the 250-bar vessel was decompressed over ~30 s. OD_{600} was measured for all three replicates at each pressure. Each decompressed culture was pelleted at 3000 RCF for 5 min at 25°C and frozen at -80°C. Total lipids were later extracted from the frozen pellets and analyzed as described below.

Bacterial cell culture and pressure incubation

Starter cultures of MG1655 (K12) *E. coli* were grown in LB + 50 mg/L kanamycin (Kn) while shaking at 250 RPM, overnight at 37°C. Following this period, all cultures were normalized to OD_{600} = 0.2 using the same medium and 3 mL aliquots were loaded into 5 mL polypropylene syringes each containing three 3 mm glass beads for agitation. Gas was manually purged from the syringes and each was sealed with a Luer-lock cap. Three syringes containing each strain were loaded into pressure vessels filled with distilled water and pre-warmed to 37°C. A manual rotary pump (High Pressure Equipment Co.) was used to pressurize one vessel to 250 bar and the other was left at ambient pressure as a 1 bar control. The pressure vessels were clamped horizontally to an orbital shaker and shaken at 250 RPM for 48 h at 37°C. Following high-pressure incubation, vessels were decompressed over the course of ~30 s. OD_{600} was measured for all three replicate cultures each pressure. Each decompressed culture was pelleted at 3000 RCF for 5 min at 25°C and frozen at -80°C. Total lipids were later extracted from the frozen pellets by the Bligh-Dyer method and samples incubated at 1 and 250 bar were analyzed as described below.

Lipidomic analyses

Mass spectrometry-based analysis of yeast phospholipids (Figures 1, 3, 4A-B; Supp. Fig. 3) was performed by Lipotype GmbH (Dresden, Germany) as described(71). Lipids were extracted using a chloroform/methanol procedure(72). Samples were spiked with internal lipid standard

mixture containing: diacylglycerol 17:0/17:0 (DAG), ergosterol ester 13:0 (EE), phosphatidate 17:0/14:1 (PA), phosphatidylcholine 17:0/14:1 (PC), phosphatidylethanolamine 17:0/14:1 (PE), phosphatidylglycerol 17:0/14:1 (PG), phosphatidylinositol 17:0/14:1 (PI), phosphatidylserine 17:0/14:1 (PS) and triacylglycerol 17:0/17:0/17:0 (TAG). After extraction, the organic phase was transferred to an infusion plate and dried in a speed vacuum concentrator. The dry extract was re-suspended in 7.5 mM ammonium formate in chloroform/methanol/propanol (1:2:4; v:v:v). All liquid handling steps were performed using the Hamilton Robotics STARlet robotic platform with the Anti Droplet Control feature for organic solvent pipetting. Samples were analyzed by direct infusion on a Q Exactive mass spectrometer (Thermo Scientific) equipped with a TriVersa NanoMate ion source (Advion Biosciences). Samples were analyzed in both positive and negative ion modes with a resolution of $R_{m/z=200}$=280,000 for MS^1 and $R_{m/z=200}$=17,500 for MS^2 experiments, in a single acquisition. MS^2 was triggered by an inclusion list encompassing corresponding MS mass ranges scanned in 1 Da increments(73). Both MS^1 and MS^2 data were combined to monitor EE, DAG and TAG ions as ammonium adducts; PC as formate adducts and PA, PE, PG, PI and PS as deprotonated anions. Data were analyzed using LipotypeXplorer, a proprietary software developed by Lipotype GmbH, which is based on LipidXplorer(74, 75). Data post-processing and normalization were performed using an in-house developed data management system. Only lipid identifications with a signal-to-noise ratio >5, and a signal intensity 5-fold higher than in corresponding blank samples were considered for further data analysis.

Mass spectrometry-based analysis of MG1655 and K562 phospholipids was performed as previously described(23). Lipid extracts were brought to dryness and reconstituted in 18:1:1 v:v:v IPrOH:CH_2Cl_2:MeOH containing deuterated internal standard (Avanti) for each of the 11 lipid classes analyzed, which include the major classes of phospholipids. These allow for semi-

quantification of species within these classes. Other potentially present lipid species, such as ceramide derivatives, glycosylated lipids, and non-sterol terpenes, were not quantified using this method. Polar lipids were measured according to a previously described method(76), with slight modifications. The Vanquish UHPLC (Thermo Fisher Scientific) was interfaced with a Q Exactive mass spectrometer (Thermo Fisher Scientific). A Waters T3 1.6 µM 2.1 mm x 150 mm column was used for chromatographic separation using a step gradient from 25% buffer A (10 mM ammonium formate and 0.1% formic acid in water) to 100% buffer B (70/30 v/v isopropanol/acetonitrile with 10 mM ammonium formate and 0.1% formic acid) over 35 min. Flow rate was set at 0.3 mL/min. Lipid samples were analyzed using data-dependent acquisition (DDA) with an NCE of 30 in negative mode and an NCE of 25 in positive mode. Ion source parameters were: Sheath Gas 48 AU; Aux Gas 11 AU; Sweet Gas 1 AU; Spray Voltage 3.5 kV for positive mode and 2.5 kV for negative mode; Capillary Temp. 250°C; S-lens RF level 60 AU; Aux Gas Heater Temp. 413°C. All ions in the mass range of 200-1200 m/z were monitored. MS^1 resolution was set at $R_{m/z=200}$=70,000 with an automatic gain control (AGC) target of 1e6 and Maximum IT of 200 ms. For MS^2, $R_{m/z=200}$=17,500 with an AGC target of 5e4, fixed first mass of 80 m/z, and Maximum IT of 50 ms. The isolation width was set at 1.2; Dynamic Exclusion was set at 3 s. Lipids were identified and quantified with Lipid Data Analyzer Software(77). All data were analyzed from normalized intensities relative to exactly measured internal deuterated standards (SPLASH LIPIDOMIX, Avanti Polar Lipids).

Due to identical fragmentation patterns, plasmanyl phosphatidylethanolamine (O-PE) and plasmenyl phosphatidylethanolamine (P-PE) species were manually separated by retention time after Lipid Data Analyzer identification of P-PE species based on MS^2 fragmentation products: PE head group (m/z = 196.038), carboxy fragment (m/z dependent on chain length), and alkenyl sn-1

chain fragment (m/z = 239.235, 265.253; dependent on chain length). It was possible to distinguish O-PE based on retention time following the principle that alkyl ether species elute sooner than their corresponding vinyl ether counterparts, putatively due to differences in H-bonding imparted by the cis-alkene bond.

To calculate PLCI from lipidomic data on phospholipids, c0operate scripts(78) were used based on inputted lipidomic data and literature values of phospholipid intrinsic curvatures(79) as previously described(23, 34).

Sterol extraction and analysis

Measurement of sterol abundances from cells was carried out as previously described (80). Briefly, cells following pressure incubation were washed with PBS, resuspended in 1 mL Milli-Q water, and spiked with internal standard (cholesterol for yeast or ergosterol for K562 cells). Glass beads (1 mL) were added to lyse cells, and the resulting cell lysate was then transferred to a 15 mL conical glass with a Teflon cap. Methanolic KOH (3 mL) was added and the mixture was incubated at 70°C for 2 h. Following cooling, 3 mL of *n*-hexane was added, vortexed for 10 s, and then centrifuged at room temperature for 5 min at 800 rpm. The upper organic phase was then transferred to a clean conical glass tube. A second extraction of the aqueous phase was performed, and the resulting organic phase was combined. The n-hexane was evaporated under a stream of nitrogen at 60°. The resulting film was dissolved in a 1:1 solution of pyridine and trimethylchlorosilane and incubated at 70°C for 1 h for derivatization. Extracts were analyzed by gas chromatography–mass spectrometry (GC-MS) as follows. Samples were injected into a 30 -m DB-5 column in an Agilent 8890 GC coupled to a 5977B mass analyzer. The GC oven was operated with the following temperature program: initial temperature of 120°C held for 1 min,

ramped at 20°C per min to 270°C, followed by an additional ramp at 2°C per min to 290°C, and then a final ramp at 20°C per min to 300°C and held for 2 min. The identities of target compounds were initially checked against the NIST17 mass spectral library using NIST MS Search software. For quantification, sterol levels were calculated relative to a calibration curve of a cholesterol or ergosterol external standard and adjusted according to the extraction efficiency for each sample. Extraction efficiency was determined on a percent recovery basis of internal standard per sample.

SAXS sample preparation

For preparation of SAXS samples using pure or synthetic lipids including DOPE, Soy PI, and DOPI (Avanti Polar Lipids). Total lipid extracts from yeast were separated into polar lipids and neutral fractions on 500 mg prepacked silica columns (Thermo Scientific) using a previously validated method(81). Polar lipids eluted in approximately 20 mL $CHCl_3$ were dried and weighed in tared 2 mL vials. For SAXS analysis, 5 mg polar lipids were dissolved in 100 µL cyclohexane (C_6H_{12}, Fisher Chemical). Alternatively, for preparation of SAXS samples using pure or synthetic lipids including DOPE, Soy PI (sodium salt), and DOPI (sodium Salt) (Avanti Polar Lipids), 5 mg of total lipid in chloroform was similarly evaporated under nitrogen gas and dissolved in 100 µL cyclohexane. 50 µL aliquots were transferred to 1.5 mm ID capillary melting point tubes (Kimble Chase 34505-99), frozen at -80°C, and lyophilized for 1h. Samples were rehydrated by the addition of 10 µL vacuum-degassed MilliQ water, then subjected to five rounds of freeze-thaw in an isopropanol-dry ice bath and homogenization with a 20 µL Wiretrol II microdispenser (Drummond Scientific) inside the melting point tube. The bottom of the tube was then scored, cut, and carefully wiped, and the suspension inside transferred to a disposable sample holder(82). This thick suspension (50% w/v lipid) was settled to the bottom of the holder centrifugation (500 RCF, 5 min

at 4°C) and topped with another 5 µL degassed water to ensure full hydration. A 22G x 100 mm needle (Air-Tite) was then used to add a pressure-transmitting cap of high vacuum grease (Dow Corning) to the top of the water. Final samples were composed of 250mg/ml lipids and samples containing Soy PI or DOPI contained 33 mM Na^+ as a result of the anionic lipids being utilized as sodium salts.

SAXS data acquisition and analysis

HPSAXS data were collected on beamline 7A at the Cornell High Energy Synchrotron Source using a custom-built temperature-controlled pressure cell(82). Photon energy was 14 keV, spot size was 200 x 250 µm (W x H), and scattering data were collected for $0.005\ Å^{-1} \leq q \leq 0.7\ Å^{-1}$ using an EIGER 4M detector (Dectris) within the beamline vacuum. 1 s exposures were taken at a flux of $1.8\text{-}3.6 \times 10^{11}$ photons/s. Five initial exposures were used to test each sample for radiation sensitivity, then pressure or temperature up- and down-sweeps were made starting at the lowest temperature or pressure and proceeding to the highest. The sample was equilibrated for at least 60 s per 100 bar of pressure change and for 30 min following each 5°C change in temperature. Because photon scattering by the lipid dispersions was strong and background was low (as assessed by shooting a sealed capillary containing the same degassed water used to hydrate the lipids), no background subtraction was used. SAXS images were azimuthally integrated using BIOXTAS RAW software(83). To determine midpoints of barotrophic phase diagrams, presence of phase signatures of L_α, L_β, Q_{II}, was identified. Midpoints of phases represent ½ of the maximum pressure under which the phase could be identified and the ratio of all phases identified at the midpoint.

Measurement of phospholipid monolayer curvature

For c_0 measurements, pure lipids were prepared as hosted mixtures in DOPE at a molar ratio of 10 mol%:90 mol% guest:host for HPSAXS, as described above. 10 mol% Soy PI or DOPI samples contained 33 mM Na^+ as a result of the anionic lipids being utilized as sodium salts. 12% w/w 9(Z)-tricosene was added to relax the H_{II} phase and c_0 was calculated from peak spacing as previously described(84). Neutral-plane c_0 was estimated by using a constant distance correction of 3.94 Å, derived from global fitting of the H_{II} scattering profile of DOPE(85). For yeast polar lipid samples, tricosene was not added and the H_{II} peak spacing was used to calculate unrelaxed curvature c in the same way as c_0. The curvature of guest lipids was determined from a weighted average of the total curvature of the guest in the hosted system.

C-Laurdan GP determination and analysis

The same polar lipid extracts used for HPSAXS analysis were used to analyze lipid packing via the general polarization (GP) of the C-Laurdan solvatochromic probe. HPFS was used to measure general polarization (GP) across a temperature-pressure grid. Polar lipid dispersions were made by drying lipid films under N_2 and high vacuum for 30 min, then resuspending them in buffer (20 mM HEPES, 2 mM EDTA, pH 7.4) to concentrations of approximately 1 mM lipid. Samples were then subjected to 4X freeze-thaw cycles and subsequently extruded using a hand-held device (Avanti Polar Lipids) incorporating a 200 nm polycarbonate track-etch filter (Whatman) at room temperature. The resultant unilamellar vesicles were stained with 2.5 μM C-Laurdan and tumbled for 30 min at room temperature. Vesicles were then loaded into a quartz cuvette and analyzed in a high-pressure optical cell (ISS Inc.) connected to a 65x SyriXus syringe pressure pump (Teledyne ISCO) and a water bath (NESLAB) for automated pressure and temperature control coordinated

by a PC running a Python script(86). The pressure cell was mounted in a Cary Eclipse fluorospectrometer (Agilent Cary). An excitation wavelength of 340 nm was used with the multiwavelength setting acquiring dual emission wavelengths of 440 nm and 490 nm with a 2.5 nm excitation slit and a 5 nm emission slit. Fluorescence data were collected in Kinetics mode concurrent with automated traversal of the temperature-pressure grid. Timestamps were used to co-register temperature and pressure with fluorescence data, which were then analyzed using R scripts.

Live cell imaging

After pressure incubation, as described above, yeast and K562 cells were washed with PBS and stained with 5 μM C-Laurdan in PBS for 20 minutes at 30°C for yeast or 37°C for K562 cells. C-Laurdan stains lipid membranes and has no fluorescence in aqueous solution. After staining, cells were put on 8-well cell slides and imaged on an LSM 880 confocal microscope (Zeiss) with a 63x/1.4 Plan-Apochromat oil objective. Images were acquired in two emission windows (418 – 464 nm and 481 – 517 nm) upon excitation with a 405 nm laser line. Cells incubated at 250 bar were imaged first to minimize recovery time following depressurization.

Lipid mixing fusion assay

A FRET-based lipid mixing assay was performed to compare fusion rates by fluorescence dequenching of liposomes with equimolar POPC, POPS, and Soy PI, POPE, or POPG (Avanti Polar Lipids). As a negative control, a condition with only equimolar POPS and POPC was tested. Lipid stocks in chloroform were mixed in equimolar amounts. The chloroform was evaporated to form thin lipid films using N_2 for 10 min and subsequently kept under high vacuum for ≥1 h to

remove residual organic solvent. The lipid film was hydrated with Buffer A (100 mM NaCl, 5 mM Na^+ HEPES, 0.1 mM EDTA, pH 7.4) and tumbled for 1 h. To form unilamellar 200 nm vesicles, the lipid dispersions were subjected to 4 freeze-thaw cycles and extrusion through a 200 nm membrane 21 times. One population of fluorescence-quenched liposomes, containing Rh-DOPE (2 mol %) and NBD-DOPE (2 mol %) with POPE/POPC/POPS (32:32:32), Soy PI/POPC/POPS (32:32:32), POPG/POPC/POPS (32:32:32), or POPC/POPS (64:32) (Avanti Polar Lipids), were mixed with a population of liposomes lacking fluorophores with (33:33:33), Soy PI/POPC/POPS (33:33:33), POPG/POPC/POPS (33:33:33), or POPC/POPS (68:32). The emission of NBD-PE dequenching was measured following the addition of 10 mM $CaCl_2$ using a Cary Eclipse spectrofluorometer set to 463/536 nm excitation/emission at 37°C. Fluorescence intensity was recorded in Kinetics mode for 5 min to allow reactions to reach equilibrium. Fluorescence of a fully dequenched control, with 1 mol% NBD-DOPE and 1 mM Rh-DOPE in POPE/POPC/POPS (32.65: 32.65: 32.65), Soy PI/POPC/POPS (32.65: 32.65: 32.65), POPG/POPC/POPS (32.65: 32.65: 32.65), or POPC/POPS (66:32), was recorded to permit normalization and determination of total % fused vesicles.

Acknowledgements

The material in this chapter, in full, is a reprint of the material as it appears in "Homeostatic regulation of intrinsic lipid curvature in eukaryotic cells". Milshteyn, Daniel; Winnikoff, Jacob R; Kocharian, Elida; Armando, Aaron M; Dennis, Edward A; Girguis, Peter R; Budin, Itay. *Cell Reports Physical Science*. 2026. The dissertation author was a primary investigator and first author of this paper. Alexander Sodt and Edward Lyman contributed helpful discussions. Kailash Venkatraman provided experimental support and comments. Richard Gililan and Qingqiu Huang

assisted in beamline measurements. Research was funded by the National Science Foundation (NSF) (MCB-2046303 and MCB-2316458 to I.B.), the Office of Naval Research (N00014-23-1-2543 to I.B.), the National Institutes of Health (NIH) (5T32EB009380-14 to D.M., GM139641 to E.A.D., GM142960 to I.B.), and NASA (postdoctoral fellowship 0017-NPP-MAR22-A-Astrobio to J.R.W.). SAXS measurements were performed at the Center for High-Energy X-ray Sciences (CHEXS), which is supported by the NSF award DMR-2342336, and the MacCHESS resource is supported by NIH award 1-P30-GM124166.

References

1. Koynova, R., and M. Caffrey. 1994. Phases and phase transitions of the hydrated phosphatidylethanolamines. *Chem. Phys. Lipids*. 69:1–34.

2. Dymond, M.K. 2016. Mammalian phospholipid homeostasis: evidence that membrane curvature elastic stress drives homeoviscous adaptation in vivo. *J. R. Soc. Interface*. 13.

3. Basu Ball, W., J.K. Neff, and V.M. Gohil. 2018. The role of nonbilayer phospholipids in mitochondrial structure and function. *FEBS Lett.* 592:1273–1290.

4. Brown, M.F. 2012. Curvature forces in membrane lipid-protein interactions. *Biochemistry*. 51:9782–9795.

5. Escribá, P.V., A. Ozaita, C. Ribas, A. Miralles, E. Fodor, T. Farkas, and J.A. García-Sevilla. 1997. Role of lipid polymorphism in G protein-membrane interactions: nonlamellar-prone phospholipids and peripheral protein binding to membranes. *Proc. Natl. Acad. Sci. U. S. A.* 94:11375–11380.

6. Kinnunen, P.K.J. 1996. On the molecular-level mechanisms of peripheral protein-membrane interactions induced by lipids forming inverted non-lamellar phases. *Chem. Phys. Lipids*. 81:151–166.

7. Gilbert, R.J.C. 2016. Protein-lipid interactions and non-lamellar lipidic structures in membrane pore formation and membrane fusion. *Biochim. Biophys. Acta*. 1858:487–499.

8. Glaser, P.E., and R.W. Gross. 1994. Plasmenylethanolamine facilitates rapid membrane fusion: a stopped-flow kinetic investigation correlating the propensity of a major plasma membrane constituent to adopt an HII phase with its ability to promote membrane fusion. *Biochemistry*. 33:5805–5812.

9. Gruner, S.M. 1985. Intrinsic curvature hypothesis for biomembrane lipid composition: a role for nonbilayer lipids. *Proc. Natl. Acad. Sci. U. S. A.* 82:3665–3669.

10. de Kruijff, B. 1997. Lipid polymorphism and biomembrane function. *Curr. Opin. Chem. Biol.* 1:564–569.

11. Kim, H., and I. Budin. 2024. Intracellular sphingolipid sorting drives membrane phase separation in the yeast vacuole. *J. Biol. Chem.* 300:105496.

12. Hoogerland, L., S.P.H. van den Berg, Y. Suo, Y.W. Moriuchi, A. Zoumaro-Djayoon, E. Geurken, F. Yang, F. Bruggeman, M.D. Burkart, and G. Bokinsky. 2024. A temperature-sensitive metabolic valve and a transcriptional feedback loop drive rapid homeoviscous adaptation in Escherichia coli. *Nat. Commun.* 15:9386.

13. Covino, R., S. Ballweg, C. Stordeur, J.B. Michaelis, K. Puth, F. Wernig, A. Bahrami, A.M. Ernst, G. Hummer, and R. Ernst. 2016. A Eukaryotic Sensor for Membrane Lipid Saturation. *Mol. Cell*. 63:49–59.

14. Dawaliby, R., C. Trubbia, C. Delporte, C. Noyon, J.-M. Ruysschaert, P. Van Antwerpen, and C. Govaerts. 2016. Phosphatidylethanolamine is a key regulator of membrane fluidity in eukaryotic cells. *J. Biol. Chem.* 291:3658–3667.

15. Levental, K.R., E. Malmberg, J.L. Symons, Y.-Y. Fan, R.S. Chapkin, R. Ernst, and I. Levental. 2020. Lipidomic and biophysical homeostasis of mammalian membranes counteracts dietary lipid perturbations to maintain cellular fitness. *Nat. Commun.* 11:1339.

16. Ballweg, S., E. Sezgin, M. Doktorova, R. Covino, J. Reinhard, D. Wunnicke, I. Hänelt, I. Levental, G. Hummer, and R. Ernst. 2020. Regulation of lipid saturation without sensing membrane fluidity. *Nat. Commun.* 11:1–13.

17. Cybulski, L.E., J. Ballering, A. Moussatova, M.E. Inda, D.B. Vazquez, T.A. Wassenaar, D. de Mendoza, D.P. Tieleman, and J.A. Killian. 2015. Activation of the bacterial thermosensor DesK involves a serine zipper dimerization motif that is modulated by bilayer thickness. *Proc. Natl. Acad. Sci. U. S. A.* 112:6353–6358.

18. Budin, I., T. de Rond, Y. Chen, L.J.G. Chan, C.J. Petzold, and J.D. Keasling. 2018. Viscous control of cellular respiration by membrane lipid composition. *Science*. 362:1186–1189.

19. Morein, S., A. Andersson, L. Rilfors, and G. Lindblom. 1996. Wild-type Escherichia coli cells regulate the membrane lipid composition in a "window" between gel and non-lamellar structures. *J. Biol. Chem.* 271:6801–6809.

20. Bao, X., M.C. Koorengevel, M.J.A. Groot Koerkamp, A. Homavar, A. Weijn, S. Crielaard, M.F. Renne, J.H. Lorent, W.J. Geerts, M.A. Surma, M. Mari, F.C.P. Holstege, C. Klose, and A.I.P.M. de Kroon. 2021. Shortening of membrane lipid acyl chains compensates for phosphatidylcholine deficiency in choline-auxotroph yeast. *EMBO J.* 40:e107966.

21. Attard, G.S., R.H. Templer, W.S. Smith, A.N. Hunt, and S. Jackowski. 2000. Modulation of CTP:phosphocholine cytidylyltransferase by membrane curvature elastic stress. *Proc. Natl. Acad. Sci. U. S. A.* 97:9032–9036.

22. Boumann, H.A., J. Gubbens, M.C. Koorengevel, C.-S. Oh, C.E. Martin, A.J.R. Heck, J.

Patton-Vogt, S.A. Henry, B. de Kruijff, and A.I.P.M. de Kroon. 2006. Depletion of phosphatidylcholine in yeast induces shortening and increased saturation of the lipid acyl chains: evidence for regulation of intrinsic membrane curvature in a eukaryote. *Mol. Biol. Cell*. 17:1006–1017.

23. Winnikoff, J.R., D. Milshteyn, S.J. Vargas-Urbano, M.A. Pedraza-Joya, A.M. Armando, O. Quehenberger, A. Sodt, R.E. Gillilan, E.A. Dennis, E. Lyman, S.H.D. Haddock, and I. Budin. 2024. Homeocurvature adaptation of phospholipids to pressure in deep-sea invertebrates. *Science*. 384:1482–1488.

24. So, P.T., S.M. Gruner, and S. Erramilli. 1993. Pressure-induced topological phase transitions in membranes. *Phys. Rev. Lett.* 70:3455–3458.

25. Shyamsunder, E., P. Botos, and S.M. Gruner. 1989. Comment on: X-ray diffraction study of the effects of pressure on bilayer to nonbilayer lipid membrane phase transitions. *J. Chem. Phys.* 90:1293–1295.

26. Winnikoff, J.R., S.H.D. Haddock, and I. Budin. 2021. Depth- and temperature-specific fatty acid adaptations in ctenophores from extreme habitats. *J. Exp. Biol.* 224.

27. Mishra, S., and H. Chakraborty. 2023. Phosphatidylethanolamine and Cholesterol Promote Hemifusion Formation: A Tug of War between Membrane Interfacial Order and Intrinsic Negative Curvature of Lipids. *The Journal of Physical Chemistry B*.

28. Baker, C.D., W. Basu Ball, E.N. Pryce, and V.M. Gohil. 2016. Specific requirements of nonbilayer phospholipids in mitochondrial respiratory chain function and formation. *Mol. Biol. Cell*. 27:2161–2171.

29. Kodaki, T., and S. Yamashita. 1987. Yeast phosphatidylethanolamine methylation pathway. Cloning and characterization of two distinct methyltransferase genes. *J. Biol. Chem.* 262:15428–15435.

30. Gruner, S.M., M.W. Tate, G.L. Kirk, P.T. So, D.C. Turner, D.T. Keane, C.P. Tilcock, and P.R. Cullis. 1988. X-ray diffraction study of the polymorphic behavior of N-methylated dioleoylphosphatidylethanolamine. *Biochemistry*. 27:2853–2866.

31. Henry, S.A., S.D. Kohlwein, and G.M. Carman. 2012. Metabolism and regulation of glycerolipids in the yeast Saccharomyces cerevisiae. *Genetics*. 190:317–349.

32. Kim, H.M., H.-J. Choo, S.-Y. Jung, Y.-G. Ko, W.-H. Park, S.-J. Jeon, C.H. Kim, T. Joo, and B.R. Cho. 2007. A two-photon fluorescent probe for lipid raft imaging: C-laurdan. *Chembiochem*. 8:553–559.

33. Rand, R.P., N.L. Fuller, S.M. Gruner, and V.A. Parsegian. 1990. Membrane curvature, lipid segregation, and structural transitions for phospholipids under dual-solvent stress. *Biochemistry*. 29:76–87.

34. Winnikoff, J.R., and I. Budin. 2025. Homeocurvature: A new dimension of membrane adaptation to extreme environments. *Prog. Lipid Res.* 101355.

35. Furse, S., N.J. Brooks, R. Woscholski, P.R.J. Gaffney, and R.H. Templer. 2016. Pressure-dependent inverse bicontinuous cubic phase formation in a phosphatidylinositol 4-phosphate/phosphatidylcholine system. *Chem. Data Coll.* 3-4:15–20.

36. Mulet, X., R.H. Templer, R. Woscholski, and O. Ces. 2008. Evidence that phosphatidylinositol promotes curved membrane interfaces. *Langmuir*. 24:8443–8447.

37. Uster, P.S., and D.W. Deamer. 1981. Fusion competence of phosphatidylserine-containing liposomes quantitatively measured by a fluorescence resonance energy transfer assay. *Arch. Biochem. Biophys.* 209:385–395.

38. Leber, R., M. Pachler, I. Kabelka, I. Svoboda, D. Enkoller, R. Vácha, K. Lohner, and G. Pabst. 2018. Synergism of antimicrobial frog peptides couples to membrane intrinsic curvature strain. *Biophys. J.* 114:1945–1954.

39. Fuller, N., and R.P. Rand. 2001. The influence of lysolipids on the spontaneous curvature and bending elasticity of phospholipid membranes. *Biophys. J.* 81:243–254.

40. Wolfe, K.H., and D.C. Shields. 1997. Molecular evidence for an ancient duplication of the entire yeast genome. *Nature*. 387:708–713.

41. Oura, T., and S. Kajiwara. 2004. Saccharomyces kluyveri FAD3 encodes an omega3 fatty acid desaturase. *Microbiology*. 150:1983–1990.

42. Fuller, N., C.R. Benatti, and R.P. Rand. 2003. Curvature and bending constants for phosphatidylserine-containing membranes. *Biophys. J.* 85:1667–1674.

43. Szule, J.A., N.L. Fuller, and R.P. Rand. 2002. The effects of acyl chain length and saturation of diacylglycerols and phosphatidylcholines on membrane monolayer curvature. *Biophys. J.* 83:977–984.

44. Degreif, D., B. Cucu, I. Budin, G. Thiel, and A. Bertl. 2019. Lipid determinants of endocytosis and exocytosis in budding yeast. *Biochim. Biophys. Acta Mol. Cell Biol. Lipids*. 1864:1005–1016.

45. Yang, S., Y. Wang, S. Huang, T. Zhang, P. Xu, C. Jiang, and C. Ye. 2025. Temporal oscillation of phospholipids promotes metabolic efficiency. *Nat. Chem. Biol.*

46. Nguyen, T.T., and G.K. Voeltz. 2022. An ER phospholipid hydrolase drives ER-associated mitochondrial constriction for fission and fusion. *Elife*. 11:e84279.

47. Chen, Y.-F., K.-Y. Tsang, W.-F. Chang, and Z.-A. Fan. 2015. Differential dependencies on [Ca2+] and temperature of the monolayer spontaneous curvatures of DOPE, DOPA and cardiolipin: effects of modulating the strength of the inter-headgroup repulsion. *Soft Matter*. 11:4041–4053.

48. Hansbro, P.M., S.J. Byard, R.J. Bushby, P.J. Turnbull, N. Boden, M.R. Saunders, R. Novelli, and D.G. Reid. 1992. The conformational behaviour of phosphatidylinositol in model membranes: 2H-NMR studies. *Biochim. Biophys. Acta*. 1112:187–196.

49. Bushby, R.J., S.J. Byard, P.M. Hansbro, and D.G. Reid. 1990. The conformational behaviour of phosphatidylinositol. *Biochim. Biophys. Acta*. 1044:231–236.

50. Bradshaw, J.P., R.J. Bushby, C.C. Giles, M.R. Saunders, and D.G. Reid. 1996. Neutron diffraction reveals the orientation of the headgroup of inositol lipids in model membranes. *Nat. Struct. Biol.* 3:125–127.

51. Bradshaw, J.P., R.J. Bushby, C.C. Giles, and M.R. Saunders. 1999. Orientation of the headgroup of phosphatidylinositol in a model biomembrane as determined by neutron diffraction. *Biochemistry*. 38:8393–8401.

52. Lessen, H.J., K.C. Sapp, A.H. Beaven, R. Ashkar, and A.J. Sodt. 2022. Molecular mechanisms of spontaneous curvature and softening in complex lipid bilayer mixtures. *Biophys. J.* 121:3188–3199.

53. Seddon, J.M., E.A. Bartle, and J. Mingins. 1990. Inverse cubic liquid-crystalline phases of phospholipids and related lyotropic systems. *J. Phys.: Condens. Matter*. 2:SA285–SA290.

54. Lindblom, G., I. Brentel, M. Sjölund, G. Wikander, and A. Wieslander. 1986. Phase equilibria of membrane lipids from Acholeplasma laidlawii: importance of a single lipid forming nonlamellar phases. *Biochemistry*. 25:7502–7510.

55. Larsson, K., K. Fontell, and N. Krog. 1980. Structural relationships between lamellar, cubic and hexagonal phases in monoglyceride-water systems. possibility of cubic structures in biological systems. *Chem. Phys. Lipids*. 27:321–328.

56. Peng, A., D.S. Pisal, A. Doty, and S.V. Balu-Iyer. 2012. Phosphatidylinositol induces fluid phase formation and packing defects in phosphatidylcholine model membranes. *Chem. Phys. Lipids*. 165:15–22.

57. Venkatraman, K., C.T. Lee, G.C. Garcia, A. Mahapatra, D. Milshteyn, G. Perkins, K.-Y. Kim, H.A. Pasolli, S. Phan, J. Lippincott-Schwartz, M.H. Ellisman, P. Rangamani, and I. Budin. 2023. Cristae formation is a mechanical buckling event controlled by the inner mitochondrial membrane lipidome. *EMBO J.* 42:e114054.

58. Wu, Y., Y.-W. Lim, K.-A. McMahon, N. Martel, J. Rae, H.P. Lo, Y. Gao, V. Tillu, E. Larsson, R. Lundmark, D.S. Levic, M. Bagnat, J. Lim, D.P. Fairlie, A. Pol, B.M. Collins, N. Ariotti, T.E. Hall, and R.G. Parton. 2025. Pro-ferroptotic lipids as key control points for caveola formation and disassembly. *Cell Rep.* 44:115789.

59. da Silva, T.F., J. Eira, A.T. Lopes, A.R. Malheiro, V. Sousa, A. Luoma, R.L. Avila, R.J.A. Wanders, W.W. Just, D.A. Kirschner, M.M. Sousa, and P. Brites. 2014. Peripheral nervous system plasmalogens regulate Schwann cell differentiation and myelination. *J. Clin. Invest.* 124:2560–2570.

60. Grapentine, S., and M. Bakovic. 2020. Significance of bilayer-forming phospholipids for skeletal muscle insulin sensitivity and mitochondrial function. *J. Biomed. Res.* 34:1–13.

61. Kaneko, H., H. Takami, A. Inoue, and K. Horikoshi. 2000. Effects of hydrostatic pressure

and temperature on growth and lipid composition of the inner membrane of barotolerant Pseudomonas sp. BT1 isolated from the deep-sea. *Biosci. Biotechnol. Biochem.* 64:72–79.

62. Boggs, K.P., C.O. Rock, and S. Jackowski. 1995. Lysophosphatidylcholine and 1-O-octadecyl-2-O-methyl-rac-glycero-3-phosphocholine inhibit the CDP-choline pathway of phosphatidylcholine synthesis at the CTP:phosphocholine cytidylyltransferase step. *J. Biol. Chem.* 270:7757–7764.

63. Jamil, H., G.M. Hatch, and D.E. Vance. 1993. Evidence that binding of CTP:phosphocholine cytidylyltransferase to membranes in rat hepatocytes is modulated by the ratio of bilayer- to non-bilayer-forming lipids. *Biochem. J.* 291 (Pt 2):419–427.

64. Cornell, R.B. 2016. Membrane lipid compositional sensing by the inducible amphipathic helix of CCT. *Biochim. Biophys. Acta*. 1861:847–861.

65. Griac, P., M.J. Swede, and S.A. Henry. 1996. The role of phosphatidylcholine biosynthesis in the regulation of the INO1 gene of yeast. *J. Biol. Chem.* 271:25692–25698.

66. Iwahashi, H., M. Odani, E. Ishidou, and E. Kitagawa. 2005. Adaptation of Saccharomyces cerevisiae to high hydrostatic pressure causing growth inhibition. *FEBS Lett.* 579:2847–2852.

67. O'Donnell, V.B. 2022. New appreciation for an old pathway: the Lands Cycle moves into new arenas in health and disease. *Biochem. Soc. Trans.* 50:1–11.

68. Lauro, F.M., R.A. Chastain, L.E. Blankenship, A.A. Yayanos, and D.H. Bartlett. 2007. The unique 16S rRNA genes of piezophiles reflect both phylogeny and adaptation. *Appl. Environ. Microbiol.* 73:838–845.

69. Zobell, C.E., and C.H. Oppenheimer. 1950. Some effects of hydrostatic pressure on the multiplication and morphology of marine bacteria. *J. Bacteriol.* 60:771–781.

70. Bligh, E.G., and W.J. Dyer. 1959. A rapid method of total lipid extraction and purification. *Can. J. Biochem. Physiol.* 37:911–917.

71. Surma, M.A., M.J. Gerl, R. Herzog, J. Helppi, K. Simons, and C. Klose. 2021. Mouse lipidomics reveals inherent flexibility of a mammalian lipidome. *Sci. Rep.* 11:19364.

72. Ejsing, C.S., J.L. Sampaio, V. Surendranath, E. Duchoslav, K. Ekroos, R.W. Klemm, K. Simons, and A. Shevchenko. 2009. Global analysis of the yeast lipidome by quantitative shotgun mass spectrometry. *Proc. Natl. Acad. Sci. U. S. A.* 106:2136–2141.

73. Surma, M.A., R. Herzog, A. Vasilj, C. Klose, N. Christinat, D. Morin-Rivron, K. Simons, M. Masoodi, and J.L. Sampaio. 2015. An automated shotgun lipidomics platform for high throughput, comprehensive, and quantitative analysis of blood plasma intact lipids: Automated shotgun lipidomics for blood plasma analysis. *Eur. J. Lipid Sci. Technol.* 117:1540–1549.

74. Herzog, R., D. Schwudke, K. Schuhmann, J.L. Sampaio, S.R. Bornstein, M. Schroeder, and

A. Shevchenko. 2011. A novel informatics concept for high-throughput shotgun lipidomics based on the molecular fragmentation query language. *Genome Biol.* 12:R8.

75. Herzog, R., K. Schuhmann, D. Schwudke, J.L. Sampaio, S.R. Bornstein, M. Schroeder, and A. Shevchenko. 2012. LipidXplorer: a software for consensual cross-platform lipidomics. *PloS one*. 7.

76. Quehenberger, O., A.M. Armando, A.H. Brown, S.B. Milne, D.S. Myers, A.H. Merrill, S. Bandyopadhyay, K.N. Jones, S. Kelly, R.L. Shaner, C.M. Sullards, E. Wang, R.C. Murphy, R.M. Barkley, T.J. Leiker, C.R.H. Raetz, Z. Guan, G.M. Laird, D.A. Six, D.W. Russell, J.G. McDonald, S. Subramaniam, E. Fahy, and E.A. Dennis. 2010. Lipidomics reveals a remarkable diversity of lipids in human plasma. *J. Lipid Res.* 51:3299–3305.

77. Hartler, J., A.M. Armando, M. Trötzmüller, E.A. Dennis, H.C. Köfeler, and O. Quehenberger. 2020. Automated annotation of sphingolipids including accurate identification of hydroxylation sites using MSn data. *Anal. Chem.* 92:14054–14062.

78. Winnikoff, J. c0operate: Quick scripts for estimating mean intrinsic curvature (bar-c0) from lipidomic data. Github.

79. Dymond, M.K. 2021. Lipid monolayer spontaneous curvatures: A collection of published values. *Chem. Phys. Lipids*. 239:105117.

80. Juarez-Contreras, I., L.J.S. Lopes, J. Holt, L. Yu-Liao, K. O'Shea, J. Ruiz-Ruiz, A. Sodt, and I. Budin. 2025. Structural dissection of ergosterol metabolism reveals a pathway optimized for membrane phase separation. *Sci. Adv.* 11:eadu7190.

81. Hamilton, J.G., and K. Comai. 1988. Rapid separation of neutral lipids, free fatty acids and polar lipids using prepacked silica Sep-Pak columns. *Lipids*. 23:1146–1149.

82. Rai, D.K., R.E. Gillilan, Q. Huang, R. Miller, E. Ting, A. Lazarev, M.W. Tate, and S.M. Gruner. 2021. High-pressure small-angle X-ray scattering cell for biological solutions and soft materials. *J. Appl. Crystallogr.* 54:111–122.

83. Hopkins, J.B., R.E. Gillilan, and S. Skou. 2017. *BioXTAS RAW* : improvements to a free open-source program for small-angle X-ray scattering data reduction and analysis. *J. Appl. Crystallogr.* 50:1545–1553.

84. Tate, M.W., and S.M. Gruner. 1989. Temperature dependence of the structural dimensions of the inverted hexagonal (HII) phase of phosphatidylethanolamine-containing membranes. *Biochemistry*. 28:4245–4253.

85. Frewein, M.P.K., M. Rumetshofer, and G. Pabst. 2019. Global small-angle scattering data analysis of inverted hexagonal phases. *J. Appl. Crystallogr.* 52:403–414.

86. Winnikoff, J. spectackler: Drivers and software for making spectrophotometric measurements under pressure. Github.

Supplementary Material

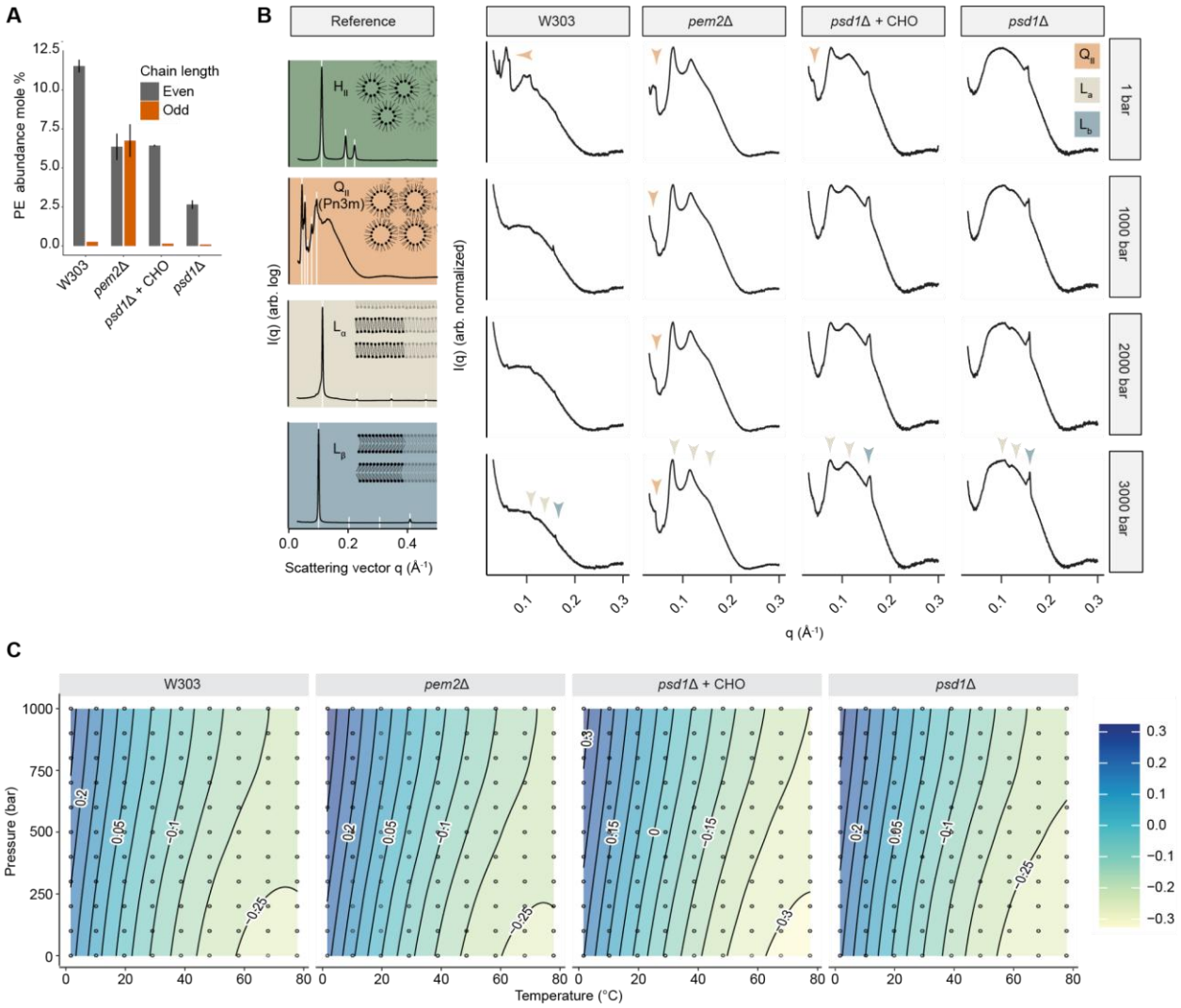

Supplemental Figure 3.1 Features of yeast with altered PE/PC ratio.

(**A**) Distribution of odd and even length acyl chains in PE in different backgrounds. The *pem*Δ strain shows an accumulation of odd chain PE which likely represents MMPE. (**B**) SAXS profiles of polar lipid extracts from yeast strains varying in PE/PC ratio under pressures at 85°C and 1-3000 bar; a subset of the data used to construct Fig. 1B. Reference SAXS profiles of pure Q_{II}, H_{II}, L_{α}, and L_{β}, are shown. Arrows indicate peaks corresponding to mesophase signatures: orange (Q_{II}), tan (L_{α}), blue (L_{β}). (**C**) Pressure-temperature phase diagrams of C-Laurdan GP values of polar lipid extracts from PE/PC mutant yeast strains. GP was determined for temperatures and pressures between 0-80°C and 1-1000 bar. Lines show fitted contours of constant GP values across temperature and pressure, while the scale key represents the coding of GP value for color. Lipid extracts show similar fluidity values. The horseshoe trend lines of GP at high temperatures observed in all systems except for *psd1*Δ reflects a non-lamellar phase transition.

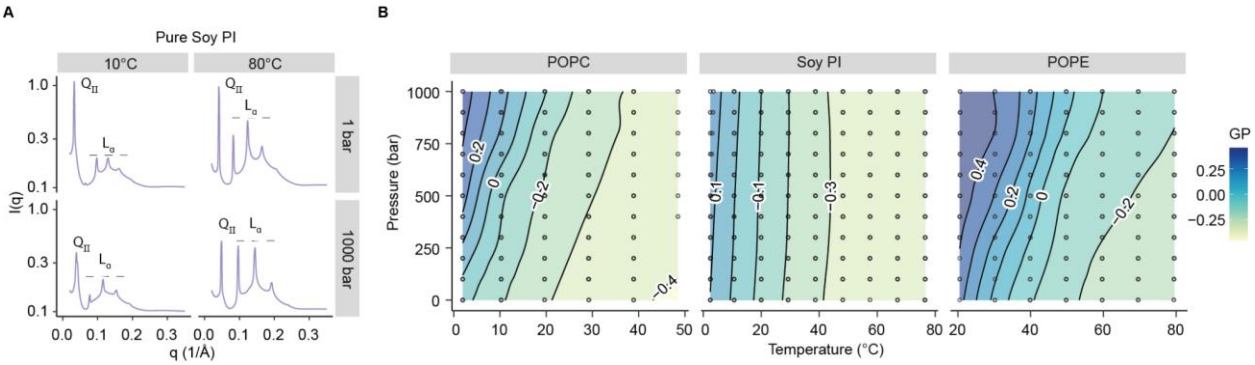

Supplemental Figure 3.2 Biophysical properties of Soy PI.

(**A**) Representative SAXS profiles taken from suspensions of Soy PI in water at 1 and 80 °C and 1 and 1000 bar, with labels indicating peaks representing the Q_{II} and L_{α} phases. Baselines are offset for clarity. (**B**) Pressure-temperature phase diagrams of C-Laurdan GP values of pure POPC, Soy PI, or POPE. GP was determined for temperatures and pressures between 0-80°C and 1-1000 bar. Lines show fitted contours of constant GP values across temperature and pressure, while the scale key represents the coding of GP value for color.

Supplemental Figure 3.3 Additional lipidic changes in pressure-grown yeast cells.

(**A**) Growth of W303 and FM628 at 1 and 250 bar pressure. Error bars indicate SEM from $N = 4$ independent cultures. **** $P < 0.0001$, unpaired two-tailed test. (**B**) Change in phospholipid chains of FM628 in total length (left) and total double bonds (right). Error bars indicate SEM from $N = 3$ independent cultures. ** $P < 0.01$, unpaired two-tailed test. (**C**) and (**D**): Distribution of total double bonds (DB) by phospholipid class from W303 (C) and FM628 (D) grown at 1 and 250 bar. (**E**) and (**F**): Distribution of total chain length by phospholipid class from W303 (C) and FM628 (D) grown at 1 and 250 bar. (**G**) Mean ergosterol abundance of W303 and FM628 grown at 1 and 250 bar from individual culture replicates. W303: $P = 0.052$, FM628: $P = 0.171$, unpaired two-tailed t-test. (**H**) Change of diacylglycerol (DAG) abundance in W303 and FM628 grown at 1 and 250 bar pressure from individual culture replicates. (**I**) Mean abundance of phospholipid classes from FM628. Error bars indicate SEM from N = 3 cultures. * $P < 0.05$, unpaired two-tailed test.

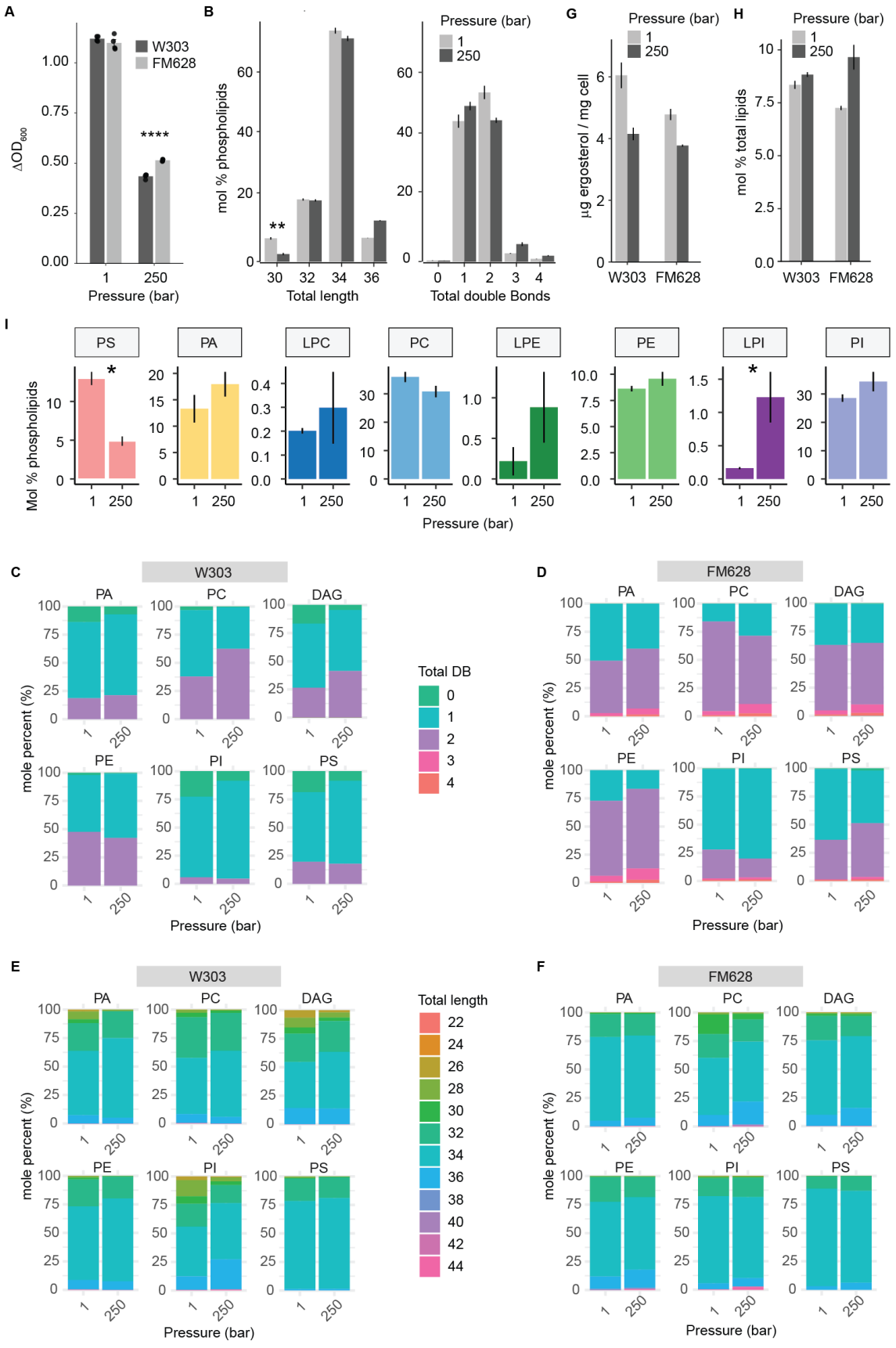
A
B
G
H
I
C
D
E
F
W303
FM628
Pressure (bar)
ΔOD600
mol % phospholipids
Total length
Total double Bonds
µg ergosterol / mg cell
mol % total lipids
Mol % phospholipids
PS
PA
LPC
PC
LPE
PE
LPI
PI
mole percent (%)
Total DB
Total length
DAG

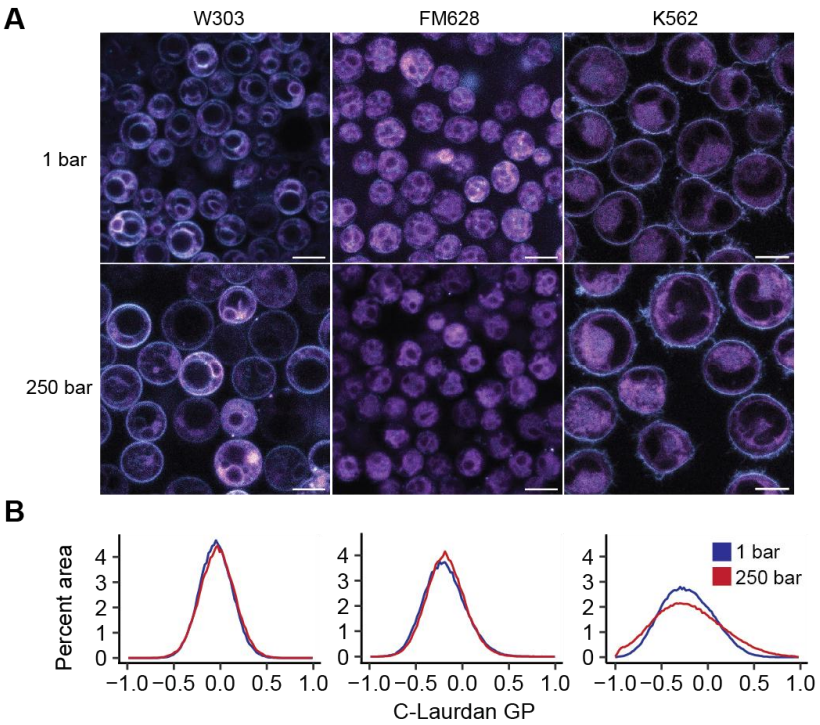

Supplemental Figure 3.4 Imaging of cell membranes after pressure incubation.

(**A**) C-Laurdan fluorescence microscopy of yeast (W303 and FM628, 16 h) and K562 cells (6 h) incubated under 1 (top) and 250 (bottom) bar pressure. The lipid staining shows cells remain intact after pressure incubations, with some changes in morphology and size. Composite images are shown of the two C-Laurdan emission channels; the ordered channel is presented as cyan, and disordered as magenta. Scale bars are 5 μm for W303 and FM628 or 10μm for K562. (**B**) Histograms of C-Laurdan GP for yeast (W303, left; FM628, middle) and K562 cells (right) incubated under 1 and 250 bar pressure. Each histogram shows the distribution of GP values from a representative field of cells. No difference is the mean GP is noted, suggesting membrane integrity and ordering is not dramatically altered by responses to the pressure incubation.

Supplemental Figure 3.5 Changes in chain composition of K562 cells grown at 1 and 250 bar pressure.

(**A**) Mean total lengths of phospholipid chains in K562 cells incubated at 1 and 250 bar pressure from individual culture triplicates. The mean length of all phospholipids for each pressure is shown with a dashed line. * $P < 0.05$, unpaired two-tailed t-test. (**B**) Mean sn-1 double bonds and length of phospholipid chains in K562 cells incubated at 1 and 250 bar pressure from individual culture triplicates. * $P < 0.05$, unpaired two-tailed t-test. (**C**) Mean sn-2 double bonds and length of phospholipid acyl chains in K562 cells incubated at 1 and 250 bar pressure from individual culture triplicates. * $P < 0.05$, *** $P < 0.001$, unpaired two-tailed t-test. (**D**) Mean sn-2 chain length within each phospholipid class of K562 growth at 1 and 250 bar pressure from individual culture replicates. (**E**) Mean sn-2 chain double bonds within each phospholipid class of K562 growth at 1 and 250 bar pressure from individual culture replicates. (**F**) Mean cholesterol abundance from K562 cells grown at 1 and 250 bar pressure from individual culture replicates. $P = 0.108$, unpaired two-tailed t-test.

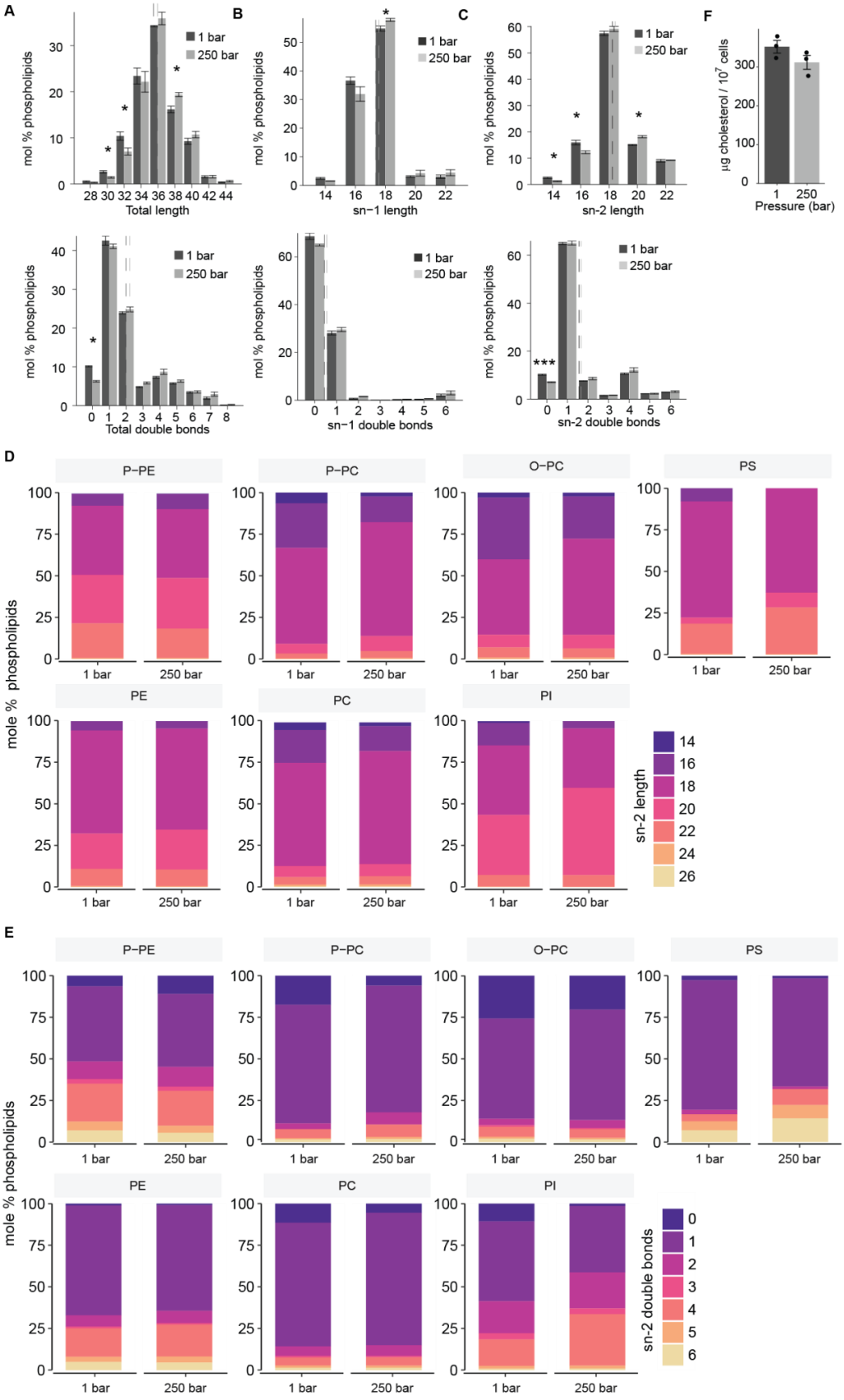
A
B
C
F
mol % phospholipids
1 bar
250 bar
Total length
sn−1 length
sn-2 length
Total double bonds
sn−1 double bonds
sn-2 double bonds
µg cholesterol / 10^7 cells
Pressure (bar)
D
E
P−PE
P−PC
O−PC
PS
PE
PC
PI
mole % phospholipids
sn-2 length
sn-2 double bonds

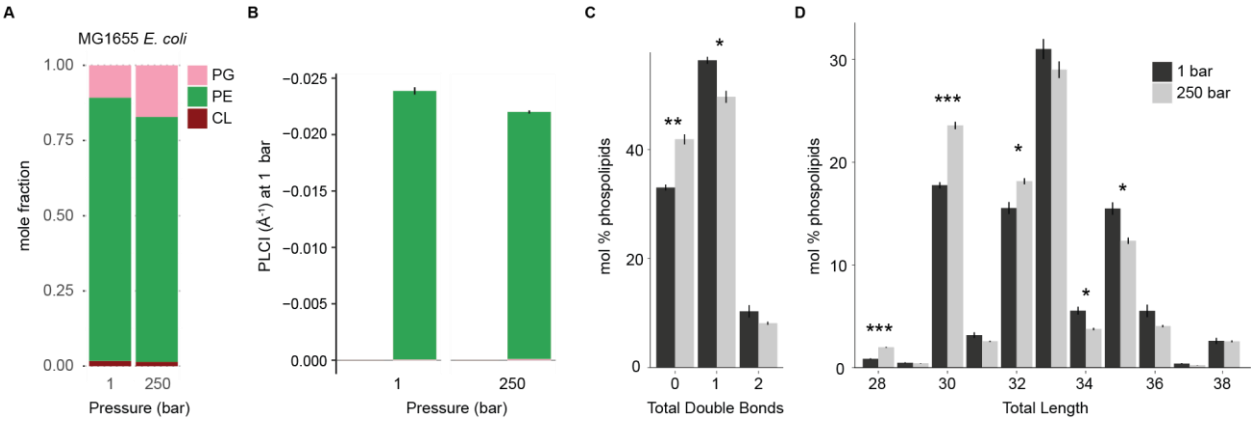

Supplemental Figure 3.6 Lipidomes and mean curvature changes from *E. coli* K12 cells growth at 1 and 250 bar.

(**A**) Class composition of phospholipids in MG1655 grown at 1 and 250 bar pressure. Data is mean mole fraction from individual culture triplicates. Cells grown under 250 bar show an increase in PG, decrease in PG, and no change in CL. (**B**) Mean curvature of phospholipids in *E. coli* grown at 1 and 250 bar pressure from individual culture triplicates. $P = 0.997$, unpaired one-tailed t-test. (**C**) Mean total lengths of phospholipid acyl chain composition in *E. coli* grown at 1 and 250 bar pressure from individual culture triplicates. * $P < 0.05$, ** $P < 0.01$, unpaired two-tailed t-test. (**D**) Mean total double bonds of phospholipid chain composition in *E. coli* grown at 1 and 250 bar pressure from individual culture triplicates. * $P < 0.05$, *** $P < 0.001$, unpaired two-tailed t-test.

Supplemental Table 3.1 Strains used in this study.

Name	Genotype	Parental strain	Reference
FM628	*ura3*	*Lachancea kluyveri*	Maitreya Dunham
W303a	*MATa ura3-52 trp1Δ2 leu2-3_112 his3-11 ade2-1 can1-100*	*Saccharomyces cerevisiae*	ATCC
*pem2*Δ	W303a, *pem2*Δ::HIS3	W303a	This study
*psd1*Δ	W303a, *psd1*Δ::HIS3	W303a	This study
MG1655	F- lambda- *ilvG- rfb*-50 *rph*-1	*Escherichia coli* K12	CGSC

Chapter 4 Energetics of stalk intermediates elucidated from hydrostatic pressure effects on membrane fusion

Abstract

Membrane fusion is an essential process in cells that requires a balance of lipid composition to establish biophysical properties conducive to topological rearrangements. During fusion, lipids of opposing membranes must invert and overcome energy barriers associated with forming highly curved stalk and pore intermediates. While theoretical work has modelled the effect of lipid intrinsic curvature on stalk formation, quantifying the relationship experimentally has posed to be a challenge due to the inability to vary lipid curvature without concomitantly changing other properties that affect fusion. Here we overcome this hurdle by utilizing hydrostatic pressure as a thermodynamic variable that modulates lipid intrinsic curvature independently of chemical composition. Using a high pressure stopped-flow fluorometry, we measured rates of calcium-mediated lipid mixing between populations of vesicles, a process that is strongly inhibited by pressure. We correlated mean lipid intrinsic curvature across with lipid mixing rates by incorporating complementary small angle x-ray scattering measurements for each individual lipid component. This analysis showed that lipid mixing rates, a proxy for hemifusion, across compositional and pressure regimes are determined entirely by changes in lipid spontaneous curvature. Consistent with previous theoretical models, we demonstrate a linear relation between lipid intrinsic curvature and the hemifusion stalk formation energy, offering direct experimental support for the stalk hypothesis. Extrapolated stalk energies were several fold lower than those estimated by continuum modeling, suggesting additional unidentified factors are relevant for fusion energetics.

Introduction

Membrane fusion is a universal biological process that underlies intracellular trafficking, neurotransmitter release, and viral infection (1–3). While the goal of fusion is to merge two membranes together, the lipids and proteins involved in this process vary widely between cells and organelles. This diversity could optimize the kinetics of fusion to occur across physical environments, lengthscales, and timescales that meet cellular demands to support specialized physiological functions. Both computational modeling and experimental evidence support a common pathway for all fusion events, the stalk hypothesis, with universal intermediate states that involve initial lipid mixing in the formation of a hemifusion stalk (Fig. 1A) and subsequent content mixing through pore formation (1, 4, 5). The main energy barriers in this pathway are hydration and curvature barriers for lipids to rearrange from a lamellar to nonlamellar topology in stalk formation, and the barrier to fusion pore opening as the hemifusion diaphragm accumulates membrane stress. While protein machinery such as soluble N-ethylmaleimide-sensitive factor attachment protein receptors (SNAREs), and viral fusion proteins supply the energy and specificity for fusion *in vivo*, the lipid bilayer itself is the substrate that must be deformed, and the energetic cost of that deformation sets the fundamental barriers that these proteins must overcome.

In both intermediate steps, lipids transition through highly curved membrane intermediates in transient nonlamellar topologies. The stalk resembles the inverted hexagonal (H_{II}) phase while the pore rim is positively curved . The formation of the stalk requires nonbilayer lipids with an inverted cone geometric shape, or negative intrinsic curvature ($c_0 < 0$), which have a smaller cross-section at the headgroup than in the hydrocarbon region. Lipids with high negative curvature, such as phosphatidylethanolamine (PE), cardiolipin (CL), cholesterol, and diacylglycerol (DAG), have been shown to promote stalk formation and increase lipid mixing rates, while lipids with positive

intrinsic curvature ($c_0 > 0$), such as lysophosphatidylcholine (LPC), inhibit stalk formation but promote pore formation (1–3, 5). Negatively curved lipids better accommodate the extreme bending required at the stalk, reducing the energy cost of forming this intermediate. Quantitatively, the tilt-splay elastic model describes the energy required to form a hemifusion stalk depending on how much the lipid monolayer must bend away from its preferred curvature (6, 7). Across a biologically relevant curvature range, the relationship between stalk energy and c_0 is predicted to be linear (7, 8). When combined with Kramers' rate theory (9), which relates energy barriers to reaction rates, this dependence predicts an exponential dependence of the hemifusion rate with c_0. Theoretical modeling supports this relationship (7, 8, 10, 11) but more comprehensive experimental evidence is needed to better quantify and support the energetics of stalk energy that theory and simulations predict.

Experimental approaches have classically used varying lipid compositions to indirectly study the roles of membrane properties in fusion (12–14). However, individual lipid species often affect more than one physical parameter, complicating attempts to distinguish energetic contributions of independent mechanical forces in each intermediate state. For example, negatively curved cholesterol increases bending rigidity, while adding positively curved LPC softens it (15–17). Because of this entanglement, estimations from composition-based experiments may not reflect the true contribution of intrinsic curvature to the hemifusion energy barrier. Whether the order of magnitude difference between experiments and theory reflects a genuine departure of the molecular transition state from the continuum elastic picture remains an open question.

In addition to lipid composition, physical parameters such as temperature, osmolarity, and hydrostatic pressure can be used to manipulate membrane properties. Pressure drives lipids into lower-volume conformations and has a particularly large effect on membrane curvature because

phospholipid compressibility is anisotropic (18). The acyl chain volume is more pressure sensitive than the headgroup region, so pressure preferentially compresses the hydrocarbon tails and shifts c_0 toward less negative values without changing the chemical identity of the lipid. This effect is reflected in the pressure sensitivity of curvature-mediated phase transitions. The dT/dP of the L_α to H_{II} transition is ~0.05 K/bar, whereas the dT/dP for the chain-ordering L_α to L_β transition is roughly 3-fold smaller (19–21). Pressure therefore has a disproportionately large effect on curvature relative to membrane fluidity, making it a single-variable perturbation of c_0 that overcomes experimental challenges that come with composition changes alone.

The biological significance of pressure acting on lipid curvature is evident in observations that organisms can adjust lipid composition to counteract the curvature-reducing effects of hydrostatic pressure (22). Deep-adapted ctenophores increase their abundance of plasmalogen PE, a lipid with strongly negative c_0, in proportion to their habitat depth (23). In yeast, decreasing the PE/PC ratio impairs growth and viability at high pressure independently of membrane fluidity (24) Both yeast and mammalian cells also respond to growth under high-pressure by increasing synthesis of high-curvature lipid species (24). In these cases, high pressure diminished the access to nonlamellar lipid phases, and this was reasoned to impair membrane fusion and, in turn, cellular fitness (24). However, the effects of pressure on membrane fusion have not been comprehensively demonstrated.

Here we use a FRET-based hemifusion assay under a range of hydrostatic pressure conditions to experimentally test the relationship between lipid intrinsic curvature and hemifusion rate. We combine this approach with variations in the PE/PC ratio of vesicle populations and estimates of mean intrinsic curvature using pressure-dependent corrections of individual lipid c_0 values determined by high-pressure small-angle X-ray scattering (HPSAXS). Together, we find

that hemifusion stalk formation energy is linearly dependent on the mean intrinsic curvature across lipid components, supporting the stalk hypothesis. In addition, simulations of stalk structures across a range of parameters show that the experimental results are consistent with theoretical calculations when relatively soft membrane bending moduli are assumed.

Methods

SAXS sample preparation

Lipid stocks of di-oleoyl phosphatidylethanolamine (DOPE), 1-palmitoyl-2-oleoyl phosphatidylcholine (POPC), or 1-palmitoyl-2-oleoyl phosphatidylserine (POPS) (Avanti Research) in chloroform were used to prepare lipid mixtures for a total mass of 5 mg lipid. Solvent was dried under a stream of nitrogen for 5 minutes and a vacuum chamber for 1 hour. Lipids were resuspended in 100 µL cyclohexane and 50 µL aliquots were dispensed into 1.5 mm inner diameter capillary melting point tubes (Kimble Chase 34505-99), flash-frozen at -80°C, and lyophilized for 1 hour to yield a lyophilized powder. Rehydration was carried out by adding 10 µL of vacuum-degassed MilliQ water, mixing with a 20 µL Wiretrol II microdispenser (Drummond Scientific), followed by five freeze-thaw cycles using an ethanol/dry ice bath. Between cycles, the suspension was homogenized by repeated pipetting with a 20 µL Wiretrol II microdispenser within the capillary tube. The resulting lipid suspension (50% w/v) was consolidated to the tube bottom by centrifugation at 500 RCF for 5 minutes at 4°C before being scored and cut to fit a sample holder. An additional 5 µL of degassed water was added on top of the suspension to ensure complete hydration of the sample. The capillary was then sealed with a plug of high vacuum grease (Dow Corning) introduced through a 22G × 100 mm needle (Air-Tite), which also served as a pressure-transmitting cap. The final lipid concentration was 250 mg/mL.

SAXS data acquisition and analysis

Collection of HPSAXS data was performed at beamline 7A in the Cornell High Energy Synchrotron Source (CHESS) using a custom-built temperature-controlled pressure cell (25). Data was acquired using a photon energy of 14 keV, 1s exposures using a flux of 1.8-3.6x10^{11} photons/s, a spot size of 200 x 250 μm (W x H), with a collection range of 0.005 $Å^{-1} \leq q \leq 0.7$ $Å^{-1}$ using an EIGER 4M detector (Dectris) within the beamline vacuum. After testing each sample for radiation sensitivity with five initial exposures, pressure sweeps were performed from lowest to highest and back with triplicate exposures for each pressure condition and 60s of equilibration per 100 bar of pressure change. No background subtraction was used following assessment of low background of a glass capillary with degassed water. SAXS images were azimuthally integrated using BIOXTAS RAW software (26).

Measurement of phospholipid monolayer curvature

Hosted mixtures at molar ratios of 10 mol%:90 mol% or 20 mol%:80 mol% guest:host with 12% w/w 9(Z)-tricosene for HPSAXS were prepared using DOPE as the host lipid, as described above. Neutral-plane c_0 was estimated by using a constant distance correction of 3.94 Å, derived from global fitting of the DOPE H_{II} scattering profile of (27). Total c_0 was calculated from peak spacing as previously described (28), and the guest lipid c_0 was extracted from a weighted average of the total curvature of the hosted system.

Lipid mixing fusion assay

Membrane fusion kinetics were assessed using a FRET-based lipid mixing assay, in which fusion is reported by fluorescence dequenching upon dilution of a self-quenching donor-acceptor pair. Chloroform stocks of POPC, POPS, and DOPE (Avanti Research) were combined at the desired molar ratios, and the solvent was removed by drying under nitrogen for 10 minutes followed by exposure to high vacuum for at least 1 hour. Resulting lipid films were hydrated with Buffer A (100 mM NaCl, 5 mM Na^+ HEPES, 0.1 mM EDTA, pH 7.4) to obtain 400 μM lipid (2X) and tumbled for 1 h. Unilamellar vesicles of approximately 100 nm diameter were produced by four freeze-thaw cycles followed by extrusion through a 100 nm polycarbonate membrane 21 times. One population of fluorescence-quenched liposomes, containing Rh-DOPE (2 mol%) and NBD-DOPE (2 mol%) with DOPE/POPC/POPS (32:32:32 mol%), DOPE/POPC/POPS (42.6:21.4:32 mol%), or DOPE/POPC/POPS (21.4:42.6:32 mol%), were mixed with a population of liposomes lacking fluorophores with DOPE/POPC/POPS (33.3:33.3:33.3 mol%), DOPE/POPC/POPS (44.6:23.4:32 mol%), or DOPE/POPC/POPS (23.4:44.6:32 mol%).

The emission of NBD-PE dequenching was measured following the addition of 20 mM $CaCl_2$ (2X) in Buffer A, for a final reaction concentration of 200 μM lipid and 10 mM $CaCl_2$, using a High-Pressure Stopped Flow System (TgK Scientific) at the Rensselaer CBIS Analytical Biochemistry Core Facility. The excitation was set with a 400 nm excitation filter and temperature was maintained 37°C using an integral thermostated jacket. Individual runs were carried out with hydrostatic pressures set from 1-1000 bar, fluorescence intensity was recorded for 5 min to allow reactions to reach equilibrium. Fluorescence of a fully dequenched control, with 1 mol% NBD-DOPE and Rh-DOPE in DOPE/POPC/POPS (32.65: 32.65: 32.65), DOPE/POPC/POPS (43.6:

22.4: 32), or DOPE/POPC/POPS (22.4: 43.6: 32) was recorded to permit normalization and determination of total % fused vesicles.

Hemifusion stalk calculations

The elastic energy of the hemifusion stalk was calculated using the continuum elastic theory of lipid monolayers as described previously (8, 29, 30). In this framework, membrane deformations are described in terms of lipid splay, saddle splay, and tilt degrees of freedom, and the equilibrium stalk structure is obtained by numerical minimization of the total membrane elastic energy. Full details of the theoretical formalism, elastic energy functional, numerical implementation, and minimization procedures are provided in these previous works. Briefly, the membrane is modeled as two coupled lipid monolayers connected by a membrane mid-plane. Each monolayer is characterized by a local lipid director field and elastic contributions associated with splay, saddle-splay, and lipid tilt deformations. The elastic energy is evaluated over the monolayer surfaces and minimized numerically with respect to both membrane shape and lipid director configuration.

For the calculations presented here, the fusion site was assumed to be axially symmetric and initially flat, and the two membranes were taken to be compositionally and mechanically symmetric. The stalk configuration corresponds to the merger of the two proximal monolayers while the distal monolayers remain separated. Similar to previous continuum descriptions of membrane fusion stalks, the lipids near the stalk undergo strong tilt and splay deformations in order to avoid hydrophobic void formation at the fusion center. In contrast to previous calculations, where the angle between the membrane mid-planes at the stalk center was fixed to 90°, here this angle was allowed to vary freely during the minimization procedure. This additional degree of freedom reduced the magnitude of lipid splay in the stalk region and resulted in lower stalk elastic

energies compared to earlier calculations with a fixed-angle constraint. The equilibrium stalk structure and corresponding stalk formation energy were obtained by minimizing the total elastic energy relative to the undeformed membrane state using an open-source code available at https://github.com/GonenGolani/Fusion_Solver.

Results

Hydrostatic pressure inhibits hemifusion

To characterize the effects of hydrostatic pressure on fusion, we employed a model fusion reaction mediated by the interactions between Ca^{2+} and phosphatidylserine (PS) lipids on opposing membranes (31). Ca^{2+} and PS form a 1:2 complex (32), which has been proposed to specifically mediate membrane fusion reactions by bringing together opposing lamellae. While simplified compared to those employing protein-mediated fusogens, the assay relies solely on lipid components and thus prevents complications from any potential pressure effects on protein conformations and dynamics. It also is compatible with the large sample volumes required for high-pressure stopped flow fluorometry.

We measured calcium-mediated lipid mixing of large unilamellar vesicles (LUVs) composed of equimolar DOPE:POPC:POPS (33:33:33). We read out lipid mixing using a FRET-based assay with a high-pressure stopped flow system (Fig. 1B), in which two solutions are pressurized and mixed isobarically. In our assays, vesicles labeled with 2 mol% NBD-PE and 2 mol% Rh-PE were rapidly mixed with a solution of unlabeled vesicles and 10 mM $CaCl_2$ (final concentration)at 37°C. The increase in NBD fluorescence upon FRET dequenching reported on lipid mixing, or hemifusion, between the two vesicle populations. Fluorescence intensities were normalized to a fully dequenched control to determine the total percentage of fused vesicles. At

ambient pressure (1 bar), mixing of equimolar vesicles led to rapid lipid mixing, reaching approximately 20% lipid mixing within 75s (Fig. 1C). Increasing hydrostatic pressure progressively reduced both the rate and extent of lipid mixing. At 250 bar, the same vesicles reached roughly 15% lipid mixing, while at 750 bar the signal plateaued below 5%. Rate constants extracted from first-order exponential fits decreased from 0.186 ± 0.009 s^{-1} at 1 bar to 0.047 ± 0.001 s^{-1} at 500 bar (Fig. 1D). On a semilogarithmic scale, ln(k) decreased linearly with pressure, consistent with an Arrhenius-like process. Thus, increasing pressures dramatically reduce rates of calcium-mediated fusion.

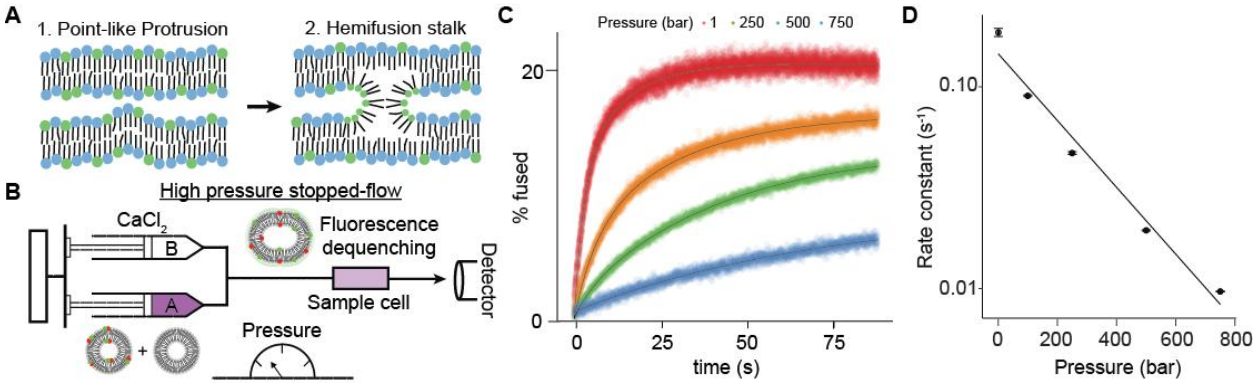

Figure 4.1 Hydrostatic pressure inhibits lipid mixing during calcium-mediated vesicle fusion. (**A**) Schematic of the classical hemifusion pathway. Two bilayers in apposition start at a point-like protrusion evolves into a hemifusion stalk which can be initiated by fusion proteins, the presence of calcium, or osmotic pressure. Stalk formation is supported by the presence of negative curvature lipids, labelled with green headgroups while bilayer-supporting lipids are labelled blue. The hemifusion stalk is a membrane topology characterized by high negative curvature which resembles nonbilayer H_{II} mesophases. (**B**) Schematic of high-pressure stopped-flow fluorometry to monitor hemifusion rates at varying pressure. FRET dequenching occurs when liposomes, labelled with 2 mol% NBD-PE and Rh-PE, fuse with unlabeled ones upon rapid mixing. Calcium is included in the buffer of the latter. (**C**) Lipid mixing assay comparing the hemifusion of liposomes with DOPE/POPC/POPS (33:33:33) in the presence of 10 mM $CaCl_2$ at 37°C under pressures of 1-750 bar pressure. Averaged intensities are normalized to values for mixed liposomes. Error bars indicate SEM from n=3 replicate runs. (**D**) Rate constants from first order exponential fits for lipid mixing of liposomes with DOPE/POPC/POPS (33:33:33 mol%) under pressures of 1-700 bar pressure. Rates decrease with increases in pressure in an exponential relationship. Error bars indicate SEM from n=3 replicate runs.

Nonbilayer lipid content buffers against pressure inhibition of hemifusion

We hypothesized that the strong inhibition of hemifusion by pressure could result from its effect on lipid intrinsic curvature (c_0). To examine how lipid composition modulates the pressure sensitivity of fusion, we measured lipid mixing kinetics at two additional DOPE:POPC:POPS ratios: 44:23:32 (high PE) and 23:44:32 (low PE), alongside the equimolar composition, across pressures from 1 to 1000 bar (Fig. 2A). Because DOPE has a strongly negative c_0 while POPC is approximately cylindrical, increasing the PE:PC ratio makes the mean membrane curvature more negative, which is expected to lower the hemifusion barrier. Consistent with this hypothesis, higher PE content increased fusion rates and capacity across all pressures. At ambient pressure, the high PE vesicles showed fast lipid mixing approaching 60% hemifusion, while the low PE vesicles plateaued at roughly 20%. At elevated pressure, the high PE composition maintained efficient lipid mixing even at 1000 bar, whereas the low PE composition showed near-complete inhibition of fusion by 750 bar. The equimolar composition showed intermediate behavior. Rate constants from first-order exponential fits (Fig. 2B) spanned nearly two orders of magnitude across compositions and pressures, from 0.72 s^{-1} (high PE, 1 bar) to 0.006 s^{-1} (low PE, 750 bar). On a semilogarithmic scale, ln(k) decreased linearly with pressure at each composition, with similar slopes across the three PE:PC ratios, suggesting that the effect of pressure on the hemifusion barrier is comparable regardless of starting composition. These results indicate that PE content effectively buffers the membrane against pressure induced inhibition.

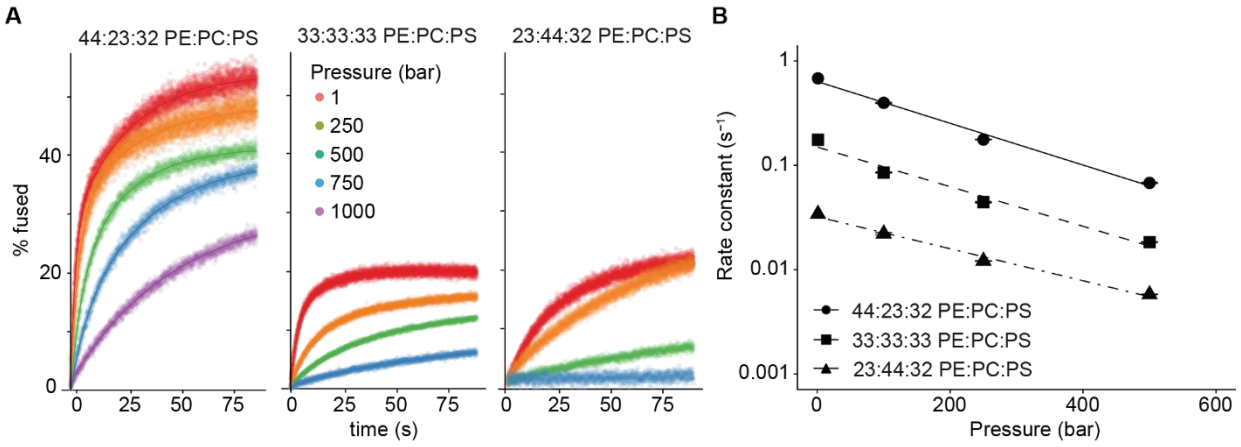

Figure 4.2 Increasing pressure inhibits vesicle hemifusion stalk formation.

(**A**) Lipid mixing assay of liposomes with different DOPE:POPC:POPS ratios at 1-1000 bar pressure and 37°C. High PE (44:23:32 mol% DOPE:POPC:POPS) results in increased lipid mixing rates and capacity, while low PE (23:44:32 mol% DOPE:POPC:POPS) results in inhibited lipid mixing failing by 750 bar pressure. Equimolar (33:23:33 mol% DOPE:POPC:POPS) mixtures showed intermediate lipid mixing to the high and low PE compositions. Averaged intensities are normalized to values for mixed liposomes. Error bars indicate SEM from n=3 replicate runs. (**B**) Rate constants from first order exponential fits for lipid mixing of liposomes with 44:23:32 mol%, 33:33:33 mol%, or 23:44:32 mol% DOPE/POPC/POPS under pressures of 1-500 bar pressure. Error bars indicate SEM from n=3 replicate runs.

Hydrostatic pressure reduces phospholipid intrinsic curvature

To quantitatively assess the role of c_0 in measured hemifusion rates, we performed HPSAXS on hydrated lipid films of DOPE, POPC, and POPS (the latter two hosted at 20 mol% in 80 mol% DOPE) at 35°C across pressures from 1 to 800 bar (Fig. 3A). In each case, the lipids adopted the H_{II} phase, and the spontaneous curvature was extracted from the first-order Bragg peak position. Addition of POPC or POPS to the DOPE host system shifted the first-order peak to lower q values (Fig. 3B), reflecting their less negative curvature contributions that increase the H_{II} lattice spacing. With increasing pressure, the first-order peak of all samples shifted progressively to lower q, indicating a decrease in the magnitude of negative curvature (Fig. 3C).

Quantification of c_0 across the pressure range revealed that all three lipid species became less negatively curved with increasing pressure (Fig. 2D). DOPE maintained strongly negative

curvature throughout, decreasing from −0.0385 $Å^{-1}$ at 1 bar to −0.0366 $Å^{-1}$ at 800 bar. POPC shifted from −0.0075 $Å^{-1}$ toward near-zero values with a cylindrical geometry. POPS exhibited a positive c_0 that increased further under pressure, moving from 0.0043 $Å^{-1}$ at 1 bar to 0.0079 $Å^{-1}$ at 800 bar. All three lipids showed linear pressure dependencies with similar slopes (dc_0/dP).

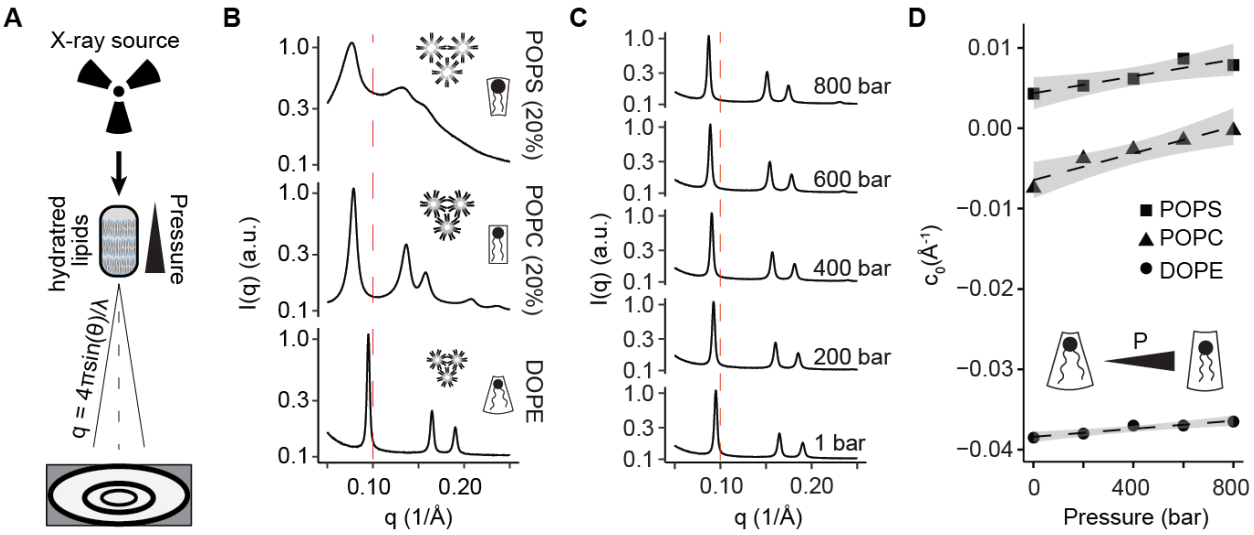

Figure 4.3 Hydrostatic pressure increases phospholipid intrinsic curvature.

(**A**) A schematic of an X-ray scattering setup where the scattering pattern on the detector can be used to determine the structural properties of lipid phases, including spontaneous curvature (c_0), from their corresponding scattering intensity profiles. Hydrostatic pressure can be applied to hydrated lipid films in a specialized sample cell to study the effects of pressure on lipids. (**B**) Bragg peak profiles of DOPE or 20 mol% POPS or POPC hosted in 80 mol% and 12% w/w tricosene. The q-spacing of the peaks reflect the inverted hexagonal phase (H_{II}) and the position of the first order peak is related to the lattice d-spacing and total spontaneous curvature. Addition of POPS and POPS results in leftward shifting of the first order peak in q-space. (**C**) Bragg peak profiles of DOPE under 1-800 bar hydrostatic pressure. As pressure increases, the first order peak of the H_{II} phase shifts leftward in q-space, representing a decrease in negative curvature. (**D**) Spontaneous curvature values of c_0 for DOPE, POPC, and POPS measured by HPSAXS across 1-800 bar hydrostatic pressure at 35°C. As pressure increases, lipid negative curvature decreases by a similar slope in all 3 lipid classes.

Lipid intrinsic curvature predicts hemifusion rates across variations in PE/PC and pressure

The above results suggest that both pressure and PE content affect fusion through their common influence on lipid intrinsic curvature. To test this directly, we calculated the corrected mean spontaneous curvature $\bar{c}_0$ for each of the 12 experimental conditions (3 compositions x 4 pressures) using the independently measured phospholipid curvatures at different pressures with HPSAXS (Fig. 1D). The mean curvature, $\bar{c}_0$, was computed as a weighted sum of the mole fraction and pressure-corrected spontaneous curvature of each lipid species. The resulting mean curvatures ranged from -0.0175 Å^{-1} (high PE at 1 bar) to -0.0060 Å^{-1} (low PE at 750 bar) (Fig. 4A). When rate constants from all 12 conditions were plotted against the corrected mean spontaneous curvature, the data collapsed in a semilogarithmic plot of ln(k) versus $\bar{c}_0$ spanning nearly two orders of magnitude in rate with a linear relationship (Fig. 4B). Data points from different compositions and different pressures fell along the same relationship, indicating that mean intrinsic curvature governs the hemifusion rate regardless of whether it was varied by changing the PE:PC ratio or by applying hydrostatic pressure.

This relationship reflects changes in c_0 due to pressure alone with negligible change in elastic moduli. However, the collapse of all data onto a single linear relationship provides experimental evidence for the linear dependence of the hemifusion barrier energy on lipid intrinsic curvature predicted by the stalk hypothesis.

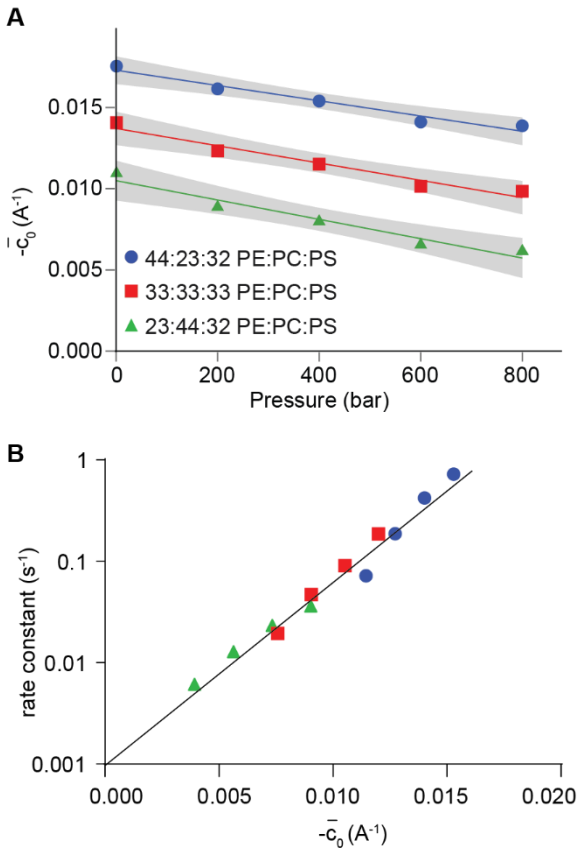

Figure 4.4 Hemifusion rate has an exponential dependence on mean lipid intrinsic curvature of liposome mixtures.

(**A**) Estimations of mean lipid intrinsic curvatures for 44:23:32 mol%, 33:33:33 mol%, or 23:44:32 mol% DOPE/POPC/POPS liposome compositions across 1-800 bar pressure. Mean curvature is calculated as a weighted sum of products of the mol% lipid and its c_0 measured over a range of pressures by HPSAXS. SEM for the fit is shown in grey. (**B**) The effect of corrected mean curvature on lipid mixing rate from 44:23:32 mol%, 33:33:33 mol%, or 23:44:32 mol% DOPE/POPC/POPS liposome compositions under 1-750 bar pressure shown on semilog axes. Error bars indicate SEM from n=3 replicate runs.

Quantifying the curvature-energy relationship for hemifusion

To understand the relationship between curvature and hemifusion rate in energetic terms, we applied Kramers' rate principle, which states that the rate of crossing an energy barrier decreases exponentially with the height of that barrier. By this principle, the ratio of hemifusion rates at two different curvature conditions reports the change in barrier energy between them, without requiring knowledge of the barrier height or the molecular attempt frequency. The energy

of the hemifusion stalk can be described using the tilt-splay elastic model (7, 33), which expresses the monolayer energy density as:

$$f_m = \tfrac{1}{2} K_{s,m}(\Delta a/a_0)^2 + \tfrac{1}{2} \kappa_m(\nabla \cdot n)[(\nabla \cdot n) - 2\bar{c}_0] + \bar{\kappa}_m \tilde{K} + \tfrac{1}{2} \kappa_t t^2$$

where the terms represent area stretch, lipid splay, saddle splay, and lipid tilt, respectively. Here, the first term is the energetic cost of stretching or compressing the area per lipid ($K_{s,m}$). The second term is the cost of splaying lipid directors away from the monolayer's preferred curvature c_0, governed by the bending rigidity κ_m. The third term accounts for Gaussian curvature deformations through the saddle-splay modulus $\bar{\kappa}_m$. The fourth term penalizes tilting of lipid molecules relative to the membrane normal, with tilt modulus κ_t. The overall stalk formation energy is obtained by integrating this energy density over both monolayers of the stalk geometry and subtracting the energy of the pre-fusion planar bilayers: $E_{stalk} = \min[E_M] - E_{pre}$. The change in fusion time, τ_1/τ_0, is proportional to the energy and change in $\bar{c}_0$. The lipid intrinsic curvature c_0 appears only in the splay term, when the barrier energy is evaluated at two different values of c_0, all terms except the splay cross-term $\nabla \cdot n$ cancel, and the change in barrier energy simplifies to (8):

$$\Delta E_{barrier} = k_B T \cdot \ln(\tau_1/\tau_0) = -\Delta \bar{c}_0 \int \kappa_m(\nabla \cdot n)\, dA$$

The slope of $\Delta E_{barrier}$ versus $\Delta \bar{c}_0$, in units of kT·nm, quantifies the sensitivity of the fusion barrier to lipid curvature and is predicted to be a property of the transition-state geometry, independent of the starting curvature itself (8).

Converting our measured rate constant ratios into barrier energy changes ΔE and plotting against $\Delta\bar{c}_0$ (Fig. 5), the energy barrier for hemifusion increased across the full range of curvatures sampled. The pooled slope corresponds to a relationship between curvature and hemifusion energy of 32.6 ± 2.4 kT·nm. Between compositions, which separate pressure induced changes in c_0 from confounding variations in elastic moduli, slopes ranged from 20.8 kT·nm to 31.5 kT·nm. The smaller values corresponded to the low-PE mixtures, suggesting a modest effect of lipid composition on stalk energy independent of c_0.

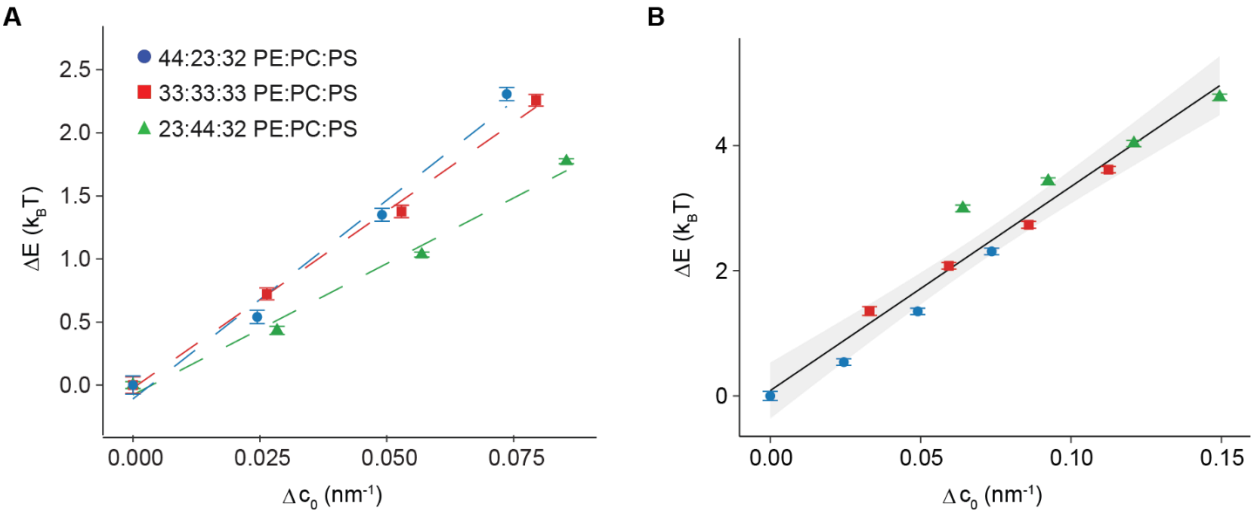

Figure 4.5 Extrapolation of stalk activation energies.

(A) Change in the stalk energy barrier with change in mean intrinsic curvature for 44:23:32 mol%, 33:33:33 mol%, or 23:44:32 mol% DOPE/POPC/POPS liposome compositions. Error bars indicate SEM from n=3 replicates. **(B)** Pooled change in the stalk energy barrier with change in mean intrinsic curvature for 44:23:32 mol%, 33:33:33 mol%, or 23:44:32 mol% DOPE/POPC/POPS liposome compositions. Change in $\Delta\bar{c}_0$ is calculated using high PE, 1 bar as a reference. Error bars indicate SEM from n=3 replicates.

Discussion

The linear relationship between lipid intrinsic curvature and hemifusion stalk formation energy has been a central prediction of the stalk hypothesis, yet has not previously been tested in

a system where c_0 is varied independently of lipid chemistry. By combining hydrostatic pressure with independent HPSAXS calibration of each lipid species, we isolated c_0 as a single variable and found that all 12 experimental conditions, spanning three lipid compositions and four pressures, collapse onto a single linear ln(k) versus $\bar{c}_0$ relationship (Fig. 4C). The corrected mean spontaneous curvature appears to be the primary variable governing the hemifusion rate regardless of whether it was varied by changing the PE:PC ratio or by applying pressure. To our knowledge, this represents the first experimental evidence of a linear relation between lipid intrinsic curvature and the hemifusion stalk formation energy, offering direct support for the stalk hypothesis.

The curvature-energy coupling slope we measure, 20–30 kT·nm from composition fits, is 5–10 fold lower than predictions from continuum elastic theory (200–400 kT·nm) (7, 8, 10), self-consistent field theory (~300 kT·nm) (10), and values inferred from coarse-grained molecular dynamics simulations (~200–300 kT·nm) (11). Notably, our pressure-derived slope falls at the upper end of the range reported from previous measurements, including ~25 kT·nm from SNARE-mediated fusion assays varying cholesterol (12), ~10 kT·nm from hemagglutinin-mediated fusion with cholesterol depletion (13), and ~6–20 kT·nm from single-vesicle optical tweezers hemifusion measurements using cholesterol and LPC perturbations (14). The convergence of measurements from independent systems, spanning protein-free, SNARE-mediated, and HA-mediated fusion across different experimental platforms, suggests that the curvature-energy coupling is in the range of 10–30 kT·nm, well below theoretical predictions.

The measured slope provides quantitative insight for understanding how lipid composition tunes fusion kinetics in living cells. Eukaryotic membranes maintain approximately 30–40% negatively curved lipids including PE, cardiolipin, and DAG, positioning the average membrane curvature in a narrow window of $\bar{c}_0 \approx -0.05$ to -0.15 nm^{-1} (6, 34). At a slope of ~32 kT·nm,

shifting $\bar{c}_0$ by 0.01 nm^{-1}, equivalent to replacing roughly 5–10 mol% PC with PE, would alter the fusion rate by approximately 1.5-fold. These effects are biologically meaningful, particularly in contexts where fusion is precisely timed such as synaptic exocytosis, yet moderate enough to buffer against stochastic lipid composition fluctuations. Cells appear to exploit this sensitivity through enzymatic pathways that locally remodel lipid curvature at sites of membrane trafficking, including phospholipase D generating phosphatidic acid (PA) at exocytic sites (35), diacylglycerol (DAG) kinases interconverting DAG and PA (36), and PE methyltransferases converting PE to PC (37). The localization of these enzymes to membranes where fusion or fission occurs suggests that local curvature remodeling serves to tune the kinetic competence of membranes for topological rearrangement. Studies have shown that mammalian cells actively maintain intrinsic curvature stress on the lipidome level (24, 38), analogous to homeoviscous adaptation for membrane fluidity (39).

Our results also provide direct evidence that hydrostatic pressure inhibits membrane hemifusion through its effect on lipid intrinsic curvature, connecting *in vitro* biophysics to emerging observations of pressure adaptation in living organisms. Deep-sea ctenophores increase their abundance of plasmalogen PE, a lipid with strongly negative c_0, in proportion to their habitat depth (23), and yeast with reduced PE/PC ratios show impaired viability at elevated pressure independently of membrane fluidity (24). In both cases, high pressure was found to diminish the accessibility of nonlamellar lipid phases, and this was reasoned to compromise membrane fusion and cellular fitness. Our data provide the mechanistic basis for these observations by showing that the pressure induced shift in c_0 slows hemifusion stalk formation. The approximately 10-fold reduction in rate constant across 750 bar of pressure at equimolar PE:PC:PS composition (Fig. 2D), and the ability of elevated PE content to buffer against this inhibition (Fig. 3), are consistent

with the organismal strategies observed in pressure-adapted species. These findings suggest that the evolutionary pressure to maintain negatively curved lipids in biological membranes may reflect a requirement to keep the hemifusion barrier within a range accessible to the cell's fusion machinery.

In summary, by exploiting the unique ability of hydrostatic pressure to tune lipid intrinsic curvature without significantly altering elastic moduli or lipid chemistry, we have provided experimental support for the predicted linear relationship between c_0 and the hemifusion stalk formation energy. The collapse of data from multiple compositions and pressures onto a single master curve suggests that the corrected mean spontaneous curvature is the dominant thermodynamic variable controlling hemifusion rate in this system. The measured slope 20-30 kT·nm, supports qualitative predictions of the stalk hypothesis, but emphasizes a persistent quantitative discrepancy with continuum elastic theory that reflects features of the fusion transition state not captured by theoretical models. More broadly, the approach demonstrated here, utilizing hydrostatic pressure to manipulate lipid geometry, provides a general strategy for dissecting the individual contributions of biophysical properties to membrane remodeling processes.

Acknowledgements

The material in this chapter is currently being prepared for submission for publication of the material. "Energetics of stalk intermediates elucidated from hydrostatic pressure effects on membrane fusion". Milshteyn, Daniel; Winnikoff, Jacob R; Morgan, Joel E; Golani, Gonen; Budin, Itay. The dissertation author is the primary researcher and author of this material. Raya Sorkin provided discussions and feedback. Cathy Royer and the Royer lab technical support for high-pressure stopped flow fluorometry. Research was supported by the National Science

Foundation (MCB-2046303 and MCB-2316458 to I.B.), the National Institutes of Health (5T32EB009380-14 to D.M.), the Office of Naval Research (N00014-23-1-2543 to I.B.), and NASA (postdoctoral fellowship 0017-NPP-MAR22-A-Astrobio to J.R.W.).

References

1. Chernomordik, L.V., and M.M. Kozlov. 2008. Mechanics of membrane fusion. *Nat. Struct. Mol. Biol.* 15:675–683.

2. Jahn, R., T. Lang, and T.C. Südhof. 2003. Membrane fusion. *Cell*. 112:519–533.

3. Chernomordik, L.V., and M.M. Kozlov. 2003. Protein-lipid interplay in fusion and fission of biological membranes. *Annu. Rev. Biochem.* 72:175–207.

4. Kozlov, M.M., and V.S. Markin. 1983. Possible mechanism of membrane fusion. *Biofizika*. 28:242–247.

5. Markin, V.S., M.M. Kozlov, and V.L. Borovjagin. 1984. On the theory of membrane fusion. The stalk mechanism. *Gen. Physiol. Biophys.* 3:361–377.

6. Cullis, P.R., and B. de Kruijff. 1979. Lipid polymorphism and the functional roles of lipids in biological membranes. *Biochim. Biophys. Acta*. 559:399–420.

7. Kozlovsky, Y., and M.M. Kozlov. 2002. Stalk model of membrane fusion: solution of energy crisis. *Biophys. J.* 82:882–895.

8. Golani, G., and U.S. Schwarz. 2023. High curvature promotes fusion of lipid membranes: Predictions from continuum elastic theory. *Biophys. J.* 122:1868–1882.

9. Kramers, H.A. 1940. Brownian motion in a field of force and the diffusion model of chemical reactions. *Physica*. 7:284–304.

10. Müller, M., K. Katsov, and M. Schick. 2003. A new mechanism of model membrane fusion determined from Monte Carlo simulation. *Biophys. J.* 85:1611–1623.

11. Poojari, C.S., K.C. Scherer, and J.S. Hub. 2021. Free energies of membrane stalk formation from a lipidomics perspective. *Nat. Commun.* 12:6594.

12. Chang, J., S.-A. Kim, X. Lu, Z. Su, S.K. Kim, and Y.-K. Shin. 2009. Fusion step-specific influence of cholesterol on SNARE-mediated membrane fusion. *Biophys. J.* 96:1839–1846.

13. Domanska, M.K., D. Wrona, and P.M. Kasson. 2013. Multiphasic effects of cholesterol on influenza fusion kinetics reflect multiple mechanistic roles. *Biophys. J.* 105:1383–1387.

14. Shendrik, P., G. Golani, R. Dharan, U.S. Schwarz, and R. Sorkin. 2023. Membrane tension inhibits lipid mixing by increasing the hemifusion stalk energy. *ACS Nano*. 17:18942–18951.

15. Chakraborty, S., M. Doktorova, T.R. Molugu, F.A. Heberle, H.L. Scott, B. Dzikovski, M. Nagao, L.-R. Stingaciu, R.F. Standaert, F.N. Barrera, J. Katsaras, G. Khelashvili, M.F. Brown, and R. Ashkar. 2020. How cholesterol stiffens unsaturated lipid membranes. *Proc. Natl. Acad. Sci. U. S. A.* 117:21896–21905.

16. Gracià, R.S., N. Bezlyepkina, R.L. Knorr, R. Lipowsky, and R. Dimova. 2010. Effect of cholesterol on the rigidity of saturated and unsaturated membranes: fluctuation and electrodeformation analysis of giant vesicles. *Soft Matter*. 6:1472.

17. Vitkova, V., D. Mitkova, and G. Staneva. 2014. Lyso- and omega-3-containing phosphatidylcholines alter the bending elasticity of lipid membranes. *Colloids Surf. A Physicochem. Eng. Asp.* 460:191–195.

18. Brooks, N.J. 2014. Pressure effects on lipids and bio-membrane assemblies. *IUCrJ*. 1:470–477.

19. So, P.T., S.M. Gruner, and S. Erramilli. 1993. Pressure-induced topological phase transitions in membranes. *Phys. Rev. Lett.* 70:3455–3458.

20. Kulkarni, C.V., O. Ces, R.H. Templer, and J.M. Seddon. 2013. Pressure effects on a protein–lipid model membrane. *Soft Matter*. 9:6525.

21. Shyamsunder, E., P. Botos, and S.M. Gruner. 1989. Comment on: X-ray diffraction study of the effects of pressure on bilayer to nonbilayer lipid membrane phase transitions. *J. Chem. Phys.* 90:1293–1295.

22. Winnikoff, J.R., and I. Budin. 2025. Homeocurvature: A new dimension of membrane adaptation to extreme environments. *Prog. Lipid Res.* 101355.

23. Winnikoff, J.R., D. Milshteyn, S.J. Vargas-Urbano, M.A. Pedraza-Joya, A.M. Armando, O. Quehenberger, A. Sodt, R.E. Gillilan, E.A. Dennis, E. Lyman, S.H.D. Haddock, and I. Budin. 2024. Homeocurvature adaptation of phospholipids to pressure in deep-sea invertebrates. *Science*. 384:1482–1488.

24. Milshteyn, D., J.R. Winnikoff, E. Kocharian, A.M. Armando, E.A. Dennis, P.R. Girguis, and I. Budin. 2026. Active regulation of intrinsic curvature by eukaryotic phospholipid metabolism. *Cell Rep. Phys. Sci.* 0:103277.

25. Rai, D.K., R.E. Gillilan, Q. Huang, R. Miller, E. Ting, A. Lazarev, M.W. Tate, and S.M. Gruner. 2021. High-pressure small-angle X-ray scattering cell for biological solutions and soft materials. *J. Appl. Crystallogr.* 54:111–122.

26. Hopkins, J.B., R.E. Gillilan, and S. Skou. 2017. *BioXTAS RAW* : improvements to a free open-source program for small-angle X-ray scattering data reduction and analysis. *J. Appl. Crystallogr.* 50:1545–1553.

27. Frewein, M.P.K., M. Rumetshofer, and G. Pabst. 2019. Global small-angle scattering data analysis of inverted hexagonal phases. *J. Appl. Crystallogr.* 52:403–414.

28. Tate, M.W., and S.M. Gruner. 1989. Temperature dependence of the structural dimensions of the inverted hexagonal (HII) phase of phosphatidylethanolamine-containing membranes. *Biochemistry*. 28:4245–4253.

29. Shendrik, P., R. Sorkin, and G. Golani. 2025. Fusion of asymmetric membranes: the emergence of a preferred direction. *Faraday Discuss.* 259:416–436.

30. Zucker, B., G. Golani, and M.M. Kozlov. 2023. Model for ring closure in ER tubular network dynamics. *Biophys. J.* 122:1974–1984.

31. Uster, P.S., and D.W. Deamer. 1981. Fusion competence of phosphatidylserine-containing liposomes quantitatively measured by a fluorescence resonance energy transfer assay. *Arch. Biochem. Biophys.* 209:385–395.

32. Feigenson, G.W. 1986. On the nature of calcium ion binding between phosphatidylserine lamellae. *Biochemistry*. 25:5819–5825.

33. Hamm, M., and M.M. Kozlov. 2000. Elastic energy of tilt and bending of fluid membranes. *Eur. Phys. J. E Soft Matter*. 3:323–335.

34. Dymond, M.K., C.V. Hague, A.D. Postle, and G.S. Attard. 2013. An in vivo ratio control mechanism for phospholipid homeostasis: evidence from lipidomic studies. *J. R. Soc. Interface*. 10:20120854.

35. Bills, B.L., M.L. Hulser, and M.K. Knowles. 2024. Phospholipase D1 produces phosphatidic acid at sites of secretory vesicle docking and fusion. *Mol. Biol. Cell*. 35:ar39.

36. Mérida, I., A. Avila-Flores, and E. Merino. 2008. Diacylglycerol kinases: at the hub of cell signalling. *Biochem. J.* 409:1–18.

37. Vance, J.E., and G. Tasseva. 2013. Formation and function of phosphatidylserine and phosphatidylethanolamine in mammalian cells. *Biochim. Biophys. Acta*. 1831:543–554.

38. Dymond, M.K. 2016. Mammalian phospholipid homeostasis: evidence that membrane curvature elastic stress drives homeoviscous adaptation in vivo. *J. R. Soc. Interface*. 13.

39. Levental, K.R., E. Malmberg, J.L. Symons, Y.-Y. Fan, R.S. Chapkin, R. Ernst, and I. Levental. 2020. Lipidomic and biophysical homeostasis of mammalian membranes counteracts dietary lipid perturbations to maintain cellular fitness. *Nat. Commun.* 11:1339.